

# Physics of Josephson diodes formed from 1T-transition metal dichalcogenides

## Dissertation

zur Erlangung des Doktorgrades der Naturwissenschaften  
(Dr. rer. nat.)

der Naturwissenschaftlichen Fakultät II  
Chemie, Physik und Mathematik

der Martin-Luther-Universität  
Halle-Wittenberg

vorgelegt von

Herrn **Pranava Keerthi Sivakumar**

Gutachter:

Prof. Dr. Stuart S. P. Parkin

Prof. Dr. Ingrid Mertig

Prof. Dr. Takis Kontos

Tag der öffentlichen Verteidigung:

29.05.2024



*To Thaathaa, Ammamma, Amma, Appa and  
Anna*

*Their unfaltering and unfettered love is what  
kept me running this far....*



# Abstract

---

## Physics of Josephson diodes formed from 1T-transition metal dichalcogenides

Non-reciprocal critical current in superconductors labelled the superconducting diode effect has attracted a lot of attention in recent years for its potential to create energy-efficient superconducting devices for computing applications. In this thesis, the observation of similar non-reciprocal critical currents in Josephson junctions made of two van der Waals transition metal dichalcogenides 1T-NiTe<sub>2</sub> and 1T-PtTe<sub>2</sub>, named the Josephson diode effect is reported. The hidden inversion-symmetry breaking in the structure of these materials naturally gives rise to a helical spin-momentum locking in the band structure. The origin of the effect is discussed in terms of a non-zero center of mass Cooper pair momentum created due to the shift of the spin-momentum locked states in an external Zeeman field.

In 1T-NiTe<sub>2</sub>, this hypothesis is verified by comparing the experimental results to a Ginzburg-Landau model of the Josephson junction expanded up to the second order. The presence of a finite momentum is further verified by measuring the evolution of the Fraunhofer pattern in the presence of an additional in-plane magnetic field that creates finite Cooper pair momentum and investigating the modification to the pattern. The Cooper pair momentum estimated from these measurements are in good agreement with those estimated from the Josephson diode effect.

In the case of 1T-PtTe<sub>2</sub>, the presence of a helical spin-momentum locking is verified through measurement of the Josephson diode effect in lateral junctions. Extrinsic mechanisms that can give rise to a Josephson diode effect are identified and nullified. A generic current-phase relationship model analogous to that used in NiTe<sub>2</sub>, is used to evaluate the evolution of the Josephson diode effect in the junction. Measurements of the Josephson diode effect in the presence of a magnetic flux at different in-plane magnetic fields reveal the presence of a large Josephson diode effect that is directly related to the second harmonic term in the current-phase relationship. The current-phase relationship now labelled as second order  $\varphi_0$  -junction current-phase relationship is shown to be unique and different from typical  $\varphi$  - and  $\varphi_0$  -junctions. The existence of a second order  $\varphi_0$  -junction behavior is further confirmed by studying the evolution of the Josephson diode effect with magnetic flux which produces oscillations that have nodes every half flux quantum ( $\frac{\Phi_0}{2}$ ) as opposed to the critical currents themselves which have one flux quantum period ( $\Phi_0$ ). The evolution of the Josephson diode effect simulated with the second

harmonic term obtained previously is also in good agreement with the measurements confirming the accuracy of the assumed current-phase relationship. The origin of the large second harmonic term in the PtTe<sub>2</sub> junction is discussed in terms of the helical spin-momentum locked states which promotes higher order Andreev reflections. The presence of a transparent interface that promotes coherent Andreev reflections is revealed by the presence of excess currents and fitting the critical current as a function of temperature. A second order  $\varphi_0$  -junction provides the unique possibility of tuning the relative phase between the two harmonics rendering it useful for practical applications in separating the two harmonics of the supercurrents in the junction.

# Zusammenfassung

---

## Physics of Josephson diodes formed from 1T-transition metal dichalcogenides

Nichtreziproke kritische Ströme in Supraleitern, die als supraleitender Diodeneffekt bezeichnet werden, haben in den letzten Jahren aufgrund ihres Potenzials zur Entwicklung energieeffizienter supraleitender Geräte für Computeranwendungen große Aufmerksamkeit erregt. In dieser Arbeit wird über die Beobachtung ähnlicher nichtreziproker kritischer Ströme in Josephson-Übergängen aus zwei Van-der-Waals-Übergangsmetaldichalkogeniden 1T-NiTe<sub>2</sub> und 1T-PtTe<sub>2</sub> berichtet, die als Josephson-Diodeneffekt bezeichnet werden. Der verborgene Bruch der Inversionssymmetrie in der Struktur dieser Materialien führt auf natürliche Weise zu einer helikalen Spin-Impuls-Verriegelung in der Bandstruktur. Der Ursprung des Effekts wird im Hinblick auf einen von Null verschiedenen Schwerpunkt-Cooper-Paar-Impuls diskutiert, der aufgrund der Verschiebung der Spin-Impuls-gesperrten Zustände in einem externen Zeeman-Feld entsteht.

In 1T-NiTe<sub>2</sub> wird diese Hypothese durch den Vergleich der experimentellen Ergebnisse mit einem bis zur zweiten Ordnung erweiterten Ginzburg-Landau-Modell des Josephson-Kontakts verifiziert. Das Vorhandensein eines endlichen Impulses wird weiter verifiziert, indem die Entwicklung des Fraunhofer-Musters in Gegenwart eines zusätzlichen Magnetfelds in der Ebene gemessen wird, das einen endlichen Cooper-Paar-Impuls erzeugt, und die Modifikation des Musters untersucht wird. Der aus diesen Messungen geschätzte Cooper-Paar-Impuls stimmt gut mit den aus dem Josephson-Diodeneffekt geschätzten Impulsen überein.

Im Fall von 1T-PtTe<sub>2</sub> wird das Vorhandensein einer helikalen Spin-Impuls-Verriegelung durch Messung des Josephson-Diodeneffekts in lateralen Übergängen bestätigt. Extrinsische Mechanismen, die zu einem Josephson-Diodeneffekt führen können, werden identifiziert und beseitigt. Zur Bewertung der Entwicklung des Josephson-Diodeneffekts im Übergang wird ein generisches Strom-Phasen-Beziehungsmodell verwendet, das dem in NiTe<sub>2</sub> verwendeten Modell ähnelt. Messungen des Josephson-Diodeneffekts in Gegenwart eines magnetischen Flusses bei verschiedenen Magnetfeldern in der Ebene zeigen das Vorhandensein eines großen Josephson-Diodeneffekts, der direkt mit dem zweiten harmonischen Term in der Strom-Phasen-Beziehung zusammenhängt. Die Strom-Phasen-Beziehung, die jetzt als Strom-Phasen-Beziehung  $\varphi_0$ -Übergang zweiter Ordnung bezeichnet wird, erweist sich als

einzigartig und unterscheidet sich von typischen  $\varphi$  – und  $\varphi_0$  – Übergängen. Die Existenz eines  $\varphi_0$  –Übergangsverhaltens zweiter Ordnung wird weiter bestätigt, indem die Entwicklung des Josephson-Diodeneffekts mit magnetischem Fluss untersucht wird, der Schwingungen erzeugt, die bei jedem halben Flussquantum  $\left(\frac{\Phi_0}{2}\right)$  Knoten haben, im Gegensatz zu den kritischen Strömen selbst, die dies haben eine Flussquantenperiode  $(\Phi_0)$ . Die mit dem zuvor erhaltenen Term der zweiten Harmonischen simulierte Entwicklung des Josephson-Diodeneffekts stimmt ebenfalls gut mit den Messungen überein, was die Genauigkeit der angenommenen Strom-Phasen-Beziehung bestätigt. Der Ursprung des großen Terms der zweiten Harmonischen im PtTe<sub>2</sub>-Übergang wird im Hinblick auf die spiralförmigen Spin-Momentum-verriegelten Zustände diskutiert, die Andreev-Reflexionen höherer Ordnung fördern. Das Vorhandensein einer transparenten Grenzfläche, die kohärente Andreev-Reflexionen fördert, wird durch das Vorhandensein von Überschussströmen und die Anpassung des kritischen Stroms als Funktion der Temperatur offenbart. Ein  $\varphi_0$  –Übergang zweiter Ordnung bietet die einzigartige Möglichkeit, die relative Phase zwischen den beiden Oberschwingungen abzustimmen, was für praktische Anwendungen nützlich ist, um die beiden Oberschwingungen der Superströme in dem Übergang zu trennen.



# Acknowledgments

---

Throughout my remarkable journey as a Ph.D. candidate at the Max Planck Institute of Microstructure Physics, I have had the unwavering support and guidance of numerous people without whom the research presented in this dissertation would be inconceivable. I am profoundly indebted to Stuart for having given me the opportunity to join and contribute to the NISE department. He had been supportive to me all through my tenure at NISE and has always encouraged being independent, embracing challenges, and choosing scientific problems meticulously with their impact in mind. This also helped think beyond my own research work, with different perspectives and an overarching picture in mind. It is the path less treaded that holds the treasures but it is also possible to easily get lost in this endeavour. A good supervisor is a guiding light who can take us to our goals without getting lost, as Stuart has been in my case. I found his remarkable ability to meet and discuss with different people on different topics from the department quite impressive and hope to catch up to half his capacity someday. He had also entrusted me with the full responsibilities of cutting-edge low temperature systems during my nascent stages as a PhD student, to which I am extremely grateful. This helped shape my journey through PhD as an experimentalist, learning to build up, manage and optimize operations on the dilution fridges.

I am grateful for all the mentoring I had in the early days of my Ph.D. from senior colleagues, Edouard Lesne and James Taylor. Their guidance helped me navigate through many difficulties during my early days at MPI and adapting to life in Halle. They trained me on a variety of equipment at the institute which helped kick starting my research at the institute. The synchrotron visits to BESSY and SOLEIL were enjoyable experiences, thanks to them. I would also like to thank senior members of the group who had helped me during my time as a Ph.D. student, transferred some of their knowledge to me and whose contributions to the group made life a lot easier, Binoy Krishna Hazra, Jae-chun Jeon, Takahiro Fujita, Kumari Gaurav Rana, Neeraj Kumar, Malleswara Rao Tangi, Andrea Miglorini, Hakan Deniz, Rana Saha, Samiran Choudhury. Though we do not have any published work together, I would like to specially thank Binoy, for without his persistence and calmness it would have not been possible to have optimized the hard

mask in MANGO for producing very high quality tunnel junctions. I wish him the best at IIT Guwahati.

I would also like to make a special mention to Elisa (Shuo-ying) Yang who first taught me to exfoliate van der Waals materials and fabricate heterostructures. During tough times in cryolab, she was always there to lighten the mood and it would be an understatement to say we learnt about electrostatic discharge protection and ground loops the hard way. I would like to thank my peer group for useful discussions inside the lab and a fun time outside the lab throughout my graduate school journey, Abhay, Amine, Andre Farinha, Ankit, Berthold, Bharat, Elena, Hao Yang, Jagganath, Jiho, Kajal, Lukas, Mihir, Pedram, Prajwal and Souvik.

As a budding researcher, it is invaluable to have to have the support and counsel of experienced scientists. I would also like to thank my distinguished collaborators who have enriched my scientific research through their support, knowledge and with whom I have had invaluable discussions, Prof. Claudia Felser (MPI-CPfS), Prof. Liang Fu (MIT), Prof. Matthew Gilbert (UIUC), Prof. Titus Neupert (Uni. Zurich), Prof. Amir Yacoby (Harvard), Prof. Ingrid Mertig (MLU), Dr. Mazhar Ali and Dr. Niels Schröter. I owe my gratitude to my alma mater Indian Institute of Science (IISc) for having given me an exceptional peer group and the opportunity to be in the company of outstanding scientists, who continue to inspire me and have had a great role in enhancing my critical thinking. I would also like to specially acknowledge DD for having mentored and guided me when I was taking just baby steps in research. His unwavering spirit and cheerful attitude has always motivated me to stay positive during tough times.

I would like to specially thank Mostafa Tanhayi Ahari (UIUC) for having worked meticulously with me in simulating and understanding the current-phase relations in PtTe<sub>2</sub>. I would also like to thank my other collaborators Yaojia Wang, Heng Wu, Börge Göbel (MLU), Anastasios Markou (MPI-CPfS), Jae-keun Kim, Banabir Pal, Margarita Davydova (MIT), Ajesh Kollakuzhiyil Gopi and Anirban Chakraborty. I also appreciate Swapna, Anvesh, Jagganth and Ankush for their efforts in proofreading my thesis. I would also like to thank the newer generation of graduate students Anvesh, Yufeng, Jitul, and Ivan for their help with measurements. I am sure the repute of the institute is safe with them.

I would like to express gratitude for the support offered by the technical staff at the institute who assisted me in the maintenance of all cryogenic equipment and upgrading their capabilities.

Special thanks goes to Kai-Uwe Aßmann, Peter Grünewald, Winfried Heichler, Pierre-Jean Zermatten, to the electrical workshop team: Klaus Haenecke, Michael Oppelt and Detlef Proske, the mechanical workshop and the haustechnik. I would like to thank Mike Borrmann and the CSG for IT support. I would like to whole-heartedly thank Antje Paetzold, Michael Strauch, Simone Jäger, Martha Schulz and Ann-Kristin Flieger for keeping track and helping me navigate the massive bureaucratic hurdles during my Ph.D. in Germany starting from my visa to university regulations to many other aspects of my life in Germany, both personal and professional. I would also like to thank people from the central administration of the institute who also helped navigate various bureaucratic procedures during purchasing of new equipment, extension of residence permit, business travel, inventory management, etc. Special thanks to Andreas Berger, Martina Witzig, Robert Gille, Tobias Schmidt, Andrea Amm, Birgit Frankenstein, Claudia Gietzelt, Katja Ballin, Manuela Kamprath and Laura Bär. I would also like to thank Karo for being the go-to German expert in Halle and a good friend.

Finally yet most importantly, I owe my gratitude the members of my family and all my relatives for their constant support and love, which were my bedrock throughout this journey. My successes are completely built on their sacrifices and it would not have been possible to grind through the arduousness of graduate school without their complete understanding and support. I would like to thank my sisters, Rima and Dipu for having served me great food, which on many days saved me from starvation and I must say some of their amazing cooking skills rubbed on to me. I would like to thank Avanindra for having helped me with Python coding many a times. His calm and composed demeanor is something that I venerate. I would also like to thank Twinkle who is one of my very few friends outside of MPI for having an open ear to my problems and helping me during tough times. This section would be incomplete without me mentioning my special, cherished cohort from IISc, Arventh, Anu, Siva, Matta, Ashwin and Hamilton, with whom I can discuss anything without any reservations at all times. Though it has been more than six years since we parted ways and we are scattered all across the globe, we always remain connected with each other through a special bond and it feels as if we are always right next to each other.

Pranava Keerthi Sivakumar

08.08.2023

# Contents

---

Title page .....	i
Abstract .....	v
Zusammenfassung .....	vii
Acknowledgments .....	ix
Contents .....	xii
Citations to previous work .....	xvii
List of Figures .....	xviii
List of Tables .....	xxii
Abbreviations .....	xxiii
<b>1 Introduction and scope of the thesis .....</b>	<b>1</b>
<b>2 Theoretical Foundations .....</b>	<b>7</b>
2.1 Introduction to superconductivity .....	8
2.1.1 Historical overview .....	8
2.1.2 Electrodynamics of superconductors – London equations .....	11
2.1.3 Ginzburg-Landau theory of superconductivity .....	13
2.1.4 BCS theory of superconductivity .....	15
2.1.5 Finite-momentum superconductivity .....	19
2.2 Josephson junctions .....	21
2.2.1 Introduction .....	21

2.2.2	DC and AC Josephson effects . . . . .	21
2.2.3	RCSJ model and current-voltage characteristics . . . . .	24
2.2.4	Quantum interference in Josephson junctions . . . . .	30
2.3	Non-reciprocal transport in superconductors . . . . .	33
2.3.1	Introduction . . . . .	33
2.3.2	Onsager's reciprocal relation . . . . .	34
2.3.3	Magneto-chiral anisotropy . . . . .	35
2.3.4	Supercurrent Diode Effect . . . . .	36
2.3.4.1	Introduction . . . . .	36
2.3.4.2	Symmetry requirements . . . . .	37
2.3.4.3	State-of-the-art in supercurrent diodes . . . . .	38
2.4	Hidden Inversion symmetry breaking and Superconductivity. .	41
2.4.1	Introduction . . . . .	41
2.4.2	Hidden spin-momentum locking in 1T(trigonal) and 2H(hexagonal) transition metal dichalcogenides (TMDCs) . . . . .	43
2.4.3	Cooper pairing in 2H- and 1T- TMDCs . . . . .	46
<b>3</b>	<b>Experimental methods . . . . .</b>	<b>49</b>
3.1	Introduction . . . . .	50
3.2	Device fabrication . . . . .	50
3.2.1	Mechanical exfoliation of van der Waals materials . . . . .	50
3.2.2	Photolithography . . . . .	53
3.2.3	Electron-beam lithography . . . . .	54
3.2.4	Ion-beam milling and Ion-beam deposition . . . . .	56

3.3	Device characterization . . . . .	58
3.3.1	Atomic Force Microscopy (AFM) . . . . .	58
3.3.2	Scanning Electron Microscopy (SEM) . . . . .	60
3.4	Electrical transport . . . . .	61
3.4.1	Physical Property Measurement System (PPMS) DynaCool® . . . . .	61
3.4.2	Bluefors LD-400 measurement setup . . . . .	62
3.4.2.1	Introduction . . . . .	62
3.4.2.2	Dilution refrigeration technique . . . . .	65
3.4.2.3	High-frequency filtering and electron thermalization . . . . .	67
3.4.2.4	Sample holder and electrostatic discharge (ESD) protection protocol . . . . .	73
3.4.2.5	Measurement and control electronics programming with LabVIEW . . . . .	75
<b>4</b>	<b>Josephson diode effect induced by finite momentum Cooper pairing in a topological Rashba system 1T-NiTe<sub>2</sub> . . . . .</b>	<b>77</b>
4.1	Introduction . . . . .	77
4.2	Crystal structure . . . . .	79
4.3	Electronic structure . . . . .	81
4.4	Josephson junctions of NiTe <sub>2</sub> . . . . .	82
4.4.1	Fabrication and basic characterization . . . . .	82
4.4.2	Josephson diode effect (JDE or $\Delta I_C$ ) in NiTe <sub>2</sub> . . . . .	85
4.4.3	Spin-momentum locking induced finite momentum pairing . . . . .	87
4.4.4	Ginzburg-Landau theory of Josephson diode effect . . . . .	92

4.4.5	Temperature dependence of $\Delta I_C$ . . . . .	94
4.4.6	Magnetic field and angular dependence of $\Delta I_C$ . . . . .	95
4.4.7	Finite momentum Cooper pairing in NiTe <sub>2</sub> from $\Delta I_C$ . . . . .	98
4.4.8	Estimating finite momentum from the evolution of Fraunhofer pattern . . . . .	99
4.4.9	Alternative explanation for the origin of $\Delta I_C$ . . . . .	103
4.5	Conclusion . . . . .	104
<b>5</b>	<b>Helical spin-momentum locking and second-order <math>\varphi_0</math>-junctions in the Dirac semimetal 1T-PtTe<sub>2</sub> probed by the Josephson diode effect . . . . .</b>	<b>107</b>
5.1	Introduction . . . . .	108
5.2	Crystal structure . . . . .	109
5.3	Electronic structure . . . . .	111
5.4	Electrical transport in PtTe <sub>2</sub> flakes . . . . .	112
5.5	Fabrication of Josephson junctions with PtTe <sub>2</sub> . . . . .	114
5.5.1	Lateral junctions of PtTe <sub>2</sub> flakes . . . . .	114
5.5.2	Vertical junctions of PtTe <sub>2</sub> . . . . .	116
5.6	Josephson diode effect in PtTe <sub>2</sub> junctions . . . . .	117
5.6.1	Basic characterization of the lateral PtTe <sub>2</sub> Josephson junction L1	117
5.6.2	Self-consistent simulations of critical currents . . . . .	120
5.6.3	Josephson diode effect due to extrinsic mechanisms . . . . .	120
5.6.3.1	Absence of geometric shape inversion asymmetry . . . . .	120
5.6.3.2	Self-field induced extrinsic JDE in wide PtTe <sub>2</sub> junctions . . .	121

5.6.4	Helical spin-momentum locking in PtTe <sub>2</sub> junctions . . . . .	124
5.7	Tunable current-phase relationship in PtTe <sub>2</sub> junctions . . . . .	128
5.7.1	Current-phase relationship model for PtTe <sub>2</sub> junctions . . . . .	128
5.7.2	Evolution of interference pattern under $\delta$ and $\varphi$ . . . . .	130
5.7.3	Second Harmonic nature of $\Delta I_c$ . . . . .	133
5.8	Possible origin of strong coherence in PtTe <sub>2</sub> . . . . .	136
5.9	Conclusion . . . . .	139
<b>6</b>	<b>Conclusions and outlook . . . . .</b>	<b>143</b>
	<b>Appendix . . . . .</b>	<b>149</b>
A	Field-free Josephson diode effect in Nb <sub>3</sub> Br <sub>8</sub> . . . . .	150
B	Self-consistent simulations of critical currents in Josephson junctions . . . . .	152
C	Flux focusing and Estimation of effective junction area for diffraction pattern calculations . . . . .	156
D	Effect of finite thickness of PtTe <sub>2</sub> on the interference pattern . .	159
E	Josephson Diode effect in other NiTe <sub>2</sub> devices . . . . .	162
F	Evolution of Fraunhofer pattern in other PtTe <sub>2</sub> devices . . . . .	164
G	Field-free $\Delta I_c$ from self-field effects in PtTe <sub>2</sub> Josephson junction . . . . .	169
	<b>Bibliography . . . . .</b>	<b>171</b>
	<b>Curriculum vitae . . . . .</b>	<b>183</b>
	<b>List of publications and patents . . . . .</b>	<b>185</b>
	<b>Eidesstattliche erklärung (Statutory declaration) . . . . .</b>	<b>187</b>



# Citations to previous work

---

The results, text and figures used in some of the chapters in this thesis are adapted from some of my previously published works and manuscripts under review. Following are the list of chapters and the corresponding works.

Chapter 4 “**Josephson diode effect induced by finite momentum Cooper pairing in a topological Rashba system 1T-NiTe<sub>2</sub>**” is adapted from reference <sup>1</sup>.

B. Pal\*, A. Chakraborty\*, **P. K. Sivakumar\***, M. Davydova\*, A. K. Gopi, A. K. Pandeya, J. A. Krieger, Y. Zhang, M. Date, S. Ju, N. Yuan, N. B. M. Schroeter, L. Fu and S. S. P. Parkin. “Josephson diode effect from Cooper pair momentum in a topological semimetal”. *Nat. Phys.* 18, 1228–1233 (2022). (\* – equal contributions)

Chapter 5 “**Helical spin-momentum locking and second order  $\varphi_0$  –junctions in the Dirac semimetal 1T-PtTe<sub>2</sub> probed by the Josephson diode effect**” is adapted from a manuscript under preparation.

**P. K. Sivakumar**, M. T. Ahari, J.-K. Kim, Y. Wu, A. Dixit, G. J. de Coster, A. K. Pandeya, M. Gilbert and S. S. P. Parkin. “Long-range Phase Coherence and Second Order  $\varphi_0$  –Josephson Effect in a Dirac semimetal 1T-PtTe<sub>2</sub>”.

under review in *Communications Physics*. Preprint available at: *arXiv:2403.19445* (2024).

Appendix section A “**Field-free Josephson diode effect in Nb<sub>3</sub>Br<sub>8</sub>**” is adapted from reference <sup>2</sup>.

H. Wu\*, Y. Wang\*, Y. Xu, **P. K. Sivakumar**, C. Pasco, U. Filippozzi, S. S. P. Parkin, Y. -J. Zeng, T. McQueen and M. N. Ali. “The field-free Josephson diode in a Van der Waals heterostructure”. *Nature* 604 (7907), 653-656 (2021). (\* – equal contributions)

# List of Figures

---

1.1	Representation of a lateral Josephson junction hosting the diode effect . . . . .	3
2.1	Timeline of superconductors . . . . .	10
2.2	Cooper pair in a lattice . . . . .	16
2.3	Finite momentum superconductivity . . . . .	20
2.4	Schematic of a Josephson junction . . . . .	23
2.5	RCSJ circuit model . . . . .	25
2.6	Tilted washboard potential . . . . .	28
2.7	Underdamped and overdamped junctions . . . . .	29
2.8	Quantum interference of the superconducting order parameter . . . . .	32
2.9	Magneto-chiral anisotropy . . . . .	36
2.10	Superconducting diode effect (SDE) in $[\text{Nb/V/Ta}]_n$ . . . . .	39
2.11	Josephson diode effect in an array of InAs junctions . . . . .	40
2.12	Polarity controlled zero field JDE in Pt/YIG heterostructure junctions . . . . .	41
2.13	Schematic of 2H and 1T structures . . . . .	43
2.14	Local electric dipoles in 1T structure . . . . .	44
2.15	Ising spin-polarization in 2H-WSe <sub>2</sub> . . . . .	45
2.16	Ising pairing in 1H-NbSe <sub>2</sub> and 1H-TaS <sub>2</sub> . . . . .	47
2.17	Fermi surface of 1T-NiTe <sub>2</sub> . . . . .	48
3.1	Mechanical exfoliation of PtTe <sub>2</sub> . . . . .	53
3.2	Optical lithography process . . . . .	54

3.3	E-beam lithography calibration . . . . .	56
3.4	Ion beam milling and deposition chamber . . . . .	58
3.5	Atomic force microscopy (AFM) . . . . .	59
3.6	Scanning electron microscopy (SEM) images . . . . .	60
3.7	Physical Property Measurement System (PPMS) options . . . . .	62
3.8	Bluefors LD-400 Dilution Refrigerator . . . . .	64
3.9	Thermodynamics of $^3\text{He}$ - $^4\text{He}$ mixture . . . . .	66
3.10	QDevil filters and high frequency characteristics . . . . .	70
3.11	Superconducting tunneling spectroscopy and electron temperature . . . . .	73
3.12	QBoard mounted on a sample puck . . . . .	75
3.13	LabVIEW program for measurement of I-V characteristics . . . . .	76
4.1	Crystal structure of $\text{NiTe}_2$ . . . . .	80
4.2	Type-II Dirac cone in $\text{NiTe}_2$ . . . . .	82
4.3	Josephson junction device structure and resistance–temperature profile of 350 nm junction . . . . .	83
4.4	Fraunhofer oscillations in 550 nm junction . . . . .	84
4.5	Josephson diode effect in presence of a magnetic field . . . . .	86
4.6	Underlying Fermi surface and Cooper pairs in a conventional BCS superconductor in the absence of a current and external magnetic field . . . . .	88
4.7	Underlying Fermi surface and Cooper pairs in a conventional BCS superconductor in the presence of a current . . . . .	89
4.8	Underlying Fermi surface and Cooper pairs of a superconductor with Rashba spin-momentum locking . . . . .	90
4.9	Underlying Fermi surface and Cooper pairs of a superconductor with Rashba spin-momentum locking in the presence of a magnetic field . . . . .	91
4.10	Underlying Fermi surface and Cooper pairs of a superconductor with Rashba spin-momentum locking in the presence of a magnetic field and current . . . . .	92

4.11	Temperature dependence of Josephson diode effect . . . . .	95
4.12	Magnetic field dependence of Josephson diode effect . . . . .	97
4.13	Angular dependence of Josephson diode effect . . . . .	98
4.14	Measurement of the finite momentum Cooper pairing in NiTe <sub>2</sub> Josephson junctions . . .	102
5.1	Locally broken inversion symmetry in PtTe <sub>2</sub> . . . . .	110
5.2	Spin- and angle-resolved photoemission spectroscopy of PtTe <sub>2</sub> . . . . .	112
5.3	Electrical transport in PtTe <sub>2</sub> Hall bars . . . . .	113
5.4	Lateral PtTe <sub>2</sub> Josephson junctions . . . . .	115
5.5	Vertical PtTe <sub>2</sub> Josephson junctions . . . . .	116
5.6	Non-reciprocal critical currents in PtTe <sub>2</sub> Josephson junctions . . . . .	119
5.7	Josephson diode effect in PtTe <sub>2</sub> junctions of different geometry . . . . .	121
5.8	Self-field effects in wide PtTe <sub>2</sub> junctions . . . . .	123
5.9	Analysis of $\Delta I_c$ with magnetic field magnitude, angle and temperature for junction L1.	125
5.10	Absence of Josephson diode effect in a vertical junction of PtTe <sub>2</sub> . . . . .	127
5.11	Evolution of the Fraunhofer pattern in the presence of $\Delta I_c$ for junction L1. . . . .	132
5.12	Evolution of $\Delta I_c$ with $\delta$ and $\phi$ in junction L1 . . . . .	135
5.13	Transparency of PtTe <sub>2</sub> Josephson junctions . . . . .	138
5.14	Coherent Andreev processes promoted by the helical spin-momentum locking in PtTe <sub>2</sub>	140
5.15	Evolution of second-harmonic supercurrents with $I_c$ in PtTe <sub>2</sub> . . . . .	142
6.1	Evaluation of Josephson diode efficiency in various materials . . . . .	147
A.1	Schematic of the vertical Josephson junction and I – V curve for the junction . . . . .	150
A.2	Non-reciprocal voltages in Nb <sub>3</sub> Br <sub>8</sub> junction . . . . .	151
A.3	Magnetic field dependence of $\Delta I_c$ in Nb <sub>3</sub> Br <sub>8</sub> junctions . . . . .	152
C.1	The calculated Fraunhofer interference pattern for various values of $I_2/I_1$ . . . . .	158

C.2	The Fraunhofer interference pattern for L1 under before and after correcting for flux focusing .....	159
D.1	Evolution of Fraunhofer pattern for L1 under an in-plane magnetic field and shift correction .....	161
E.1	Josephson Diode effect in a 40nm thick NiTe <sub>2</sub> flake .....	162
E.2	Distance dependence of the Josephson energy ( $I_c R_n$ ) in NiTe <sub>2</sub> Josephson junctions ..	164
F.1	Evolution of the Fraunhofer pattern in the presence of $\Delta I_c$ for L4 .....	164
F.2	Evolution of the Fraunhofer pattern in the presence of $\Delta I_c$ for L3 .....	165
F.3	Fraunhofer interference pattern for L1 under positive and negative magnetic fields after shift correction .....	166
F.4	Behavior of $\Delta I_c$ in presence of a small magnetic flux .....	167
F.5	Accidental SQUID in junction L2 .....	167
F.6	Possible multiple Andreev reflections .....	168
G.1	Field-free $\Delta I_c$ from self-field effect in PtTe <sub>2</sub> junction L1 .....	170

# List of Tables

---

2.1	Classification of non-reciprocal responses in non-centrosymmetric materials based on the type of response and the presence or absence of time-reversal symmetry . . . . .	33
2.2	Classification of centrosymmetric and non-centrosymmetric space groups based on atomic point group symmetries along with possible spin-momentum locking . . . . .	42
5.1	Summary of PtTe <sub>2</sub> junctions . . . . .	141

# Abbreviations

---

GL	Ginzburg-Landau
BCS	Bardeen-Cooper-Schrieffer
DC	Direct current
AC	Alternating current
RCSJ	Resistively and capacitively shunted Josephson junctions
TMDC	Transition metal dichalcogenide
T	Trigonal
H	Hexagonal
AFM	Atomic force microscope
SEM	Scanning electron microscope
PPMS	Physical Property Measurement System
ESD	Electrostatic discharge
SDE	Superconducting diode effect
JDE	Josephson diode effect
FMCP	Finite momentum Cooper pairing
FFLO	Fulde-Ferrell-Larkin-Ovchinnikov
YIG	Yttrium iron garnet
SOC	Spin orbit coupling
CPR	Current phase relationship
IBM	International Business Machines
SQUID	Superconducting Quantum Interference Device
CC	Creative Commons
MCA	Magneto-chiral anisotropy
ARPES	Angle resolved photoemission spectroscopy
SARPES	Spin and angle resolved photoemission spectroscopy

DFT	Density functional theory
MLA	Maskless aligner
GDS	Graphic data system
PMMA	Polymethylmethacrylate
PDMS	Polydimethylsiloxane
PPC	Polypropylenecarbonate
IPA	Isopropanol
SIMS	Secondary-ion mass spectrometry
IBD	Ion beam deposition
MFC	Mass flow controller
VdW	Van der Waals
RF	Radio frequency
RC	Audio frequency
FC/PC	Fiber channel/ Physical contact
GHS	Gas handling system
MXC	Mixing chamber
FSE	Fast sample exchange
PCB	Printed circuit board
MFLI	Multi-frequency lock-in amplifier
QAHE	Quantum anomalous Hall effect
TSS	Topological surface state
SFE	Self field effect
FFT	Fast Fourier transform
OTBK	Octavio-Tinkham-Blonder-Klapwijk
MAR	Multiple Andreev reflections



# 1

---

## Introduction and scope of the thesis

The non-reciprocal electrical conductivity in a semiconducting  $p - n$  junction diode is a crucial, fundamental technological discovery that has helped the exponential development of computing power since the late 20<sup>th</sup> century and has enabled today's modern semiconducting devices that permeate our everyday life. The semiconductor industry has been able to roughly double the computing power of the integrated circuits every year by miniaturizing the semiconductor components as predicted by Gordon Moore in 1965<sup>3</sup>. As these components reach their fundamental physical limit and Moore's law comes to an end, there is the need to look for alternative platforms for solutions that can provide greater and more energy efficient computing power. Superconductivity, the physical state of solids with zero resistance, has been of great interest fundamentally and technologically since its discovery for its ability to transmit electrical currents with no Joule dissipation, which is the major source of energy loss in most electronic devices. It has already found some applications in the form of Josephson junctions, which are the most important circuit elements of a superconducting quantum bit<sup>4</sup>, used in quantum computation. Quantum computing holds great promise in unlocking a new realm of solutions to problems that were previously inaccessible by classical computing. However, this does not obviate the need for better and energy efficient classical computers. Hence, it is key to explore superconductors as an alternate platform for classical computing bits and logic elements. There has been a lot of interest over the years in the development of superconducting logic and memory<sup>5</sup>.

The discovery of controlled non-reciprocal critical currents in a superconducting heterostructure in 2020, dubbed the 'superconducting diode effect'<sup>6</sup> renewed this interest and provided impetus along this new direction of research. The effect was attributed to the presence of Rashba spin-momentum locking due to the broken inversion symmetry at the interface of the superconductors but a more detailed explanation to the temperature and magnetic field behavior was lacking theoretically and microscopically. Non-reciprocal conductivity in such systems offered by the unidirectional flow of supercurrents is analogous to a semiconductor diode and provides a natural platform for exploring applications in superconducting logic devices. Hence, it is of great interest to understand the underlying origin of this effect to be able to tune it precisely. A similar supercurrent diode effect was observed in a Josephson junction array made of InAs and aluminium<sup>7</sup>, dubbed the 'Josephson diode effect'. The observation of a supercurrent diode effect in Josephson junctions is rather advantageous, as the utility of Josephson junctions as non-linear circuit elements in superconducting elements has been already well studied.

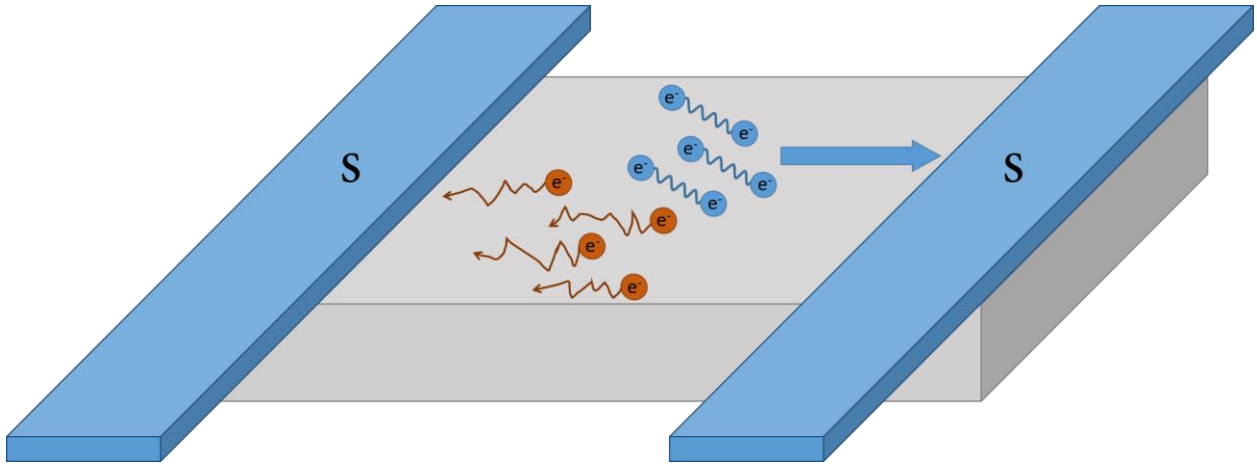


**Fig. 1.1 Representation of a lateral Josephson junction hosting the diode effect:** When a current is applied between the superconducting electrodes (blue) in a Josephson junction, Cooper pairs (blue) carry it in the form of supercurrents in one direction, while normal electrons (dark orange) that dissipate energy carry the current along the opposite direction, inside the material (grey).

This thesis provides a brief and lucid overview to the field of superconductivity and non-reciprocal transport effects in solids that helps the reader better understand the context of the results and their significance before moving on to explore in detail the Josephson diode effect in two van der Waals materials with similar crystal structures 1T-NiTe<sub>2</sub> and 1T-PtTe<sub>2</sub>. The 1T structure, though centrosymmetric, has a hidden local inversion symmetry breaking on the Te site that gives rise to spin polarization and band inversions, leading to the formation of multiple topological states in the band structure. The existence of these spin-polarized bands is confirmed with the help of spin- and angle-resolved photoemission experiments and density functional theory calculations in literature<sup>8</sup>.

In the case of 1T-NiTe<sub>2</sub>, it is shown in this thesis through analysis of lateral Josephson junctions that the helical spin-momentum locking in the system plays an important role in the creation of a finite-momentum superconducting state, similar to a Fulde-Ferrell-Larkin-Ovchinnikov (FFLO) state<sup>9,10</sup>, in the presence of a magnetic field that can give rise to a Josephson

diode effect in these systems. The temperature, magnetic field magnitude and angular dependence of the Josephson diode effect experimentally observed is in good agreement with that predicted from a Ginzburg-Landau model description of finite momentum pairing in a Josephson junction. Further, the presence of finite-momentum pairing in the system is confirmed independently by measuring the evolution of the Fraunhofer interference pattern in the presence of momentum-inducing magnetic fields.

In the case of 1T-PtTe<sub>2</sub> Josephson junctions, similar experiments are performed in lateral geometry to confirm the existence of helical spin-momentum locking. Vertical Josephson junctions of PtTe<sub>2</sub> are used to demonstrate the absence of any spin-momentum locking along the *c*-axis of the crystal. It is shown through analysis of the Josephson diode effect along with the current-phase relationship that a strong second-harmonic supercurrent component is present in these junctions comparable to that in high transparency semiconductor<sup>11</sup> and topological Josephson junctions<sup>12</sup>. It is also shown through the evolution of the Fraunhofer pattern with magnetic flux that the behavior of the Josephson diode effect essentially mimics the second harmonic term in the current-phase relationship (CPR). The origin of the strong second-harmonic component can be attributed to the significant contribution of the topological states present in the system that suppress the normal reflections in the junction. Furthermore, possible extrinsic mechanisms that can give rise to the Josephson diode effect such as self-field effects and geometric asymmetries of the flake are identified and eliminated as the source of the experimental observations.

Overall, this dissertation is a collection of results and observations that attempt to signify the reader on the importance of the Josephson diode effect as a simple yet effective ‘tool’ to probe unconventional superconductivity in materials, beyond its advertised utility as a logic element in superconducting circuits and quantum sensing applications. The inversion and time reversal symmetry breaking requirements of the Josephson diode effect leads to the possibility of discerning the type of spin-momentum locking in the superconducting state of materials and the identification of spontaneous time-reversal symmetry in the superconducting state, which is of great interest. The reader is also alerted to the existence of extrinsic mechanisms that can mimic the observed effects and how to avoid or eliminate such false positives while performing experiments.

The thesis is organized as follows. Chapter 2 contains the basic theoretical aspects of superconductivity, Josephson junctions and non-reciprocal transport in superconductors that are requisite in understanding the results that appear in later chapters of the thesis. Chapter 3 describes in detail the major experimental methods used in fabricating devices, characterizing and measuring them. Chapter 4 contains the main experimental results on the Josephson diode effect measurements in 1T-NiTe<sub>2</sub> and relates it to the effects derived for a junction with non-zero Cooper pair momentum<sup>1</sup>. The Cooper pair momentum is also independently measured to verify its existence. Two possible origins for the Cooper pair momentum are suggested. One derived from the Rashba-spin momentum locked topological surface states and the other based on Meissner screening currents in the niobium electrodes. Chapter 5 describes through Josephson diode effect, the helical spin-momentum locking in 1T-PtTe<sub>2</sub>. The Josephson diode effect is studied as a function of the magnetic flux through the junction. A large value of second harmonic supercurrent component is obtained in the junction from a CPR model. Oscillations that have a frequency twice that of the magnetic flux quantum are obtained as predicted from the CPR indicating the importance of the second harmonic component in the observation of the Josephson diode effect. The possible origin of the large second harmonic supercurrents is discussed. Chapter 6 discusses the results in a broader context and provides future prospects for non-reciprocal transport effects in superconductors and Josephson junctions. The appendix contains a brief discussion on the field-free Josephson diode effect in Nb<sub>3</sub>Br<sub>8</sub><sup>2</sup> and results supporting the conclusions in the main chapters of the thesis.



# 2

---

## Theoretical Foundations

## 2.1 Introduction to superconductivity

### 2.1.1 Historical overview

Superconductivity is one of the most fascinating scientific discoveries of the 20<sup>th</sup> century, the mysteries of which have pervaded into the current century and captures the attention of many scientists to date. Superconductivity was discovered in 1911 by H. Kamerlingh Onnes in Leiden<sup>13</sup>, after he had perfected liquefaction of helium a few years before, allowing him to reach temperatures as low as 4.2 K. Onnes won the Nobel Prize in Physics in 1913 for this discovery of new state of matter. Elemental mercury was the first discovered superconductor, through its hallmark defining property of a zero-resistance electrical conductivity state (also known as perfect conductivity) upon cooling down to liquid helium temperatures. But perfect conductivity is not the only defining property of a superconductor. Another defining property of superconductors is the perfect diamagnetic state discovered by Meissner and Ochsenfeld in 1933<sup>14</sup>, which showed that a superconductor is much more complex than what one would expect from a perfect conductor. Superconductors that exhibit a complete Meissner state are known as type-I superconductors and there are other superconductors that can develop superconducting vortices on the application of a magnetic field that allow flux to pass through, known as type-II superconductors.

Since then, there has been a lot of work in discovering new superconductors and understanding the fundamental properties of superconducting materials. The most prominent theories that could best explain the observed properties of superconductivity were the Ginzburg-Landau (GL) theory<sup>15</sup> and the Bardeen-Cooper-Schrieffer (BCS) theory<sup>16</sup>. The GL theory is a phenomenological theory proposed by Vitaly Ginzburg and Lev Landau in 1950 based on the Landau theory of phase transitions, which could explain some of the observed thermodynamic properties of the superconductors such as critical current, critical field and even some important parameters such as the GL coherence length. Vitaly Ginzburg won the Nobel Prize in Physics in 2003 along with Alexei Abrikosov and Sir Anthony Leggett for pioneering contributions to the theory of superconductors and superfluids.

The BCS theory<sup>16</sup> came later on in 1957 as a microscopic theory establishing the existence of correlated electron pairs called Cooper pairs that move without scattering in the superconductor. For this important discovery, John Bardeen, Leon Cooper and John Robert Schrieffer won the



Nobel Prize in Physics in 1972. It was shown by Lev Gor'kov in 1959 that the GL theory could be derived starting from the microscopic BCS theory close to the superconducting transition, thus validating the phenomenological model<sup>17</sup>. Another important postulate of the BCS theory was the existence of a macroscopic quantum wave function of the superconducting condensate. This opened up the possibility of exploring quantum mechanics and performing quantum experiments at a macroscopic scale. A direct consequence of this was Brian D. Josephson solving the problem of quantum tunneling of the macroscopic superconducting wave function from one superconductor to another through a non-superconducting barrier<sup>18</sup> in 1962 leading to what is known today as Josephson junctions. Josephson received the Nobel Prize in Physics for this work in 1973. These junctions allow for controlling the phase difference of the superconducting wave function between the electrodes with a current or vice versa. Josephson junctions have been explored a lot over the past decades for possible applications in building quantum sensors and superconducting electronics such as DC-SQUIDS, superconducting computing elements, and in the current decade they serve as the prime building block of superconducting quantum bits, which are the front-runner candidates for building a quantum computer.

While important fundamental discoveries concerning the nature of superconductivity were taking place in the 1950s and 1960s, the search for a room temperature superconductor that would make the applications of superconductors more feasible was going on in parallel in the materials front. Superconductivity, as of yet had been observed mostly in metals or metallic alloys at very low temperatures requiring the use of liquid helium cooling. In 1986, two IBM researchers at Zurich, Georg Bednorz and Karl Alex Müller discovered superconductivity in a ceramic copper oxide material  $\text{La}_{2-x}\text{Ba}_x\text{CuO}_4$ , with a relatively high critical temperature of 35 K, which was well above the critical temperature of any known superconductor at that time<sup>19</sup>. This led to a flurry of research on copper oxide or cuprate-based superconductors in pursuit of superconductors with higher critical temperatures. As of 2021, the cuprate superconductor with the highest transition temperature under ambient pressure is  $\text{Hg}_{12}\text{Tl}_3\text{Ba}_{30}\text{Cu}_{45}\text{O}_{127}$  with a critical temperature of 138 K.

The discovery of high-temperature superconductors has also prompted scientists to think beyond conventional BCS theory, in which the pairing potential is assumed to be mediated by

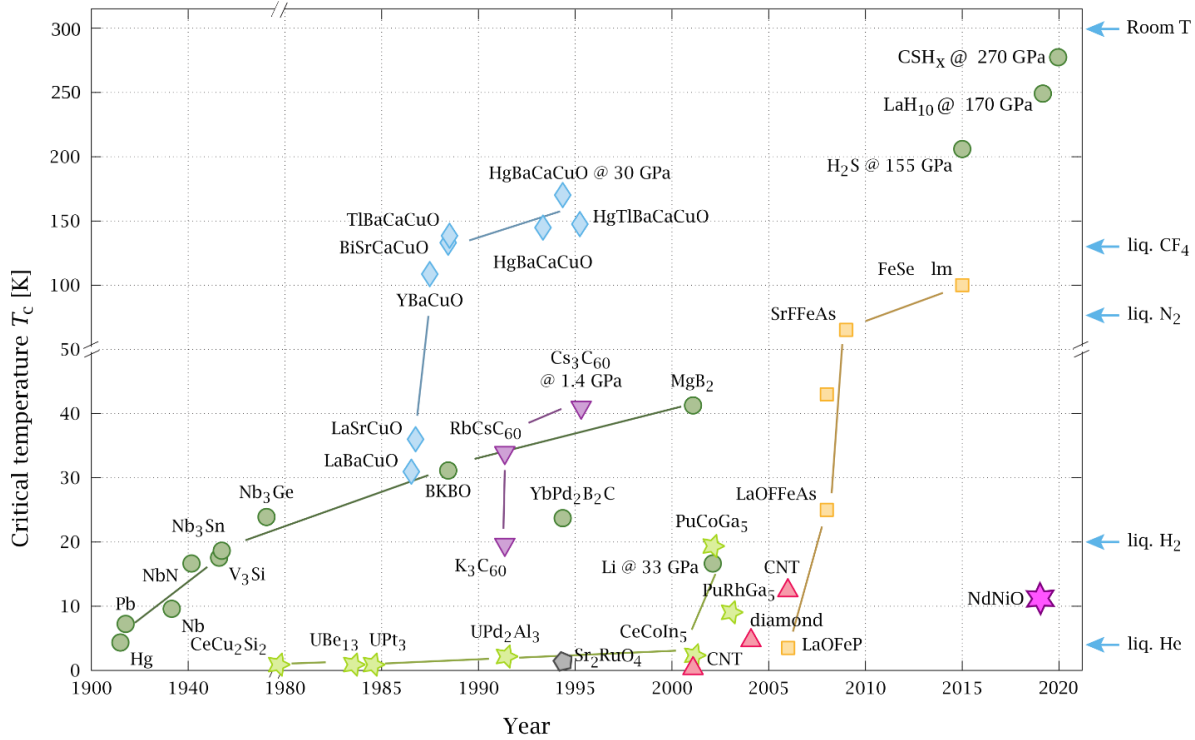


**Fig. 2.1 Timeline of superconductors:** Discovery of different superconducting materials over the years along with their critical temperatures. Green circles refer to conventional metallic superconductors that are considered to be BCS superconductors. Some of the highest critical temperatures achieved to-date are in hydride superconductors under very high pressures. Blue diamonds refer to cuprate superconductors, which have the highest critical temperatures at ambient pressures discovered so far. Inverted triangles refer to fullerene-based superconductors, red triangles correspond to carbon nanotube-based superconductors, yellow squares refer to iron-based superconductors, magenta star refers to the newly discovered nickel-based superconductor. Green stars refer to the unconventional heavy-fermion based superconductors. ‘Timeline of Superconductivity from 1900 to 2015’ by PJRay is licensed under CC-BY-SA-4.0

phonons. This general class of materials that do not fall under the purview of BCS theory are known as unconventional superconductors and form a sub-field of research of their own, which cuprates are a part of. In general, BCS theory requires the presence of inversion and time-reversal symmetry in a system for the form of conventional spin-singlet Cooper pairs or s-wave superconductivity. Certain intrinsic superconductors lack inversion or time-reversal symmetries

and can't be explained by the formation of Cooper pairs as in BCS theory. Some examples of unconventional superconductors include  $\text{Sr}_2\text{RuO}_4$ <sup>20</sup>, heavy fermion superconductors such as  $\text{UPt}_3$ <sup>21</sup>,  $\text{UTe}_2$ <sup>22</sup>,  $\text{CePt}_3\text{Si}$ <sup>23</sup>,  $\text{CeRh}_2\text{As}_2$ <sup>24</sup>, hybrid-superconducting structures composed of ferromagnet-superconductor heterostructures<sup>25</sup>. A more detailed discussion of the topics discussed in this chapter can be found in Michael Tinkham's book 'Introduction to Superconductivity'<sup>26</sup>.

### 2.1.2 Electrodynamics of superconductors – London Equations

In order to build devices with superconductors for practical applications and understand the observed properties of superconductors, it is important to comprehend the basic properties of superconductors in electric and magnetic fields. This section focuses on key concepts and ideas on some electromagnetic properties of superconductors that shall be encountered throughout this thesis.

The two fundamental properties observed in superconductors were perfect conductivity and perfect diamagnetism. The brothers F. and H. London proposed two phenomenological equations<sup>27</sup> that govern the electrodynamic properties of superconductors under electric and magnetic fields that could describe these properties. These were known as the London equations.

$$\frac{\partial \mathbf{j}_s}{\partial t} = \frac{ne^2}{m} \mathbf{E} \quad (2.1)$$

$$\nabla \times \mathbf{j}_s = -\frac{ne^2}{m} \mathbf{B} \quad (2.2)$$

where  $n$  is the superconducting electron density,  $e$  is the charge of an electron,  $m$  is the mass of an electron,  $\mathbf{j}_s$  is the supercurrent density,  $\mathbf{E}$  is the electric field and  $\mathbf{B}$  is the magnetic field.

Though there is no rigorous derivation for this equation, equation (2.1) arises from the perfect conductivity that is found in a superconductor. The London brothers noted that the electrons in a superconductor feel no resistance in the presence of an electric field and accelerate continuously as if they were free electrons, as opposed to electrons in a metal that would maintain a velocity against a resistance, which is described by Ohm's law. Hence, the force on the superconducting condensate in the presence of an electric field can be written as:

$$\mathbf{F} = m \frac{\partial \mathbf{v}}{\partial t} = -e\mathbf{E} + e\mathbf{v} \times \mathbf{B}$$

The supercurrent density can be written as  $\mathbf{j}_s = -nev$  which gives

$$\frac{\partial \mathbf{j}_s}{\partial t} = -ne \frac{\partial \mathbf{v}}{\partial t} = \frac{ne^2}{m} \mathbf{E}$$

The second London equation (2.2) can be obtained by taking the curl of (2.1) and using Faraday's law ( $\nabla \times \mathbf{E} = -\frac{\partial \mathbf{B}}{\partial t}$ )

$$\frac{\partial}{\partial t} \left[ \nabla \times \mathbf{j}_s + \frac{ne^2}{m} \mathbf{B} \right] = 0$$

Writing the magnetic field in terms of the vector potential  $\mathbf{B} = \nabla \times \mathbf{A}$  gives  $\mathbf{j}_s = -\frac{ne^2}{m} \mathbf{A}$

Taking the curl of Ampere's law  $\nabla \times \mathbf{B} = \mu_0 \mathbf{j}_s$  one can obtain

$$\nabla \times (\nabla \times \mathbf{B}) = \mu_0 (\nabla \times \mathbf{j}_s) = -\frac{\mu_0 ne^2}{m} \mathbf{A}$$

which on further simplification gives

$$\nabla^2 \mathbf{B} = \frac{1}{\lambda_L^2} \mathbf{B} \quad (2.3)$$

where  $\lambda_L = \sqrt{\frac{m}{\mu_0 ne^2}}$  is an important characteristic length scale in superconductors known as the 'London penetration depth'. Solving equation (2.3) in one dimension would lead to the solution

$$\mathbf{B} = \mathbf{B}_0 e^{-\frac{x}{\lambda_L}}$$

which shows that the magnetic field decays exponentially inside a superconductor over the characteristic length scale of the London penetration depth  $\lambda_L$ . This explains the observation of a Meissner state within a superconductor wherein an external magnetic field is screened completely inside a superconductor.  $\lambda_L$  is an important parameter that needs to be taken into account while calculating effective separation between the electrodes of a Josephson junction, while the presence of Meissner screening can lead to flux focusing effects, as will be discussed in later parts of the thesis.

### 2.1.3 Ginzburg-Landau theory of superconductivity

The Ginzburg-Landau (GL) theory is a phenomenological theory of superconductivity put forth by Vitaly Ginzburg and Lev Landau based on the Landau theory of phase transitions<sup>15</sup>. The theory concerns the macroscopic behavior of superconductors in which the free energy of the superconductor becomes significant and is useful in predicting critical fields, critical currents and other thermodynamic properties of a superconductor. This is achieved by considering a complex order parameter  $\psi(r)$ , which is identical to a superconducting wavefunction, whose magnitude represents the probability of finding superconducting electrons in a system. The GL theory of superconductivity is valid when the temperature is close to the critical temperature ( $T_c$ ) where  $\psi(r)$  is small and varies smoothly across space. In this case, the free energy of the superconductor can be written as an expansion of  $\psi(r)$

$$F = F_n + \alpha|\psi|^2 + \frac{\beta}{2}|\psi|^4 + \dots$$

Where  $F_n$  is the free energy in the normal state,  $\alpha$  and  $\beta$  are GL parameters. The higher order terms are usually very small and can be neglected. In the presence of a magnetic field, the free energy can be written as

$$F = F_n + \alpha|\psi|^2 + \frac{\beta}{2}|\psi|^4 + \frac{1}{2m^*} \left| \left( -\frac{i\hbar}{2\pi} \nabla - e^* \mathbf{A} \right) \psi \right|^2 + \frac{\mathbf{B}^2}{2\mu_0}$$

Where  $m^*$  and  $e^*$  correspond to the mass and charge of the ‘supercurrent carrier’ respectively. The free energy is minimized ( $\frac{\partial F}{\partial \psi} = 0$ ) to obtain the GL differential equations.

$$\alpha\psi + \beta|\psi|^2\psi + \frac{1}{2m^*} \left( -\frac{i\hbar}{2\pi} \nabla - e^* \mathbf{A} \right) \psi = 0 \quad (2.4)$$

and

$$\mathbf{J} = \nabla \times \mathbf{B} = -\frac{ie^*\hbar}{4\pi m^*} [\psi^\dagger \nabla \psi - \psi \nabla \psi^\dagger] - \frac{e^{*2}}{m^*} \psi^\dagger \psi \mathbf{A} \quad (2.5)$$

where  $\mathbf{J}$  is the current due to the magnetic field.

These differential equations can be used to derive various quantities such as the current, coherence length, etc. for a superconductor by modifying the boundary conditions appropriately depending on the external magnetic field.

Now, in the presence of a magnetic field, deep inside the superconductor where there are no fluctuations of the order parameter, equation (2.5) can be written as:

$$\mathbf{J} = -\frac{e^{*2}}{m^*}\psi^2\mathbf{A}$$

Comparing this with  $\mathbf{j}_s = -\frac{ne^2}{m}\mathbf{A}$  derived from the London equations leads to defining the London penetration depth in GL formalism as  $\lambda_L = \sqrt{\frac{m}{\mu_0\psi^2e^2}}$  where  $n$ , the superconducting electron density is replaced by  $\psi^2$ , the probability amplitude of the superconducting order parameter.

Now considering the interface of a superconductor with a non-superconductor in one-dimension, the order parameter  $\psi$  becomes non-uniform and variant in space, close to the boundary. In the absence of a magnetic field, this scenario can be expressed using equation (2.4) as

$$\alpha\psi + \beta|\psi|^2\psi - \frac{\hbar^2}{2m^*}\frac{d^2\psi}{dx^2} = 0$$

Replacing  $\xi(T) = \frac{\hbar^2}{2m^*|\alpha(T)|}$  and  $\frac{\beta}{|\alpha|}\psi^2 = f^2$ , we get

$$f - f^3 + \xi^2(T) f'' = 0 \tag{2.6}$$

where  $\xi(T)$  is a characteristic length scale of the superconductor, which gives the variation of  $\psi$  close to the boundary, known as the GL coherence length. Since  $\alpha \propto \left(1 - \frac{T}{T_c}\right)$ ,  $\xi(T) \propto \frac{1}{\left(1 - \frac{T}{T_c}\right)}$  which means  $\xi(T)$  diverges when  $T$  is close to  $T_c$ . Equation (2.6) can be rewritten in terms of  $f'$  as

$$\frac{d}{dx} \left[ \frac{f^2}{2} - \frac{f^4}{4} + \frac{\xi^2 f'^2}{2} \right] = 0$$

which implies  $\left(\frac{f^2}{2} - \frac{f^4}{4} + \frac{\xi^2 f'^2}{2}\right)$  is a constant. Solving this equation gives

$$f(x) = \tanh\left(\frac{\sqrt{2}x}{\xi(T)}\right)$$

$$\psi(x) = \sqrt{\frac{|\alpha|}{\beta}} \tanh\left(\frac{\sqrt{2}x}{\xi(T)}\right)$$

To understand better the significance of  $\xi(T)$ , let us consider  $f(x) = 1 + g(x)$  in (2.6), where  $g(x) \ll 1$  and drop the  $g^2$  and  $g^3$  terms. This gives

$$\frac{d^2g}{dx^2} = \frac{2}{\xi^2} g$$

and

$$g(x) = e^{\frac{\pm\sqrt{2}x}{\xi(T)}}$$

which shows that a small change in  $x$  can lead to an exponential decay of  $\psi$  with the characteristic length scale  $\xi(T)$ .

The existence of type-II superconductors and the vortex lattice phase was discovered by Alexei A. Abrikosov in 1957 using the GL theory by tuning the dimensionless GL parameter  $\kappa = \frac{\lambda_L(T)}{\xi(T)}$  which is the ratio of two characteristic length scales<sup>28</sup>. It was discovered that  $\kappa > \frac{1}{\sqrt{2}}$  leads to the formation of superconducting vortices, now known as Abrikosov vortices that form a hexagonal lattice in the presence of a magnetic field and superconductors that host such vortices are known as type-II superconductors. Superconductors with  $\kappa < \frac{1}{\sqrt{2}}$  are known as type-I superconductors and do not host any vortices. This discovery led to the Nobel prize of Abrikosov along with Ginzburg for his work on GL theory in 2003.

#### 2.1.4 BCS theory of superconductivity

The Bardeen-Cooper-Schrieffer (BCS) theory of superconductivity<sup>16</sup> is the most successful microscopic theory of superconductivity laid out in 1957. The BCS theory explains many observed properties of superconductivity at the quantum level such as the existence of a superconducting energy gap, heat capacity, the role of phonons in the formation of so-called Cooper pairs, Bogoliubov quasiparticles, and thermodynamic properties such as critical temperature, critical fields and currents. The basis for the theory was the proposal of Leon Cooper<sup>29</sup> in 1956 when he laid out that an arbitrary attractive interaction between two electrons above the Fermi sea due to

screened Coulomb repulsions enabled by phonons would lead to an instability and the formation of a bound state and pairing of electrons known as Cooper pairs. This idea was later built upon together with Bardeen and Schrieffer to come up with the BCS theory.

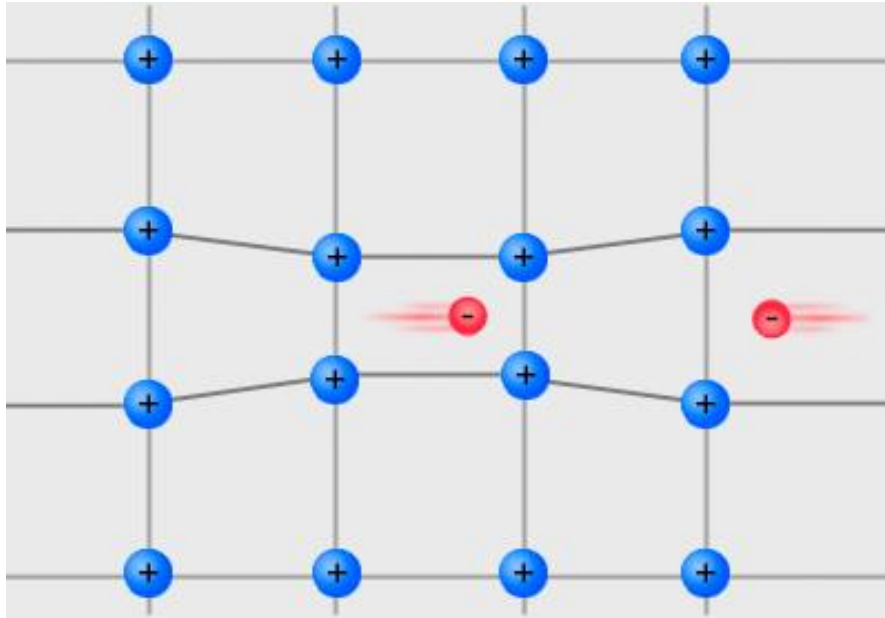


**Fig. 2.2 Cooper pair in a lattice:** Schematic of attractive interaction between free electrons in a metal mediated by the lattice vibrations (phonons). ‘Cooper pairs’ by Tem5psu is licensed under CC-BY-SA-4.0

Consider a Fermi sea of  $N$  electrons. In the presence of an attractive interaction between electron pairs, they form a bound state given by the wave function

$$f(\mathbf{r}_i - \mathbf{r}_j)\chi_{ij}$$

where  $f(\mathbf{r}_i - \mathbf{r}_j)$  is the spatial part of the wave function between electrons located at coordinates  $\mathbf{r}_i$  and  $\mathbf{r}_j$ .  $\chi_{ij}$  is the spin part of the wave function for spins  $\sigma_i$  and  $\sigma_j$ . Now, this is a fermionic wave function of two particles and has to be anti-symmetric for it to obey the Fermi statistics. BCS enforced this by considering the spatial part to be symmetric (s-wave) and the spin part to be antisymmetric (spin singlet). This choice makes sense for the superconductors that were known until then, as most of them were non-magnetic metals and time-reversal symmetric in nature and



have equal spin density of states that is ideal for spin-singlet pairing. The spin-singlet wave function can be written as  $\chi_{ij} = \frac{1}{\sqrt{2}} [|\uparrow\downarrow\rangle\delta_{\uparrow,\sigma_i}\delta_{\downarrow,\sigma_j} - |\downarrow\uparrow\rangle\delta_{\downarrow,\sigma_i}\delta_{\uparrow,\sigma_j}]$  where  $\delta_{x,y}$  is a delta function.

With this we can write down the total wave function of all the  $N$  electrons in the bound state as

$$\Psi[(\mathbf{r}_1\sigma_1), (\mathbf{r}_2\sigma_2), \dots, (\mathbf{r}_N\sigma_N)] = C\mathcal{A} \prod_{i=1}^{N-1} [f(\mathbf{r}_i - \mathbf{r}_{i+1})\chi_{i,i+1}]$$

Where  $C$  is the normalization constant and  $\mathcal{A}$  is the antisymmetrization operator that sums over all permutations of the wave function and ensures the antisymmetric nature of the total wave function. This total wave function can be written in a simpler form in the second quantized notation as

$$|\Psi\rangle \propto \left[ \int d^3\mathbf{r}_1 d^3\mathbf{r}_2 \psi_{\uparrow}^{\dagger}(\mathbf{r}_1)\psi_{\downarrow}^{\dagger}(\mathbf{r}_2)f(\mathbf{r}_1 - \mathbf{r}_2) \right]^{\frac{N}{2}} |0\rangle$$

where  $|0\rangle$  is the vacuum state with no Cooper pairs and just the Fermi sea of electrons. This wave function automatically obeys the antisymmetry condition upon exchange of particles provided  $f$  is even. This wave function can be Fourier transformed and written in terms of momentum states as

$$|\Psi\rangle \propto \left[ \sum_{\mathbf{k}} f(\mathbf{k}) c_{\mathbf{k}\uparrow}^{\dagger} c_{-\mathbf{k}\downarrow}^{\dagger} \right]^{\frac{N}{2}} |0\rangle \quad (2.7)$$

The equation (2.7) is the total wave function of  $N$  particles written in the momentum representation and it can be seen clearly that the pairing happens between electrons at  $(\mathbf{k}, \uparrow)$  and  $(-\mathbf{k}, \downarrow)$  with the center of mass momentum being zero. This is an important observation from BCS theory that requires the presence of inversion symmetry for the presence of states at momenta  $\mathbf{k}$  and  $-\mathbf{k}$  at a given energy and time reversal symmetry for equal  $\uparrow$  and  $\downarrow$  spin states in the system for the formation of an  $s$ -wave spin singlet superconducting wave function with zero center of mass momentum. The BCS Hamiltonian can be written as

$$H = \sum_{\mathbf{k}\sigma} \varepsilon_{\mathbf{k}} c_{\mathbf{k}\sigma}^{\dagger} c_{\mathbf{k}\sigma} - \frac{U_0}{V} \sum_{\mathbf{k}, \mathbf{k}', q} \sum_{\sigma, \sigma'} c_{\mathbf{k}+\mathbf{q}, \sigma}^{\dagger} c_{\mathbf{k}'-\mathbf{q}, \sigma'}^{\dagger} c_{\mathbf{k}'\sigma'} c_{\mathbf{k}\sigma}$$

where  $U_0$  is the attractive potential and  $V$  is the volume of the system. This Hamiltonian can be simplified from four-fermion operators to two fermion operators using Wick's theorem as:

$$H_B = \sum_{k\sigma} \varepsilon_k c_{k\sigma}^\dagger c_{k\sigma} - \sum_k \Delta c_{k\uparrow}^\dagger c_{-k\downarrow}^\dagger + \Delta^* c_{-k\downarrow} c_{k\uparrow} + \text{constant} \quad (2.8)$$

$$\text{where } \Delta = \frac{U_0}{V} \sum_k \langle c_{-k\downarrow} c_{k\uparrow} \rangle \quad (2.9)$$

is the superconducting energy gap in the spectrum that is predicted by BCS theory as shall be seen later.

The eigenstates and eigenvalues of  $H_B$  are determined by using a linear transformation known as Bogoliubov transformation that helps diagonalize  $H_B$  as done independently by Nikolai Bogoliubov<sup>30</sup> and John Valatin<sup>31</sup> in 1958.

$$\begin{pmatrix} c_{k\uparrow} \\ c_{-k\downarrow}^\dagger \end{pmatrix} = \begin{pmatrix} u_k^* & v_k \\ -v_k^* & u_k \end{pmatrix} \begin{pmatrix} \gamma_{k\uparrow} \\ \gamma_{-k\downarrow}^\dagger \end{pmatrix}$$

where the coefficients  $u_k$  and  $v_k$  satisfy the equation  $|u_k|^2 + |v_k|^2 = 1$ . After transformation to the Bogoliubov basis, in order to diagonalize  $H_B$ , the coefficients  $u_k$  and  $v_k$  need to be chosen such that terms such as  $\gamma_{k\uparrow} \gamma_{k\downarrow}$  and  $\gamma_{-k\downarrow}^\dagger \gamma_{-k\uparrow}^\dagger$  vanish. It can be seen that the following values satisfy the requirement  $u_k = \sin(\varphi_k)$ ,  $v_k = \cos(\varphi_k) e^{i\theta}$ ,  $\Delta = |\Delta| e^{i\theta}$  and  $\sin(2\varphi_k) = \frac{|\Delta|}{\sqrt{\varepsilon_k^2 + |\Delta|^2}}$  leaving only  $\gamma_{k\sigma}^\dagger \gamma_{k\sigma}$  terms which gives the number of the Bogoliubov quasiparticles or Bogoliubons in a particular state. It can be seen that substituting these values simplifies the Bogoliubov Hamiltonian to

$$H_B = \sum_{k\sigma} E_k \gamma_{k\sigma}^\dagger \gamma_{k\sigma} + \text{constant}$$

where  $E_k = \sqrt{\varepsilon_k^2 + |\Delta|^2}$  is the Bogoliubov quasiparticle dispersion. It can be seen that there is an energy gap  $\Delta$  below which no Bogoliubons exist ( $E < |\Delta|$ ) and the system requires a minimum energy of  $c$  to create such excitations. It can also be seen that the energy spectrum is symmetric with respect to  $\mathbf{k}$ . This implies the existence of particle-hole symmetry in the system. Now, the ground state wave function of the BCS Hamiltonian can be found using the argument that no Bogoliubons exist in the ground state and hence  $\gamma_{k\sigma} |BCS\rangle = 0$ . The BCS ground state wave function that satisfies this criteria can be written as

$$|BCS\rangle_\theta = \prod_k (u_k + v_k e^{i\theta} c_{k\uparrow}^\dagger c_{-k\downarrow}^\dagger) |0\rangle$$

which is the form of wave function that BCS originally assumed for their ground state.

The energy gap  $\Delta$  can be obtained by transforming equation (2.9) to the Bogoliubov basis. Upon further simplification, the gap can be obtained as

$$\Delta(T) = U_0 n(0) \int_0^{\hbar\omega_D} d\varepsilon \frac{\tanh\left(\frac{\sqrt{\varepsilon^2 + |\Delta|^2}}{2k_B T}\right)}{\sqrt{\varepsilon^2 + |\Delta|^2}} \quad (2.10)$$

where  $n(0)$  is the density of states at the Fermi level and  $\omega_D$  is the Debye frequency.  $\Delta(T)$  can be numerically calculated from equation (2.10) and this equation can be used to define the critical temperature of the superconductor ( $T_c$ ), the temperature at which  $\Delta(T)$  reaches zero. This would give the  $T_c$  of the superconductor to be

$$\Delta_0 \approx 1.764 k_B T_c \quad (2.11)$$

where  $\Delta_0$  is the superconducting energy gap at zero temperature. Near  $T_c$ ,  $\Delta(T)$  drops to zero as

$$\Delta(T) \approx 1.74 \Delta_0 \sqrt{1 - \frac{T}{T_c}}$$

which gives a  $\sqrt{T_c - T}$  dependence of the superconducting gap. Further details on BCS can be found in ref.<sup>26</sup>

### 2.1.5 Finite-momentum superconductivity

As described in the previous section, the BCS theory of superconductivity allows for the existence of Cooper pairs with net zero center of mass momentum, which requires electronic states at momenta  $\mathbf{k}$  and  $-\mathbf{k}$ , that is guaranteed by the inversion symmetry of a crystal. It was first proposed by Fulde and Ferrell<sup>9</sup> and independently by Larkin and Ovchinnikov<sup>10</sup> in 1964 that in the presence of a strong exchange splitting of the electronic bands, it is possible to obtain pairing between electrons located at states that are at  $\mathbf{k}$  and  $-\mathbf{k} + \mathbf{q}$  with a finite non-zero pairing momentum of  $\mathbf{q}$  leading to the formation of an order parameter that is spatially modulated by the

wave vector  $\mathbf{q}$  (i.e.)  $\Delta e^{i\mathbf{q}\mathbf{x}}$  (FF) or  $\Delta \cos(\mathbf{q}\mathbf{x})$  (LO). The exchange splitting can be due to the presence of ferromagnetic impurities or strong magnetic fields that create Zeeman splitting of the bands. The value of this momentum  $\mathbf{q}$  can be controlled by the strength of the Zeeman splitting or the exchange field, depending on the origin. Such a state is called as a Fulde-Ferrell-Larkin-Ovchinnikov or an FFLO state, named after the four scientists who originally proposed it. A schematic of the order parameter modulation in FFLO state is shown in Fig. 2.3.

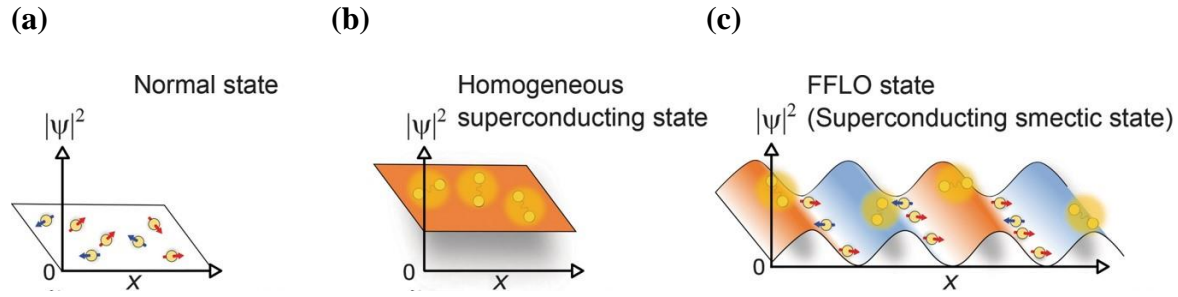


**Fig. 2.3 Finite momentum superconductivity:** Schematic of the variation of superconducting order parameter with space in (a) normal state (b) uniform BCS state (c) FFLO state. Figure from ref.<sup>32</sup>. Reprinted with permission from AAAS.

Other than FFLO states, it is also possible to have finite momentum Cooper pairing in superconductors with spin-momentum locking in the presence of a strong Zeeman field<sup>33</sup>. This is a much more viable route to create finite momentum pairing as the Zeeman fields required to create finite momentum shift in a spin-momentum locked superconductor is much lower than in regular BCS superconductors. Hence, a natural platform to look for finite-momentum superconductivity is in non-centrosymmetric superconductors where the spin-momentum locking can be used to create relative shifts of the electronic bands as will be discussed later in the thesis. Signatures of finite momentum superconductivity have been identified in a non-centrosymmetric heavy fermion superconductor  $\text{CeCoIn}_5$ <sup>34,35</sup> and in an organic superconductor BEDT-TTF<sup>36</sup> (bisethylendithiotetrathiofulvalene). With the advent of 2D materials, more and more candidate finite momentum superconductors are being identified as the orbital depairing effect of the Zeeman field is minimal in these systems and it is more plausible to realize a finite momentum state before the superconductivity is destroyed<sup>37,38</sup>.

## 2.2 Josephson junctions

### 2.2.1 Introduction

The Josephson effect<sup>18</sup>, first put forth by Brian D. Josephson in 1962 is an extension of the quantum tunneling problem of single particles to that of Cooper pairs. It is a direct consequence of the macroscopic nature of the wave function of a superconductor as described by BCS theory in the last section. A non-superconducting material like a metal or an insulator sandwiched by two superconductors can host the flow of supercurrents, provided the barrier to tunneling of the Cooper pairs is not very large compared to the superconducting energy gap ( $eV < \Delta$ ). Such a junction is called as a Josephson junction and hosts interesting properties that has amplified the functionality of superconductors. It serves as a platform for observation and engineering of quantum phenomena at the macroscale such as quantum interference, quantum coherence, quantum entanglement, etc. It was first observed experimentally by Philip W. Anderson and John Rowell<sup>39</sup>. Brian Josephson won the Nobel Prize in Physics in 1973 for his prediction of tunneling supercurrents. This section will briefly introduce Josephson junctions and the concepts related to them that will be discussed throughout the thesis. A more detailed discussion on the Josephson effect beyond what is discussed in the thesis can be found in ref.<sup>26,40</sup>

### 2.2.2 DC and AC Josephson effects

Two major effects were predicted by Josephson to occur in a Josephson junction. These are known as DC and AC Josephson effects respectively based on the nature of response of the junction to the external stimuli in terms of frequency. The DC Josephson effect is exploited throughout the thesis and will be described in considerable detail. The DC Josephson effect gives the supercurrent across the junction as a function of phase difference between the superconductors also known as current-phase relationship (CPR), according to the equation:

$$I(\varphi) = I_c \sin(\varphi) \quad (2.12)$$

where  $I(\varphi)$  is the current across the junction,  $\varphi$  is the phase difference between the two superconducting electrodes and  $I_c$  is the critical current of the junction beyond which supercurrents cease to exist.

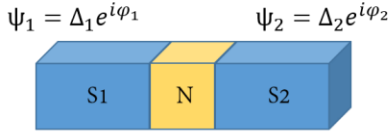
The AC Josephson effect is an interesting effect and is the basis for making the Josephson junction a voltage and frequency standard but its detailed description is beyond the scope of this thesis. The AC Josephson effect is given by:

$$\frac{d\varphi}{dt} = \frac{2e}{\hbar} V = \frac{2\pi}{\Phi_0} V \quad (2.13)$$

where  $V$  is the voltage across the junction and  $\Phi_0 = \frac{h}{2e}$  is the superconducting flux quantum. When a finite voltage  $V$  is applied across the junction, it creates a phase difference across the junction that changes with time and produces an alternating current according to equation (2.12) with frequency  $\frac{2eV}{\hbar}$  irrespective of the specifics of the junction like the shape, material in question, etc. and made up of fundamental constants. This makes the AC Josephson effect useful in creating very precise frequencies by application of DC voltages and the voltage across the junction can be determined by detecting the frequency of radiation in the finite voltage state of the junction, which can be measured much more precisely. This makes the Josephson junction a useful tool in quantum metrology and in measuring voltages precisely. The inverse AC Josephson effect, wherein a specific frequency of current is applied across the junction that creates a voltage across the junction is also possible. This makes creation of a voltage standard using Josephson junctions possible. A frequency of  $483597.7 \text{ GHz}$  is required to create  $1V$  across the junction but this frequency can be arbitrarily modified by connecting arrays of multiple Josephson junctions in series and parallel.

We can derive the DC Josephson effect using a Ginzburg-Landau formalism. Let us consider a simple model of a Josephson junction with two superconductors ( $S_1, S_2$ ) separated by a normal ( $N$ ) region consisting of a metal as shown in Fig. 2.4 (a).

(a)



(b)

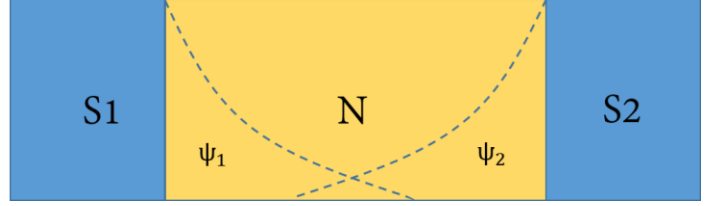


**Fig. 2.4 Schematic of a Josephson junction:** (a) Two superconductors with macroscopic quantum coherence separated by a non-superconducting metal. (b) shows the ‘leakage’ of the superconducting wave function inside the metallic region with considerable overlap. This is a useful picture to appreciate the tunneling of the superconducting condensate similar to the tunneling of single particle wave functions across barriers in quantum mechanics.

The free energy of the whole system can be written in terms of an expansion as:

$$F = \sum_{j=1,2} \left( \alpha_j |\psi_j|^2 + \frac{1}{2} \beta_j |\psi_j|^4 \right) - \gamma_1 \psi_1^* \psi_2 - \frac{1}{2} \gamma_2 (\psi_1^* \psi_2)^2 + c. c.$$

where  $\psi_1$  and  $\psi_2$  are the macroscopic wave functions of the two superconductors.  $\alpha_j$  and  $\beta_j$  are Ginzburg-Landau parameters. The terms with  $\psi_1^* \psi_2$  give the overlap of the two superconducting wave functions that define the Josephson effect with  $\gamma_1$  and  $\gamma_2$  being the two coupling constants of the first and second order Cooper pair tunneling processes respectively. The higher order terms beyond the first are usually dropped in the description of conventional Josephson junctions, as they are negligible.

The free energy of the junction can be rewritten with only the first order term as:

$$F = F_0 - \gamma_1 \psi_1^* \psi_2 - \frac{1}{2} \gamma_2 (\psi_1^* \psi_2)^2 + c. c.$$

where  $F_0 = \sum_{j=1,2} \left( \alpha_j |\psi_j|^2 + \frac{1}{2} \beta_j |\psi_j|^4 \right)$  is the free energy of the superconducting electrodes. The wave functions of the superconductors can be written in terms of their amplitude and phase as  $\psi_i = \Delta_i e^{i\varphi_i}$  which gives

$$F = F_0 - 2\gamma_1 \Delta^2 \cos(\varphi) - \gamma_2 \Delta^4 \cos(2\varphi)$$

Where  $\varphi = \varphi_2 - \varphi_1$  is the phase difference between the two superconductors. The CPR of the Josephson junction can then be obtained from the free energy as

$$I(\varphi) = \frac{2\pi}{\Phi_0} \frac{\partial F}{\partial \varphi} = \frac{4e}{\hbar} \{\Delta^2 \gamma_1 \sin(\varphi) + \Delta^4 \gamma_2 \sin(2\varphi)\} \quad (2.14)$$

The  $\gamma_2$  term is usually negligible in comparison to the  $\gamma_1$  term and can be dropped but it can be significant and play an important role in the observation of the Josephson diode effect as will be discussed in later chapters. Thus, the critical current can be written as:

$$I(\varphi) = I_c \sin(\varphi)$$

which is the DC Josephson equation and  $I_c = \frac{4e}{\hbar} \Delta^2 \gamma_1$  is the critical current of the junction. The critical current of the junction can then be obtained by maximizing  $I(\varphi)$  with respect to  $\varphi$ . The function is maximized when  $\varphi = \frac{\pi}{2}$ . This is the standard CPR used to describe a Josephson junction made from BCS superconductors and a normal metal. When the barrier is replaced with materials with properties like large spin-orbit coupling, magnetism, etc. or the superconductor is replaced with an unconventional superconductor, this modifies the CPR of the junction accordingly and gives rise to interesting effects, which also makes the Josephson junction a useful platform to tailor and study unconventional superconductivity.

### 2.2.3 RCSJ model and current-voltage characteristics

The resistively and capacitively shunted junction (RCSJ) model is a complete model used to describe the complex impedance of a Josephson junction above and below the critical current and is important in understanding the dynamics of a superconductor Josephson junction on sweeping the current. It can be considered the superconducting analogue of an inductor-capacitor-resistor (LCR) electrical circuit model where there are three parallel current channels with the Josephson junction replacing the role of the inductor. In addition to the supercurrent flowing through the junction below the critical current dictated by the Josephson relations, a Josephson junction can have other contributions to its impedance in the finite voltage phase. The resistance  $R$  refers to the resistance of the junction above the critical current, in the finite voltage state while  $C$  refers to the capacitance, which builds up in the junction due to finite size effects or due to the



presence of a dielectric barrier. The capacitance is smaller in *SNS* junctions made of metals while it is considerable in *SIS* junctions made of insulators. The Josephson junction, itself acts as an intrinsic non-linear kinetic inductor in the RCSJ model, in which the inductive energy is derived from the kinetic energy of the Cooper pairs. This can be understood by taking a look at the Josephson equations.

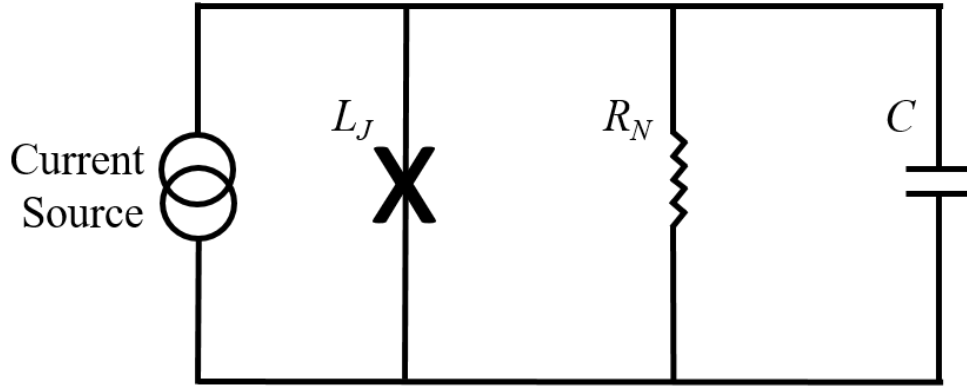


**Fig. 2.5 RCSJ circuit model:** Josephson junctions can be considered as a non-linear inductor in their superconducting state with a resistance and capacitance in parallel that get activated in the finite voltage state. The current dynamics in the junction is described by the differential equation (2.18)

Equation (2.12) can be written as

$$\frac{\partial I}{\partial \varphi} = I_c \cos \varphi \quad (2.15)$$

Applying chain rule to (2.13) and (2.15) we can write

$$\frac{\partial I}{\partial t} = I_c \cos \varphi \frac{2\pi}{\Phi_0} V$$

which can be rewritten as

$$V = L(\varphi) \frac{\partial I}{\partial t}$$

Where  $L(\varphi) = \frac{\Phi_0}{2\pi I_c \cos \varphi} = \frac{L_0}{\cos \varphi}$  is the kinetic inductance across the junction as a function of the phase difference and  $L_0 = \frac{\Phi_0}{2\pi I_c}$  is a junction parameter known as the Josephson inductance.

Above the critical current the junction possesses a resistance given by the normal state resistance of the material ( $R_N$ ). The value of  $R_N$  can be obtained by performing a linear fit of the  $I - V$  data far above  $I_c$ . This can be used to determine the characteristic voltage of the junction ( $I_c R_N$ ), which is a material dependent parameter that does not depend on the dimensions of the Josephson junction. As can be seen from equation (2.13) the voltage applied in the normal state can give rise to a time dependent phase difference and a current. Thus, the total current due to the resistive component of the junction can be written as:

$$I_R = \frac{V_J}{R_N}, \quad \text{where } V_J = \begin{cases} 0, & \text{for } I < I_c \\ \frac{\Phi_0}{2\pi} \frac{d\varphi}{dt}, & \text{for } I > I_c \text{ is the AC component} \\ V_N, & \text{for } I > I_c \text{ is the DC component} \end{cases} \quad (2.16)$$

In case of *SIS* junctions, the capacitance between the two superconducting electrodes can be quite significant. The displacement current due to the capacitance can be written in the presence of a time dependent voltage as:

$$I_D = C \frac{dV}{dt} = C \frac{\Phi_0}{2\pi} \frac{d^2\varphi}{dt^2} \quad (2.17)$$

$C = \frac{\epsilon\epsilon_0 A}{d}$  is the capacitance of the junction both in the normal and superconducting states.  $\epsilon$  is the dielectric constant of the barrier material.  $A$  is the junction area and  $d$  is the separation between the electrodes. Thus, the total current across the junction can be written as the sum of currents across the three parallel current channels:

$$I = I_J + I_R + I_D$$

$$I = I_c \sin \varphi + \frac{V_J}{R_N} + C \frac{\Phi_0}{2\pi} \frac{d^2\varphi}{dt^2} \quad (2.18)$$

$$I = I_c \sin \varphi + \frac{1}{R_N} \frac{\Phi_0}{2\pi} \frac{d\varphi}{dt} + C \frac{\Phi_0}{2\pi} \frac{d^2\varphi}{dt^2} \quad (2.19)$$

It is to be noted that in the superconducting state, only the first term is non-zero and the other terms vanish. We can define three characteristic time scales for the junction based on this equation by considering different combinations of the three parallel current channels.

$$\tau_p = \sqrt{LC} = \frac{1}{\omega_p}$$

$$\tau_c = \frac{\Phi_0}{2\pi V} = \frac{1}{\omega_c}$$

$$\tau_{RC} = R_N C = \frac{1}{\omega_{RC}}$$

$\omega_p$  is the plasma frequency of the junction.  $\omega_c$  and  $\omega_{RC}$  are characteristic frequencies of the junction above which the normal current and the displacement current dominate the total current respectively. The quality factor of the junction is defined as:

$$Q = \frac{\omega_p}{\omega_{RC}} = \frac{RC}{\sqrt{LC}} = \sqrt{\beta_C} \quad (2.20)$$

where  $\beta_C$  is a dimensionless damping parameter known as Stewart-McCumber parameter. Junctions with  $\beta_C \ll 1$  have small  $C$  and  $R_N$  and are known as overdamped junctions. Junctions with  $\beta_C \gg 1$  have large  $C$  and  $R_N$  and are known as underdamped junctions.

The overdamped and underdamped junctions can be better understood in analogy to a massive particle in a tilted-washboard potential with damping whose differential equation is given by:

$$M \frac{d^2x}{dt^2} + \eta \frac{dx}{dt} + \nabla U = 0 \quad (2.21)$$

where  $M$  is the mass of the particle,  $\eta$  is the damping parameter and  $U$  is the potential. Equation (2.19) can be rearranged to read

$$I_c \sin \varphi + \frac{1}{R_N} \frac{\Phi_0}{2\pi} \frac{d\varphi}{dt} + C \frac{\Phi_0}{2\pi} \frac{d^2\varphi}{dt^2} = 0$$

$$I_c \left( \sin \varphi - \frac{I}{I_c} \right) + \frac{1}{R_N} \frac{\Phi_0}{2\pi} \frac{d\varphi}{dt} + C \frac{\Phi_0}{2\pi} \frac{d^2\varphi}{dt^2} = 0$$

Multiplying by  $\left(\frac{\Phi_0}{2\pi}\right)$  gives:

$$E_J \left( \sin \varphi - \frac{I}{I_c} \right) + \frac{1}{R_N} \left( \frac{\Phi_0}{2\pi} \right)^2 \frac{d\varphi}{dt} + C \left( \frac{\Phi_0}{2\pi} \right)^2 \frac{d^2\varphi}{dt^2} = 0$$

where  $E_J = \left(\frac{\Phi_0}{2\pi}\right) I_c$  is the Josephson energy.

$$\frac{d}{d\varphi} \left\{ E_J \left( 1 - \cos \varphi - \frac{I\varphi}{I_c} \right) \right\} + \frac{1}{R_N} \left( \frac{\Phi_0}{2\pi} \right)^2 \frac{d\varphi}{dt} + C \left( \frac{\Phi_0}{2\pi} \right)^2 \frac{d^2\varphi}{dt^2} = 0 \quad (2.22)$$

Comparing equation (2.21) and (2.22), we can make an analogy with a phase particle in a tilted washboard potential with  $M = C \left(\frac{\Phi_0}{2\pi}\right)^2$ ,  $\eta = \frac{1}{R_N} \left(\frac{\Phi_0}{2\pi}\right)^2$  and  $U = E_J \left( 1 - \cos \varphi - \frac{I\varphi}{I_c} \right)$ . It can be seen that the mass of the phase particle is identical to its capacitance, the damping parameter is proportional to  $\frac{1}{R_N}$  and  $U$  is the tilted-washboard potential.

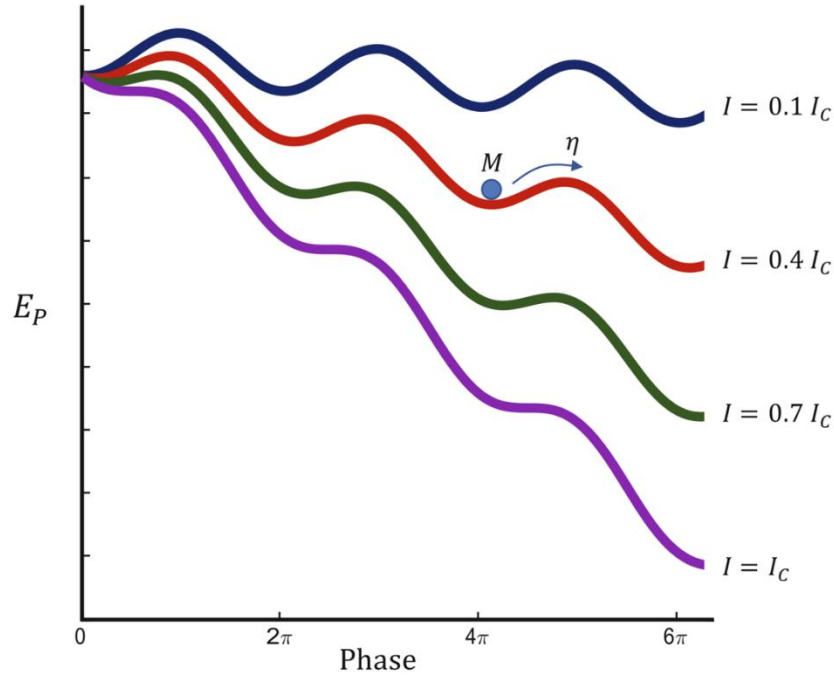


**Fig. 2.6 Tilted washboard potential:** A schematic of a phase particle of mass  $M$  and damping  $\eta$  on the tilted washboard potential. As the current is increased beyond  $I_c$ , the phase particle can escape the potential well into a finite voltage state with continuously increasing  $\varphi$ . (i.e.)  $\frac{d\varphi}{dt} \neq 0$ . Figure reproduced with permission from ref.<sup>41</sup>, Springer International Publishing.

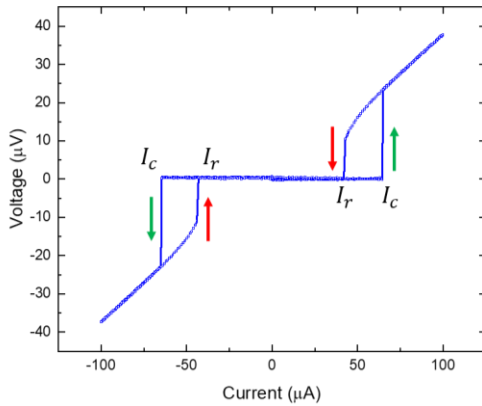
Equation (2.22) can be simplified and rewritten using the Stewart-McCumber parameter as:

$$\beta_C \frac{d^2\varphi}{d\tau^2} + \frac{d\varphi}{d\tau} + \sin\varphi - \frac{I}{I_C} = 0$$

where  $\tau = \frac{t}{I_C R_N} \frac{\Phi_0}{2\pi}$ . An underdamped junction ( $\beta_C \gg 1$ ), the junction capacitance or/and the resistance are large. This means the mass of the particle ( $M \propto C$ ) is large or the damping ( $\eta \propto \frac{1}{R_N}$ ) is weak. For an overdamped junction ( $\beta_C \ll 1$ ), the conditions are reversed and  $M$ (or  $C$ ) or  $R_N$ (or  $\frac{1}{\eta}$ ) or both are small. Now let us consider the motion of the phase particle in these two situations.

When the current is increased, the potential starts to tilt and form a staircase in the negative direction. When the current goes beyond the critical current, the phase particle acquires enough energy to roll down the stairwell continuously, defining the finite voltage state of the junction. When the current is ramped down again to  $I_C$ , two scenarios are possible depending on whether the junction is underdamped or overdamped.

(a)



(b)

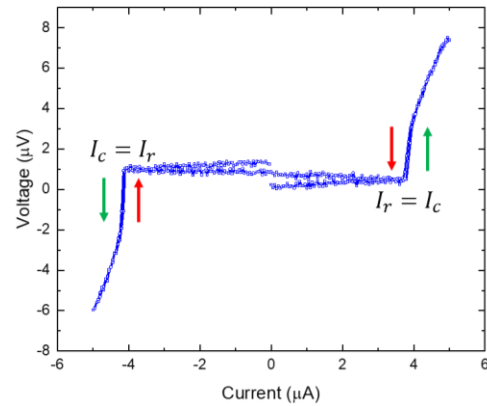


**Fig. 2.7 Underdamped and overdamped junctions:** (a) An example of a characteristic current-voltage curve of an underdamped junction with  $I_c$  and  $I_r$  that are different. (b) An example of a current voltage curve of an overdamped junction with  $I_c = I_r$ .

In the case of an underdamped phase particle, upon reaching  $I_c$  from larger critical currents, the particle continues to roll in the potential stairwell due to its large mass (kinetic energy) or lower

damping and the phase particle remains in the finite voltage state even though the current is below  $I_c$ . This leads to a hysteresis in the  $I - V$  curve and the current where the phase particle stops its motion upon sweeping down the current is known as reentrant current ( $I_r$ ), where it enters back into the superconducting state. In the case of an overdamped phase particle, the motion of the particle stops as soon as the current reaches  $I_c$ , which corresponds to the junction entering the superconducting state. Hence, there is no hysteresis  $I - V$  curve in the case of an overdamped junction. Most measured junctions in the thesis are hysteretic in nature and have an  $I_c$  and  $I_r$  indicating that they have a high quality factor ( $\beta_c \gg 1$ ) and are underdamped. Thus, the RCSJ model can explain the observed features of  $I - V$  characteristics in a Josephson junction.

#### 2.2.4 Quantum interference in Josephson junctions

One of the most important aspects of superconductivity is the presence of macroscopic quantum coherence, which enables quantum computation using superconductors. A Josephson junction provides an effective platform to utilize this property by placing two superconductors with different wave functions in proximity to each other separated by a non-superconducting material as in Fig. 2.4, which can lead to either their constructive or destructive interference depending on their phase difference, as in wave optics. The phase difference between the two superconductors can be controlled with the help of magnetic flux provided by an external magnetic field according to the equation

$$\varphi = \varphi_2 - \varphi_1 = \frac{2\pi\Phi}{\Phi_0}$$

where  $\Phi = \int \mathbf{A} \cdot d\mathbf{s}$  is the magnetic flux through the sample. Hence, the phase difference between the two superconductors can be continuously tuned with the help of an external magnetic field. Combining this with the simplified DC Josephson equation in equation (2.12) shows that the critical current of the Josephson junction oscillates with a magnetic flux period of  $\Phi_0$  or correspondingly a phase difference period of  $2\pi$ . In a rectangular junction, this would lead to the critical current behaviour of the following form as derived elsewhere.

$$I_c(\Phi) = I_c(0) \left| \frac{\sin\left(\frac{\pi\Phi}{\Phi_0}\right)}{\left(\frac{\pi\Phi}{\Phi_0}\right)} \right| \quad (2.23)$$

This functional form is quite similar to the Fraunhofer interference pattern obtained from single slit diffraction in wave optics and hence, the same name has stuck with such interference patterns in Josephson junctions. This interference effect forms the basis for many important applications of the Josephson junction like the Superconducting Quantum Interference Devices (SQUIDs) which can act as very sensitive magnetometers, voltmeters, gradiometers, amplifiers, etc. The interference pattern can also be used to determine the current distribution across the junction by performing an inverse Fourier transform of the obtained interference pattern. Any deviation of the interference pattern from that expected in equation (2.23) is considered unconventional and due to modifications to the current-phase relationship of the junction. Studying the nature of the current-phase relationship in the system allows us to comment on various aspects of superconductivity in the system. For example, a  $2\Phi_0$ - or  $4\pi$ -periodic Josephson effect<sup>42</sup> is expected for a topological Josephson junction and the presence of a  $\left(\frac{\Phi_0}{2}\right)$  period in the Fraunhofer pattern indicates the presence of a second harmonic term in the CPR. Unconventional superconducting pairing such as d-wave pairing can also be detected from the interference pattern by looking at different current geometries of the junction. In the case of d-wave pairing, this would result in a critical current minimum at zero flux rather than a maximum due to the  $\pi$ -phase difference in the wave function along the two adjacent edges as shown in Fig. 2.8. In fact, the strongest evidence for the existence of a *d*-wave order parameter in the cuprates comes from such an experiment<sup>43</sup>.

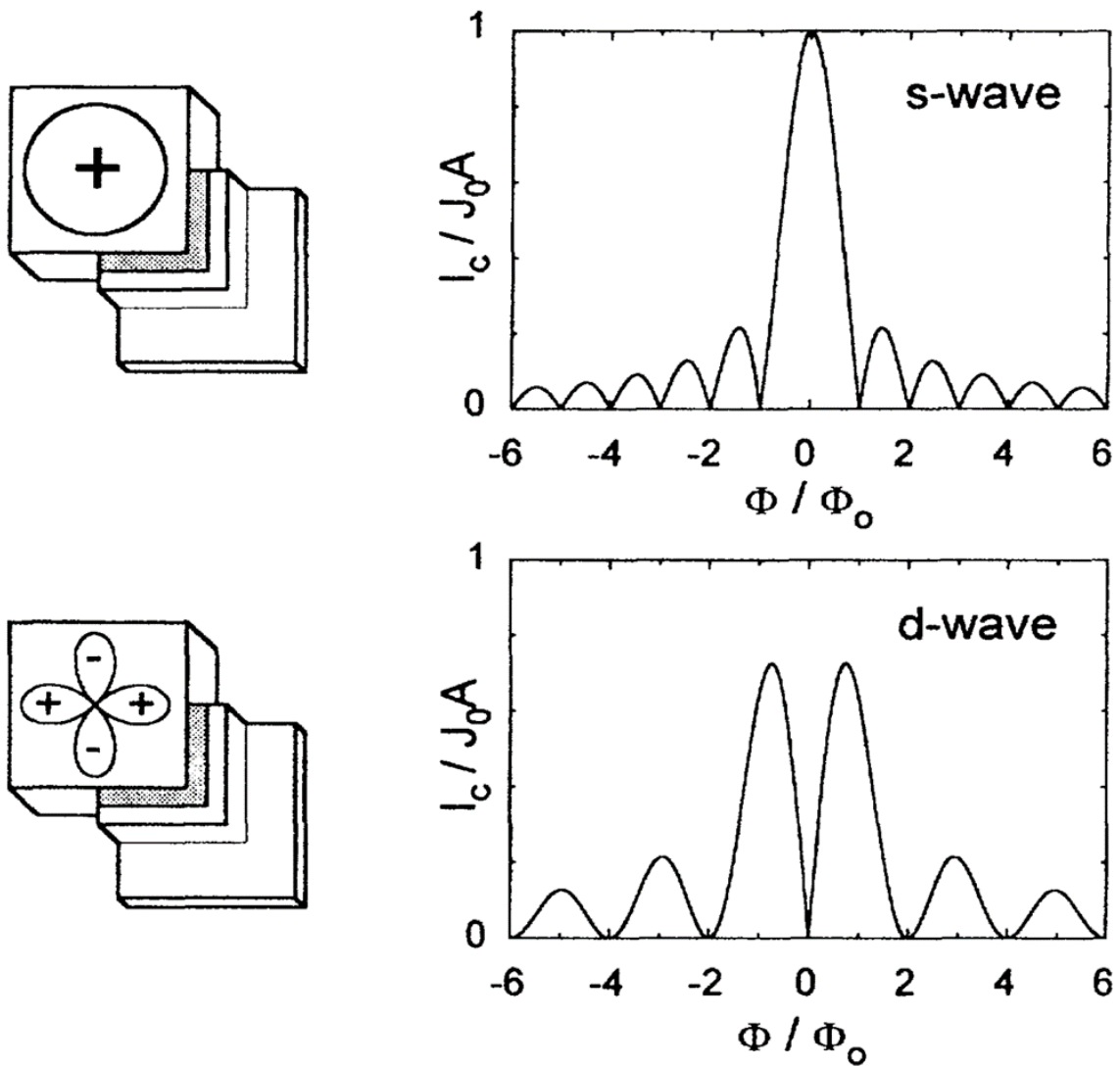


*Fig. 2.8 Quantum interference of the superconducting order parameter: The expected Fraunhofer interference pattern of the superconducting order parameter in a corner Josephson junction for an s-wave superconductor (on top) and a d-wave superconductor (on bottom). Figure adapted with permission from ref.<sup>43</sup>.*



## 2.3 Non-reciprocal transport in superconductors

### 2.3.1 Introduction

A non-reciprocal response is one in which the response of a system to an external stimulus like light, heat, electric fields, etc. is not the same when the direction of the stimulus is reversed. Non-reciprocal responses to external stimuli in condensed matter are of great importance both fundamentally for understanding the implications of symmetries on the system and for various technological applications in memory, sensor and logic devices. The starting point for the semiconductor industry, which has been at the forefront of important technological developments since the 20<sup>th</sup> century was the discovery of the  $p$ - $n$  junction diode, which has a non-reciprocal current response to the application of a voltage stimulus in forward and backward directions. The fundamental requirement for the observation of any non-reciprocal response is the breaking of inversion ( $\hat{I}$ ) symmetry in the system. In addition, certain non-reciprocal processes may require the breaking of time-reversal ( $\hat{T}$ ) symmetry as well. The engineering of non-reciprocal responses in superconductors is quite interesting as it allows for the creation of technologies with minimal energy dissipation.

Non-reciprocal responses can be classified into four different categories based on whether the response is linear or non-linear and if the system has  $\hat{T}$  –symmetry or not, as done by Y. Tokura and N. Nagaosa<sup>44</sup>.

Nonreciprocal response	Linear response	Nonlinear response
Time-reversal unbroken	Forbidden (diagonal) Natural circular dichroism (off-diagonal)	Shift current Nonlinear Hall effect $p$ - $n$ junction
Time-reversal broken	Optical ME effect Magnetochiral effect Nonreciprocal magnon	Nonreciprocal nonlinear optical effect Electrical magnetochiral effect Inverse Edelstein effect Magnetochiral anisotropy

**Table 2.1 Classification of non-reciprocal responses in non-centrosymmetric materials based on the type of response and the presence or absence of time-reversal symmetry. Table reproduced with permission from ref.<sup>44</sup>, Springer Nature**

### 2.3.2 Onsager's reciprocal relation

The Onsager reciprocal relation laid out by Lars Onsager in 1930 forms the basis for existence of reciprocal relations in macroscopic thermodynamic systems with microscopic reversibility<sup>45,46</sup>. He applied this idea to a few different examples like thermoelectric phenomena, electrical conduction and diffusion. Of particular interest to us is the case of electrical conductivity. The general Onsager relation for any process can be written using a linear response function, which satisfies the relation

$$J_{AC}(\mathbf{q}, \omega, \mathbf{B}) = \varepsilon_A \varepsilon_C J_{CA}(-\mathbf{q}, \omega, -\mathbf{B})$$

Where  $\varepsilon_A, \varepsilon_B = \pm 1$  depending on whether  $A$  or  $C$  is even or odd with respect to  $\mathbb{T}$  operation.  $\mathbf{q}$  is the wave vector and  $\omega$  is the frequency. Applied specifically to the electrical conductivity tensor this gives,

$$\sigma_{ij}(\mathbf{q}, \omega, \mathbf{B}) = \sigma_{ji}(-\mathbf{q}, \omega, -\mathbf{B})$$

Certain non-reciprocal processes such as magneto-chiral effect, circular dichroism, Kerr and Faraday rotation can be described under this linear response formalism of the Onsager reciprocal relation. It is to be noted that non-reciprocal responses for diagonal elements (i.e.)  $\sigma_{ii}$ , require the explicit breaking of  $\mathbb{T}$  –symmetry whereas it is possible to obtain non-reciprocal linear responses for off-diagonal elements without the need for  $\mathbb{T}$  –symmetry breaking. However, it's quite different for the case of non-reciprocity in non-linear responses. Non-linear non-reciprocal responses usually result in directional  $I - V$  characteristics and may or may not require explicit  $\mathbb{T}$  –symmetry breaking. It is possible to obtain non-reciprocal responses in non-linear process that are multiband effects or involve electron correlations that break down the ideal Bloch picture of electronic wave functions. The Bloch wave functions are essentially single-particle wave function of electrons that do not include electron correlations. In the presence of  $\mathbb{T}$  –symmetry, they obey the condition

$$\varepsilon_{\mathbf{k}, \sigma} = \varepsilon_{-\mathbf{k}, \sigma'}$$

Where  $\mathbf{k}$  is the crystal momentum and  $\sigma$  is the spin state. This can break down in the presence of electron correlations or if the process concerned is a multiband process that does not necessarily obey Bloch equations or if there are dissipative processes involved<sup>47</sup>. In the presence of electron

correlations, the band structure of a non-centrosymmetric material can be modified asymmetrically depending on the direction of the applied electric field ( $\mathbf{E}$ ).

$$\varepsilon_{\mathbf{k},\sigma}(\mathbf{E}) \neq \varepsilon_{-\mathbf{k},\sigma'}(-\mathbf{E})$$

The best example for this is the  $p - n$  junction diode, which shows non-reciprocal  $I - V$  characteristics without  $\mathbb{T}$  -symmetry breaking. The non-reciprocity in this system originates due to change in the width of the depletion layers upon applying a voltage and can be attributed to the electron correlations induced by Coulomb interactions in the depletion layer of the system. Another example of non-reciprocity in the presence of  $\mathbb{T}$  -symmetry is the observation of shift currents in polar insulators, which is essentially an interband current induced by optical excitations related to the Berry phase of the bands as opposed to regular transport which is an intraband process. However, the supercurrent diode effect that we shall discuss in this thesis is a non-linear non-reciprocal single-band process that requires the explicit breaking of  $\mathbb{T}$  -symmetry.

### 2.3.3 Magneto-chiral anisotropy

The electrical magneto-chiral anisotropy is a non-linear non-reciprocal phenomenon that requires the explicit breaking of  $\mathbb{T}$  -symmetry. It is when the resistance of an inversion symmetry lacking material depends on the direction and magnitude of the applied magnetic field. It was put forth by Geert L. J. A. Rikken in 2001 to explain the phenomenological observation of non-reciprocal resistance under a magnetic field of chiral  $R$  - and  $L$  - bismuth helices based on symmetry arguments<sup>48</sup>. The resistance of a non-centrosymmetric material is given by:

$$R(\mathbf{I}, \mathbf{B}) = R_0 + \gamma^i \mathbf{B} \cdot \mathbf{I} + \beta \mathbf{B}^2$$

Where  $R_0$  is the resistance in the absence of any external magnetic field,  $\gamma^i$  is the magneto-chiral anisotropy and  $\beta$  is the co-efficient for normal magnetoresistance. For chiral materials, usually  $\gamma^R = -\gamma^L$ . Since then, magneto-chiral anisotropy has been observed in many non-centrosymmetric materials. Magneto-chiral anisotropy ( $\gamma$  or MCA) is essentially an empirical quantity used to quantify non-reciprocity in electrical transport.  $\gamma$  in metals is usually quite small of the order of  $10^{-3} - 10^{-2} T^{-1} A^{-1}$  as the spin-orbit coupling energy is usually smaller than the Fermi energy. It is predicted that the effects of spin-orbit coupling in the superconducting state are

enhanced, as they are comparable to the superconducting energy gap  $\Delta$ .  $\gamma$  has been measured in some superconductors with broken inversion symmetry. The value of  $\gamma$  for MoS<sub>2</sub> in the superconducting fluctuation regime<sup>49</sup> was found to be around  $1200 T^{-1}A^{-1}$ . This observation provided the first signature of possible non-reciprocal transport in superconductors with broken inversion symmetry. For a heterostructure composed of multiple superconductors such as Nb/V/Ta,  $\gamma$  reaches around  $550 T^{-1}A^{-1}$  close to  $T_c$ , supporting the hypothesis of an enhanced spin-orbit coupling effect in the superconducting state. It was in this heterostructure that the superconducting diode effect was also first reported<sup>6</sup>.

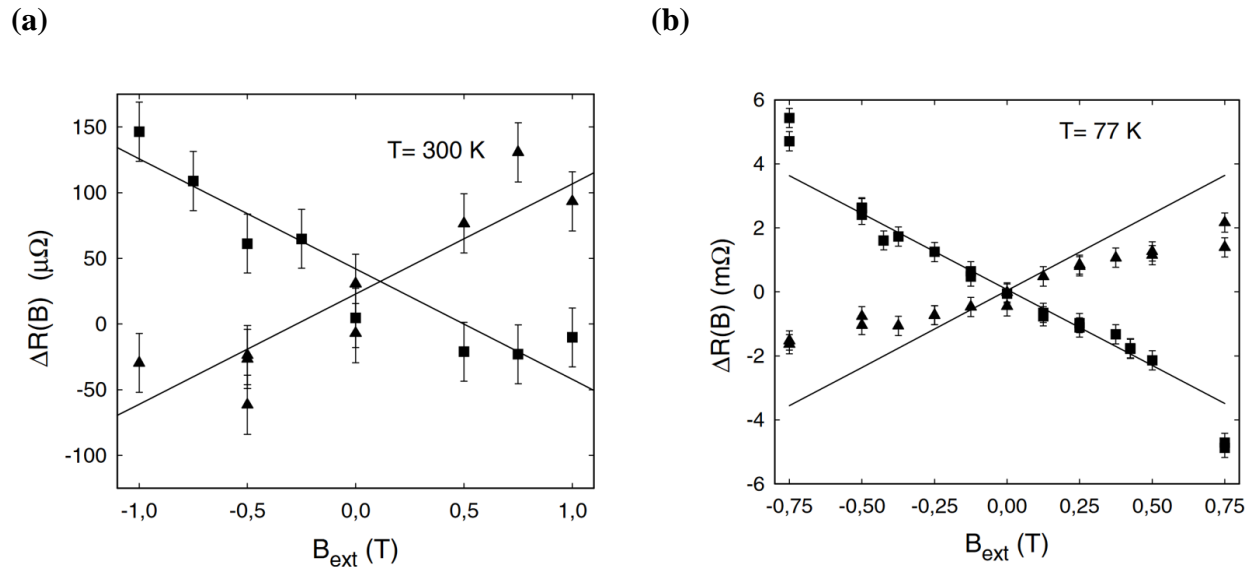


**Fig. 2.9 Magneto-chiral anisotropy:** (a) The change in resistance of chiral bismuth helices of opposite chiralities L-(triangle) and D-(square) upon application of a magnetic field at 300 K and (b) 77 K. Figure adapted with permission from ref.<sup>48</sup>

### 2.3.4 Supercurrent diode effect

#### 2.3.4.1 Introduction

The supercurrent diode effect is achieved when the critical currents of a superconductor or a Josephson junction are unequal when the currents are applied along opposite directions. This

leads to the interesting possibility of sourcing unidirectional supercurrents while the currents are dissipative along the opposite direction. The terminology of the supercurrent diode effect is in analogy with the non-reciprocal conductivity of a semiconductor diode. The semiconductor diode has many applications like in rectifiers, sensors, logic, etc. and has led to the invention of the modern bipolar transistor, which forms the basis of most computing devices today. With Moore's law for semiconducting transistors nearing its end, it is crucial to look for alternative energy efficient platforms to perform computations with scalability. Superconductors provide a fascinating, near dissipationless platform for performing computations in an energy efficient way and at a rapid pace. As discussed in the previous section, in order to observe the supercurrent diode effect induced by the spin-orbit coupling in the superconducting state, the spin-orbit coupling energy scale needs to be comparable to the superconducting energy gap ( $\Delta$ ) which is of the order of  $meV$  instead of the Fermi energy ( $E_F$ ) which can be of the order of  $eV$ .

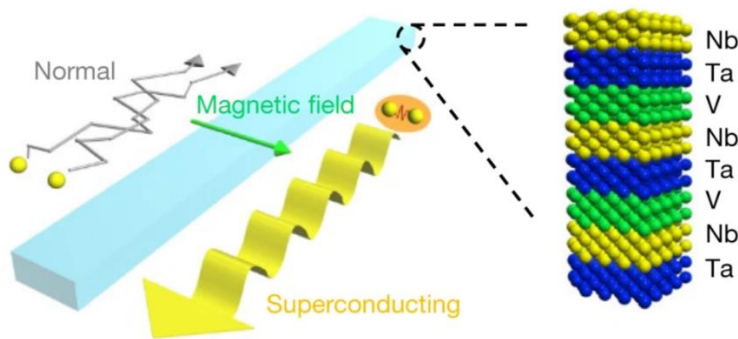
#### 2.3.4.2 Symmetry requirements

Now, let us look at the symmetry requirements for a supercurrent diode effect. Conventional BCS superconductors require the existence of particle-hole symmetry in the system (Refer section on BCS theory) which implies that the superconducting energy gap ( $\Delta$ ) and thereby the gap closing current ( $I_C$ ) is the same in opposite directions. The presence of non-reciprocal critical currents in the system indicates the existence of unequal superconducting gaps in opposite directions, thereby requiring the breaking of particle-hole symmetry in the superconductor. (i.e.) the energy spectrum of the superconductor needs to be asymmetric with respect to  $\mathbf{k}$ . We shall see in later chapters on how this symmetry breaking can be achieved leading to the supercurrent diode effect. This non-linear process requires the breaking of time-reversal symmetry of the system and like any other non-reciprocal effect, inversion-symmetry breaking is an inherent requirement as discussed in Onsager's reciprocal relation. Therefore, intrinsically the presence of a supercurrent diode effect indicates the presence of a strong deviation from the BCS theory and the possibility of unconventional pairing mechanisms.

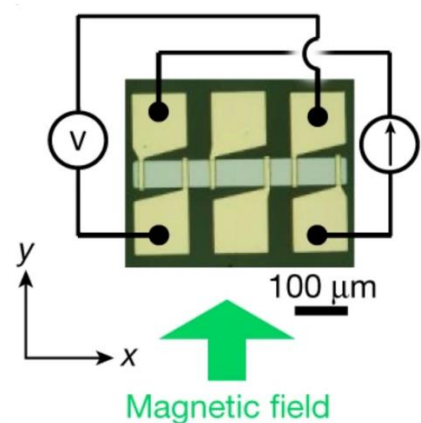
### 2.3.4.3 State-of-the-art in supercurrent diodes

This section gives the developments in the field of supercurrent diode effects at the time before the thesis. The superconducting diode effect (SDE) was first reported<sup>6</sup> to have been observed by Teruo Ono's group in 2020 in an artificial super lattice of superconductors  $[\text{Nb}/\text{V}/\text{Ta}]_n$ , which lacks a center of inversion. The lack of inversion symmetry at the interface between the elemental superconductors leads to the presence of a Rashba-type spin-orbit interaction that causes a spin-dependent band splitting in the system that in the presence of a magnetic field perpendicular to the direction of current breaks the time-reversal symmetry of the system and creates unequal critical currents in the system. The diode effect, defined as  $\Delta I_c = I_c^+ - |I_c^-|$  was found to be large close to the  $T_c$  around 4.2 K and vanish at lower temperatures. The MCA of the system was also calculated from the second-harmonic resistance and was found to be very large close to  $T_c$ . The observation of SDE in the system was rather phenomenological and no detailed description of the underlying mechanism was provided. Later, SDE was also reported in few layer  $\text{NbSe}_2$ <sup>50</sup>, which is an Ising superconductor and is expected to have a Zeeman type spin-orbit coupling. The marked difference here as compared to the previous case, comes from the nature of spin-orbit coupling in the system and consequently an out-of-plane magnetic field was required to observe an SDE. A SDE was reported in small-twist angle trilayer graphene<sup>51</sup> in the absence of an applied magnetic field indicating the presence of spontaneous time reversal breaking in the system. A valley-polarized occupation of the underlying Fermi surface was attributed as the cause of the spontaneous time reversal breaking in the system.

(a)



(b)



(c)

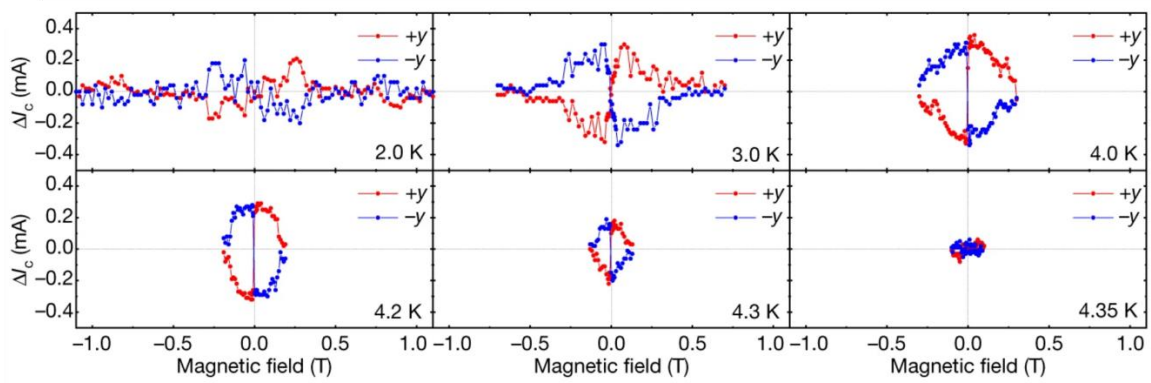


**Fig. 2.10 Superconducting diode effect (SDE) in  $[Nb/V/Ta]_n$ :** (a) Schematic of the multilayer superconductor structure depicting the flow of electrons in one direction and Cooper pairs in the opposite direction. (b) Optical image of the device used for measurements with the magnetic field perpendicular to the current direction. (c) Temperature dependence of  $\Delta I_c$  measured in positive and negative magnetic fields showing that the effect is maximized around 4.2K. Figure reproduced with permission from ref.<sup>6</sup>, Springer Nature.

Another avenue to realize supercurrent diode effects is in Josephson junctions, where the supercurrents can flow through the normal barrier when in proximity to superconducting electrodes. The non-reciprocity in critical currents obtained in a Josephson junction is labelled Josephson diode effect (JDE). Josephson diode effect was first reported in a Josephson junction array of InAs quantum wells proximitized with aluminium electrodes by measurements of both the critical currents and the kinetic inductance of the Josephson junctions<sup>7</sup>. InAs is a semiconductor with a 2D electron gas and known to have a strong spin-orbit coupling and has been explored a lot in connection with topological superconductivity. A very large MCA of  $4.1 \times 10^6 T^{-1}A^{-1}$  was also observed closed to the  $T_c$  of the junction. The presence of a JDE was correlated with the presence of a non-sinusoidal term in the CPR of the junction.

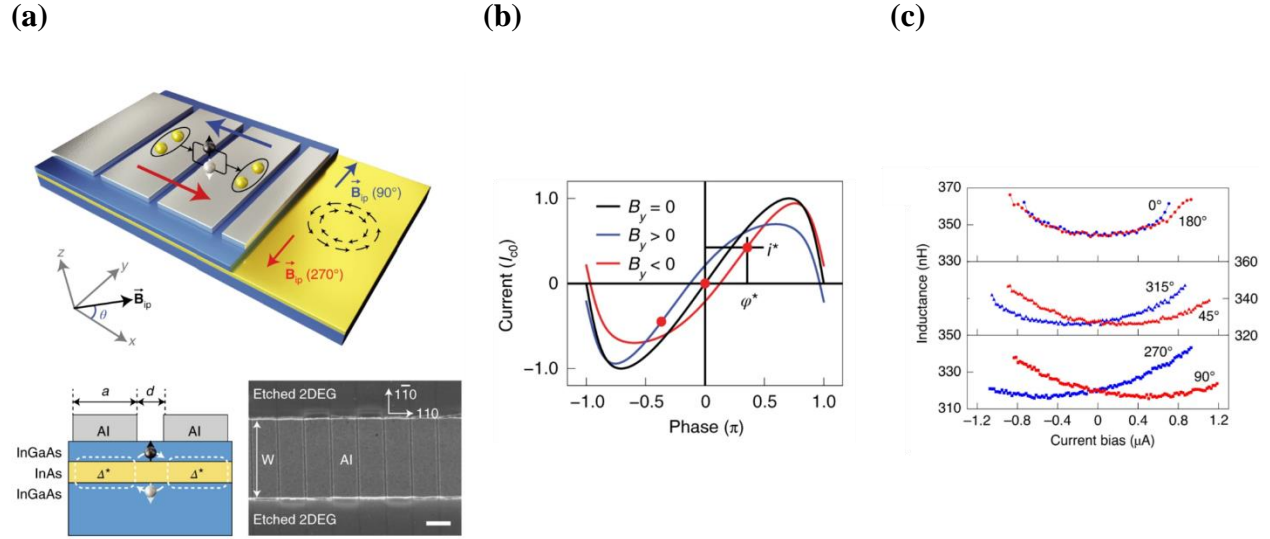


**Fig. 2.11 Josephson diode effect in an array of InAs junctions:** (a) Schematic of the InAs Josephson array consisting of the 2DEG at the bottom with the superconducting aluminium electrodes on the top. (b) The evolution of the CPR expected for positive and negative magnetic fields perpendicular to the current direction. (c) Inductance measurements show a shift in the minima at different magnetic fields that can be used to estimate the CPR. Figure reproduced with permission from ref.<sup>7</sup>, Springer Nature.

The first observation of a magnetic field-free JDE was reported in a vertical van der Waals heterostructure of  $\text{Nb}_3\text{Br}_8$  sandwiched by  $\text{NbSe}_2$  on the top and bottom<sup>2</sup>. Though the exact origin of this effect is not fully understood, since  $\text{Nb}_3\text{Br}_8$  does not have a magnetic ground state that breaks time-reversal symmetry, the spontaneous time reversal symmetry breaking in the system was attributed to the obstructed atomic insulator nature of  $\text{Nb}_3\text{Br}_8$  with Wannier charge centers symmetrically pinned at the unoccupied inversion centers between two Br-Nb-Br layers. The effect observed in this paper was very different from the previous reports as the JDE in this case was found to be symmetric with respect to the field. More details on this work are discussed in the appendix. Later, a field-free JDE was also reported in platinum on top of a ferrimagnetic insulator yttrium iron garnet  $\text{Y}_3\text{Fe}_5\text{O}_{12}$  (YIG), proximitized by niobium electrodes<sup>52</sup>. The proximity-induced magnetization in platinum was used to induce a field-free JDE, the polarity of which could be switched by reversing the magnetization of the underlying YIG layer. The efficiency of the diode effect in various materials so far can be found in the appendix.



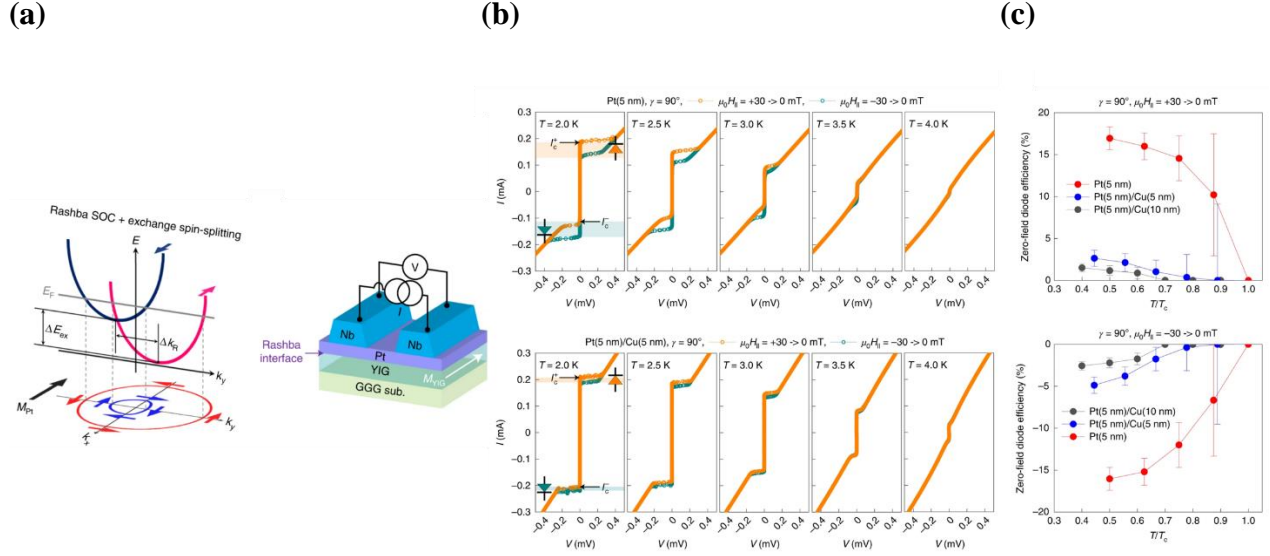


**Fig. 2.12 Polarity controlled zero field JDE in Pt/YIG heterostructure junctions:** (a) Schematic of the Pt/YIG Josephson junction with the superconducting niobium electrodes on the top and the momentum shift induced by the combination of the exchange spin splitting and Rashba SOC. (b) The polarity of the JDE is reversed when the magnetization of the underlying YIG layer is switched. (c) Efficiency of the JDE for various separations of the platinum layer from the YIG. Figure reproduced with permission from ref.<sup>52</sup> Springer Nature.

## 2.4 Hidden Inversion symmetry breaking and Superconductivity

### 2.4.1 Introduction

As discussed in BCS theory the existence of inversion and time reversal symmetries are crucial for spin-singlet  $s$ -wave pairing. But the breaking of inversion symmetry is necessary for the observation of non-reciprocal effects in transport. Though non-centrosymmetric superconductors exist, they are not plenty in number as superconductivity is inherently not supported in them according to BCS theory. One way to go about this is to look at materials that are centrosymmetric globally but there is a lack of inversion symmetry locally. In this case, the superconductivity can still be sustained but the local spin polarizations induced by the inversion symmetry breaking can modify the pairing symmetries and lead to unconventional superconductivity in the system. Different centrosymmetric point groups that host locally non-centrosymmetric atomic point groups and the corresponding spin-momentum locking are shown

in Table 2.2. A more detailed discussion of spin polarization due to local inversion symmetry breaking and its implication on superconductivity can be found in the literature<sup>53,54</sup>. This section discusses one such structure (1T) with local inversion symmetry breaking that is present in both the materials (NiTe<sub>2</sub> and PtTe<sub>2</sub>) studied in this thesis.

Site point group Bulk space group	Non-centrosymmetric (at least one site)			Centrosymmetric (all sites)  ( $C_i, C_{2h}, D_{2h}, C_{4h}, D_{4h}, S_6, D_{3d}, C_{6h}, D_{6h}, T_h, O_h$ )
	Non-polar (all sites) ( $D_2, D_3, D_4, D_6, S_4, D_{2d}, C_{3h}, D_{3h}, T, T_d, O$ )	Polar (at least one site) ( $C_1, C_2, C_3, C_4, C_6, C_{1v}, C_{2v}, C_{3v}, C_{4v}, C_{6v}$ )		
		Dipoles add up to zero	Dipoles add up to non-zero	
Non-centrosymmetric (for example, $F\bar{4}3m$ )	<b>a</b> D-1 Example: GaAs, ZrCoBi	<b>b</b> D-1 Example: $\gamma$ -LiAlO <sub>2</sub>	<b>c</b> R-1 & D-1 Example: BiTeI, $\alpha$ -SnTe	Not possible (Site point group cannot be centrosymmetric if space group is non-centrosymmetric)
Centrosymmetric (for example, $R\bar{3}m$ )	<b>d</b> D-2 Example: Si, NaCaBi	<b>e</b> R-2 & D-2 Example: MoS <sub>2</sub> , Bi <sub>2</sub> Se <sub>3</sub> , LaOBiS <sub>2</sub>		<b>f</b> Absence of spin polarization Example: $\beta$ -SnTe

**Table 2.2: Classification of centrosymmetric and non-centrosymmetric space groups based on atomic point group symmetries along with possible spin-momentum locking. Table reproduced with permission from ref.<sup>53</sup>, Springer Nature.**

## 2.4.2 Hidden spin-momentum locking in 1T(trigonal) and 2H(hexagonal) transition metal dichalcogenides (TMDCs)

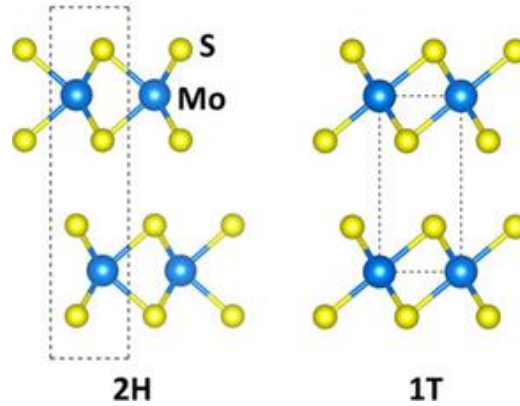


**Fig. 2.13 Schematic of 2H and 1T structures:** The 2H structure is non centrosymmetric in the monolayer but center of inversion is restored in the bilayer. The 1T structure is centrosymmetric down to the monolayer but hosts atomic sites that lack inversion symmetry. Figure reproduced with permission from ref.<sup>55</sup>

In order to understand the physics of Cooper pairing in 1T(trigonal)-TMDCs, let us first start by considering their crystal structure. 1T systems crystallize in the  $P-3m1$  space group, which is a centrosymmetric space group that is not expected to have any asymmetric spin-orbit coupling interactions like the Rashba or Dresselhaus effects. Each layer consists of three sublayers with a layer of transition metal atoms located in the center and sandwiched by two sublayers of chalcogenide atoms on the top and bottom as shown in the schematic in Fig. 2.14. The transition metal atoms are coordinated with the chalcogenide atoms in their close vicinity in an octahedral fashion. This gives the transition metal atoms a  $D_{3d}$  point group symmetry, which includes a center of inversion. The chalcogenide atoms on the other hand, have a  $C_{3v}$  point group symmetry, which lacks a center of inversion. This lack of inversion symmetry, locally within the unit cell leads to the existence of equal but opposite electric dipoles pointing out-of-plane and consequently asymmetric helical spin-orbit couplings on the top and bottom layers of chalcogenide atoms as shown in Fig. 4.1. Though globally the spin-orbit coupling strength adds up to zero, the existence

of locally broken symmetries and hence, a ‘local Rashba effect’ in the system leads to the existence of a layer-dependent spin-momentum locking in the system where the spins in the top and bottom chalcogenide layers are oppositely spin-polarized. This is known as ‘spin-layer locking’ and has been observed through ARPES in few layers of  $\text{PtTe}_2$ <sup>56</sup>,  $\text{PtSe}_2$ <sup>57</sup>, etc. and in bulk  $\text{MoS}_2$ <sup>58</sup>. The existence of such a spin-polarization and the formation of bulk Dirac cones in 1T systems due to non-centrosymmetry of the chalcogen atom, has been explained in detail and also observed experimentally by Bahramy M. S. et. al.<sup>8</sup> in a variety of TMDCs. Though compensated globally, the existence of such a ‘hidden spin polarization’ due to locally broken symmetries can lead to interesting transport effects and exotic order parameters such as pair density waves<sup>24</sup> in the superconducting state of such materials.

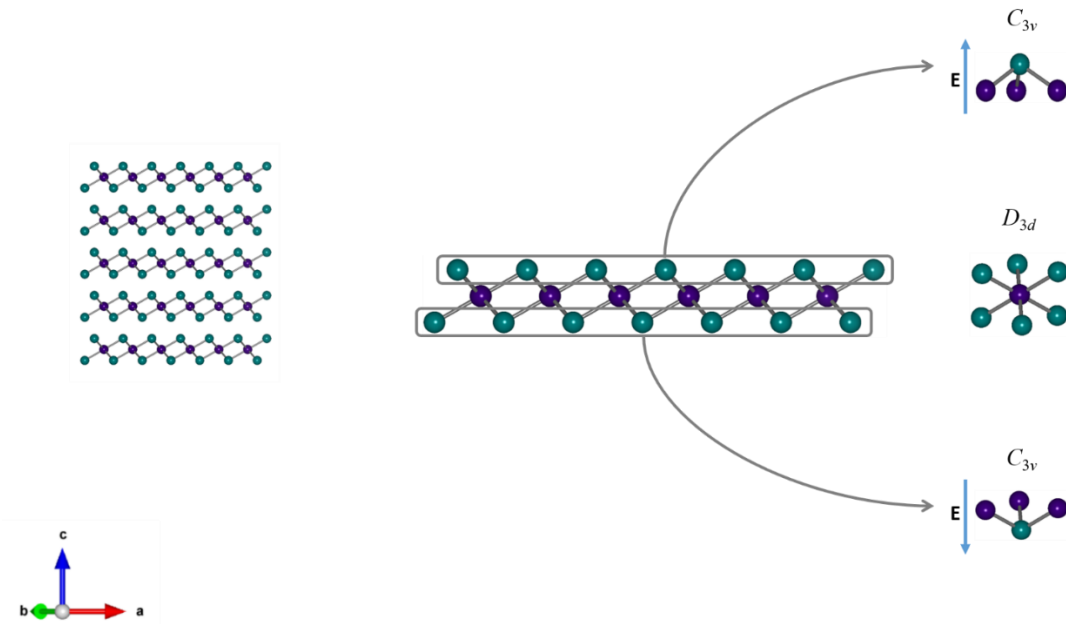


**Fig. 2.14 Local electric dipoles in 1T structure:** The centrosymmetric 1T structure hosts atomic sites that lack inversion symmetry leading to electric dipoles of opposite polarity on the chalcogen sites and consequently spin polarization and helical spin-momentum locking in the chalcogen-derived electronic bands.

Let us now digress a bit and discuss the structure of 2H(hexagonal)-TMDCs as the structure-property correlations in them are well studied and are understood better. 2H-TMDCs have a trigonal prismatic coordination with the transition metal having a  $D_{3h}$  point group symmetry

that lacks an inversion symmetry. Unlike 1T-TMDCs which are centrosymmetric in the monolayer but non-centrosymmetric when considering the atomic site point group symmetry, 2H-TMDCs break inversion symmetry at the monolayer level and have it restored in the bilayer by an AB type stacking. The electric dipole in this case lies in the plane of atoms as shown in Fig leading to a spin-orbit field  $\mathbf{B}_{so} \propto \mathbf{E} \times \mathbf{k}$ . This results in a spin-momentum locking in the system that points out-of-plane called as Zeeman-type spin momentum locking and alternates with each layer. This is reflected in the electronic structure as out-of-plane spin-polarized bands with opposite signs around K and K' valleys in the momentum space as shown through spin- and angle- resolved photoemission spectroscopy (SARPES) in Fig. 2.15 for 2H-WSe<sub>2</sub><sup>59</sup> and through DFT calculations in Fig. 2.16 for a monolayer of 1H-NbSe<sub>2</sub> and 1H-TaS<sub>2</sub><sup>60</sup>. This opposite spin-momentum locking at alternating valleys in semiconducting 2H-TMDCs has led to the field of valleytronics, which involves controlling the valley degree of freedom of electrons. However, this is outside the scope of this discussion and won't be discussed further. Some examples of TMDCs with this structure include MoS<sub>2</sub>, NbSe<sub>2</sub>, TaS<sub>2</sub>, WSe<sub>2</sub>, etc.

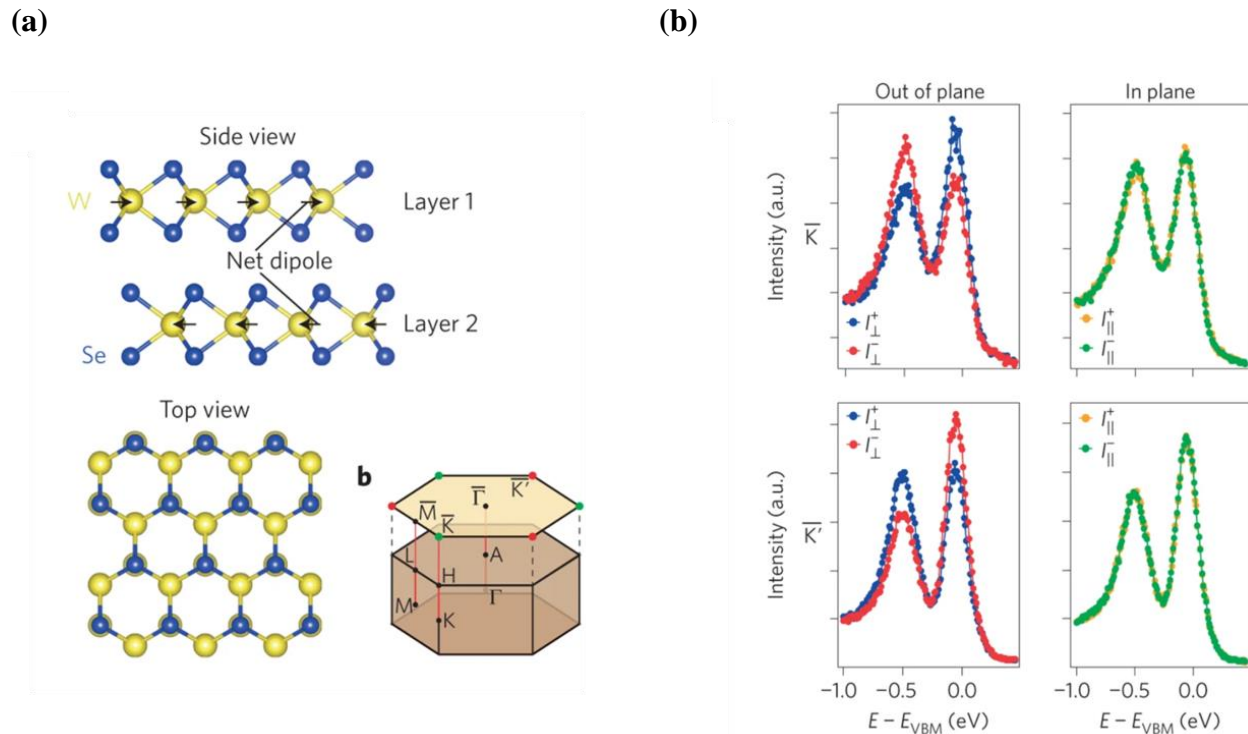


**Fig. 2.15 Ising spin-polarization in 2H-WSe<sub>2</sub>:** (a) The 2H structure of WSe<sub>2</sub> viewed along the *a*-axis. It is non-centrosymmetric in the monolayer and has electric dipoles on the transition metal

atom. Consequently, the bands derived from the transition metal atom orbitals have an Ising spin polarization. (b) Out-of-plane spin polarization is observed in the spin resolved density of states while in-plane spin polarization is absent indicating the presence of an Ising spin-momentum locking. Figure reproduced with permission from ref.<sup>59</sup>, Springer Nature.

### 2.4.3 Cooper pairing in 2H- and 1T- TMDCs

For this discussion, the object of interest in these systems is the superconducting state in these spin-polarized systems. Some of the 2H-TMDCs like NbSe<sub>2</sub> and TaS<sub>2</sub> are known to be superconducting. The Fermi surface of NbSe<sub>2</sub> and TaS<sub>2</sub> computed by density functional theory (DFT)<sup>60,61</sup> displaying the spin-polarized bands derived from the Nb and Ta orbitals are shown in Fig. 2.16. It has a hexagonal Brillouin zone and a Fermi surface with three-fold symmetry as reflected from the lattice. As it can be noticed, there are out-of-plane spin-polarized pockets around  $\Gamma$ , K and K' with K and K' having opposite spin polarizations. As discussed in BCS theory, the Cooper pairs are formed between electrons located at opposite points in momentum space with net-zero center of mass momentum and of opposite spin angular momentum to conserve the momentum and antisymmetric nature of the fermionic wave function respectively. In this case, the electrons at opposite momenta have opposite spins with their spin quantization axis only in the out-of-plane direction leading to the formation of Cooper pairs with strong spin-momentum locking leading to what is known as 'Ising' superconductivity. The pairing can occur between electrons in pockets centered at  $\Gamma$  point or between electrons in pockets centered at K and K' points. The strong spin-orbit field in thin layers of Ising superconductors provide them immunity from depairing effects of the magnetic field applied parallel to the surface plane, leading to upper critical fields far above the Pauli paramagnetic limit<sup>60,62,63</sup>. There has been a recent report of an orbital Fulde-Ferrell-Larkin-Ovchinnikov (FFLO) state created in NbSe<sub>2</sub> under very strong parallel magnetic fields as the spins remain unaffected by the strong parallel magnetic fields which couple to the orbital angular momentum of the system<sup>38</sup>.

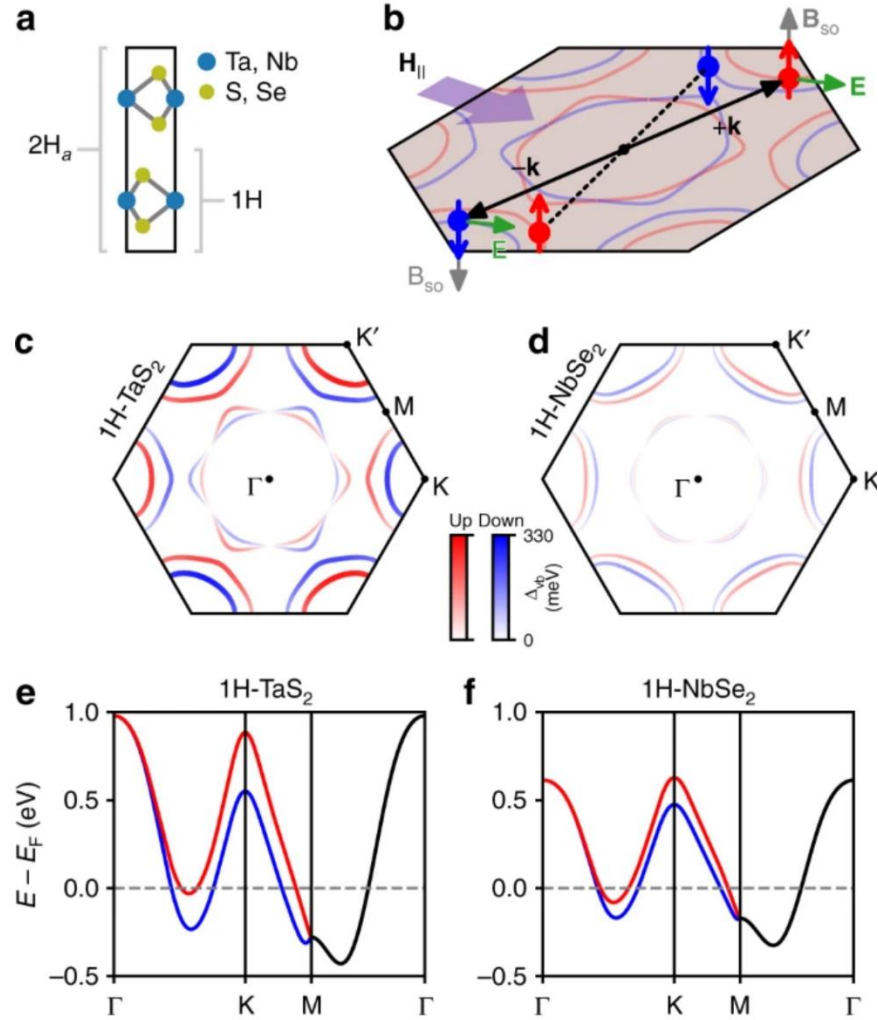


**Fig. 2.16 Ising pairing in 1H-NbSe<sub>2</sub> and 1H-TaS<sub>2</sub>:** (a) The 2H structure of consisting of a bilayer of NbSe<sub>2</sub> or TaS<sub>2</sub>. (b) The Ising pairing mechanism in 2H-superconductors lead to strong protection from external pair breaking magnetic fields far above the Pauli paramagnetic limit. Pairing of spin-locked electrons occurs in bands centered around the  $\Gamma$  point and in bands centered around K and K' points. Figure reproduced from ref.<sup>60</sup>, Springer Nature.

Now with this in mind, the Cooper pairing in 1T structures can be discussed. As stated earlier, 1T structures are centrosymmetric but the presence of electric dipoles pointing out-of-plane on the top and bottom chalcogen sites in a monolayer gives rise to an in-plane helical spin-momentum locking on the bands arising from the chalcogen orbitals<sup>8</sup>. Let us consider the example of 1T-NiTe<sub>2</sub>. In this system, close to the Fermi level there are spin-polarized topological surface

states. The spin-polarized Fermi surface of NiTe<sub>2</sub> calculated by DFT is shown in Fig. 2.17. There are multiple pockets located around  $\Gamma$  and K points with an overall helical spin-momentum locking structure. Cooper pairing of spin-momentum locked electrons occurs between electrons located at  $\mathbf{k}$  and  $-\mathbf{k}$  points in the momentum space. The spin-momentum locking allows for control of the electronic bands with the help of a Zeeman field. A detailed explanation on the creation of non-zero momentum Cooper pairing and how it leads to the creation of a supercurrent diode effect in 1T structures is discussed in chapter 4.

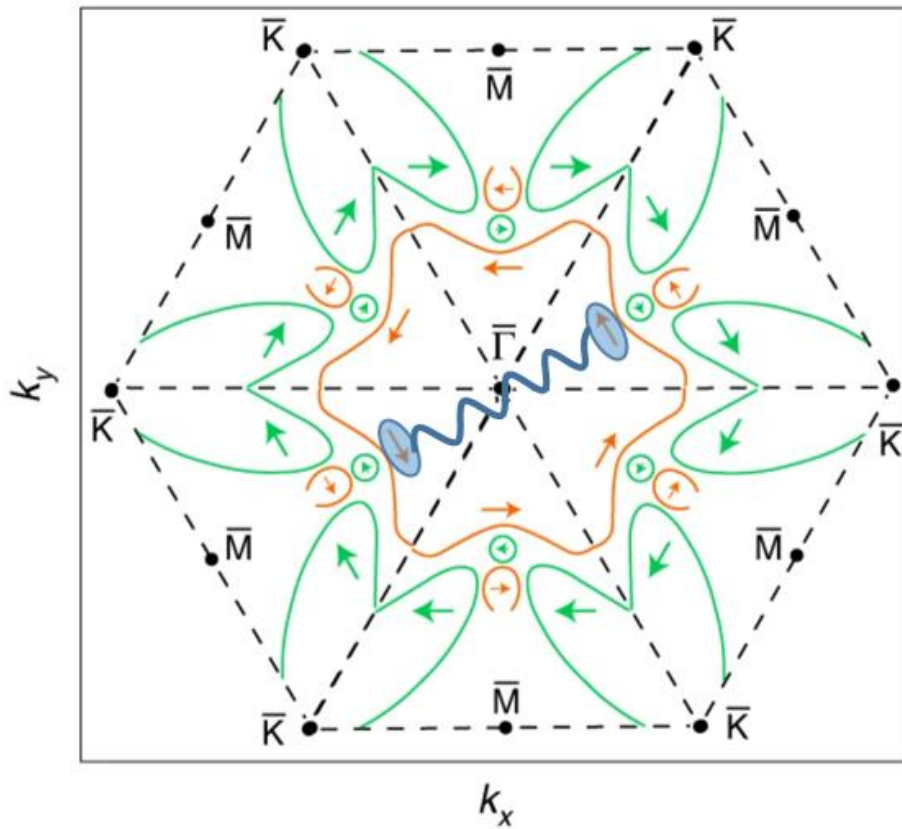


**Fig. 2.17 Fermi surface of 1T-NiTe<sub>2</sub>:** DFT calculations showing the spin-polarized Fermi surface of 1T-NiTe<sub>2</sub> with hexagonal symmetry and helical spin-momentum locking across multiple pockets. Figure reproduced from ref.<sup>1</sup>, Springer Nature.



# 3

---

## Experimental methods

## 3.1 Introduction

Throughout the thesis, multiple experimental tools are used to fabricate, characterize and measure electronic devices pertaining to the Josephson diode effect in certain van der Waals transition metal dichalcogenide (TMDC) systems. In this chapter, the working principles of the tools and the methods used extensively are explained in detail. Especially the dilution refrigerator setup, which I had the privilege to set up and work with on many exciting experiments. The device fabrication process includes mechanical exfoliation of the van der Waals crystals, defining the electrodes using electron-beam lithography and photolithography, deposition of the superconducting electrodes on top of the flakes and lifting off the residual resist. The device is then characterized using a scanning electron microscope to find the exact spacing between the electrodes and an atomic force microscope is used to measure the thickness of the flake and deposited electrodes. The electrical transport characterization that involves the bulk of the data presented in the thesis is then performed in a dilution refrigerator setup that is capable of reaching temperatures below  $10\text{ mK}$ . Some basic electrical characterizations are performed in a Physical Property Measurement System (PPMS).

## 3.2 Device fabrication

### 3.2.1 Mechanical exfoliation of van der Waals materials

Van der Waals materials or more commonly known as two-dimensional (2D) materials are materials that are held together strongly by covalent chemical bonds in two directions (usually the crystallographic  $ab$  directions) while weakly connected by van der Waals force in the third dimension<sup>64</sup>. The van der Waals force is usually very weak and can be broken using either physical or chemical forces. This process is known as exfoliation and can be used to break down three-dimensional bulk crystals of the material to form two-dimensional sheets of the material. The reduction in the dimensionality created by this top-down process opened a new door to study the physics of materials in lower dimensions. For example, the physics of two-dimensional electron gases (2DEG) which was previously studied by fabricating complicated semiconductor heterostructures<sup>65</sup> can now easily be accessed by exfoliation of van der Waals crystals down to the

monolayer limit. This was first discovered by A.K. Geim and K.S. Novoselov by mechanically exfoliating graphene using scotch tape<sup>66</sup>, which is a single two-dimensional layer of graphite, for which they won the Nobel prize in 2010.

Mechanical exfoliation is a physical exfoliation process wherein a bulk van der Waals crystal is thinned down into few layers by repeatedly peeling it with the help of an adhesive tape like Scotch<sup>®</sup> tape or Nitto<sup>®</sup> tape and then attached to a clean substrate like silicon coated with SiO<sub>2</sub>. In our case, we exfoliate van der Waals transition metal dichalcogenides (TMDCs) like NiTe<sub>2</sub> and PtTe<sub>2</sub> which have relatively stronger van der Waals force compared to other van der Waals materials like graphite or other TMDCs like MoS<sub>2</sub>, NbSe<sub>2</sub>, WTe<sub>2</sub>, etc. and are hence difficult to exfoliate down to the monolayer limit. The ratio of *c*-axis lattice parameter to *a*-axis lattice parameter known as *c/a* ratio is a good indicator of the strength of van der Waals force between the layers. In the case of graphite, 2H-MoS<sub>2</sub> and 2H-NbSe<sub>2</sub>, the *c/a* ratios are 2.73, 3.90 and 3.65 respectively, whereas in the case of 1T-NiTe<sub>2</sub> and 1T-PtTe<sub>2</sub>, the *c/a* ratios are 1.34 and 1.29 respectively. Hence, we try to find very thin layers of these materials (not down to the monolayer) with dimensions reasonable enough to fabricate devices for our studies. Both 1T-NiTe<sub>2</sub> and 1T-PtTe<sub>2</sub> are extremely air stable and do not require an inert atmosphere. Exfoliation of the flakes is done both under ambient and inert atmospheres and does not produce any significant difference in the quality of the devices. The exfoliation process is as follows:

- 1) The exfoliation process is done on silicon substrates with 300 nm SiO<sub>2</sub> coating that provides electrical isolation of the exfoliated layers (flakes) and provides a good optical contrast due to the difference in the optical path of the reflected light to identify and distinguish the thickness range of the flakes under an optical microscope.
- 2) Prior to the exfoliation process, the silicon substrates undergo a lithography process to deposit gold markers on the substrate to locate the flakes and to do the alignment during device fabrication.
- 3) The silicon substrates then undergo a thorough cleaning process to remove any adsorbed impurities. They are cleaned with acetone, ethanol and isopropanol for 10 minutes each with ultrasonication. They are then heated on a hot plate for 2 minutes at 100 °C to dry them and then treated under oxygen plasma for 15 minutes to remove the residual organic solvents.

- 4) Meanwhile the flat side of a bulk TMDC crystal of NiTe<sub>2</sub> or PtTe<sub>2</sub> is placed on the adhesive side of blue Nitto tape, covered with the tape on top and pressed thoroughly, applying a strong force using the thumbs to make it stick to the tape. The tape is then pulled apart in one swift motion to cleave the crystal. This process is repeated three to four times to thin the crystal down to a few layers.
- 5) The exfoliated crystal on the tape is then transferred on to the silicon substrate by placing it on the substrate area and gently rubbing it with a tweezer to remove any air bubbles.
- 6) The tape is then gently peeled off the substrate with a very slow motion moving at roughly 0.5 mm/s to leave behind some thin flakes on the substrates. It is to be noted that heating the substrate during exfoliation doesn't significantly improve the yield of thin flakes.

The substrate is then inspected under an optical microscope to identify flakes of suitable thickness. It is hard to distinguish the exact thickness of the flakes in this case from the optical contrast. Thicker flakes are more reflective and appear brighter while thinner flakes appear relatively dull as shown in Fig. 3.1 (d)-(e). Flakes of suitable sizes are selected by comparing their sizes with the 10 μm wide alignment markers and their thickness is checked using an atomic force microscopy (AFM).

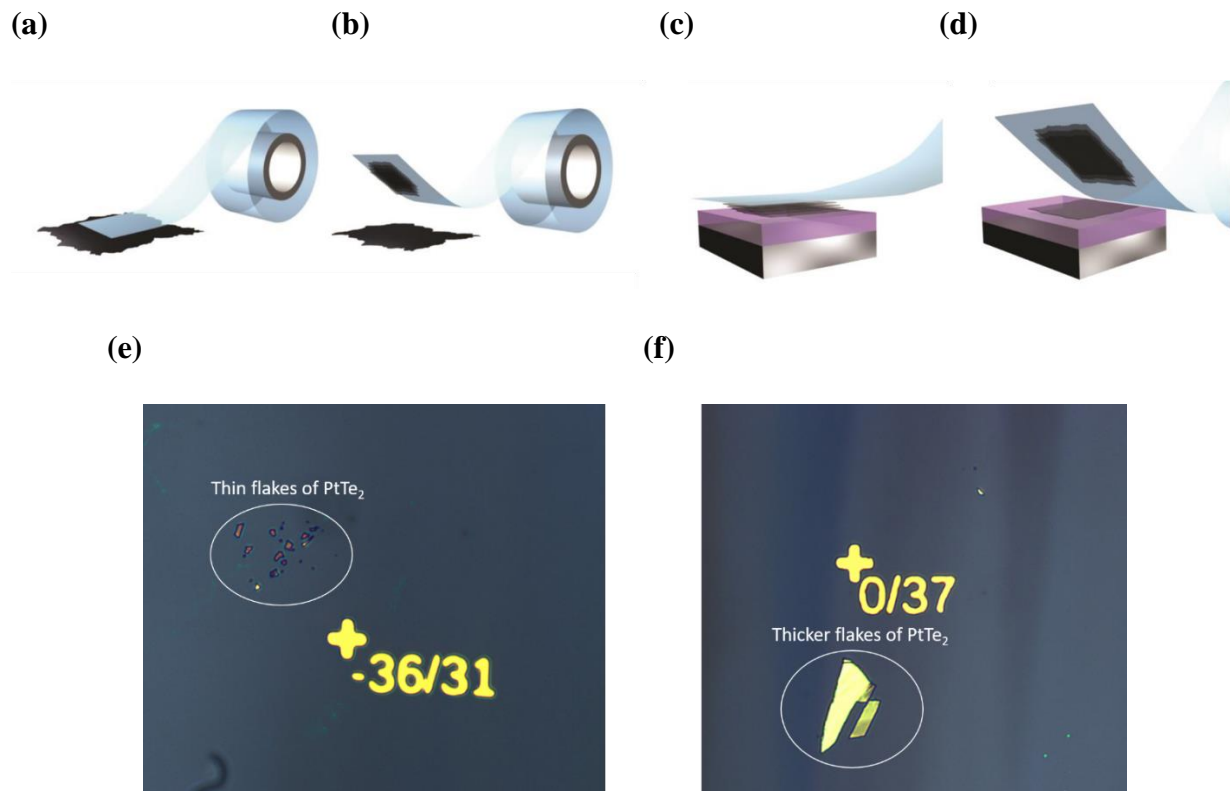


**Fig. 3.1 Mechanical exfoliation of PtTe<sub>2</sub>:** (a)-(d) A schematic showing the mechanical exfoliation process of a van der Waals crystal. Figures reproduced with permission from <sup>67</sup>. (e)-(f) Optical images of thin and thick flakes of PtTe<sub>2</sub> on Si/SiO<sub>2</sub> under an optical microscope. The thicker flakes are highly reflective and have a metallic sheen while the thin flakes appear dull and have a different colour.

### 3.2.2 Photolithography

Photolithography is the process in which a photosensitive polymer coated on a substrate is exposed to a beam of photons on a desired area to produce the required structures. The typical resolution that photolithography can achieve is around 1  $\mu\text{m}$  and is used to make larger structures such as contact pads and alignment markers. Photolithography is performed using a Maskless Aligner 150 (MLA 150) from Heidelberg Instruments. The Maskless Aligner uses a 375 nm solid-state laser and has a high-speed spatial light modulator and an ultrafast 2D sample stage that helps expose the substrate without the need for any hard mask. The photolithography process involves two types of photosensitive polymers known as positive and negative photoresists. The exposure of the positive (negative) resist to the laser softens (hardens) it during the development process. A schematic of the photolithography process is shown in Fig. 3.2. Prior to the photolithography process, the required design is written in the “.GDS” format using a software such as Layout Editor. The photolithography process is as follows:

- 1) The silicon substrate is cleaned in acetone, ethanol and IPA for 5 minutes each. Care is taken that no strong force that displaces the flakes from the substrates such as an ultrasonic force is applied.
- 2) The substrate is then heated at 100 °C for 2 minutes to dry the solvent residues.
- 3) The substrate is spin-coated with a positive (AR – P 3540 T) or negative photoresist (AR – N 4340) from Allresist as required at 4000 rpm for 1 minute and heated at 100 °C for 1 minute.
- 4) The substrate is then exposed to the laser using MLA 150 with the required design.
- 5) The exposed substrate is then developed using a developer such as AR 300 – 44 (for positive resist) or AR 300 – 475 (for negative resist) for 1 minute to remove the resist

from unwanted areas, stopped with water for 60 seconds and the developed design is checked using an optical microscope. The developed substrate is then used for etching and deposition.

- 6) The subsequent liftoff of the undeveloped resist is performed by immersing the substrate in acetone for 30 minutes followed subsequently by gentle ultrasonication in case no fragile structures are present on top of the substrate.

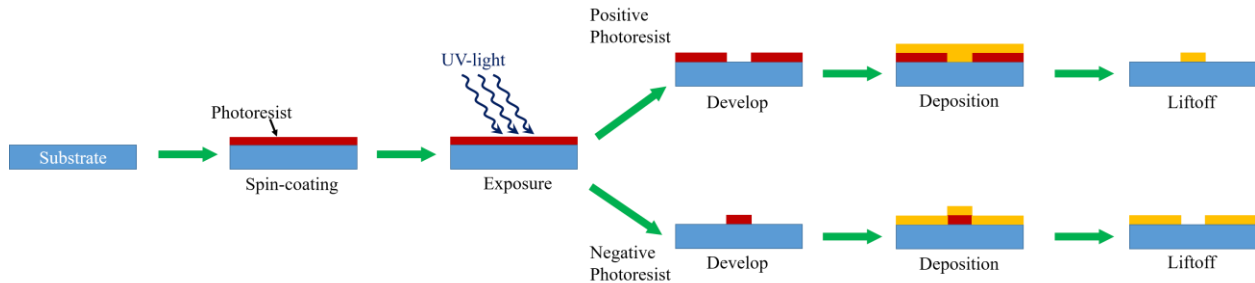


**Fig. 3.2 Optical lithography process:** A schematic showing the different steps involved in the photolithography process with both positive and negative resists. The two resists form structures complimentary to each other and can be chosen based on the process requirement.

### 3.2.3 Electron-beam lithography

The electron-beam lithography (e-beam lithography or EBL) process is similar to the photolithography process except it uses a high-energy focused electron beam from an electron column, which provides a much better resolution in comparison to a photon beam and is used to fabricate smaller structures of the order of  $\sim 100\text{ nm}$  and uses a polymer sensitive to the high-energy electrons (PMMA) rather than photons. The electron beam lithography is performed using a Raith Pioneer Two system and has a similar 2D stage like the photolithography system that is controlled by a laser interferometer. When using the electron-beam, it is important that the substrate used is conducting and grounded to avoid charging effects that might affect the imaging and patterning process. Insulating substrates are usually covered with a conductive polymer to achieve this. The EBL process involves a lot of parameters like the acceleration voltage, beam current, aperture size, dose, working distance, stigmation, etc. that need to be optimized in order

to obtain the best results. The optimization of these individual parameters can be found in the Raith manual.

In our case, a double layer e-beam resist where the lower layer is a weak polymer that develops faster is used. This creates an undercut in the resist and promotes easier lift-off after deposition and helps avoid ultra-sonication of the flake. This undercut can also lead to formation of structures that are slightly larger than that intended by the actual design. A dose test is performed with closely-spaced wires like in our Josephson junctions to optimize the dose at which the best resolution is obtained and to find the difference between the intended separation and actual separation between the wires for a given acceleration voltage. The results of this test are presented in Fig. 3.3. The steps to perform the EBL process are as follows:

- 1) The silicon substrate is cleaned in acetone, ethanol and IPA for 5 minutes each. Care is taken that there is no strong force that displaces the flakes from the substrates such as an ultrasonic force is applied.
- 2) The substrate is then heated at 100 °C for 2 minutes to dry the residual solvents.
- 3) The substrate is spin-coated with a positive EBL resist *AR – P 669.04* from Allresist at 4000 rpm for 1 minute and heated at 150 °C for 1 minute. The substrate is then cooled down for 1 minute and then the same procedure is repeated with the resist *AR – P 679.03*.
- 4) The substrate is spin-coated with a conductive polymer *Electra AR – PC 5090.02* from Allresist at 2000 rpm for 1 minute and heated at 85 °C for 2 minutes. The conductive polymer is water-soluble and helps avoid charging of the substrate by the electron beam.
- 5) The substrate is then cooled down, attached to the sample holder, loaded into the EBL system and pumped down until the vacuum goes below  $10^{-5}$  mbar.
- 6) The sample stage is then moved under the electron column and the electron column is activated by setting the acceleration voltage to 10 kV and aperture size to 10  $\mu\text{m}$ .
- 7) The previously optimized settings are loaded followed by the origin correction, angle correction and three-point alignment using the markers on the substrate. The design is then loaded into the Raith Pioneer Two Litho software and the dose set to 100  $\mu\text{J}/\text{cm}^2$  and the writefield to 100  $\mu\text{m}$ . The exposure time is calculated and the e-beam exposure is started.
- 8) After the exposure is finished, the substrate is unloaded, the *Electra* is removed by immersing in water for 60 seconds and the sample is developed for 90 seconds in

AR 600 – 56, stopped with IPA for 30 seconds and the developed design is checked using an optical microscope. The developed substrate is then used for etching and deposition.

- 9) The subsequent liftoff of the undeveloped resist is performed by immersing the substrate in acetone overnight to gently remove the underlying resist without damaging the fragile nano-structures present on top of the substrate. The excess deposits on the top are gently blown away using a pipette in acetone and the substrate is cleaned with IPA to remove the acetone residue on the substrate.

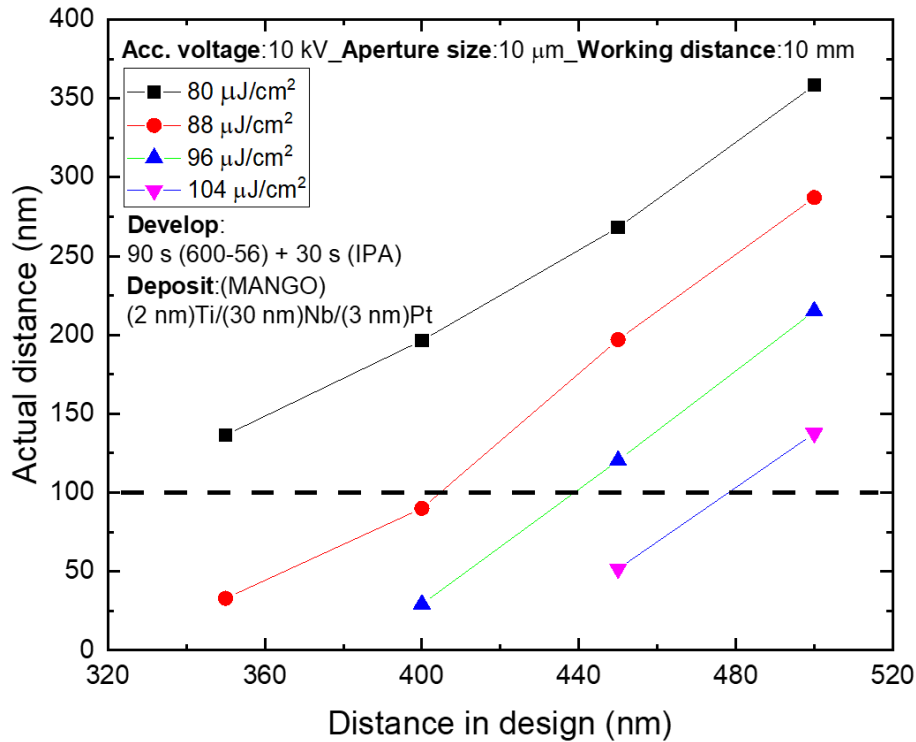


**Fig. 3.3 E-beam lithography calibration:** A calibration of the EBL process with different doses for different electrode separations in the design for 10 kV acceleration voltage and 10 μm aperture. The separations are measured with SEM after liftoff. The dashed line is used to infer the design separation at which 100 nm actual separation can be achieved at different doses.

### 3.2.4 Ion-beam milling and Ion-beam deposition

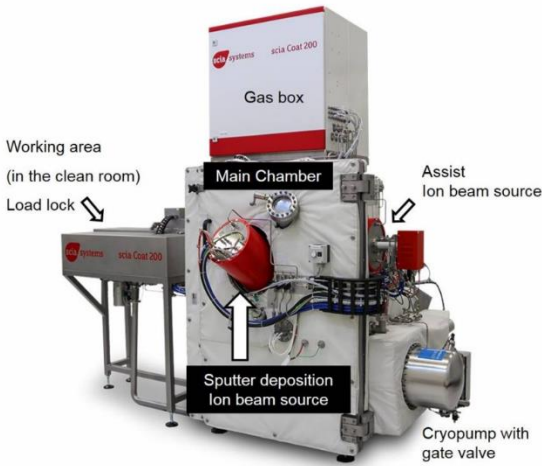
After lithography and development, the substrate is ready for etching and deposition of electrode material. This process is performed in the Scia Coat 200 system, which is capable of



ion-beam milling and sputter deposition of up to 4" wafer sizes. Ion beam milling uses a broad beam of positive charged ions, such as argon ions ( $\text{Ar}^+$ ) to physically etch material from the wafer substrate by ion bombardment. Controlled etching of the thin films in the system is possible with the help of secondary-ion mass spectrometry (SIMS). Ion beam sputtering or ion beam deposition (IBD) uses a high-energy ion beam facing the target material. The resulting ion bombardment physically removes material from the target, which is deposited on the substrate surface as shown in Fig. 3.4(b). The Scia system has low sputtering pressure and has low process temperatures enabled by helium cooling on the backside of the wafer. The Scia system can host up to six different target materials on a carousel, which makes the deposition of multiple materials without breaking vacuum feasible.

In our case, the substrate is attached to the 4" wafer holder after the lithography process with the help of kapton tape. All etching and deposition processes in the system are fully automated with the help of recipes. The substrate is loaded in to the load lock of the Scia system and pumped down to  $10^{-6}$  mbar quickly with the help of a turbo pump. The substrate is then automatically transferred into the main chamber by a robotic arm. The deposition rates of the targets were calibrated by Dr. Jae-Chun Jeon. The substrate is gently etched at 120 degrees at 280 W power, 100 V beam voltage and 500 V acceleration voltage for 1 minute before deposition to clean the surface of the material from residual resist and other surface contaminants before deposition. The angle is then set to 155 degrees for the deposition of titanium, niobium and gold of the desired thicknesses as described later in the thesis using the following parameters: Power = 500 – 600 W (regulated by beam current), Beam Voltage = 1200 V, Accelerator Voltage = 250 V, Beam Current  $\sim 125$  mA, Accelerator Current  $\sim 3$  mA, Neutralizer Current = 200 mA, Ar Pressure =  $1 - 2 \times 10^{-4}$  mbar MFC1 (Sputter Source) = 15 sccm.

(a)



(b)

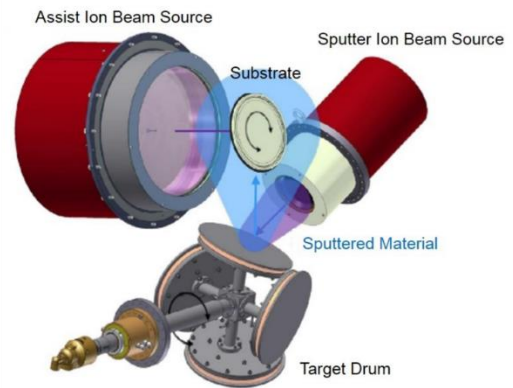


**Fig. 3.4 Ion beam milling and deposition chamber:** (a) The overall view of the Scia Coat 200 system showing the load lock, assist ion beam etching source, sputter ion beam source and the gas manifold on top used to control the flow of Ar, O<sub>2</sub> and N<sub>2</sub>. (b) Inner view of the Scia process chamber showing the relative orientations of the substrate holder, assist ion beam source and the target carousel. The substrate holder angle can be changed from 90 (perpendicular to Ar<sup>+</sup> ions from assist source) to 160 degrees during etching and deposition. Images reproduced from Scia Coat 200 manual.

### 3.3 Device characterization

#### 3.3.1 Atomic Force Microscopy (AFM)

The Atomic Force Microscope (AFM) consists of a silicon cantilever with a sharp tip used to map the surface topography and height of thin films and flakes with sub-nanometer resolution based on measuring the van der Waals force between atoms on the tip and the substrate. The AFM can be operated in one of two different measurement modes: the tapping mode and the contact mode. For both modes, first the tip is brought in close contact with the surface of the substrate. When the AFM is operated in the tapping mode, the tip attached with the cantilever is oscillated at its resonance frequency with the help of a piezoelectric actuator. The tip comes in contact with the sample only during its lowest point. The amplitude of the cantilever oscillation is kept constant

and tracked with the help of a laser and a position sensitive photodiode. When there is a change in height, there is a deflection in the mean position of the laser beam that activates a feedback loop to keep the oscillation amplitude constant, and thus detecting the height change with sub-nanometer resolution. The tip is then scanned across the sample to map the sample topography. In contact mode AFM, the tip is at a constant height from the surface of the sample, essentially in contact with the sample, maintaining a constant force and it is moved laterally across the sample. Any difference in height would cause a deflection of the cantilever and consequently the laser spot, activating the feedback loop of the system to maintain constant height. The lateral forces in contact mode can easily scratch soft samples, while the tapping mode can blunt the tip after repeated use. The AFM is used in tapping mode to map the height of the exfoliated flakes and thickness of the electrodes in the fabricated devices.

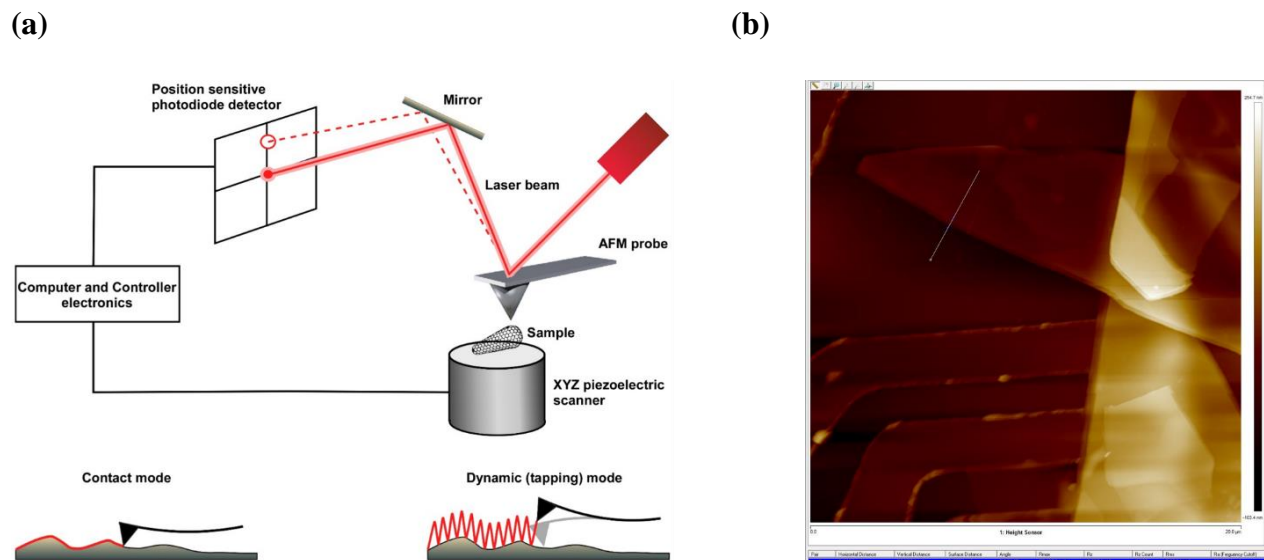


**Fig. 3.5 Atomic force microscopy (AFM):** (a) A schematic of an AFM cantilever with an atomically sharp tip mounted on a cantilever. The displacement of the tip is detected by the deflection of a laser beam reflected from the cantilever and the feedback loop is controlled by the control electronics. The schematic below shows the difference between contact mode and tapping mode AFM. Figure reproduced with permission from<sup>68</sup> (b) An AFM image of a vertical Josephson junction of PtTe<sub>2</sub> fabricated with NbSe<sub>2</sub> on top and bottom. The thickness of the PtTe<sub>2</sub> flake can be seen to be around 59 nm.

### 3.3.2 Scanning Electron Microscopy (SEM)

Scanning Electron Microscopy (SEM) is a technique used to image samples using an electron beam scanned across a conducting sample with nanometer resolution. The secondary electrons reflected off the surface of the sample in combination with the position of the electron beam is used to image the surface of the sample. The SEM images are also obtained using the Raith Pioneer Two system. The sample is coated with Electra to avoid charging of the sample. SEM is used to image the alignment markers during EBL process and the separation between the superconducting electrodes in the devices after deposition as shown in Fig. 3.6.

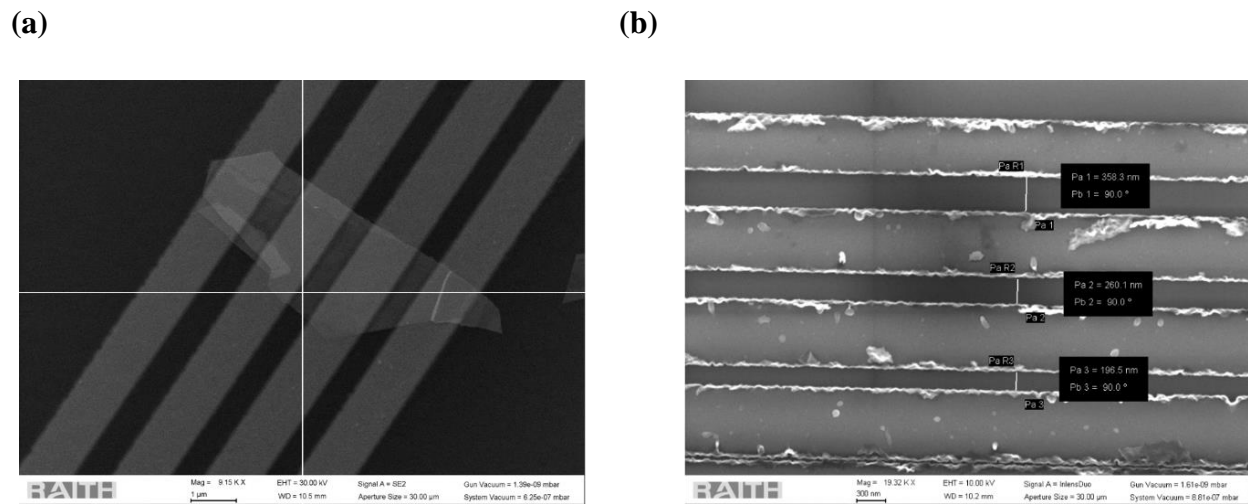


**Fig. 3.6 Scanning electron microscopy (SEM) images:** (a) A scanning electron microscopy (SEM) image of a Josephson junction fabricated on an exfoliated PtTe<sub>2</sub> flake after lithography, deposition and lift-off. (b) SEM image of electrodes fabricated using EBL for dose test and their separations measured.

## 3.4 Electrical transport

### 3.4.1 Physical Property Measurement System (PPMS) DynaCool®

The Physical Property Measurement System (PPMS) DynaCool® is a cryogen-free, commercially available automated low-temperature and magnet system for the quick measurement of electrical properties of materials at the variable temperature range between 1.9 and 300 K and magnetic fields up to 14 T (Fig. 3.7 (a)). The PPMS is cooled down to 4.2 K by helium in a closed-cycle loop, which is liquefied using a Gifford-McMahon compressor. It can then be cooled down to 1.9 K by controlling the vapour pressure of  $^4\text{He}$ . The typical cool down or warm up rates in the PPMS are 10 – 20 K/min and the magnetic field sweep rates are around 100 Oe/s, which allows for fast turnaround. The magnet is a superconducting solenoid made of NbTi, which is cooled down by a closed loop of liquefied helium and operated around 4.2 K.

Electrical transport measurements are done on a sample holder with 12 twisted pairs for electrically contacting the sample. The standard sample holder shown in Fig. 3.7(b) top, consists of a copper base for making thermal contact to the cold finger of the cryostat, bonding pads for wire bonding and a 12-pin plug that mates with the internal sockets inside the PPMS chamber. It is also possible to use a rotator probe in combination with a rotation sample puck (Fig. 3.7(b) bottom) that can be used to rotate the sample over one full 360 degree rotation. The rotator probe has a fixed rotation axis perpendicular to the magnetic field direction. Two types of rotator pucks are available, one with the sample normal perpendicular to the rotation axis, and another with the sample normal parallel to the rotation axis. These two different configurations of the pucks allow for rotation of the sample with respect to the magnetic field, with magnetic field changing from out-of-sample plane to in-plane of the sample and the magnetic field direction changing completely within the plane of the sample, respectively. In our case, the PPMS is only used for quick testing of the fabricated devices.

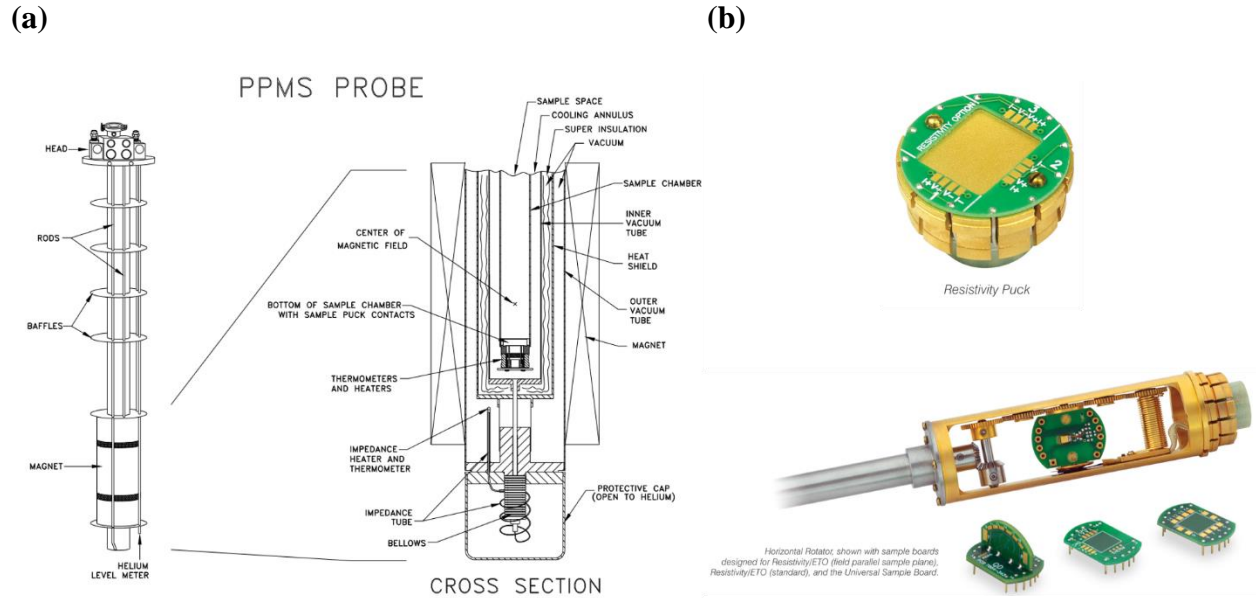


**Fig. 3.7 Physical Property Measurement System options:** (a) A schematic of the inner chamber of the PPMS. The puck is loaded in the chamber and sealed. The wires connecting to the puck are located in the bottom of the chamber, which helps in thermalizing the system rapidly and preventing it from bringing additional heat from the surroundings through the top of the chamber. (b) Various sample holders used for electrical transport measurements in the PPMS. The standard puck is quite large, can hold samples up to 15mm x 15mm in size. The rotator holder can host different pucks with different sample plane orientations allowing for different configurations of the sample with respect to the magnetic field with the use of only a single magnet axis.

### 3.4.2 Bluefors LD-400 measurement setup

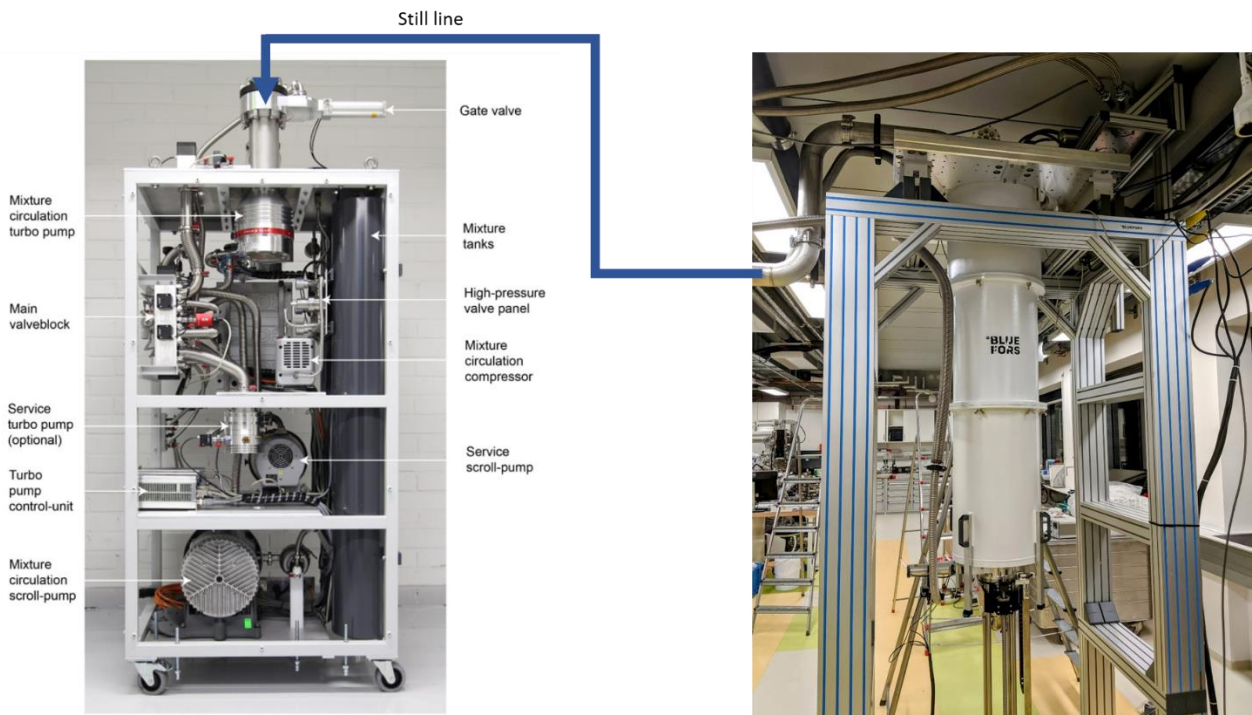
#### 3.4.2.1 Introduction

The LD-400 is a highly automated cryogen-free dilution refrigerator from Bluefors Oy. This system was commissioned and installed at the end of 2019 and is capable of reaching temperatures below 10 mK. The fridge has a fast sample exchange where in the sample can reach the base temperature of the system in about 12 hours. It has a cooling power of 20  $\mu W$  at 20 mK and it is fitted with a 2-axis 9 T – 3 T superconducting vector magnet. It has 24 twisted pairs made of high-resistance phosphor-bronze, thermalized at each stage of the cryostat, which makes for 48

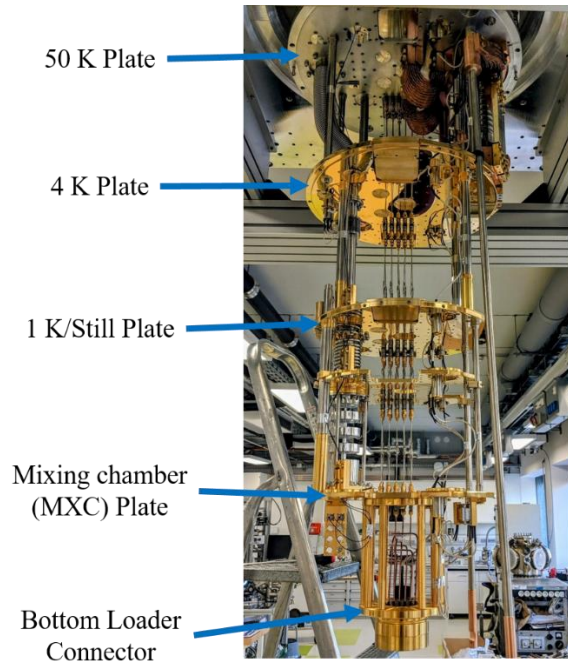
DC contacts for low-frequency measurements and 21 coaxial lines made up of CuNi and superconducting NbTi semi-rigid cables for RF measurements. The system also has six low-resistance wires that can be used to operate piezo-positioners, rotators, etc. and optical fibers of FC/PC type that can be used for optical experiments, in principle.

The cryostat is mounted on a heavy-duty aluminium frame with a roughly 200 kg aluminium plate and suspended from the top to decouple it from the rest of the room and damp any vibrations or mechanical noise coming into the system as shown in Fig. 3.8. It also has an active damping system to remove any vibrations in the frequency range 1.2 – 200 Hz. The cryostat has multiple radiation shields made from mylar, aluminium and gold-plated copper to shield it from external electromagnetic radiation.

(a)



(b)



(c)

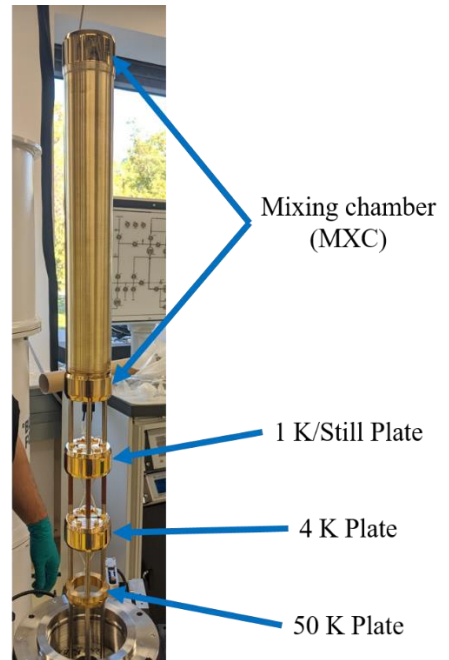


**Fig. 3.8 Bluefors LD-400 Dilution Refrigerator:** (a) The Bluefors LD-400 cryostat (right) in operation mode, located on a sturdy aluminium frame with heavy aluminum plates and active damping on top. The fast sample exchange enters the bottom of the cryostat through a gate valve. The  $^3\text{He}$ - $^4\text{He}$  mixture in the cryostat is pumped by a turbo pump located in the gas handling system (GHS) on the left through a large pipe called the still line and is then circulated back into the cryostat through the condensation line by a scroll pump. The  $^3\text{He}$ - $^4\text{He}$  mixture is stored in the tanks in the GHS when not in circulation. (b) The inside of the cryostat with the shields and the magnet removed shows the various temperature stages along with the DC and RF wiring. The Still is connected to the 4 K plate (HS-STILL) and the MXC is connected to the Still (HS-MXC) by heat switches made of stainless steel rods, which have bad thermal conductivity. This rod is filled with He gas that transfers the heat from one stage to another at higher temperatures. Active charcoal is attached to the top part of these stainless steel rods, which acts as a sorption pump below 10 K, effectively adsorbing all the He gas inside the rods and thermally disconnecting the two stages. In order to activate the heat switches and thermally connect the two stages, a small heater next to the sorption pump is activated, thereby releasing the adsorbed He gas back between the two stages. (c) The bottom loader probe with the fast sample exchange (FSE) mechanism to which the sample is attached and loaded in the cryostat. As it can be seen, the FSE mechanism also has multiple



*stages that is used to thermalize the sample while loading and each stage is thermally decoupled from the other.*

### 3.4.2.2 Dilution refrigeration technique

The dilution refrigerator works on a cooling mechanism that involves a mixture of helium isotopes ( $^3\text{He}$  and  $^4\text{He}$ ) in a specific ratio called as a ‘dilution mixture’, hence the name. The dilution refrigerator is the only cooling mechanism till now that can provide continuous cooling power down to  $2\text{ mK}$ . The cryostat consists of multiple temperature stages ( $50\text{ K}$  plate,  $4\text{ K}$  plate,  $1\text{ K}$  or still plate, mixing chamber) as shown in Fig. 3.8(b). The  $4\text{ K}$  plate and the magnet are cooled to roughly  $4\text{ K}$  by a Gifford-McMahon compressor and a pulse tube from Cryomech Inc. using helium gas in a closed circuit. This is also required for the subsequent cool down of the incoming  $^3\text{He}$  gas. The  $^3\text{He}$ - $^4\text{He}$  mixture is located in tanks in the Gas Handling System (GHS), which is shown in Fig. 3.8(a) left. The sample is attached to a sample holder on a probe (as shown in Fig. 3.12(a)), pumped for  $3 - 4$  hours and loaded in the cryostat using a fast sample exchange mechanism (shown in Fig. 3.8(c)) that attaches to the mixing chamber directly from the bottom using a pre-optimized recipe that cools down the probe in stages. Then, when all parts attached to the  $4\text{ K}$  plate,  $1\text{ K}$  plate and the mixing chamber reach temperatures below  $4\text{ K}$ , the recipe for condensation is started. The mixing chamber and still plate are thermally disconnected from the rest of the cryostat by the use of electrically activated heat switches. The  $^3\text{He}$ - $^4\text{He}$  mixture from the tank is pushed in stages into a U-shaped tube (mixing chamber) located inside the cryostat attached to the mixing chamber plate (MXC), thereby condensing the entire mixture from the tank into the chamber. Controlling the vapour pressure of the condensed mixture is used to reach temperatures below  $4\text{ K}$  (down to  $\sim 800\text{ mK}$ ) before beginning the dilution process. The phase diagram of the  $^3\text{He}$ - $^4\text{He}$  mixture is shown in Fig. 3.9(a).  $^4\text{He}$  has the property that it turns into a superfluid at around  $2\text{ K}$ . The presence of  $^3\text{He}$  in the mixture decreases its superfluid transition temperature to around  $800\text{ mK}$ . If the concentration of  $^3\text{He}$  in the mixture is above a critical threshold as shown in the phase diagram, phase separation can take place leading to the formation of two distinct phases as the miscibility of these two isotopes becomes energetically unfavourable. At around  $800\text{ mK}$ , the  $^3\text{He}$  and  $^4\text{He}$  phases are almost immiscible, leading to the formation of separated dilute ( $6.4\%$ ) and concentrated ( $100\%$ )  $^3\text{He}$  regions with the boundary level between

these two phases located exactly at the mixing chamber plate. Now, two important properties of the dilution mixture make cooling down further possible.

1) Mixing of  $^3\text{He}$  and  $^4\text{He}$  is an endothermic process. The mixing of these two isotopes absorbs heat from the surroundings and hence the enthalpy of mixing is positive ( $\Delta H > 0$ ). Though the mixing of these two isotopes increases the entropy of the system ( $\Delta S > 0$ ), the free energy change is still positive ( $\Delta G = \Delta H - T\Delta S > 0$ ), making this a non-spontaneous process and requiring external energy.

2)  $^4\text{He}$  is heavier than  $^3\text{He}$  making the concentrated  $^3\text{He}$  phase to float on top of the dilute  $^3\text{He}$  phase, which contains only 6.4 %  $^3\text{He}$ .

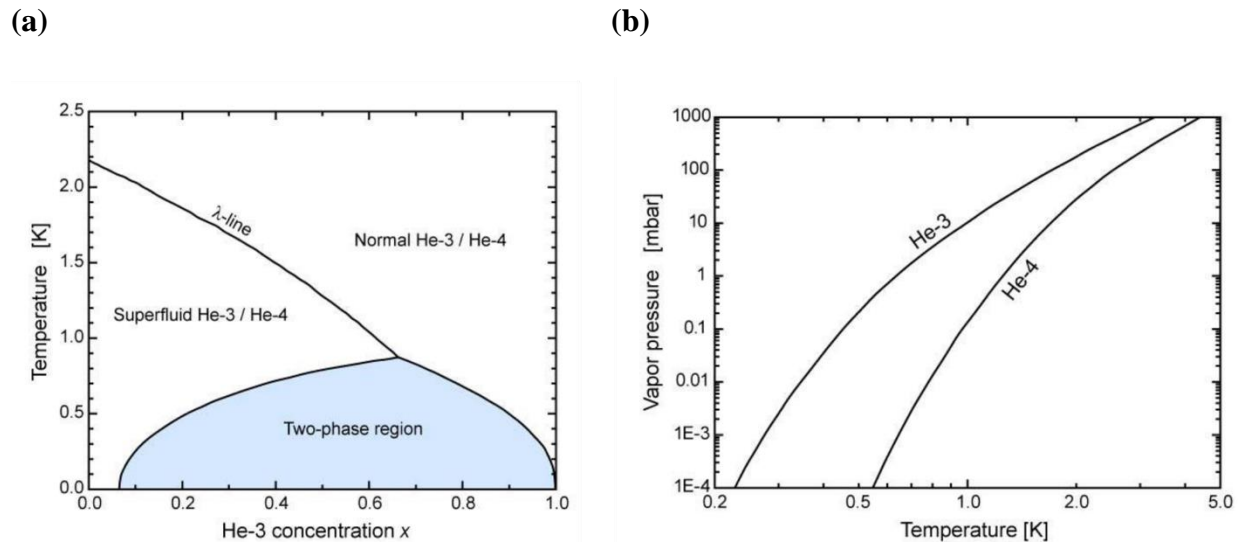


**Fig. 3.9 Thermodynamics of  $^3\text{He}$ - $^4\text{He}$  mixture:** (a) The phase diagram of the  $^3\text{He}$ - $^4\text{He}$  mixture at various temperatures and concentrations. At  $^3\text{He}$  concentration of around 65% and temperatures below 850 mK, the  $^3\text{He}$ - $^4\text{He}$  mixture separates out into two distinct phases which forms the basis for dilution refrigeration. (b) The vapour pressure curves of  $^3\text{He}$  and  $^4\text{He}$  shows that at very temperatures below 500 mK,  $^3\text{He}$  has a vapour pressure that is at least three orders of magnitude larger than the  $^4\text{He}$  isotope. This makes pumping  $^3\text{He}$  much easier than  $^4\text{He}$ , which is also crucial for the dilution process to work.

Now when the mixture is pumped with the help of a turbo pump located in the GHS through the still line on the side of dilute  $^3\text{He}$ , the  $^3\text{He}$  atoms are pumped selectively faster than  $^4\text{He}$ , as they are lighter in size and the vapour pressure of  $^3\text{He}$  is larger than that of  $^4\text{He}$  as shown in Fig. 3.9(b). Since, the dilute phase is driven out of equilibrium, the  $^3\text{He}$  atoms from the concentrated phase move into the dilute phase to maintain the equilibrium  $^3\text{He}/^4\text{He}$  ratio of 6.4 %. During this process, heat from their surroundings is absorbed, since the mixing of  $^3\text{He}$  and  $^4\text{He}$  is an endothermic process. Therefore the MXC plate, which is in thermal contact with the interface between the two phases get cooled further down to the base temperature of the cryostat. The pumped out  $^3\text{He}$  is injected back into the system by a dry scroll pump through the condensation line with flow impedance to cool it back down to liquid helium temperatures. In addition, a heat exchanger between the still pumping line and condensation line uses the enthalpy of the cold  $^3\text{He}$  gas, which is pumped away from the still to pre-cool the incoming  $^3\text{He}$  stream. The cooling power of the system is determined by the number of  $^3\text{He}$  atoms crossing the phase boundary, which in turn depends on how fast the  $^3\text{He}$  atoms are pumped from the dilute phase or the  $^3\text{He}$  flow rate. This can be controlled by changing the temperature of the still plate, which changes the temperature of the dilute  $^3\text{He}$  phase, and hence the vapour pressure (Fig. 3.9(b)) and pumping speed of  $^3\text{He}$ .

### 3.4.2.3 High-frequency filtering and electron thermalization

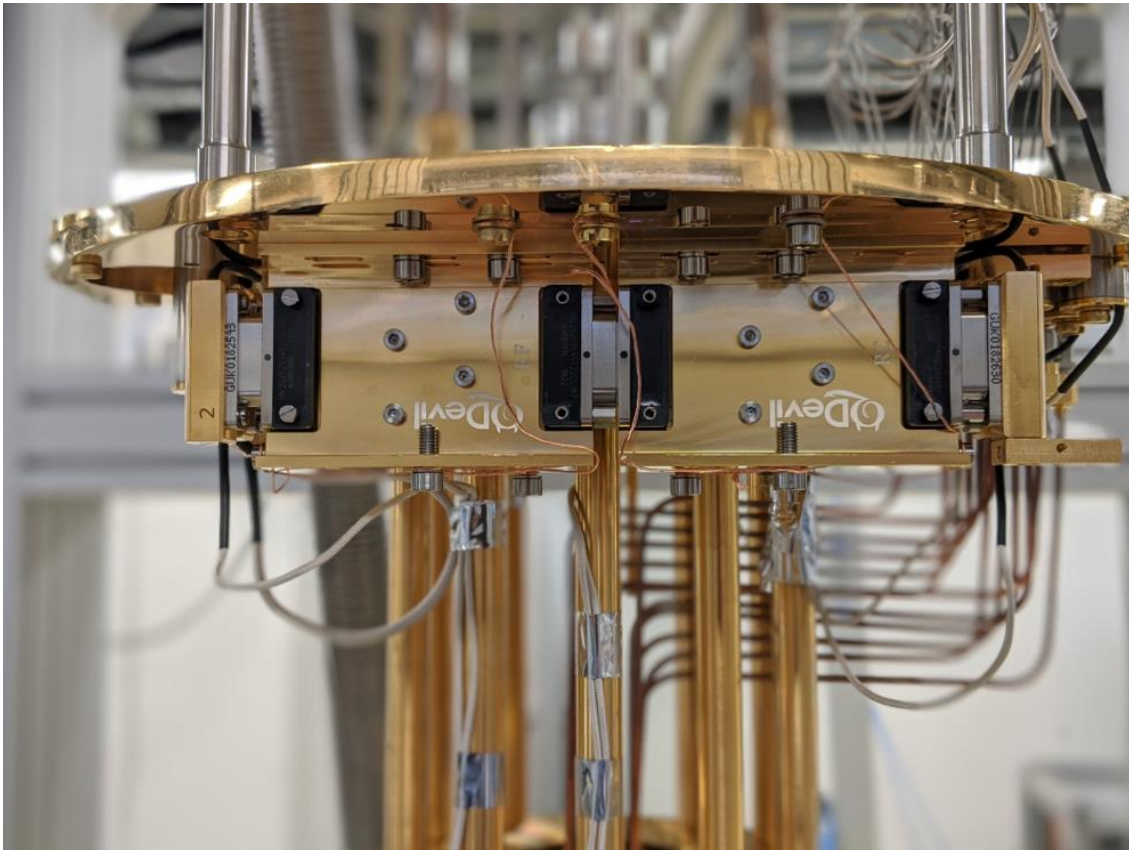
In order to maintain the low temperatures obtained in the system by the dilution process, it is important to thermally isolate the mixing chamber plate and the sample completely from any external sources of heat. Another source of heat is the external electromagnetic radiation from the surroundings. While performing any measurement at cryogenic temperatures, it is to be kept in mind that the power that can be applied by the probe to the sample is limited by the cooling power of the system and hence the measurement probe needs to be used at low-levels which does not perturb the sample beyond the required level and modify its energy state significantly. In such low-level measurements, the obtained signals are also very small and requires the use of instruments with extremely high sensitivity. In order for these instruments to be sensitive at such low-levels, it is important to minimize the various sources of noise and background signals present in the setup. In our case, we predominantly use current bias as the probe and sense the voltage across the

junction using a nanovoltmeter. The steps taken to ensure that the sample is thermally isolated and the noise is minimized are as follows:

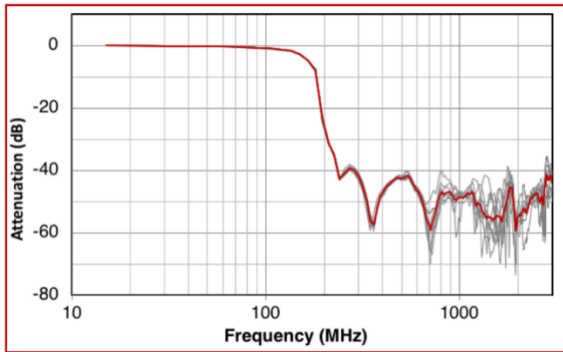
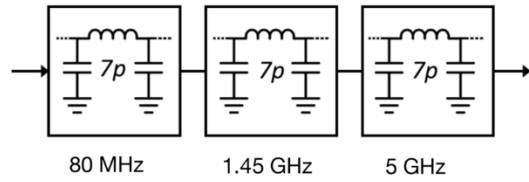
- 1) **Electromagnetic radiation shielding:** The mixing chamber and the still plate are thermally isolated from the rest of the cryostat with the help of gas-gap heat switches. The cryostat and sample region are further shielded from electromagnetic radiation using multiple layers of shielding using gold-plated copper and aluminized Mylar-coated vacuum cans.
- 2) **Low-frequency vibration isolation:** The entire cryostat is mounted on an aluminium frame with a heavy aluminium plate on top and active vibration isolation to decouple it from vibrations in the lab and damp the vibrations coming in from the pumps in the GHS and the pulse tube unit, which can increase the base temperature of the system. This also helps avoid low-frequency noise in the electrical measurements coming from vibrations.
- 3) **Shielded cables and breakout boxes:** The breakout box used to connect to various contacts on the outside and the measurement cable running from the breakout box to the top of the cryostat is made by QDevil and is completely shielded and grounded, hence shielding the signal from external noise from the breakout box down to the device. The wires inside the breakout box and in the cryostat are also made of twisted pair wiring to avoid noise from electromagnetic induction. The 24-twisted pairs in the measurement cables connect from the breakout box to the top of the cryostat which then runs inside the cryostat as twisted pair cables down to the mixing chamber and the sample holder, thermalized at each stage to prevent heat or hot electrons from entering the lower temperature stages.
- 4) **High-frequency filters:** Though the cryostat is shielded from external electromagnetic radiation, the measurement cables from the instrument to the breakout box can still carry some high frequency radiation ( $\sim GHz$ ) that can move into the cryostat and excite the electrons present in the mixing chamber and prevent them from reaching the same temperature as the phonon bath, which is at  $20 mK$ . In order to filter out this high-frequency radiation, we use QFilters from QDevil, which was developed at Harvard University and the University of Copenhagen<sup>69</sup>. The QFilter is attached to the mixing chamber plate, close to the sample and operated at the base temperature of the cryostat to be fully effective. The QFilter typically consists of one audio frequency (RC) and radio

frequency (RF) filter bank connected in series. The RC filter consists of one 7-pole Pi filter stage followed by two RC filter stages that acts as a low-pass filter that attenuates signals above 10 kHz, and is effective up to 80 MHz range as shown in Fig. 3.10(c) The RF filter bank contains three stages of 7-pole Pi filter that attenuates signals from 80 MHz up to tens of GHz with roughly  $-50$  dB attenuation as shown in Fig. 3.10(b).

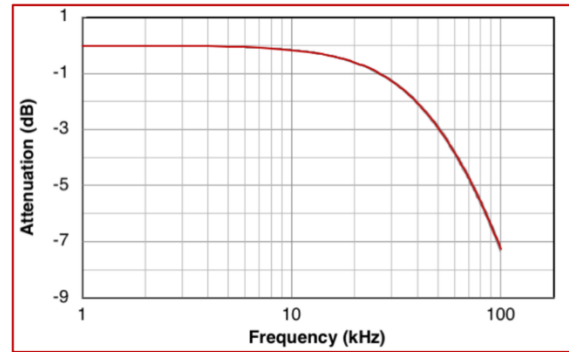
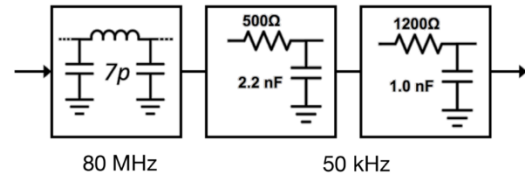
(a)



(b)



(c)



(d)

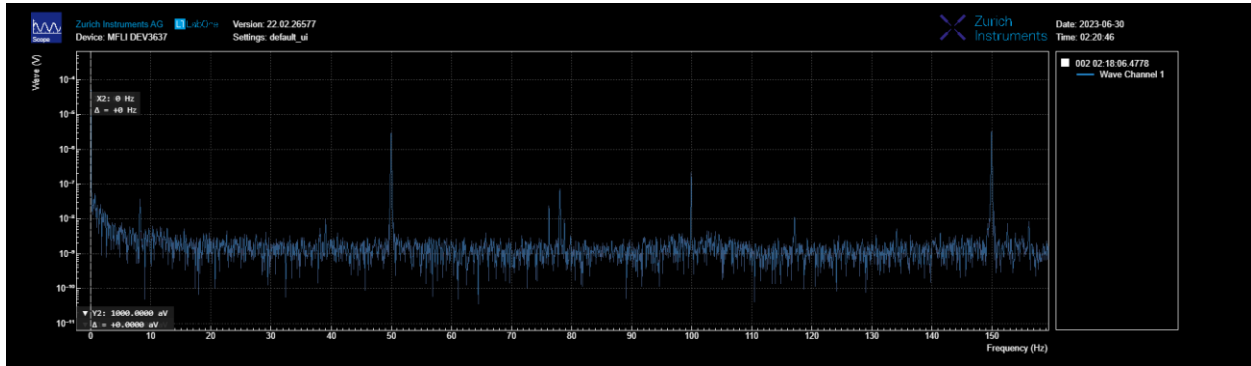


**Fig. 3.10 QDevil filters and high frequency characteristics:** (a) QDevil RC and RF filter banks connected in series and mounted on the MXC plate of the Bluefors LD-400. The QFilters are further thermalized with the mixing chamber with the help of copper braids. (b) The RF filter bank consists of three 7-pole Pi filters with different cut-off frequencies starting from 80 MHz and going up to 30 GHz. It has up to -50 dB attenuation at 30 GHz. (c) The RC filter bank consists of one 7-pole Pi filter with 80 MHz cut-off frequency and two RC filters with cut-off frequency around 10 kHz. (d) Noise spectrum of the setup measured at low frequencies with an oscilloscope built-in with the lock-in amplifier shows that the noise floor is at the nanovolt range, which is ideal for our measurements and signals in the 10's of nanovolt range can be measured with accuracy. The peaks

at multiple of 50 Hz correspond to the line frequency noise and its harmonics, which is of the order of a few microvolts.

After installing the shielding and filters, it is important to test their effectiveness by measuring the electron temperature. This can be done in many different ways by measuring quantities that are extremely sensitive to the electron temperature like measuring the Coulomb blockade in a quantum dot or the shot noise in a tunnel junction. In our case, the electron temperature when the cryostat is at base temperature can be extracted from the differential conductance across a superconducting tunnel junction (MA2479) made of Ru (5 nm)/Mn<sub>3</sub>Ge (10 nm)/MgO (2 nm)/AlSi (4.5 nm) which was grown by Dr. Binoy Hazra using hard masks in our home-designed and home-built sputtering chamber. The normalized tunneling conductance of the sample measured at 20 mK MXC temperature is shown as red dots in Fig. 3.11(b). The differential conductance is directly proportional to the density of states in the superconductor, assuming the density of states is constant in the metal over the probed energy range, which is a valid assumption. It is then fit with a BCS density of states equation derived by Maki<sup>70-72</sup> considering orbital depairing and spin-orbit coupling effects using a code developed by Dr. See-Hun Yang at IBM Almaden to derive the temperature. The theoretical density of states is given by:

$$N_s(E) = \frac{N_s(0)}{2} \text{sgn}(E) \text{Re} \left( \frac{u_{\pm}}{\sqrt{u_{\pm}^2 - 1}} \right)$$

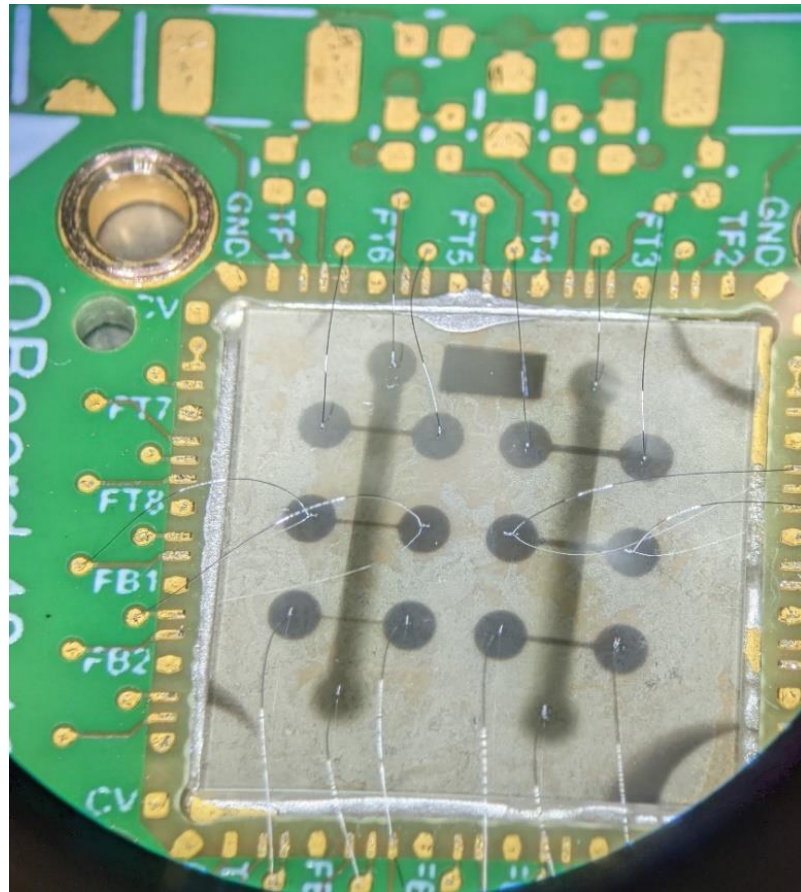
Where  $u_{\pm}$  is given by

$$u_{\pm} = \frac{E \mp \mu H}{\Delta} + \frac{\zeta u_{\pm}}{\sqrt{1 - u_{\mp}^2}} + b \left( \frac{u_{\mp} - u_{\pm}}{\sqrt{1 - u_{\mp}^2}} \right)$$

Here  $\Delta$  is the energy gap, which depends on the temperature of the electron ( $\Delta = \Delta_0 \sqrt{1 - \frac{T}{T_c}}$ ),  $N_s(0)$  is the normal density of states,  $\zeta$  is the orbital depairing parameter and  $b$  is the

spin-orbit scattering parameter. The superconducting condensate formed in the system should be extremely sensitive to the electron temperature  $T$  that determines the gap  $\Delta$  in the spectrum. Hence, by fitting the experimentally obtained differential conductance with the BCS density of states, we can get the actual electron temperature of the system. This equation involves the fine-tuning of at least four parameters in this case, that needs to be done with care to determine the actual temperature  $T$ , however the use of physical intuition can help simplify things and fix some of the parameters. The parameter  $\Delta_0$ , which is essentially the superconducting energy gap at zero temperature, is given by  $1.76 k_B T_c$  and the spin-orbit coupling in aluminum is almost zero. The black curve gives the best theoretical fit for the parameters  $T = 75 \text{ mK}$ ,  $\zeta = 0.008$ ,  $b = 0$  and  $\Delta_0 = 0.31 \text{ eV}$ . Hence, we can roughly estimate the electron temperature in the system to be around  $75 \text{ mK}$ .

(a)





(b)

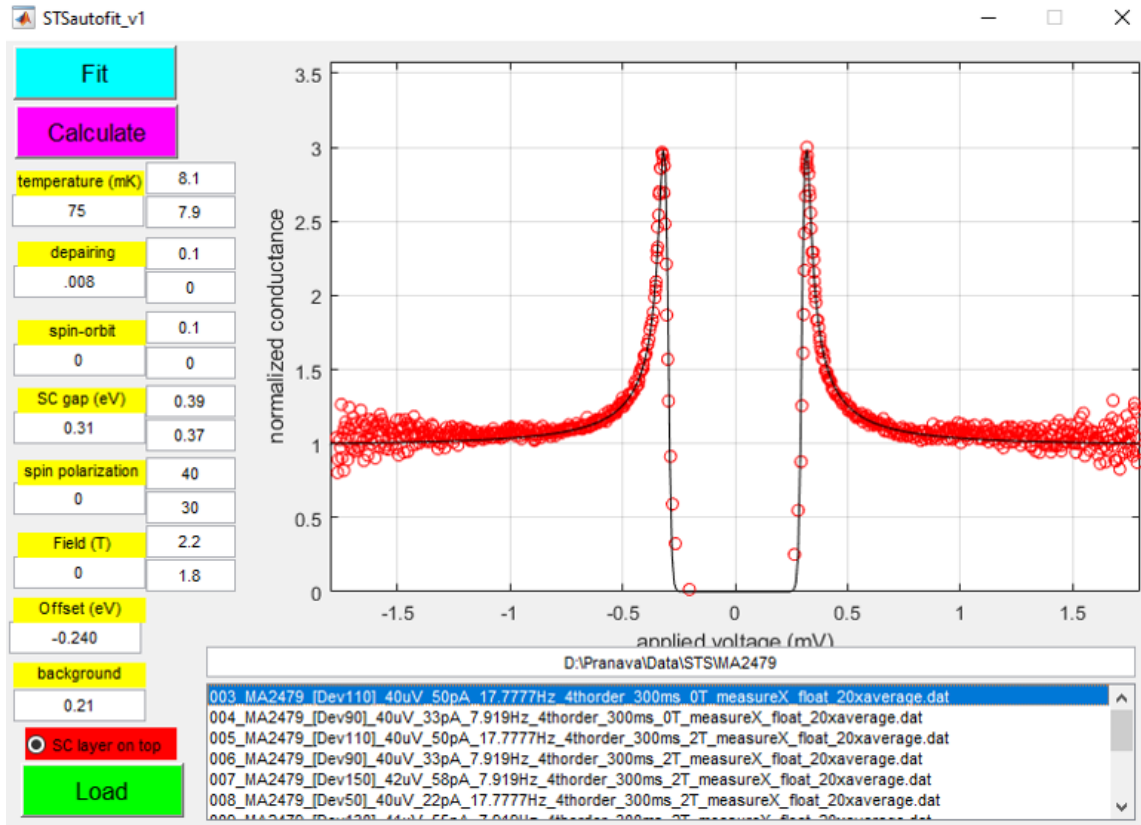


**Fig. 3.11 Superconducting tunneling spectroscopy and electron temperature:** (a) A tunnel junction device mounted on a QBoard and bonded, with 4.5 nm AlSi superconductor on top and 5 nm Ru and 10 nm Mn<sub>3</sub>Ge as the bottom electrodes separated by a 2 nm MgO tunnel barrier. The voltage is applied from the bottom to the top and the differential conductance is measured using a standard lock-in technique. (b) The measured differential conductance (red) is normalized and fit using a BCS density of states equation derived by Maki. The best fit is obtained at a temperature of 75 mK.

#### 3.4.2.4 Sample holder and electrostatic discharge (ESD) protection protocol

The sample holder for performing electrical measurements in the system is also designed by QDevil called as QBoard. The QBoard is a PCB-based sample holder with 48 DC contacts and 16 RF channels. The presence of a large number of contacts allows for high throughput of the system. The sample holder is pre-designed to fit perfectly on a Bluefors fast-sample exchange

puck. The sample holder is attached to the puck via gold-plated copper adapters and fastened tight with titanium screws that are non-magnetic. The QBoard consists of a motherboard, which is fixed to the puck, and the daughterboard, which contains the sample, can be exchanged easily. The sample is attached to the  $10.5\text{ mm} \times 10.5\text{ mm}$  area of the daughterboard using silver paste and wire-bonded using aluminum wires to the DC contacts. After wire bonding, the daughter board is screwed tight to the motherboard and they mate together via an interposer layer with gold springs. The top of the sample puck has a 51-pin titanium micro-D connector saver, which mates with the connector on the mixing chamber. The other end connects to the QBoard via a 51-pin nano-D connector with copper wires covered in Teflon. These wires are wrapped around the gold-plated parts of the puck and tightly wrapped with Teflon and Kapton tape to help them thermalize better as shown in Fig. 3.12(a).

The devices made with van der Waals materials are prone to damage from electrostatic discharge (ESD) as they are only held to the substrate by a weak van der Waals force and an electrostatic force coming in from the surroundings can easily displace and damage the device, if it is not properly grounded. Hence, after device fabrication great precaution is taken in protecting the device from any possible damage due to ESD. ESD protective gear such as coats, gloves, and shoes are worn at all times, ESD protective tools such as tweezers and sample boxes are used, and a wrist strap is used to ground the user. ESD mats are used in the lab to avoid charging from the floor during movement. The sample is always kept grounded during and after wire bonding. While loading the sample on the holder, the contact pins are connected to the ground via the connector saver on top and while the sample is attached to the fast sample exchange mechanism, the sample is grounded via the bottom part of the QBoard, which is connected to the grounding wiring. Once the sample mates with the MXC from the top with the pins kept grounded from the breakout box, the bottom grounding wiring disconnects thermally and electrically and the sample is ready to be measured.

(a)



(b)

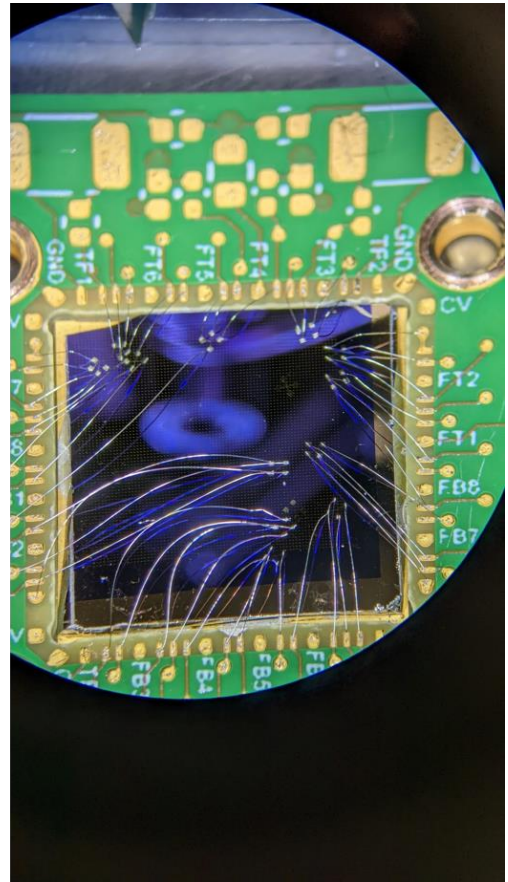


*Fig. 3.12 QBoard mounted on a sample puck: (a) The QBoard sample holder attached to the probe that mates with the MXC flange through the FSE mechanism. The wires are thermalized by attaching them to the probe with Teflon and kapton tapes. (b) QBoard containing a sample with multiple devices and all contacts bonded. The 48 DC contacts available on the QBoard allows for a high throughput in the testing of devices at low temperatures. The aluminium wire bonding acts as the main source of thermalizing the sample at very low temperatures. Hence multiple bonds, if possible, would be encouraged.*

#### 3.4.2.5 Measurement and control electronics programming with LabVIEW

For efficient measurement of the sample, it is important to automate the loading and measurement process as much as possible. The control of sample loading (unloading) and cool down (warm up) is fully automated with the help of Bluefors software. The measurement control

involves multiple instruments such as the current source (Keithley 6221), nanovoltmeter (Keithley 2182A), lock-in amplifier (MFLI), magnet controller (AMI 430), temperature controller (Lakeshore 372), etc. with different interfaces. To make the measurements more optimized with an easy and simple user interface (UI), all these instruments are programmed to be controlled in unison by LabVIEW with the help of LabVIEW drivers. An example of UI for one such program used to measure the current-voltage characteristics of multiple devices at different magnetic fields and temperatures is shown in Fig. 3.13. (Thanks to Ivan for help with the temperature control). This program is used extensively to map the current-voltage ( $I - V$ ) characteristics of the Josephson junctions that are measured throughout the thesis. The critical currents are extracted from each  $I - V$  curve from a peak in the  $\frac{dV}{dI}$  using a Python program written with help from Avanindra Kumar Pandeya. The programs that I wrote during my Ph.D. tenure can be found at:

<https://github.com/TheDarkKnightUnmasked/Bluefors-DC>

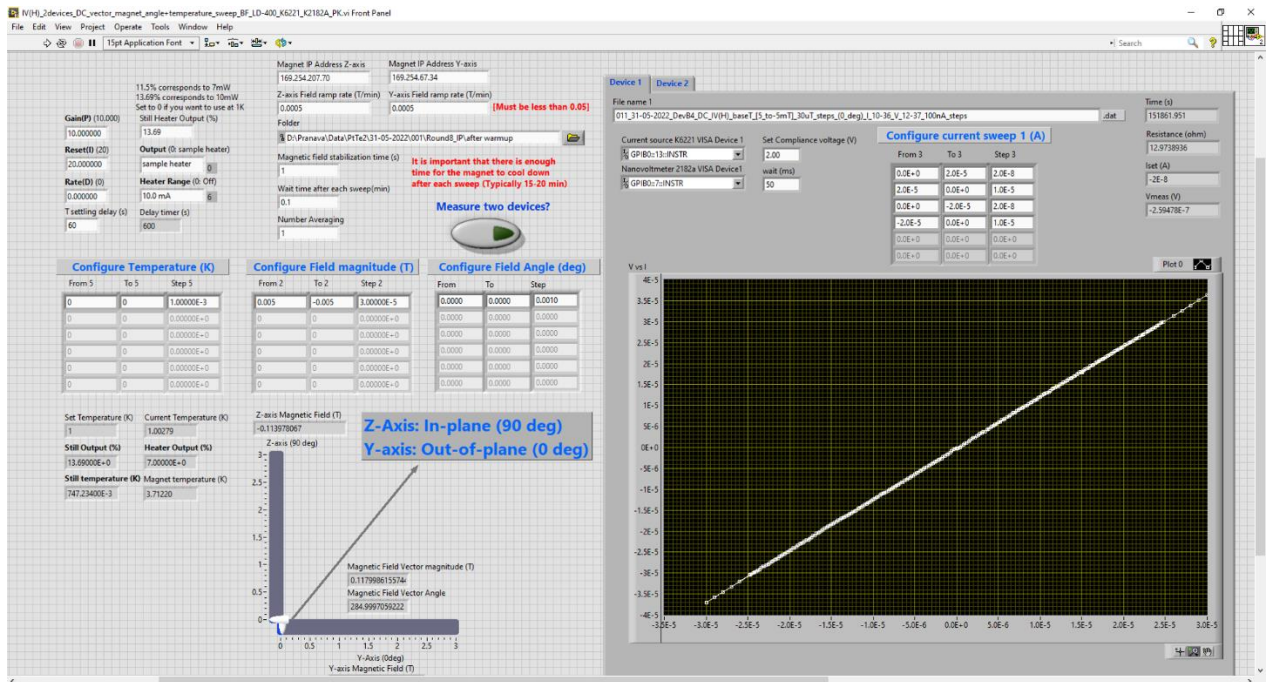


**Fig. 3.13 LabVIEW program for measurement of I-V characteristics:** The user interface for a LabVIEW program that allows for measurement of current-voltage characteristics in multiple devices at the same time with comprehensive control of the temperature, magnetic field vector magnitude and angle.

# 4

---

**Josephson diode effect induced by  
finite momentum Cooper pairing  
in a topological Rashba system**

**1T-NiTe<sub>2</sub>**

## 4.1 Introduction

Ever since the existence of topological materials was predicted theoretically<sup>73-75</sup>, there has been a surge in finding a variety of different topological materials such as topological insulators<sup>76-79</sup>, Dirac and Weyl semimetals<sup>80,81</sup>, higher order topological materials with Chern number greater than one<sup>82,83</sup>, etc. These topological materials are predicted to exhibit a plethora of interesting properties/phenomena such as spin-momentum locked surface states<sup>77,84,85</sup>, quantum anomalous Hall effect (QAHE)<sup>86,87</sup>, chiral anomaly<sup>88</sup>, etc. In the superconducting state, these materials are expected to host exotic Majorana bound states<sup>89</sup>, which have applications in fault-tolerant quantum computing. On a similar note, ever since the discovery of graphene<sup>90</sup>, a single hexagonal layer of carbon atoms, the field of two-dimensional van der Waals materials has been booming. Many quantum states or phenomena found in bulk three-dimensional materials have also been found in two-dimensional materials, providing a promising platform for the dimensional scale down of present-day technologies. The top down approach provided by the mechanical exfoliation technique of van der Waals materials also makes for a great platform for making heterostructures with clean interfaces, fabricating nano-devices and studying the rich physics offered by these interfaces in addition to technological prospects<sup>91,92</sup>. With the very recent discovery of twisted bilayer graphene hosting flat bands with strongly correlated states and superconductivity, the twist angle between two layers serves as another knob in tuning different quantum states of matter<sup>93</sup>.

In this chapter, we study the Josephson diode effect (JDE or  $\Delta I_c$ ) in a material, which combines the properties of topological states and reduced dimensionality offered by van der Waals materials. NiTe<sub>2</sub> is a van der Waals material and a type-II Dirac semimetal with the Dirac cone close to the Fermi level, as evidenced from ARPES studies<sup>94,95</sup>. It also has a surface state with a Rashba spin-momentum locking and a large spin-splitting of 120 *meV* close to the Fermi energy. Since NiTe<sub>2</sub> has these surface states right at the Fermi energy, the spin-orbit coupling emerging from these states are expected to dominate its electrical transport characteristics. We study the effects of this spin-orbit coupling arising from the topological surface states (TSS) in the superconducting phase by fabricating lateral Josephson junctions of NiTe<sub>2</sub>. The very low resistance of NiTe<sub>2</sub> and its high stability in air makes it suitable to fabricate lateral Josephson junctions without much preclusions. We observe a JDE in the presence of an in-plane magnetic field. JDE in this system is quantified and found to have an antisymmetric dependence on the magnitude and

direction of the applied magnetic field. We attribute the existence of this effect in this system to the Cooper pairs from the helical surface states acquiring a non-zero pair momentum in the presence of a magnetic field, as opposed to zero momentum Cooper pairs in a conventional BCS superconductor. This phenomenon is called as finite momentum Cooper pairing (FMCP)<sup>9,10,33</sup>. Together with our theory collaborators, Margarita Davydova, Noah Yuan and Liang Fu from MIT, we use a simple Ginzburg-Landau analysis to describe the Josephson junction with broken inversion and time-reversal symmetries to show the existence of asymmetric critical currents and their dependence on temperature and applied magnetic fields. We confirm that this simple model captures all the experimental features of our observed JDE. We also perform independent studies verifying the existence of finite momentum Cooper pairing in the system by applying in-plane magnetic fields along the direction of current and quantify it by looking at the evolution of the Fraunhofer interference pattern<sup>96,97</sup>. We find that the value of finite-momentum obtained from this measurement is of the same order of magnitude as the value of finite-momentum along the perpendicular direction, determined using the model used to calculate JDE. We suggest two possible microscopic mechanisms as the origin of finite-momentum Cooper pairing in the system in the presence of a magnetic field: 1) the existence of spin-momentum locked surface states with large Rashba spin splitting on the surface of NiTe<sub>2</sub> as seen through ARPES and 2) the presence of screening currents on the niobium electrodes that generate finite momentum Cooper pairs. We estimate that the FMCP created due to screening currents is an order of magnitude lower than that created by the spin-orbit splitting in NiTe<sub>2</sub>.<sup>98</sup>

## 4.2 Crystal structure

Nickel ditelluride (NiTe<sub>2</sub>) is a transition metal dichalcogenide material that crystallizes in the centrosymmetric space group  $P-3m1$  with a trigonal structure similar to CdI<sub>2</sub>. Layers of NiTe<sub>2</sub> are stacked together via a relatively strong van der Waals force compared to other two-dimensional van der Waals dichalcogenides and hence not easily exfoliable down to a monolayer. Fig. 4.1 shows the crystal structure of NiTe<sub>2</sub> in which each layer of nickel atoms is sandwiched between two layers of tellurium atoms. The NiTe<sub>2</sub> family of materials structurally varies from other transition metal dichalcogenides like MoS<sub>2</sub>, MoTe<sub>2</sub>, WTe<sub>2</sub>, NbSe<sub>2</sub>, TaS<sub>2</sub>, etc. in the fact that it is

found to crystallize only in the octahedral phase as opposed to 1T (trigonal) and 2H (hexagonal) phases in the other systems. Other members of the  $\text{NiTe}_2$  family include  $\text{PtTe}_2$ ,  $\text{PdTe}_2$ ,  $\text{PtSe}_2$ ,  $\text{PdSe}_2$ , etc. The  $\text{NiTe}_2$  family of materials are also extremely stable in air as opposed to most other TMDCs and have a wide variety of applications in electro-catalysis<sup>99</sup>, hydrogen evolution reaction<sup>100</sup>, terahertz photodetection<sup>101</sup>, etc.  $\text{NiTe}_2$  also offers the added advantage that it can be synthesized layer by layer on a large scale using chemical vapour deposition<sup>102</sup> making it viable for industrial applications.

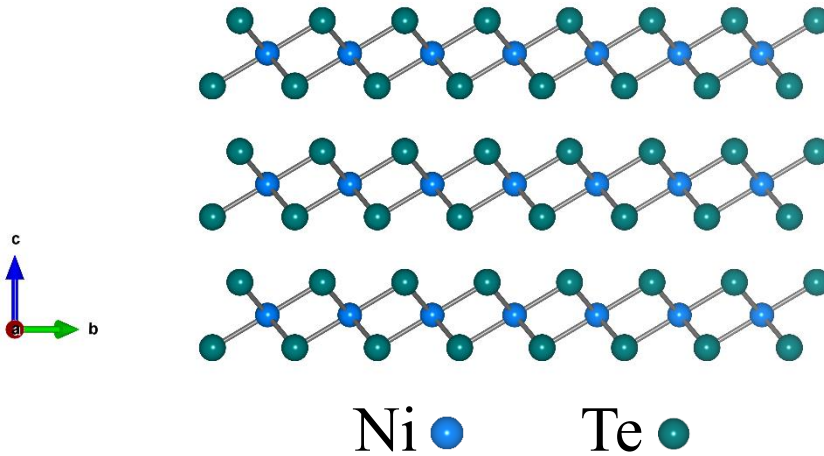


**Fig. 4.1 Crystal structure of  $\text{NiTe}_2$ :** An illustration showing the 1T crystal structure of  $\text{NiTe}_2$  in which the nickel atoms are sandwiched between the tellurium atoms and located in an octahedral coordination environment. Each  $\text{NiTe}_2$  layer is centrosymmetric and separated by a van der Waals gap that make it exfoliable.

$\text{NiTe}_2$  crystallizes in the  $P-3m1$  space group, with  $a = b = 4.025 \text{ \AA}$  and  $c = 5.22 \text{ \AA}$ . It is a centrosymmetric space group that is not expected to have any asymmetric spin-orbit coupling interactions like the Rashba or Dresselhaus effects. Each layer of  $\text{NiTe}_2$  consists of three sublayers with a layer of nickel atoms located in the center and sandwiched by two sublayers of tellurium atoms on the top and bottom. Consider a single layer of  $\text{NiTe}_2$  from the schematic shown in Fig. 4.1. The nickel atoms are located in the center of the layer with the tellurium atoms at the top and bottom in an octahedral fashion. This gives the Ni atoms a  $D_{3d}$  point group symmetry, which includes a center of inversion. The tellurium atoms on the other hand, have a  $C_{3v}$  point group



symmetry, which lacks a center of inversion. This lack of inversion symmetry, locally within the unit cell leads to the existence of equal but opposite asymmetric spin-orbit couplings on the top and bottom layers of tellurium atoms. Though globally the spin-orbit coupling strength adds up to zero, the existence of locally broken symmetries and hence, a ‘local Rashba effect’ in the system leads to the existence of a layer-dependent spin-momentum locking in the system where the spins in the top and bottom tellurium layers are oppositely spin-polarized. This is known as ‘spin-layer locking’ and has been observed through ARPES in few layers of PtTe<sub>2</sub><sup>56</sup>, PtSe<sub>2</sub><sup>57</sup>, etc. and in bulk MoS<sub>2</sub><sup>58</sup>. Though expected to be compensated globally, the existence of such a ‘hidden spin polarization’ due to locally broken symmetries can lead to interesting effects in transport and exotic order parameters in the superconducting state of such materials as we will see in this chapter.

### 4.3 Electronic structure

NiTe<sub>2</sub> is a type-II Dirac semimetal, in which pair of Dirac cones<sup>94,95</sup> (as shown in Fig. 4.2), tilted in energy-momentum space that breaks the Lorentz symmetry of the system, is present. While other members of the group-X transition metal dichalcogenides also host a type-II Dirac cone, the Dirac cone in NiTe<sub>2</sub> is special as it is located very close to the Fermi level and is expected to dominate the transport properties of the system. In PdTe<sub>2</sub>, PtTe<sub>2</sub> and PtSe<sub>2</sub> the type-II Dirac cones lie 0.6, 0.8 and 1.2 eV below the Fermi energy respectively, whereas in NiTe<sub>2</sub> the Dirac cones lie just 20 meV above the Fermi energy, which can be easily tuned to the Fermi level by slight doping.

In addition to the bulk Dirac nodes, NiTe<sub>2</sub> also hosts a series of inverted bandgaps that can be shown to arise from the Te 5p manifold simply considering crystal field splitting and spin-orbit coupling<sup>8</sup>. These states with inverted bandgaps are labelled as topological surface states (TSS). These TSS are spin-polarized due to the large spin-orbit coupling and there is one very closely located to the Fermi energy with a Rashba-type helical spin momentum locking and a very large spin splitting of 120 meV. The strong dominating contribution of this TSS to electrical transport in NiTe<sub>2</sub> can lead to the formation of finite momentum Cooper pairs in the presence of a magnetic field and consequently a Josephson diode effect when proximitized by a conventional superconductor, as we will discuss in the following sections.

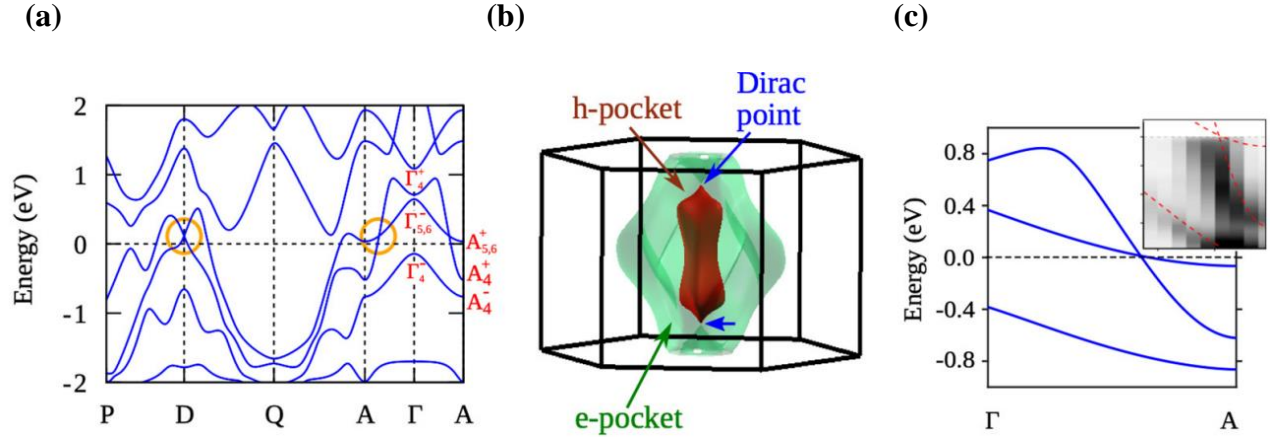


**Fig. 4.2 Type-II Dirac cone in NiTe<sub>2</sub>:** (a) Band structure of NiTe<sub>2</sub> showing the tilted type-II Dirac cone along  $\Gamma$ -A direction. (b) Three-dimensional Fermi surface of NiTe<sub>2</sub> showing the electron and hole pockets along with a Dirac point at the intersection of the two pockets. (c) Angle-resolved photoemission measurements along  $\Gamma$ -A direction showing the existence of type-II Dirac like band dispersion with the Dirac point just above the Fermi level. Figure reproduced with permission from ref.<sup>95</sup>

## 4.4 Josephson junctions of NiTe<sub>2</sub>

### 4.4.1 Fabrication and basic characterization

NiTe<sub>2</sub> flakes that are just a few layers thick are exfoliated from a commercially purchased single crystal of 1T-NiTe<sub>2</sub> (from HQgraphene) onto a Si substrate with 300nm SiO<sub>2</sub> coating. Thin flakes are identified with the help of an optical microscope and an atomic force microscope. Josephson junctions on these flakes are fabricated by performing electron beam lithography and sputtering titanium (2 nm) / niobium (30 nm) / gold (20 nm) electrodes on top of these flakes with varying separations (100 – 700 nm). The liftoff process is then performed in acetone overnight. The presence of titanium improves the adhesion of the niobium to the substrate and the gold capping on top prevents the niobium from being oxidized thereby improving the quality of the junction. These junctions were fabricated by Anirban Chakraborty. The junctions, thus fabricated are loaded in a dilution refrigerator to perform electrical transport measurements. The resistances of the junctions are measured using a standard 4-probe configuration in which current

flows between two consecutive niobium electrodes and the voltage is measured across the same niobium electrodes. The resistance of one particular junction (with a 350 nm separation) as a function of temperature is shown in Fig. 4.3(b). The resistance of the junction decreases with decreasing temperature and a drop in resistance is observed around 5.5 K corresponding to the superconducting transition of niobium ( $T_c$ ) and the resistance continues to decrease with decreasing temperature. Another drop in resistance is observed around 2.5 K, which corresponds to the temperature below which the junction turns completely superconducting ( $T_j$ ). The device is cooled down further to the base temperature of the dilution refrigerator (20 mK) where most of the measurements are carried out.

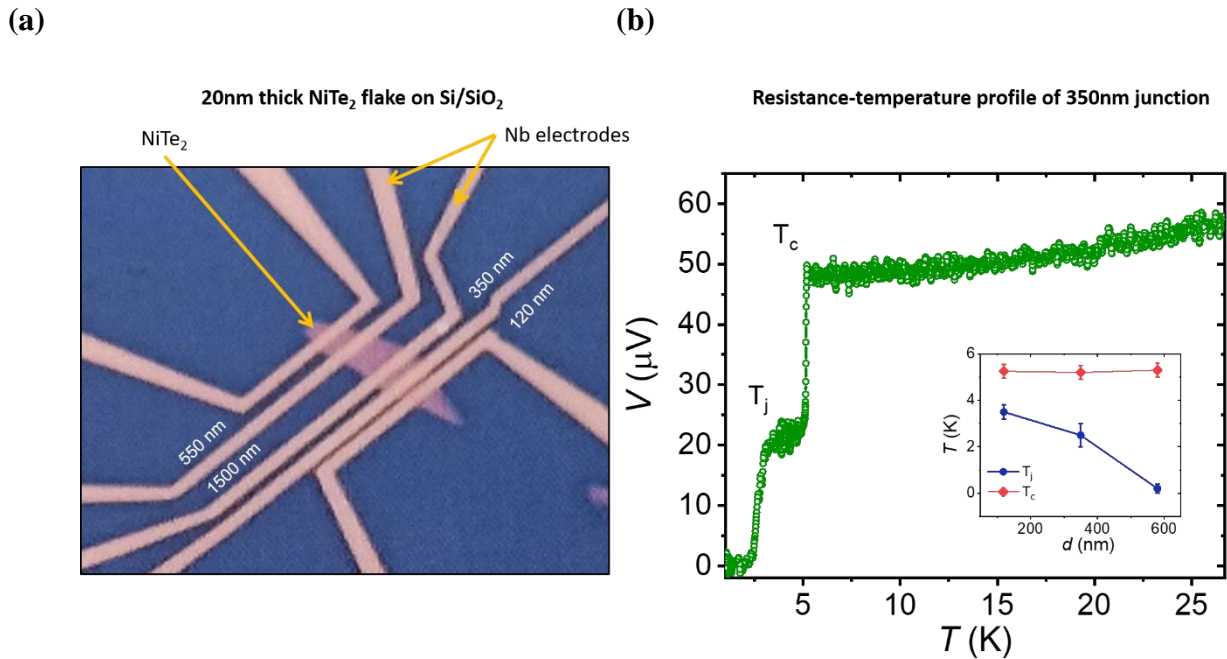


**Fig. 4.3 Josephson junction device structure and resistance–temperature profile of 350 nm junction:** (a) A 20 nm thick NiTe<sub>2</sub> flake exfoliated on top of Si/SiO<sub>2</sub> substrate with Ti (2 nm) / Nb (30 nm) / Au (20 nm) electrodes on top with varying separations to create Josephson junctions of different energy. (b) The pseudo two-probe resistance of the junction with 350 nm separation measured during its cool down in zero field. The drop in resistance around 5.5 K corresponds to the superconducting transition of the niobium electrodes and the drop to zero resistance around 2.5 K corresponds to the superconducting transition of the junction. Inset shows the superconducting transition temperatures for junctions of various separations. Figure adapted with permission from ref.<sup>98</sup>, Springer Nature.

The evolution of the phase across the junction is mapped by studying the variation of critical current ( $I_c$ ) of the junction with a magnetic field applied perpendicular to the plane of the flake. The critical current oscillates with the magnetic field showing the expected Fraunhofer pattern with a period corresponding to a single flux quantum ( $\Phi_0 = \frac{h}{2e}$ ) as expected.

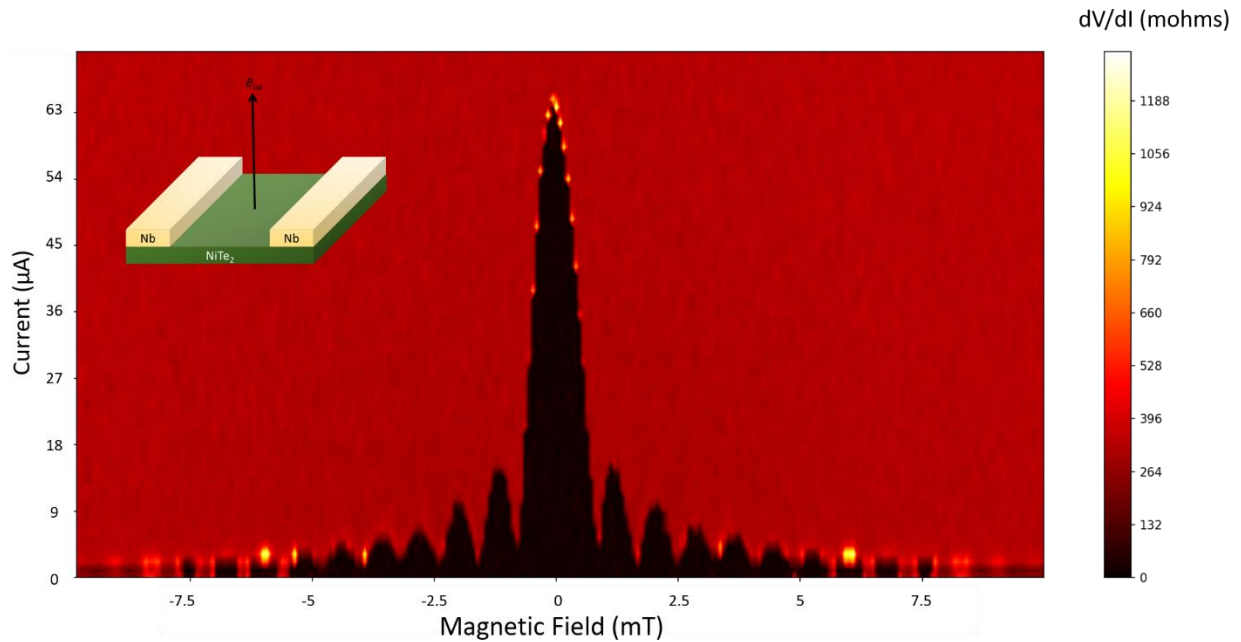


**Fig. 4.4 Fraunhofer oscillations in 550 nm junction:** Graph showing the differential resistance measurement and evolution of the critical current and oscillations for the 550 nm junction as a function magnetic field applied perpendicular to the plane of the sample. The differential resistance measurement is carried out by sweeping the DC bias on top of a small AC signal of around 1  $\mu$ A.

It is to be noted that the Josephson energy and the temperature below which the junction turns superconducting ( $T_j$ ) are expected to decay rapidly with the separation between the superconducting electrodes (inset of Fig.4.3(b)). Supercurrents in the NiTe<sub>2</sub> junctions are found to persist up to separations of 1600 nm, which indicates that, the induced superconducting coherence length in NiTe<sub>2</sub> is extremely long. Such extremely long coherence lengths have been observed only in a handful of materials such as graphene and topological semimetals such as BiSb<sup>103</sup> and

also in graphene<sup>104,105</sup>. It is a different study of its own merit, requires further investigations on its origin and is outside the scope of this thesis.

#### 4.4.2 Josephson diode effect (JDE or $\Delta I_c$ ) in NiTe<sub>2</sub>

The current-voltage characteristics of the junction are measured at the base temperature of 20 mK in the absence of any external applied magnetic field. Direct current is applied through the junction in the positive direction starting from zero until the positive critical current ( $I_c^+$ ), above which the resistance is non-zero, is reached. Experimentally, the critical current is obtained from the data as the current at which differential resistance exceeds a specific threshold value. The current is then decreased back to zero and the junction then reenters the superconducting state ( $I_r$ ). Note that this hysteresis and the difference in  $I_c^+$  and  $I_r$  can arise due to the presence of additional intrinsic capacitance of the junction as described by the resistively and capacitively shunted Josephson junction (RCSJ) model (as discussed in section 2.2.3). The current is then swept in the negative direction starting from zero and the negative critical current ( $I_c^-$ ) is obtained. In the absence of any external magnetic field, it is observed that  $I_c^+$  and  $I_c^-$  have the same magnitude and the difference between them is zero.

When an external magnetic field is applied along the direction of the current, there is an equal decrease in both the positive and negative critical currents ( $I_c^+$  and  $I_c^-$ ), as expected for Josephson junctions in a magnetic field yet no difference in their magnitudes is observed. When a magnetic field is applied perpendicular to the direction of the current in the plane of the device, there is a difference in the magnitudes of  $I_c^+$  and  $I_c^-$  that develops and evolves with an increasing magnetic field. This difference in the magnitudes of  $I_c^+$  and  $I_c^-$  is labelled as Josephson diode effect (JDE or  $\Delta I_c$ ) and is given by  $\Delta I_c = I_c^+ - |I_c^-|$ . By choosing a magnitude of current between  $I_c^+$  and  $|I_c^-|$ , one can obtain non-reciprocal behavior, in which the junction is superconducting along one direction and resistive along the opposite direction as shown in Fig. 4.5(c). The efficiency of the diode is defined using the formula:  $\eta = \frac{I_c^+ - |I_c^-|}{I_c^+ + |I_c^-|}$ . The origin of the JDE can be explained due to the formation of finite momentum Cooper pairs in the system as we discuss in the following section.

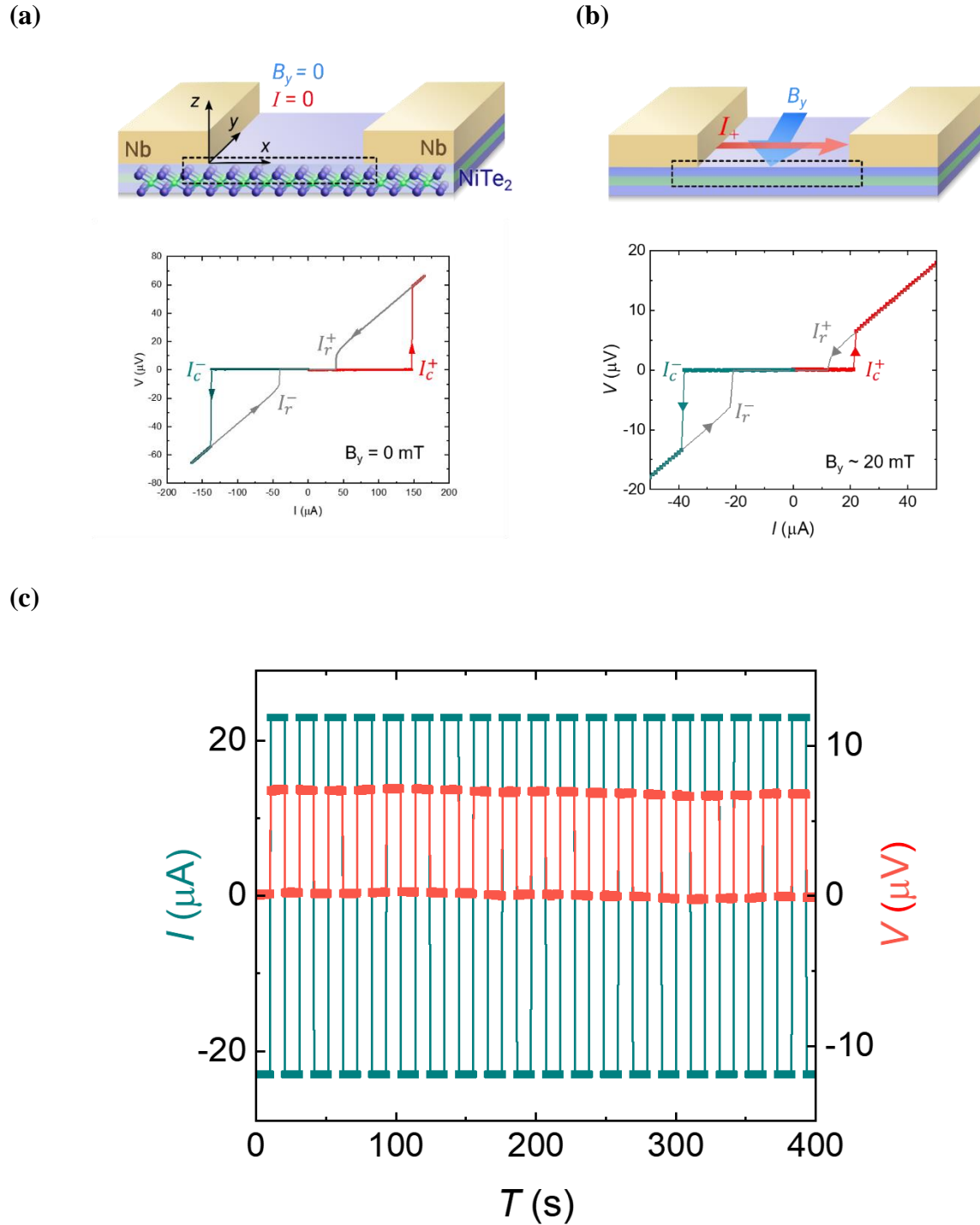


**Fig. 4.5 Josephson diode effect in presence of a magnetic field:** (a) shows the current-voltage characteristics of a junction at 20 mK temperature right after cooling it down in zero magnetic field.  $I_c^+$  and  $|I_c^-|$  are equal in magnitude with a value of around  $\sim 145 \mu\text{A}$  leading to a zero Josephson diode effect. (b) shows the current-voltage characteristics of the same junction with a

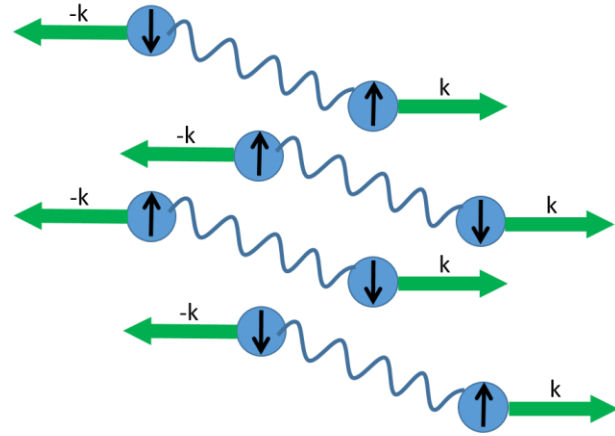
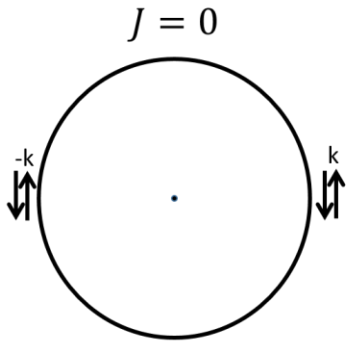
20 mT in-plane magnetic field applied perpendicular to the direction of the current. This leads to a decrease in the critical current and also the appearance of a large  $\Delta I_c$  of around 20  $\mu\text{A}$ . (c) By choosing a current between  $I_c^+$  and  $|I_c^-|$ , we can obtain supercurrents along one direction while obtaining resistive currents along the opposite direction, thus displaying the existence of a Josephson diode effect. Figure adapted with permission from ref.<sup>98</sup>, Springer Nature.

### 4.4.3 Spin-momentum locking induced finite momentum pairing

As discussed above, NiTe<sub>2</sub> hosts a topological surface state with a very large Rashba-like spin-splitting close to the Fermi level. Following a simple heuristic argument, we can try to understand how this spin-splitting can lead to the formation of Cooper pairs with non-zero momentum and in turn lead to JDE.

Let us consider a conventional BCS superconductor with inversion and time-reversal symmetries and a two-dimensional circular Fermi surface. In a conventional superconductor, Cooper pairs are formed at opposite momentum points with opposite spins. For example, electrons at  $(\mathbf{k}, \uparrow)$  state pair with electrons at their time-reversed state at  $(-\mathbf{k}, \downarrow)$  in the ground state as shown in Fig. 4.6. In this scenario, the Cooper pairs have a net momentum that adds up to zero leading to the formation of zero momentum Cooper pairs.

With inversion and time-reversal symmetries



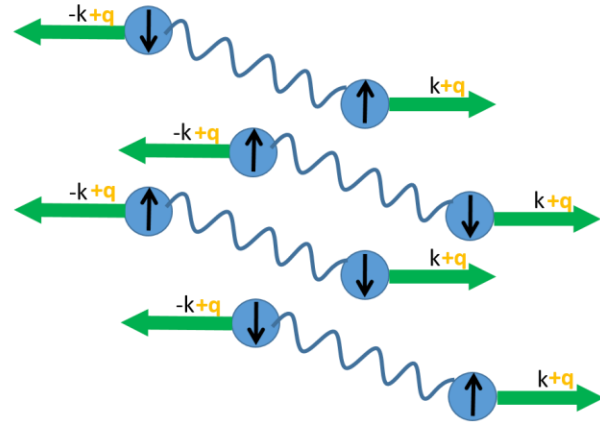
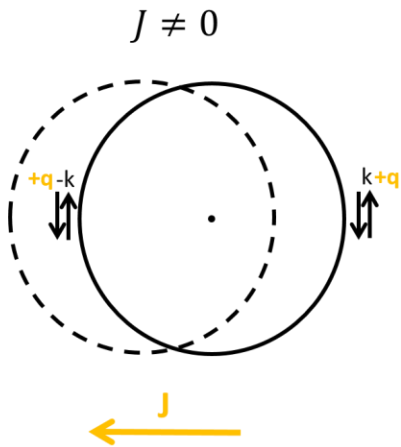
Net momentum =  $k + (-k) = 0$   
Zero-momentum Cooper pairs

***Fig. 4.6 Underlying Fermi surface and Cooper pairs in a conventional BCS superconductor in the absence of a current and external magnetic field***

When a current is applied along one direction, there is a corresponding shift of the underlying Fermi surface along the opposite direction that gives the electrons an additional momentum  $q$  to the system and the Cooper pairs are now formed between electrons at  $(\mathbf{k} + \mathbf{q}, \uparrow)$  and  $(-\mathbf{k} + \mathbf{q}, \downarrow)$ , leading to a net momentum that adds up to  $2q$  and to a net current along one direction as shown in Fig. 4.7. This corresponds to a kinetic energy of  $\left| \frac{2k \cdot q}{m} \right|$  and when this value of energy, which can lead to the depairing of Cooper pairs, reaches the superconducting energy gap of the system, superconductivity vanishes and the current at which this is reached is essentially equal to the critical current of the system. As it can be seen, this depairing energy is independent of the direction of current and hence the superconducting energy gap remains the same for all current directions. However, this is not the case for a system with spin-momentum locking.



With inversion and time-reversal symmetries



$$\text{Net momentum} = (k + q) + (-k + q) = 2q$$

$$\text{Net depairing energy} = \left| \frac{2k \cdot q}{m} \right|$$

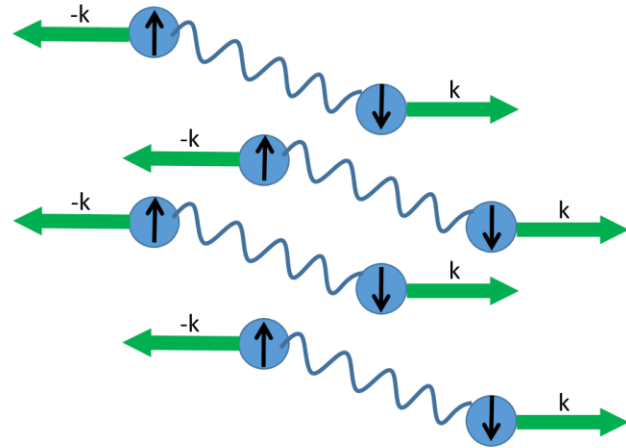
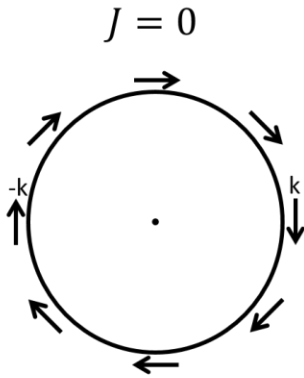
$$\text{At critical current } (I_c), \left| \frac{2k \cdot q}{m} \right| = 2\Delta$$

Same for forward and backward currents

**Fig. 4.7 Underlying Fermi surface and Cooper pairs in a conventional BCS superconductor in the presence of a current:** In the presence of a current, the Cooper pairs acquire a finite momentum that results in net charge transport and a depairing energy that is reciprocal.

Let us look at a simple representation of a system with broken inversion symmetry by considering just the two-dimensional outer Fermi surface of the topological surface states of NiTe<sub>2</sub> with Rashba spin-orbit coupling. In this case, the spin of the electron is locked perpendicular to the direction of the current as shown in Fig. 4.8. In the absence of any external magnetic field that can break the time-reversal symmetry of the system, the depairing energy due to the application of a current is similar to that of conventional superconductors and is independent of the direction of current.

With broken inversion symmetry  
(Rashba spin-momentum locking)



Net momentum =  $k + (-k) = 0$   
Zero-momentum Cooper pairs

**Fig. 4.8 Underlying Fermi surface and Cooper pairs of a superconductor with Rashba spin-momentum locking**

When an external magnetic field is applied, the spin-locked states are split further by an additional Zeeman energy ( $E_z = g\mu B_x$ ) which shifts the center of mass of the Fermi surface and the system appears to have gained a pseudo-momentum ( $2\mathbf{q}'$ ). In this case, the electrons available at states  $(\mathbf{k} + \mathbf{q}', \uparrow)$  and  $(-\mathbf{k} + \mathbf{q}', \downarrow)$  can form Cooper pairs leading to the formation of finite momentum Cooper pairs with net momentum ( $2\mathbf{q}'$ ) as shown in Fig. 4.9. This net momentum is along the direction perpendicular to the magnetic field and can be controlled by the magnitude of the magnetic field. Since a non-zero Cooper pair momentum exists in the absence of any applied current, this should give rise to spontaneous supercurrents in the junction.

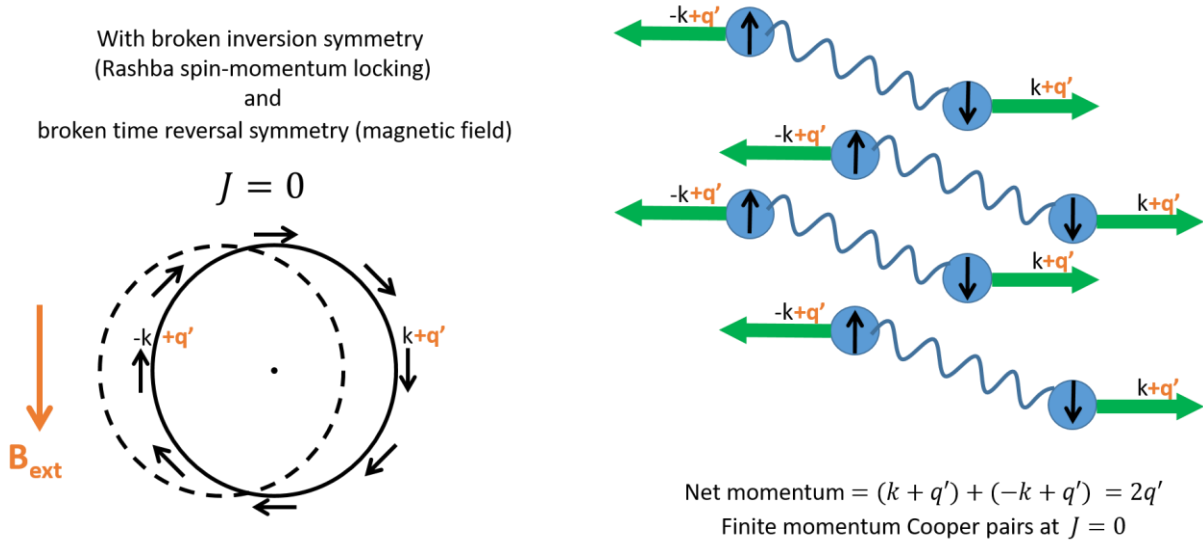


**Fig. 4.9 Underlying Fermi surface and Cooper pairs of a superconductor with Rashba spin-momentum locking in the presence of a magnetic field:** When a magnetic field is applied to spin-momentum locked surface, the Zeeman field creates a shift of the Fermi surface that gives an additional pseudo-momentum  $2q'$  to the Cooper pairs in the absence of an external current.

Now when an external current is applied in a direction perpendicular to the magnetic field, it provides an additional momentum to the Cooper pairs ( $2q$ ) and the states are further shifted to  $(\mathbf{k} + \mathbf{q}' + \mathbf{q}, \uparrow)$  and  $(-\mathbf{k} + \mathbf{q}' + \mathbf{q}, \downarrow)$  as shown in Fig. 4.10. In this case, the net momentum depends on the direction of the current relative to the magnetic field and the depairing energy can be written as  $\left| \frac{2\mathbf{k} \cdot (\mathbf{q}' \pm \mathbf{q})}{m} \right|$ . For a given magnetic field direction there are two possible depairing energies depending on the direction of current  $\left| \frac{2\mathbf{k} \cdot (\mathbf{q}' + \mathbf{q})}{m} \right|$  and  $\left| \frac{2\mathbf{k} \cdot (\mathbf{q}' - \mathbf{q})}{m} \right|$ . This, in turn, gives rise to critical currents ( $I_c^+$  and  $I_c^-$ ) that are unequal in opposite direction and hence giving rise to a diode effect. This picture gives us a very intuitive understanding of how spin-momentum locking can give rise to a diode effect.

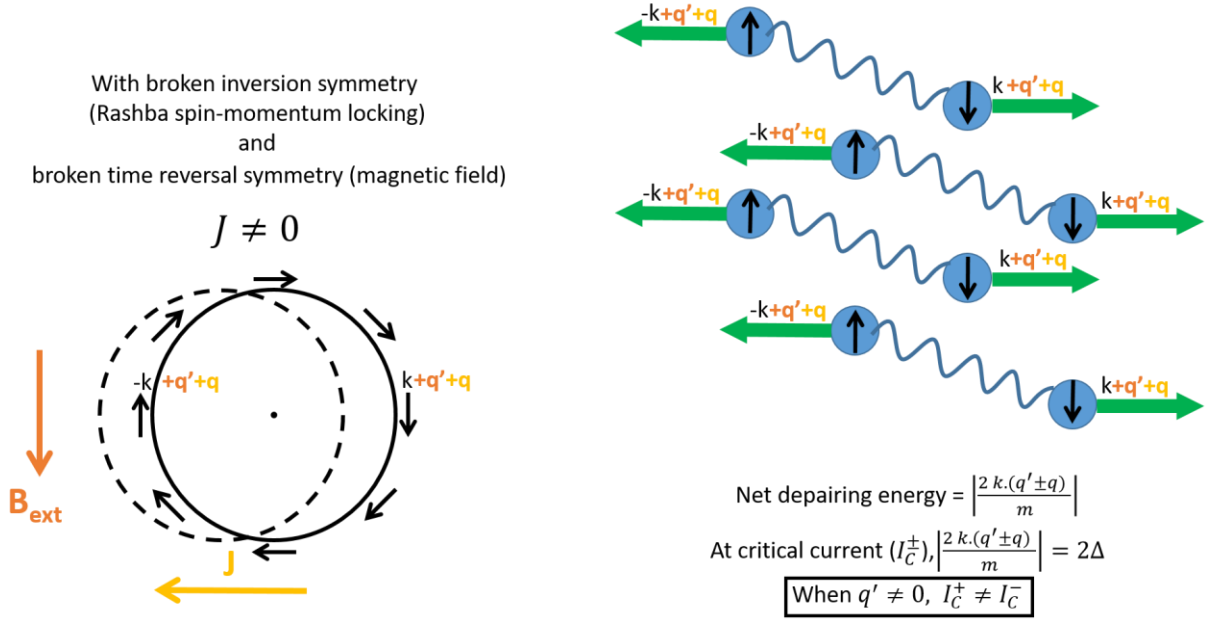


**Fig. 4.10 Underlying Fermi surface and Cooper pairs of a superconductor with Rashba spin-momentum locking in the presence of a magnetic field and current:** In the presence of an additional current, the Cooper pair acquires a momentum that depends on the direction of the current, giving rise to non-reciprocal supercurrents.

#### 4.4.4 Ginzburg-Landau theory of Josephson diode effect

This theoretical model was proposed by Margarita Davydova, Noah Yuan and Liang Fu and it is presented in this thesis for the sake of clarity. To understand better and quantify the effect of finite momentum Cooper pairing on the JDE in NiTe<sub>2</sub>, let us consider a Ginzburg-Landau model of a Josephson junction with two superconducting electrodes separated by a weak link. Near the superconducting transition temperature of the junction, the free energy of the junction can be expanded in terms of the wave functions of the two superconducting electrodes.

$$F = \sum_{j=1,2} \left( \alpha_j |\Delta_j|^2 + \frac{1}{2} \beta_j |\Delta_j|^4 \right) - \gamma_1 \Delta_1^* \Delta_2 - \frac{1}{2} \gamma_2 (\Delta_1^* \Delta_2)^2 + c. c.$$

In this case,  $\Delta_1$  corresponds to wave function of the first electrode and  $\Delta_2$  corresponds to wave function of the second electrode and the term  $\Delta_1^* \Delta_2$  denotes the order parameter of the weak link.

$\alpha_j$  and  $\beta_j > 0$  are Ginzburg-Landau constants corresponding to the two superconducting electrodes ( $j = 1, 2$ ).  $\gamma_1$  and  $\gamma_2$  denote the first and second order Cooper pair tunneling processes across the weak link, respectively.  $\gamma_1$  and  $\gamma_2$  can turn complex under the presence of external magnetic fields. In this equation, we have included the second order tunneling processes as it is typically found in junctions with high transmission, can lead to non-sinusoidal current-phase relationships and can lead to non-reciprocal supercurrents as will be shown below. As the transition temperature of the superconducting weak link is much lower than that of the superconducting electrodes, the equation can be rewritten to focus on tunneling across the weak link.

$$F = F_0 - \gamma_1 \Delta_1^* \Delta_2 - \frac{1}{2} \gamma_2 (\Delta_1^* \Delta_2)^2 + c. c. \quad (4.1)$$

The wave function of the superconducting electrodes, which have the same superconducting gap can be written in terms of their amplitudes and phases as  $\Delta_1 = \Delta e^{i\phi_1}$  and  $\Delta_2 = \Delta e^{i\phi_2}$  where  $\Delta$  is the magnitude of the order parameter and  $\phi_{1,2}$  are the corresponding phases. Substituting these values, the free energy takes the form:

$$F = F_0 - 2|\gamma_1| \Delta^2 \cos \varphi - |\gamma_2| \Delta^4 \cos(2\varphi + \delta) \quad (4.2)$$

where  $\varphi = \phi_2 - \phi_1 + \arg(\gamma_1)$  is effectively the phase difference between the two superconducting regions and  $\delta = \arg(\gamma_2) - 2 \arg(\gamma_1)$  is the phase difference between the first and second order Cooper pair tunneling processes. The Josephson current-phase relationship can then be derived from the free energy as:

$$I(\varphi) = \frac{2\pi}{\Phi_0} \frac{\partial F}{\partial \varphi} = \frac{4e}{\hbar} \{ \Delta^2 |\gamma_1| \sin \varphi + \Delta^4 |\gamma_2| \sin(2\varphi + \delta) \} \quad (4.3)$$

where  $\Phi_0 = \frac{h}{2e}$  is the superconducting flux quantum.

In order to get the critical current values, we need to maximize this function with respect to the phase. Assuming the contribution of the second harmonic term  $|\gamma_2|$  to be smaller in comparison to the first harmonic  $|\gamma_1|$ , we can maximize  $I(\varphi)$  when  $\varphi = \pm \frac{\pi}{2}$  giving,

$$I_c^\pm \approx \left| I \left( \pm \frac{\pi}{2} \right) \right| = \frac{4e}{\hbar} \{ \Delta^2 |\gamma_1| \mp \Delta^4 |\gamma_2| \sin \delta \} \quad (4.4)$$

The Josephson diode effect can be written as:

$$\Delta I_c \equiv I_c^+ - |I_c^-| = -\frac{8e}{\hbar} \Delta^4 |\gamma_2| \sin \delta \quad (4.5)$$

In the following sub-sections, the variation of JDE with temperature, magnetic field magnitude and direction are discussed in detail to compare it with the presented model and determine its possible origins.

#### 4.4.5 Temperature dependence of $\Delta I_c$

It can be seen that  $\Delta I_c \propto \Delta^4$  and the temperature dependence of the order parameter can be written as  $\Delta \propto \sqrt{1 - \frac{T}{T_j}}$ , where  $T$  is the temperature of the junction and  $T_j$  is the superconducting transition temperature of the junction. Hence, we can say from this derivation just by introducing a higher order term in the Ginzburg-Landau equation for a weak link and without the loss of any generality that:

$$\Delta I_c \propto (T - T_j)^2 \quad (4.6)$$

In the following graph, we have plotted the experimentally measured evolution of JDE at 12 mT in-plane magnetic field perpendicular to the direction of current, where  $\Delta I_c$  is found to be maximum as a function of temperature. It can be seen that  $\Delta I_c$  decays with increasing temperature and that close to the superconducting transition temperature of the junction ( $T_j$ ),  $\Delta I_c$  very closely follows a  $(T - T_j)^2$  dependence as shown in Fig. 4.11 agreeing well with the Ginzburg-Landau model that has been used.

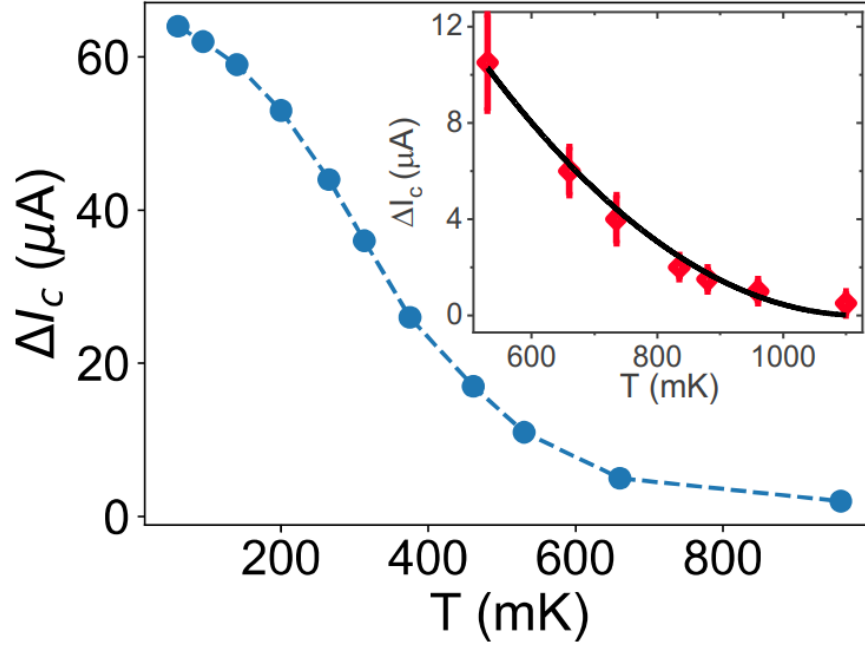


**Fig. 4.11 Temperature dependence of Josephson diode effect:** The evolution of  $\Delta I_c$  is shown as a function of temperature.  $\Delta I_c$  is found to decrease as a function of temperature. Dotted line is a guide to the eye. Inset shows  $\Delta I_c$  close to  $T_j$  and the black line represents a  $(T - T_j)^2$  fit. Figure adapted with permission from ref.<sup>98</sup>, Springer Nature.

#### 4.4.6 Magnetic field and angular dependence of $\Delta I_c$

In order to study the evolution of  $\Delta I_c$  under various conditions and look for consistency with our model, the magnetic field magnitude and angular dependence of  $\Delta I_c$  were studied experimentally. Interestingly, change in the sign of  $\Delta I_c$  and decaying oscillations in  $\Delta I_c$  as a function of the magnetic field magnitude were observed. A sinusoidal behavior of  $\Delta I_c$  was observed when varying the angle of the in-plane magnetic field with respect to the direction of the current. However, as the magnitude of the magnetic field was increased,  $\Delta I_c$  displayed a more complex behavior and had more nodes. In order to understand these experimental results, we can look again into our GL model and study the evolution of  $\Delta I_c$  with respect to magnetic field. We can go back to equation (4.5) and look at the order parameter as a function of the magnetic field.

The magnetic field dependence of the order parameter can be written as  $\Delta \propto \sqrt{1 - \left(\frac{|B_y|}{B_c}\right)^2}$ , where  $B_c$  is the critical field of the junction and  $B$  is the applied magnetic field.

$$\Delta I_c \propto \left[1 - \left(\frac{|B_y|}{B_c}\right)^2\right]^2 \sin \delta$$

Now if we consider the presence of finite momentum Cooper pairs in the system induced by a magnetic field  $B_y$ , the additional momentum  $q_x$  makes the junction behave like a finite momentum superconductor and gives it an additional phase shift  $\delta \approx 2q_x d$  as the Cooper pair propagates through the junction with separation  $d$ . In this case with finite momentum Cooper pairs,  $\Delta I_c$  can be written as:

$$\Delta I_c \propto \left[1 - \left(\frac{|B_y|}{B_c}\right)^2\right]^2 \sin\left(\pi \frac{B_y}{B_d}\right) \quad (4.7)$$

where  $B_d$  is a parameter that contains all the properties that are intrinsic to the junction. It can be seen that there is a sinusoidal dependence of  $\Delta I_c$  on the magnetic field  $B_y$  and the magnitude of  $\Delta I_c$  decays with increasing magnetic field as we observe in our experiments. The number of oscillations that can be expected in  $\Delta I_c$  depends on the ratio  $\left(\frac{B_c}{B_d}\right)$ . The function  $\sin\left(\pi \frac{B_y}{B_d}\right)$  changes sign whenever  $B_y = nB_d$  where  $n$  is an integer. The maximum value that  $B_y$  can reach without destroying the superconductivity depends on the critical field  $B_c$ . Hence the maximum number of oscillations that we can get is given by  $n = \text{int}\left(\frac{B_c}{B_d}\right)$ . The value of  $B_d$  can be obtained by looking at the magnetic field at which  $\Delta I_c$  reaches zero and reverses sign. In the case of our junction  $\Delta I_c$  reaches zero at a magnetic field of  $22 \text{ mT}$  which gives the value of  $B_d$ . To get the value of  $B_c$ ,  $\Delta I_c$  is simulated with the obtained  $B_d$  and the same ratio of first and second maxima of  $\Delta I_c$  as obtained from experiments. This yields the value of  $B_c$  to be  $45 \text{ mT}$ . Correspondingly, we can see two oscillations in  $\Delta I_c$  before this value is reached. Hence, the model is able to successfully capture the experimentally observed features with increasing magnitude of the magnetic field.



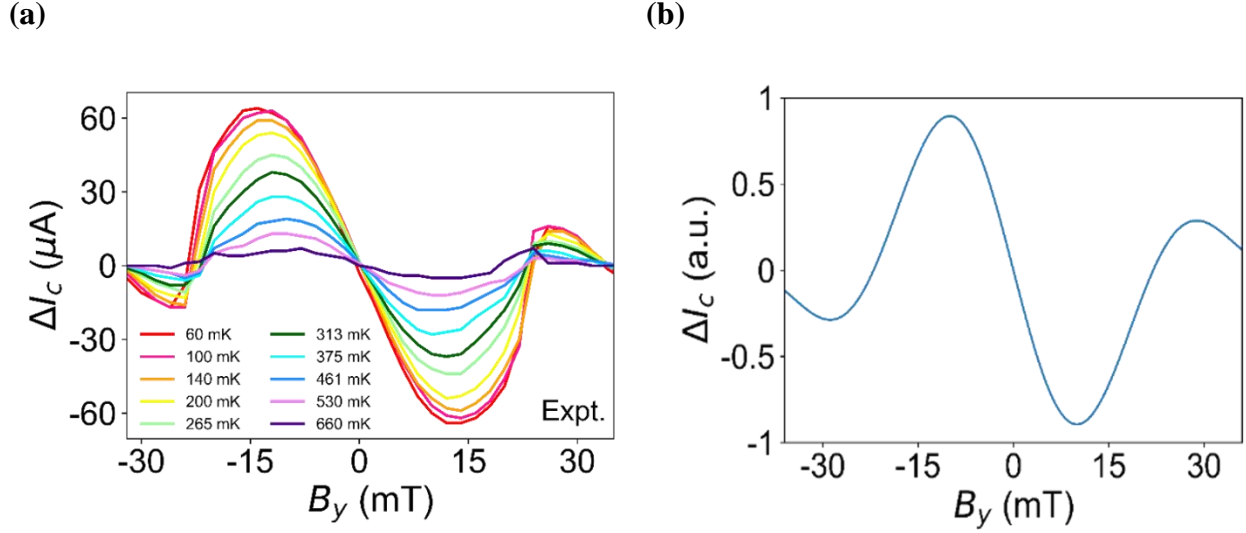


**Fig. 4.12 Magnetic field dependence of Josephson diode effect:** (a) Experimentally obtained curves for  $\Delta I_c$  as a function of magnetic field at various temperatures.  $\Delta I_c$  oscillates sinusoidally as a function of magnetic field and changes sign periodically. (b) Theoretically calculated  $\Delta I_c$  as a function of magnetic field from the model using the ratio of first two maxima from the experiment and  $B_d = 22$  mT. Figure adapted with permission from ref.<sup>98</sup>, Springer Nature.

To understand the experimentally observed complex dependence of  $\Delta I_c$  on the angle of magnetic field, we look back at equation (4.7) which gives the total magnetic field dependence of  $\Delta I_c$  and substitute the total magnetic field with  $= B_{ip} \cos \theta$ , where  $\theta$  is the angle between the current and magnetic field. This gives  $\Delta I_c$  as:

$$\Delta I_c \propto \left[ 1 - \left( \frac{|B_{ip} \cos \theta|}{B_c} \right)^2 \right]^2 \sin \left( \pi \frac{B_{ip} \cos \theta}{B_d} \right) \quad (4.8)$$

It can be noted that  $\Delta I_c$  changes sign when  $\sin \left( \pi \frac{B_{ip} \cos \theta}{B_d} \right) = 0$ . With increasing  $B_{ip}$ , the frequency of the sign change increases and when  $B_{ip}$  crosses  $B_d$ , more nodes are introduced in the system. Using the values of  $B_c$  and  $B_d$  obtained in the previous section, one can model the evolution of  $\Delta I_c$  with magnetic field amplitude and angle with respect to the direction of current. This calculated evolution of  $\Delta I_c$  is in great agreement with the experimentally obtained values as shown in Fig. 4.13 providing further validation to the theoretical model.

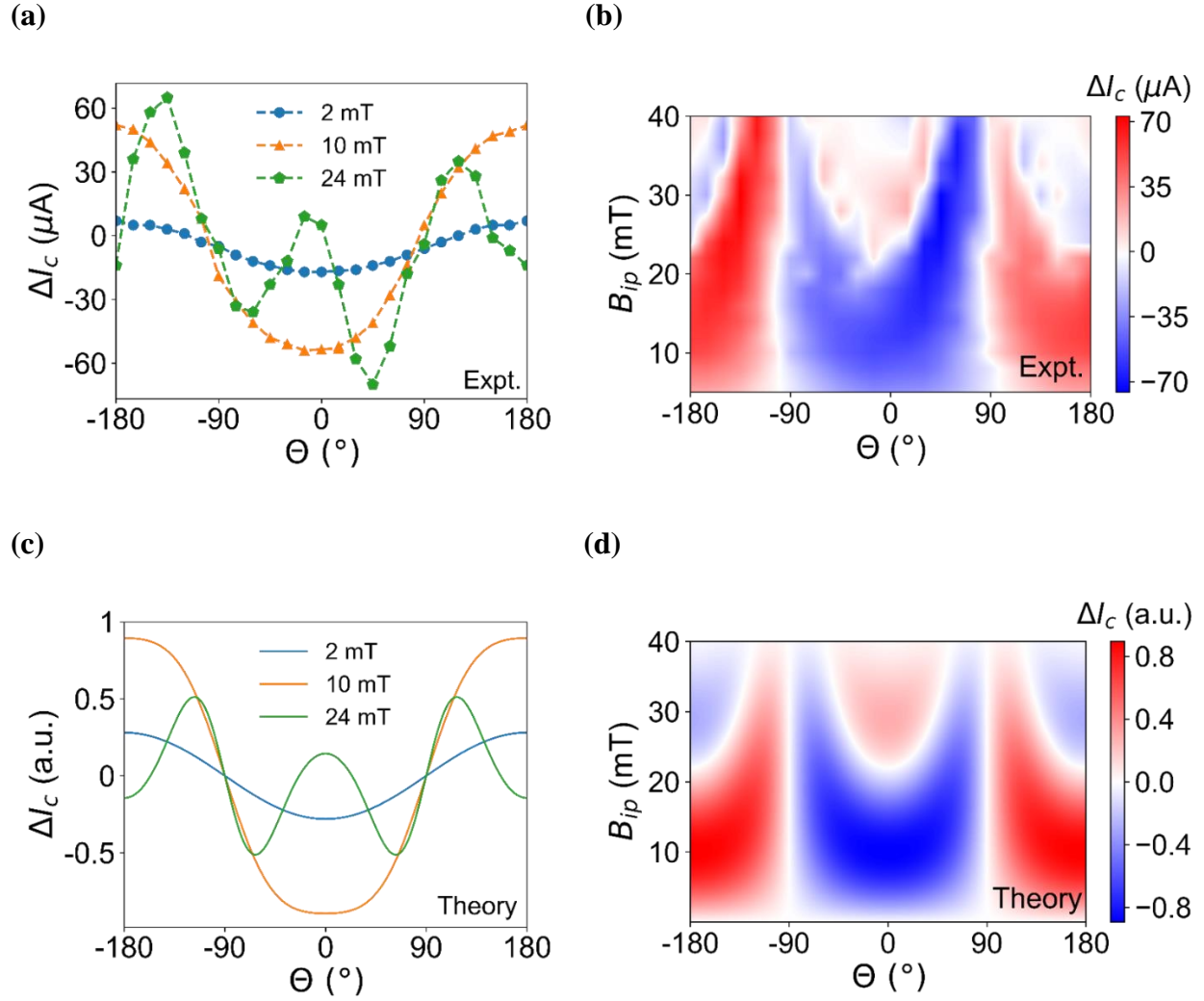


**Fig. 4.13 Angular dependence of Josephson diode effect:** (a), (b) Experimentally measured angular dependence map of the Josephson diode effect at various magnetic fields. (c), (d) Theoretically simulated angular dependence map of the Josephson diode effect using the GL model and the value of parameters  $B_c = 45$  mT and  $B_d = 22$  mT obtained experimentally. Figure adapted with permission from ref.<sup>98</sup>, Springer Nature.

#### 4.4.7 Finite momentum Cooper pairing in NiTe<sub>2</sub> from $\Delta I_c$

Using all the above experimental data and the GL model, we can estimate the induced Cooper pair momentum in NiTe<sub>2</sub>. From equation (4.5),  $\Delta I_c$  reaches maximum value when  $\delta = \frac{\pi}{2}$ .

As discussed before, in the presence of finite momentum the phase shift induced can be written as  $\delta \approx 2q_x d$ . From Fig. 4.11 it can be seen that  $\Delta I_c$  reaches maximum value when  $B_y = 12 mT$ . Hence the value of Cooper pair momentum when  $\Delta I_c$  at  $B_y = 12 mT$  can be estimated for the  $350 nm$  junction as,  $2q_x = \frac{\pi}{2d} \approx 4.5 \times 10^6 m^{-1}$ .

#### 4.4.8 Estimating finite momentum from the evolution of Fraunhofer pattern

In order to independently verify the existence of finite momentum Cooper pairing in NiTe<sub>2</sub> and the value that was estimated from the Josephson diode effect, we study the evolution of the Fraunhofer pattern as a function of in-plane magnetic field along the direction of current as shown in Fig. 4.14(a). This measurement is quite significant as it would demonstrate that finite momentum Cooper pairing exists along the direction of current even though it does not give rise to a Josephson diode effect and that there is a Rashba-like spin-momentum locking in the system. The Fraunhofer pattern for a Josephson junction gives the actual phase difference between the two superconducting electrodes, which can in turn be used to estimate the Cooper pair momentum in the system. To calculate the Josephson current as a function of the phase difference, all possible quasi-classical trajectories are summed over.

$$I(\Delta\varphi(B_x, B_z)) = \int_0^W \int_0^W dy_1 dy_2 \frac{1}{d_{eff}^2 + (y_2 - y_1)^2} \sin(\Delta\varphi(B_x, B_z)) \quad (4.9)$$

where,

$$\Delta\varphi(B_x, B_z) = \Delta\varphi_0 + \frac{2\pi B_z d_{eff}(y_1 + y_2)}{\Phi_0} + 2q_y(B_x)(y_2 - y_1) \quad (4.10)$$

is the phase difference for a trajectory that starts at  $(0, y_1)$  and ends at  $(d_{eff}, y_2)$  and  $d_{eff} = d + 2\lambda$ , where  $\lambda = 140 nm$  is the London penetration depth of  $30 nm$  thick niobium. The critical current and the Fraunhofer pattern is calculated by maximizing  $I(\Delta\varphi(B_x, B_z))$  with respect to  $\Delta\varphi(B_x, B_z)$ . The actual value of  $d_{eff}$  used in the simulations is adjusted by using the position of the first node in the Fraunhofer pattern at zero in-plane magnetic fields obtained from experiments. This variation in  $d_{eff}$  can be due to flux focusing effects in the junction.  $\Delta\varphi_0$  is the phase difference between the superconducting electrodes in the absence of an applied magnetic field.

The effect of in-plane magnetic flux through the thickness of the flake is not added to equation (4.10) since it is small as can be shown below. For a film of thickness  $t$ , the phase difference due to the magnetic flux in the plane of the sample can be written as:

$$\Delta\varphi_t(B_x) = \frac{B_x(y_2 - y_1)t}{\Phi_0}$$

Comparing the maximum contribution of this phase to that of the phase due to the finite momentum Cooper pairing, we get

$$\frac{\Delta\varphi_t(B_x)}{\Delta\varphi_{FM}(B_x)} = \frac{\frac{B_x(y_2 - y_1)t}{\Phi_0}}{2q_y(B_x)(y_2 - y_1)} = \frac{B_x t}{2\Phi_0 q_y(B_x)}$$

As given by the calculations in references<sup>96,97</sup>, we get  $\frac{2q_y}{B_z} \approx \frac{\pi d_{eff}}{\Phi_0}$

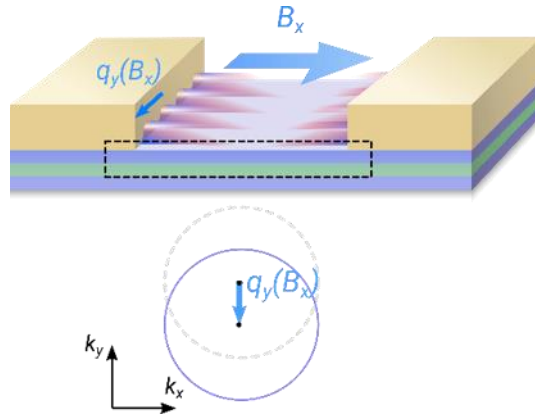
$$\frac{\Delta\varphi_t(B_x)}{\Delta\varphi_{FM}(B_x)} = \frac{tB_x}{\pi d_{eff} B_z}$$

By using the value of  $\left(\frac{B_x}{B_z}\right) \sim 13$  from experiment and the value of  $t = 20nm$  and  $d_{eff} \sim 1\mu m$  we get  $\left(\frac{\Delta\varphi_t(B_x)}{\Delta\varphi_{FM}(B_x)}\right) \sim 0.08$ , indicating that the contribution of the in-plane magnetic flux induced phase shift is more than ten times smaller than that induced by finite momentum Cooper pairing and hence can be neglected in our calculations. Also, considering the ratio of in-plane magnetic flux for a  $100 mT$  magnetic field to a magnetic flux quantum using the device dimensions as  $20 nm \times 350 nm$  is  $\left(\frac{\Phi_t}{\Phi_0}\right) \sim 0.06$  which is quite small to have any significant effect.

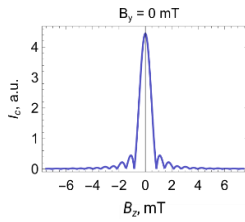
The Fraunhofer pattern calculated from equation (4.9) is shown below. It can be seen that the interference pattern looks like a conventional one at zero in-plane magnetic field with a dependence that looks just like  $\left(\frac{\sin\left(\frac{\pi\Phi}{\Phi_0}\right)}{\left(\frac{\pi\Phi}{\Phi_0}\right)}\right)$ . When the in-plane magnetic field is increased, the central peak decreases in magnitude and the intensity of two side branches on the positive and negative side of the out-of-plane magnetic field increases in magnitude as shown in Fig. 4.14(b-e), which looks as if the intensity of the central peak is transferred to the two side branches due to the finite momentum Cooper pairing. This can be construed as a signature of finite momentum Cooper

pairing in the system and the value of the slope at which these side peaks evolve can be used to estimate the momentum of the Cooper pairs.

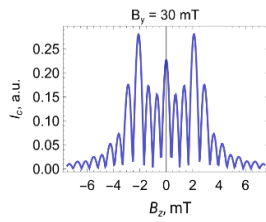
(a)



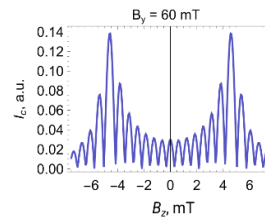
(b)



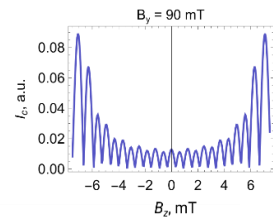
(c)



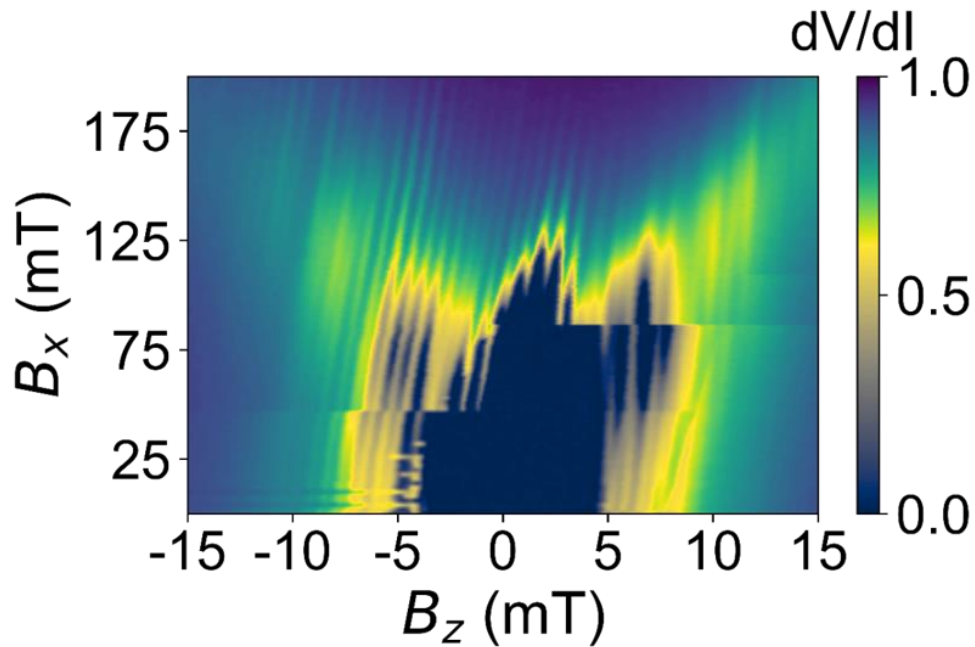
(d)



(e)



(f)



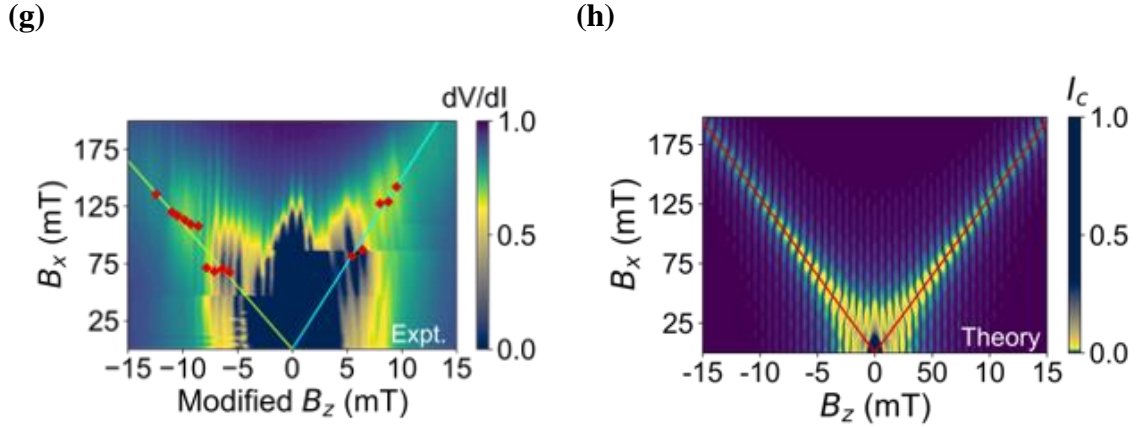


**Fig. 4.14 Measurement of the finite momentum Cooper pairing in NiTe<sub>2</sub> Josephson junctions:** (a) shows the measurement geometry of the finite momentum Cooper pairing in the system by applying a magnetic field parallel to the direction of current which shifts the Fermi surface perpendicular to the direction of current. Though this does not lead to a Josephson diode effect, finite momentum Cooper pairs are still created with a momentum shift perpendicular to the current direction. (b)-(e) Theoretical simulations of the evolution of the Fraunhofer pattern under an in-plane magnetic field. The central peak is found to decrease in magnitude while two new peaks that look like horns appear on the side and spread out with increasing in-plane magnetic field. (f) Experimentally measured differential resistance ( $\frac{dV}{dI}$ ) is used to track the evolution of the central peak of the Fraunhofer pattern with the in-plane magnetic field. The intensity of the central peak is found to be split and redistributed to the side branches, as the field strength is increased. (g) Experimentally measured differential resistance after tilting correction. The red data points indicate resistance minima used to estimate the slope of evolution of the peak. (h) Theoretical simulation of the evolution of critical current with in-plane magnetic field. The slope of the side branches, which is determined by the finite momentum, is extracted from the experimental slope. Figure adapted with permission from ref.<sup>98</sup>, Springer Nature.

Experimentally measuring the Fraunhofer pattern for each in-plane magnetic field over a large range is a time-consuming measurement. In order to make the measurement more efficient, the differential resistance of the sample is mapped as a function of out-of-plane and in-plane magnetic fields. This measurement helps to effectively track the position of the central peak with

maximum intensity as a low resistance state instead of measuring the complete interference pattern over the entire range of magnetic fields. In order to perform this measurement a small AC bias of a  $300 \text{ nA}$  is applied to the sample at a frequency of  $27.777 \text{ Hz}$  and  $\left(\frac{dV}{dI}\right)$  is measured as the magnetic field is swept to determine the position of the low resistance state. The experimentally measured map is shown in Fig. 4.14(f). The measured pattern is tilted due to the flux induced shift of the Fraunhofer pattern by the in-plane magnetic field and this tilt is corrected by subtracting a slope and the resultant map is shown in Fig. 4.14(g). It can be observed clearly that as the in-plane magnetic field is increased the central peak decreases in magnitude and two side branches emerge as predicted. The position of these side branches in the experimental data is obtained by fitting the sweeps to a polynomial and getting their minima. Then the slope of evolution of these side branches is obtained by a linear fit. The slopes  $\left(\frac{B_x}{B_z}\right)$  for positive and negative  $B_z$  are 15 and 11, respectively. The small asymmetry in the slopes can arise due to flux focusing effects which change the direction of the applied magnetic fields. So, the average value of the two slopes  $\left(\frac{B_x}{B_z} \sim 13\right)$  is used to estimate the momentum of the Cooper pairs. Theoretically, calculated evolution of critical currents in the presence of a magnetic field with slope is shown in Fig. 4.14(h). Using the value of slope from experiments, we get the value of the finite momentum Cooper pairing to be  $2q_y \approx 1.6 \times 10^6 \text{ m}^{-1}$ .

The value of Cooper pair momentum obtained along  $y$ -direction obtained from measurement of the evolution of Fraunhofer pattern under an in-plane magnetic field is of the same order of magnitude as that along the  $x$ -direction obtained from the GL model using Josephson diode effect experiments. Thus, we have strong evidence that points towards the existence of FMCP in this system and it possibly giving rise to the observed Josephson diode effect.

#### 4.4.9 Alternative explanation for the origin of $\Delta I_c$

While we have shown clearly that there is a non-zero Cooper pair momentum in the presence of a magnetic field in our system and attribute this to the helical spin-momentum locked surface states in  $\text{NiTe}_2$ , there is also another possible origin to the observed Cooper pair momentum that can give rise to the same effect in the system, that is independent of the junction material. This

is due to the Meissner screening currents that arise in the superconducting leads in the presence of a magnetic field<sup>106</sup>.

When a Josephson junction made of conventional superconducting leads is placed in a magnetic field, screening currents are generated in the superconducting leads due to Meissner effect. Correspondingly, the superconducting order parameter on the surface of the electrodes gains an additional phase similar to FFLO states due to the finite momentum generated. This finite momentum generated on the surface of the electrodes can be transferred from one electrode to the other, when the junction is in the ballistic limit. It shows the same characteristics as that induced by the Rashba spin-momentum locking present in the system, namely maximum Josephson diode effect when the magnetic field is aligned perpendicular to the direction of current and similar angular and temperature dependencies. In our case, the thickness of Nb leads (30 nm) is much smaller than the London penetration depth and the estimated value of finite-momentum Cooper pairing arising from the screening in Nb contacts is therefore  $q_x \approx \frac{e}{\hbar} B_y \frac{\hbar_{Nb}}{2}$ . At  $B_y = 20$  mT, this corresponds to  $2q_x \approx 10^6$  m<sup>-1</sup>. Since this is smaller than the value of the Cooper pair momentum estimated from the Fraunhofer pattern and the Josephson diode effect measurements, it cannot account solely for the observed effect. Moreover, superconducting diode effect has been observed in thin flakes of 2H-NbSe<sub>2</sub> in the presence of an out-of-plane magnetic field<sup>107</sup>, which is expected if the FMCP is induced by the Ising spin-orbit coupling in the system.

## 4.5 Conclusion

In conclusion, non-reciprocal supercurrents leading to a Josephson diode effect in lateral junctions of exfoliated NiTe<sub>2</sub> flakes with a maximum efficiency close to 60% has been observed which is one of the largest effects reported so far. In order to comprehend the possible origins of the observed diode effect, a Ginzburg-Landau model which takes second order term into account with an additional phase shift is used. This additional phase shift is argued to arise from non-zero Cooper pair momentum in the presence of a magnetic field. This model captures all experimentally observed features such as the magnetic field dependence, angular dependence and temperature dependence. Additional measurements to independently measure the Cooper pair momentum, point to a value close to the one suggested by measurements of the diode effect, thus confirming



the presence of finite momentum in NiTe<sub>2</sub> junctions and reinforcing its role in the creation of the Josephson diode effect in NiTe<sub>2</sub>. Finite momentum Cooper pairing, though considered rather uncommon, has been observed in Josephson junctions of NiTe<sub>2</sub>. The value of such large Cooper pair momentum at low magnetic fields is commensurate with a very large  $\left(\frac{g}{v_F}\right)$  ratio in the system. Since, the  $v_F$  in the system is already known from ARPES measurements to be much smaller than normal metals, it can be used to calculate  $g$ -factor of the electrons. The Cooper pair momentum can be expressed as  $2q = \frac{g\mu_B B}{\hbar v_F}$ , which gives the  $g$ -factor to be around 170. This value of  $g$ -factor is extremely large, even larger than typically found in topological semimetals in the normal state<sup>108</sup> and that recently discovered in InAsSb/InSb heterostructures<sup>109</sup> of around 104, which warrants further investigation in the future.

The origin of the non-zero Cooper pair momentum in NiTe<sub>2</sub> has been attributed to the Zeeman shift of the topological surface state close to the Fermi level with a helical spin-momentum locking due to a strong Rashba splitting of 120 *meV*. An alternative explanation to the origin of finite momentum Cooper pairing based on Meissner screening currents<sup>106</sup> is also discussed. Nevertheless, the possible role of finite momentum Cooper pairing in the creation of a Josephson diode effect has been revealed, which could lead to a better understanding and possibly a microscopic theory in the future.



# 5

---

**Helical spin-momentum locking  
and second order  $\varphi_0$  –junctions  
in the Dirac semimetal 1T-PtTe<sub>2</sub>  
probed by the  
Josephson diode effect**

## 5.1 Introduction

Josephson diode effect (JDE or  $\Delta I_c$ ) is considered to be of great interest in the creation of novel low dissipative superconducting technologies as it allows for unidirectional propagation of supercurrents. There have been many theoretical and experimental efforts on understanding the various mechanisms that give rise to it. Beyond its utility in novel superconducting technologies, JDE can also function as an effective ‘tool’ of a material’s properties in the superconducting state as it explicitly requires the breaking of inversion and time-reversal symmetries. JDE can be used to demonstrate the existence and the nature of spin-orbit coupling in a system by probing it in different directions. The appearance of a spontaneous JDE in a superconducting system can point to the existence of an intrinsic spontaneous time-reversal symmetry broken superconducting phase or an effective exchange coupling between the Cooper pairs and a magnetic layer in proximity<sup>110</sup>. In the previous chapter, it was demonstrated how the generation of finite momentum Cooper pairs (FMCP) could give rise to the JDE in a type-II Dirac semimetal NiTe<sub>2</sub>. This FMCP manifests as a relative phase shift between the two harmonics in the CPR. The presence of tiny second harmonic supercurrents is usually hard to detect and requires the use of complicated AC measurements.

In this chapter, we build further on the results from the previous chapter and show how  $\Delta I_c$  can serve as a good pointer for the second harmonic supercurrents flowing through the junction and for quantifying it. Lateral and vertical Josephson junctions were fabricated on 1T-PtTe<sub>2</sub> flakes, another van der Waals material from the same group as NiTe<sub>2</sub>. The nature of spin-momentum locking in the material is established qualitatively through measurements of the JDE. Most significantly, other extrinsic mechanisms that can give rise to a  $\Delta I_c$  in such lateral junctions such as self-field and geometrical effects, and ways to identify and minimize them are discussed in detail. The current-phase relationship (CPR) that gives rise to a  $\Delta I_c$  in the system is explored in detail and the necessity of a higher harmonic term in the CPR for the observation of a  $\Delta I_c$  is discussed. The evolution of the oscillations in  $\Delta I_c$  in the presence of magnetic flux is also studied. The nodes in  $\Delta I_c$  are found to have a period of half magnetic flux quantum as opposed to the nodes in  $I_c^+$  and  $I_c^-$  which have a single flux quantum period. This shows that  $\Delta I_c$  is strongly related to the second harmonic term in the CPR. The presence of a strong second harmonic supercurrent over large distances is quite unusual for a normal metallic system, which typically has a short mean free path. The transparencies of junctions determined from fits of  $I_c(T)$  to a diffusive behavior and

from the excess currents present in the junction point to the existence of both diffusive and ballistic channels. This observation further supports the contribution of ballistic topological states with spin-momentum locking to the supercurrents in the system together with the diffusive metallic channels.

## 5.2 Crystal Structure

Platinum Ditelluride ( $\text{PtTe}_2$ ) is a transition metal dichalcogenide material that crystallizes in the centrosymmetric space group  $P-3m1$  with a trigonal structure similar to  $\text{CdI}_2$  with  $a = b = 4.025 \text{ \AA}$  and  $c = 5.22 \text{ \AA}$ . Layers of  $\text{PtTe}_2$  are held together by a strong Van der Waals force compared to other two-dimensional Van der Waals dichalcogenides and hence not easily exfoliable down to a monolayer. Fig. 5.1(a) shows the crystal structure of  $\text{PtTe}_2$  in which each layer of platinum atoms is sandwiched between two layers of tellurium atoms. Similar to  $\text{NiTe}_2$ ,  $\text{PtTe}_2$  also structurally varies from other transition metal dichalcogenides like  $\text{MoS}_2$ ,  $\text{MoTe}_2$ ,  $\text{WTe}_2$ ,  $\text{NbSe}_2$ ,  $\text{TaS}_2$ , etc. in the fact that it is found to crystallize only in the octahedral phase as opposed to 1T (trigonal) and 2H (hexagonal) phases in the other systems. Other members of the  $\text{PtTe}_2$  family include  $\text{NiTe}_2$ ,  $\text{PdTe}_2$ ,  $\text{PtSe}_2$ ,  $\text{PdSe}_2$ , etc. Just like  $\text{NiTe}_2$ ,  $\text{PtTe}_2$  is also extremely air-stable making it useful for industrial applications. It can be synthesized layer-by-layer using chemical vapour deposition and is useful for a variety of applications including terahertz photodetection, near and mid-infrared photodetection, electrocatalysis, etc.

Just like  $\text{NiTe}_2$ , the crystal and atomic point group symmetries play an important role in determining the properties of  $\text{PtTe}_2$ .  $\text{PtTe}_2$  crystallizes in a centrosymmetric space group that is not expected to have any asymmetric spin-orbit coupling interactions like the Rashba or Dresselhaus effects. Each layer of  $\text{PtTe}_2$  consists of three sublayers with a sublayer of platinum atoms located in the center and sandwiched by two sublayers of tellurium atoms on the top and bottom. Consider a single layer of  $\text{PtTe}_2$  from the schematic shown in Fig. 5.1(b). The platinum atoms are coordinated with the tellurium atoms in an octahedral fashion. As in the case of  $\text{NiTe}_2$ , the Pt atoms have a  $D_{3d}$  point group symmetry, which includes a center of inversion as shown in Fig. 5.1(d) whereas the Te atoms have a  $C_{3v}$  point group symmetry, which lacks a center of inversion that leads to the existence of equal but opposite asymmetric spin-orbit couplings within

the unit cell. This creates a ‘local Rashba effect’ in the system which leads to the existence of a layer-dependent spin-momentum locking in the system where the spins in the top and bottom tellurium layers are expected to be oppositely spin-polarized as shown in Fig. 5.1(c) and (e).

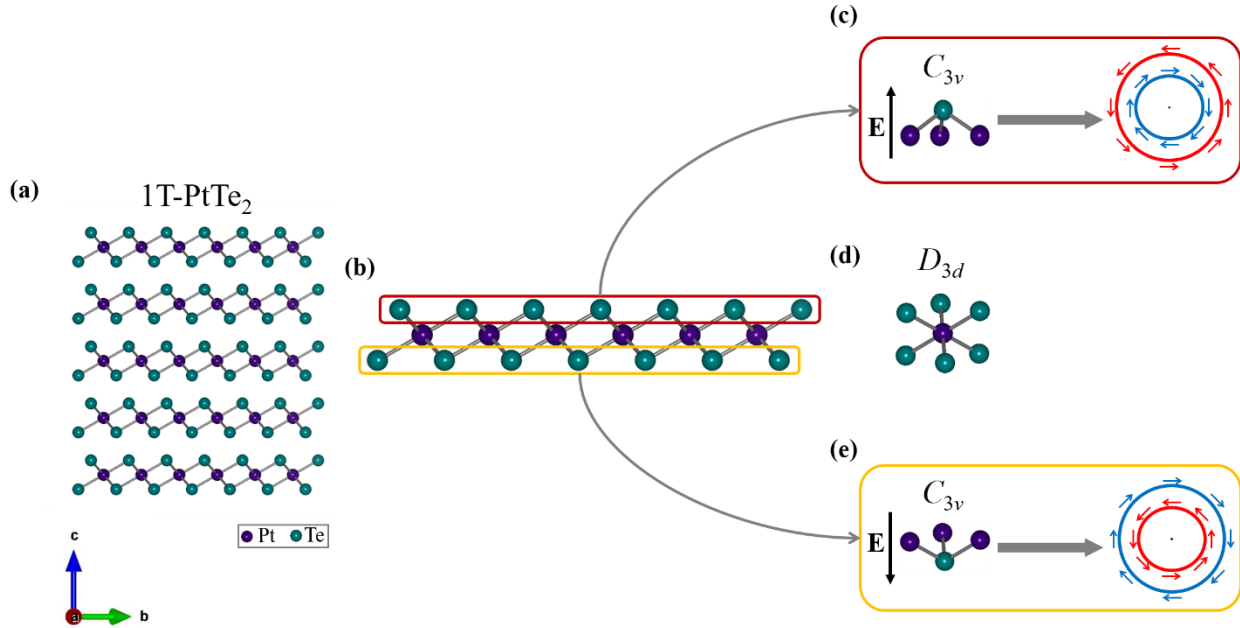


**Fig. 5.1 Locally broken inversion symmetry in PtTe<sub>2</sub>:** (a) shows the structure of five layers of platinum ditelluride with an octahedral coordination (1T-PtTe<sub>2</sub>). 1T-PtTe<sub>2</sub> is a group-X transition metal dichalcogenide composed of two-dimensional layers of PtTe<sub>2</sub> stacked on top of each other separated by a Van der Waals gap. Each monolayer of 1T-PtTe<sub>2</sub> is centrosymmetric with a AA-type stacking that makes it globally centrosymmetric. (b) A monolayer of PtTe<sub>2</sub> consists of a sheet of platinum atoms with sheets of tellurium atoms covering it on the top and bottom. (c)-(e) The platinum atoms are in an octahedral environment of tellurium atoms giving it a D<sub>3d</sub> point group symmetry with a center of inversion, while the tellurium atoms on the top and bottom layers have a trigonal pyramidal coordination to the platinum atoms that give them a C<sub>3v</sub> point group symmetry that lacks a center of inversion. This gives rise to two equal local electric dipoles with moments pointing out of the plane and away from each other. The electric fields corresponding to these dipoles give rise to a Rashba type spin-momentum locking that are equal in magnitude but have opposite helicities for the top and bottom sub-layers of tellurium atoms and hence leading to a staggered Rashba SOC in a single layer.

### 5.3 Electronic Structure

PtTe<sub>2</sub> is a type-II Dirac semimetal, which hosts Dirac fermions that violate Lorentz invariance. Naturally arising from its locally broken inversion symmetry are also several bands with strong spin-splitting and topologically protected surface states. Spin- and angle-resolved photoemission measurements (ARPES) on thin films of PtTe<sub>2</sub> of varying thickness grown by chemical vapour deposition from literature reveals that it evolves from a 2D metal to a 3D Dirac semimetal on increasing the thickness from two monolayers to six monolayers, which is evidenced by the appearance of a V-shaped conical dispersion in thicker samples.

Of great interest is the nature of spin-momentum locking in the system as revealed from the spin-dependent ARPES measurements. At the M' point in momentum space, a pocket with a gapped Dirac-like dispersion is observed with the Dirac point roughly 200 *meV* below the Fermi level. Measuring the spin contrast of the energy distribution curves along the in-plane tangential direction at four different momentum points of this pocket reveals a strong difference in the spin-resolved density of states. The lower half of the Dirac cone has an opposite spin polarization compared to the upper half of the Dirac cone, which lies at the Fermi energy, leading to a non-zero spin polarization. This non-zero spin polarization with a helical spin-momentum locking can give rise to a JDE as will be seen later in this chapter. Two other Dirac cones with similar spin dispersion are also present as shown in the schematic.

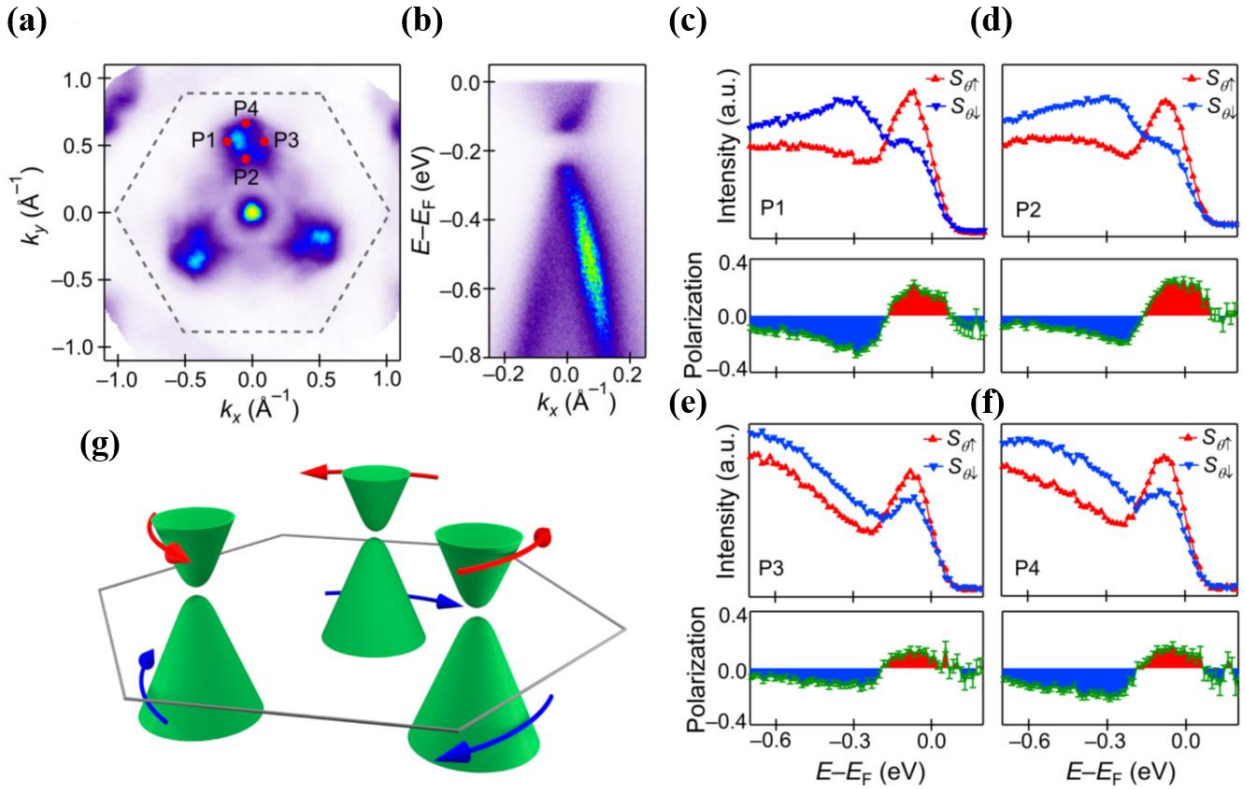


**Fig. 5.2 Spin- and angle-resolved photoemission spectroscopy of  $\text{PtTe}_2$ :** (a) Intensity maps of  $\text{PtTe}_2$  thin films measured at  $-600$  meV below the Fermi energy shows three different pockets at  $M'$  points in momentum space. (b) A gapped Dirac cone-like dispersion is found at each  $M'$  point. (c)-(f) Measurement of the spin-resolved energy dispersion curves at 4 different points labelled P1-P4 in (a) reveals the presence of a Rashba-like tangential spin polarization which differs in sign above and below the Dirac point. (g) Schematic of the gapped Dirac cones with the arrows pointing to the helicity of spin polarization. At the Fermi energy, the top Dirac cone is partially filled, leading to a net spin polarization in bulk  $\text{PtTe}_2$ .

## 5.4 Electrical Transport in $\text{PtTe}_2$ flakes

Before proceeding to study the properties of  $\text{PtTe}_2$  in the superconducting state, the electrical transport properties of  $\text{PtTe}_2$  were studied in the normal state. Few layer thick  $\text{PtTe}_2$  flakes are exfoliated from a commercially purchased single crystal of 1T- $\text{PtTe}_2$  (from HQgraphene) onto a Si substrate with  $300$  nm  $\text{SiO}_2$  coating as described in detail in section 3.2.1.

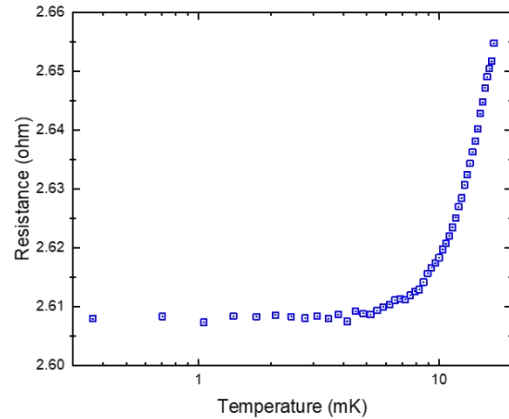


Thin flakes are identified with the help of an optical microscope and an atomic force microscope and a Hall bar device with Ti (2 nm) / Au (40 nm) contacts was fabricated on a 30 nm thick PtTe<sub>2</sub> flake using a similar method as described elsewhere in the thesis to measure its electrical properties in the normal state as shown in Fig. 5.3. The Hall bar was fabricated with help from Yufeng Wu. Electrical measurements are performed using a current source (Keithley 6221) with a constant current bias of 10  $\mu\text{A}$  and the voltage measured using a nanovoltmeter (Keithley 2182A). It is found that PtTe<sub>2</sub> remains metallic down to 20 mK temperature and does not turn superconducting. It can also be seen from the positive magnetoresistance and linear Hall effect that PtTe<sub>2</sub> is non-magnetic down to the base temperature and hence time-reversal symmetric. The mobility of the flake as estimated by fitting the obtained magnetoresistance, using the formula  $MR = a(1 + \mu^2 B^2)$  is  $\mu_{MR} = 835 \text{ cm}^2 \text{V}^{-1} \text{s}^{-1}$  and the carrier concentration calculated from the Hall resistance is  $n = 1.424 \times 10^{28} \text{ m}^{-3}$  indicating that the material is highly metallic.

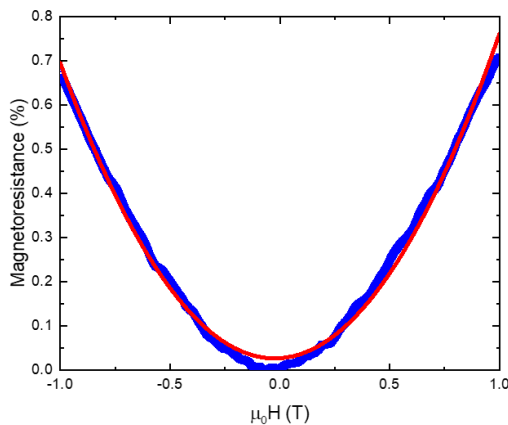
(a)



(b)



(c)



(d)

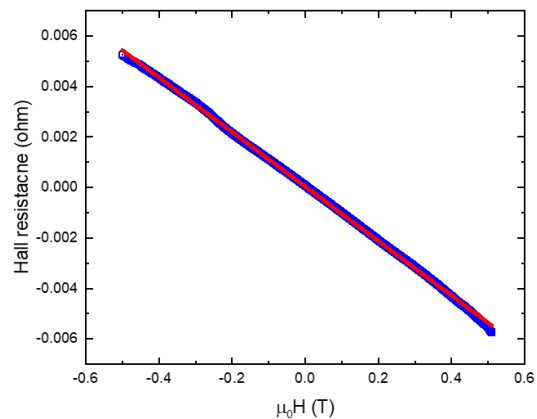


**Fig. 5.3 Electrical transport in PtTe<sub>2</sub> Hall bars:** (a) Optical image of a Hall bar fabricated on a 40 nm thick PtTe<sub>2</sub> flake. (b) Electrical resistance of PtTe<sub>2</sub> as a function of temperature measured from the longitudinal voltage in the Hall bar, in the presence of a constant current bias. The resistance saturates at lower temperatures but never drops to zero. (c) The magnetoresistance of the flake measured with a magnetic field perpendicular to the plane of the flake. PtTe<sub>2</sub> displays a parabolic positive magnetoresistance as in a non-magnetic material. (d) Hall resistance of the PtTe<sub>2</sub> flake shows linear behavior with negative slope indicating hole-type carriers with a large carrier density and once again confirming the absence of any anomalous Hall behavior due to time-reversal symmetry breaking in the system.

## 5.5 Fabrication of Josephson Junctions with PtTe<sub>2</sub> flakes

Josephson junctions in PtTe<sub>2</sub> flakes are fabricated both in lateral and vertical geometries to study the JDE along different directions and verify the nature of spin-orbit coupling in the system.

### 5.5.1 Lateral junctions of PtTe<sub>2</sub> flakes

Lateral junctions of PtTe<sub>2</sub> are fabricated on a 17.5 nm thick flake of PtTe<sub>2</sub> (as shown in Fig. 5.4(a)) exfoliated on a 300 nm SiO<sub>2</sub> coated Silicon substrate using a Nitto tape and standard physical exfoliation technique as described in other parts of the thesis. The thickness of the flake is measured using AFM (as shown in Fig. 5.4(b)) and the Josephson junctions of varying separations (L1-L4) were fabricated on this flake using electron-beam lithography. The substrate containing the flake was spin-coated at 4000 rpm with a positive resist AR-P 669.04 and annealed at 150 °C for 60 s followed by the same procedure for AR-P 679.03 (purchased from Allresist GmbH). The substrate was then exposed to the electron beam at 10 kV energy and developed using AR 600-56 for 90 s. After developing the substrate, it was gently ion milled for 60 s at 100 kV to remove residual resist on the top surface, superconducting electrodes Ti (2nm) / Nb (40nm) / Au (4nm) substrate was sputtered on the substrate. The lift-off was performed by immersing the substrate in acetone overnight and removing the underlying resist. An SEM image of the fabricated devices along with the separations between the different superconducting

electrodes is shown in Fig. 5.4(c) and an optical image is shown in Fig. 5.4(d). The junction L2 is shorted by another PtTe<sub>2</sub> flake that lies in parallel and couldn't be used for measurements.

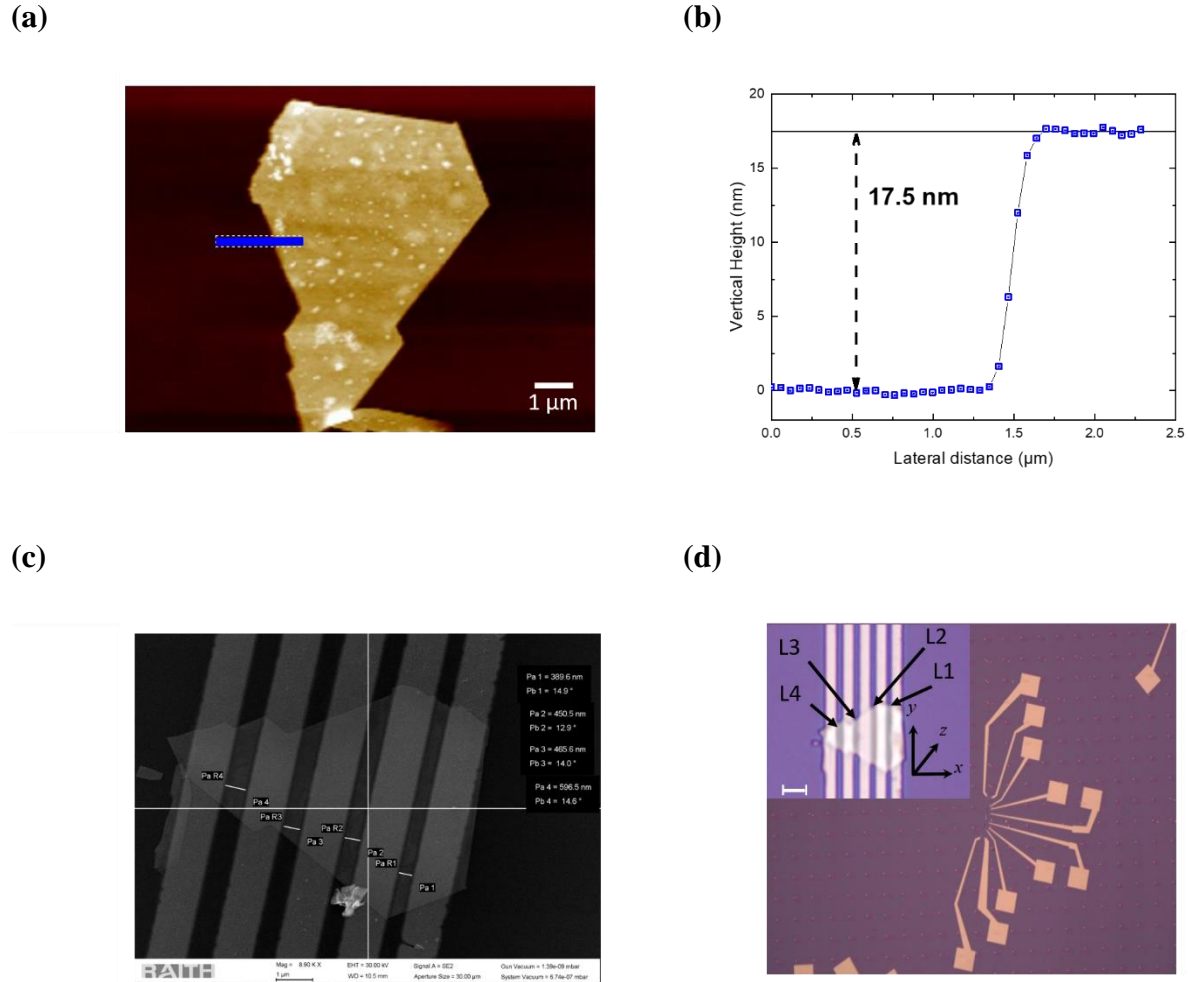


**Fig. 5.4 Lateral PtTe<sub>2</sub> Josephson junctions:** (a) Image of a 17.5 nm thick PtTe<sub>2</sub> flake on a 300 nm SiO<sub>2</sub> coated Si substrate, measured using atomic force microscopy (AFM). Scale bar corresponds to 1 μm. (b) The thickness of the flake measured from the region marked by blue in (a). (c) Scanning electron microscopy (SEM) image of the PtTe<sub>2</sub> flake after fabrication of the lateral Josephson junctions with the superconducting electrodes Ti (2 nm) / Nb (40 nm) / Au (4 nm) on top and the varying separations measured. (d) Optical image of the lateral Josephson junction device fabricated showing the various electrodes. Inset shows a close-up of the junctions labelled from L1-L4 and the coordinate axes used for the measurements. The scale bar corresponds to 1 μm.

### 5.5.2 Vertical junction of PtTe<sub>2</sub>

A vertical junction (V1) of PtTe<sub>2</sub> is fabricated using an exfoliated PtTe<sub>2</sub> flake of around 60 nm thickness and NbSe<sub>2</sub> flakes acting as the superconducting electrodes on the top and bottom using a dry transfer technique with a polycarbonate (PC) film supported by a polydimethylsiloxane (PDMS) stamp as described in the literature<sup>111</sup>, to look for a Josephson diode effect ( $\Delta I_c$ ) by passing supercurrents along the c-axis. The vertical heterostructure formed is then dropped on pre-sputtered gold electrodes at 200 °C. After dissolving the polymer in chloroform, the heterostructure is annealed in vacuum at 300 °C for an hour to improve the electrical contact to the flakes. The optical image of the junction formed is shown in Fig. 5.5. The vertical heterostructure was fabricated with help from Dr. Jae-Keun Kim.

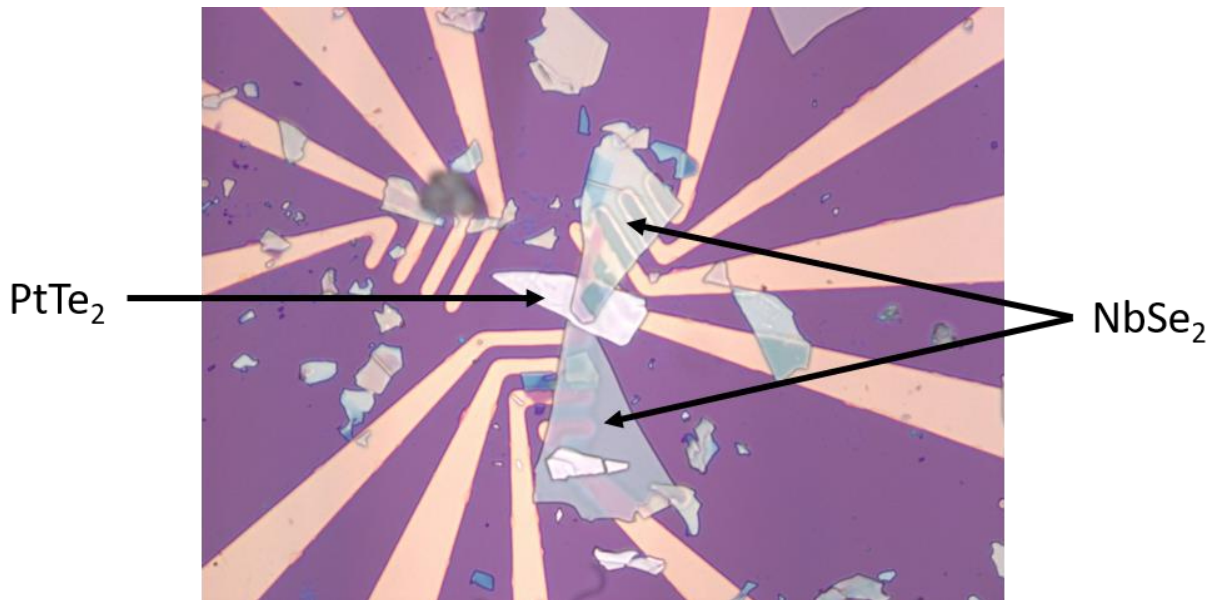


**Fig. 5.5 Vertical PtTe<sub>2</sub> Josephson junctions:** Vertical heterostructure consisting of NbSe<sub>2</sub>/PtTe<sub>2</sub>/NbSe<sub>2</sub> sandwich on top of gold electrodes used to probe supercurrent transport in the vertical direction, along the c-axis of PtTe<sub>2</sub>.

## 5.6 Josephson diode effect in PtTe<sub>2</sub> junctions

### 5.6.1 Basic characterization of the lateral PtTe<sub>2</sub> Josephson junction L1

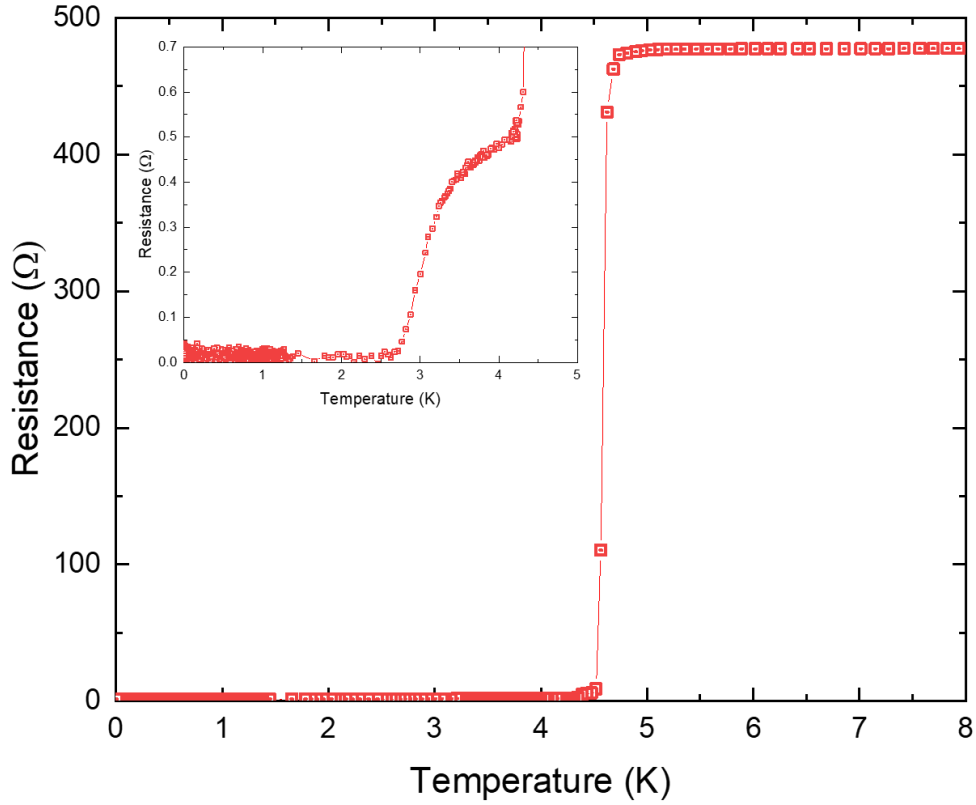
Of the four lateral junctions fabricated L1-L4 (Fig. 5.4(d)), the junction with the shortest separation between the niobium electrodes (L1) is around 390 nm, and the device is roughly 5 – 6 μm in width with tapering edges. Most of the results and analysis presented in the following sections focus on this device (referred to as L1 hereafter). The direction of current bias in these devices is fixed along the  $x$ -axis as shown in the inset of Fig. 5.4(d). The resistance of this junction is measured with a small alternating current of 350 nA at 7.919 Hz as the junction is cooled down in zero magnetic field (Fig. 5.6(a)). A drop in resistance is observed around 4.5 K corresponding to the superconducting transition of the niobium electrodes and another drop in resistance to zero ohm at about 2.7 K (Fig. 5.6(a) inset), below which the junction becomes fully superconducting ( $T_j$ ).

The sample is allowed to reach the base temperature of the cryostat (20 mK) and thermalize before the current voltage characteristics of L1 at zero magnetic field are studied with a DC bias (Keithley 6221) and a nanovoltmeter (Keithley 2182A). The critical currents on sweeping the current from zero bias in the positive ( $I_c^+$ ) and negative ( $I_c^-$ ) directions are obtained at zero magnetic field (Fig. 5.6(b)) and a negligible difference in their magnitude ( $\Delta I_c = I_c^+ - |I_c^-|$ ) or JDE is observed. The presence of retrapping currents in the junction different from the critical currents indicate that it is underdamped according to the RCSJ model. The positive and negative retrapping currents are also equal in magnitude.

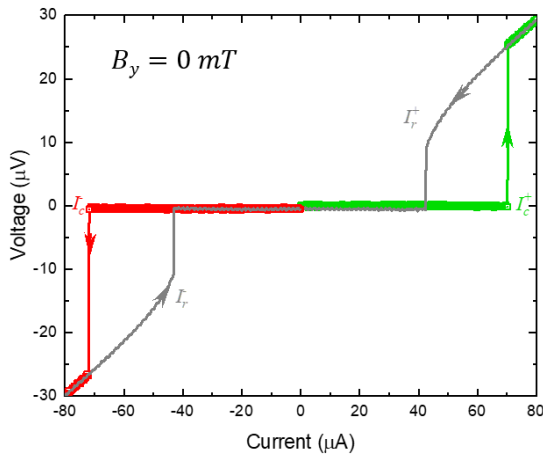
As the in-plane magnetic field perpendicular to the direction of current ( $B_y$ ) is increased and the current-voltage characteristics are measured again, a non-uniform suppression of  $I_c^+$  and  $I_c^-$  and hence the appearance of a non-zero  $\Delta I_c$  is observed just like in the case of NiTe<sub>2</sub>. The current-voltage characteristic of L1 at  $B_y = 8$  mT is shown in Fig. 5.6(c).  $I_c^+$  is around 56 μA whereas  $|I_c^-|$  is around 34 μA. By choosing a magnitude of current between  $I_c^+$  and  $|I_c^-|$ , one can obtain non-reciprocal behavior, in which the junction is superconducting along one direction and resistive along the opposite direction. The non-reciprocal behavior with 37 μA current along both

directions at  $B_y = 8 \text{ mT}$  is shown in Fig. 5.6(d). The switching characteristic of the junction measured over an hour appears stable and robust.

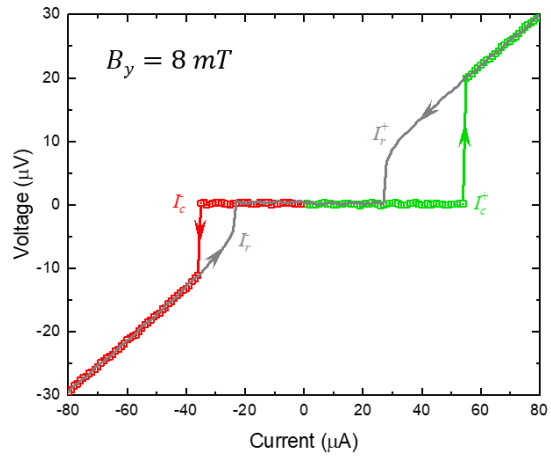
(a)



(b)



(c)



(d)

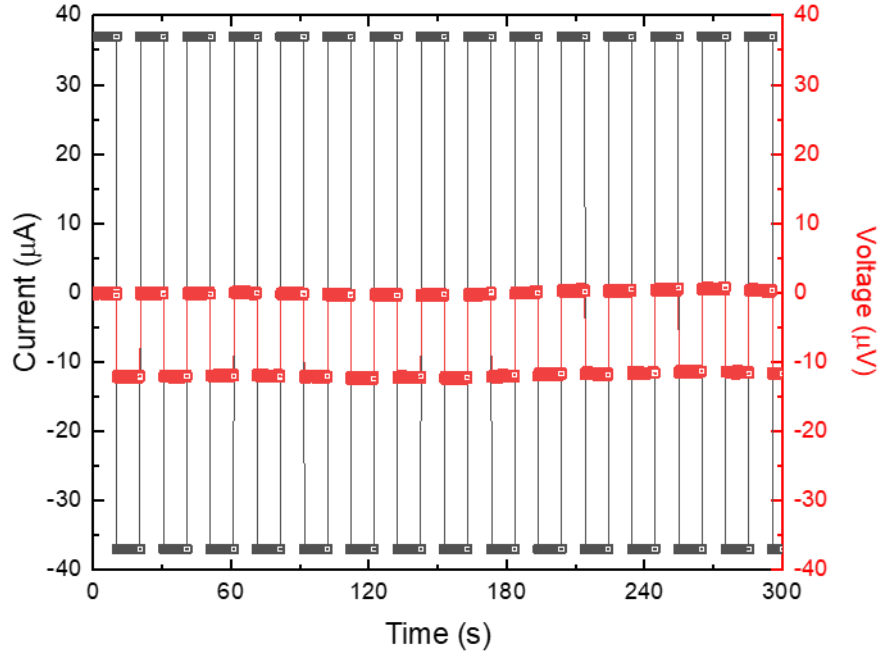


**Fig. 5.6 Non-reciprocal critical currents in  $\text{PtTe}_2$  Josephson junctions:** (a) Resistance-temperature curve of junction L1 measured while cooling down in zero field. Two transitions at around 4.5 K and 2.7 K (inset) corresponding to the superconductivity of niobium ( $T_c$ ) and the junction ( $T_j$ ) are observed. (b) Current-Voltage characteristics of L1 measured in the absence of any external magnetic field after cooling down to 20 mK in zero magnetic field. The critical currents in the positive ( $I_c^+$ ) and negative ( $I_c^-$ ) directions are the same within the limit of error, leading to  $\Delta I_c = 0$ . The retrapping currents in both directions ( $I_r^+$  and  $I_r^-$ ) are also equal. (c) Current-Voltage characteristics of L1 measured in the presence of an 8 mT magnetic field applied along y-axis ( $B_y$ ). In addition to a suppression of the energy gap of the junction, we also observe that there is a significant difference in  $I_c^+$  and  $I_c^-$  leading to a  $\Delta I_c$ . (d) The non-reciprocal behavior of supercurrents or the diode effect measured under 8 mT magnetic field with a 37  $\mu\text{A}$  current shows that the device is superconducting along one direction but resistive in the opposite direction. The switching was measured over a period of one hour and showed robust behavior.

## 5.6.2 Self-consistent simulations of critical currents in the junction

Throughout this chapter, there are several simulations of the critical currents evolution with magnetic field presented to support the experimental observations. This is done by considering the evolution of phase along different directions in the presence of a magnetic field and solving the resulting differential equations self-consistently. All the simulations presented in this chapter were done by Dr. Mostafa Tanhayi Ahari from Prof. Matthew Gilbert's group at University of Illinois Urbana Champaign (UIUC). More details of the simulation can be found in the appendix.

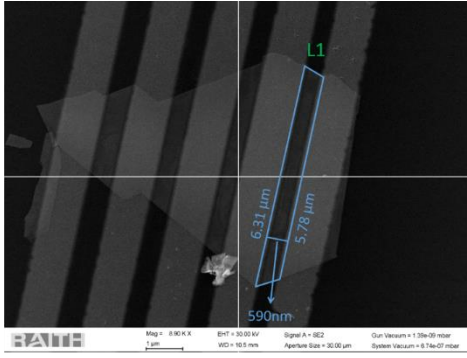
## 5.6.3 Josephson diode effect due to extrinsic mechanisms

### 5.6.3.1 Absence of geometric shape inversion asymmetry in PtTe<sub>2</sub> junctions

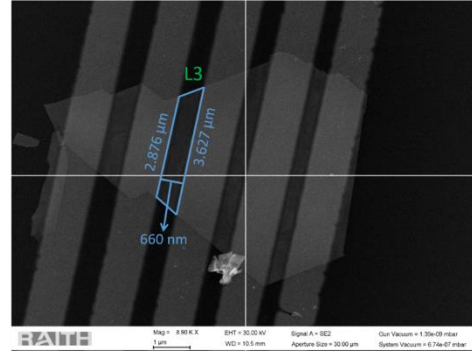
As it can be observed from Fig. 5.4(c), the shape of the PtTe<sub>2</sub> flake is not exactly rectangular. It has tapering edges, which gives the junctions the shape of a trapezoid that naturally breaks the geometric inversion symmetry of the junctions and can be considered as the source for the observed asymmetry in critical currents in the presence of a magnetic field. To eliminate this possibility a simple check is performed, wherein the critical currents  $I_c^+$  and  $I_c^-$  of two junctions (L1 and L3) whose edges taper along the opposite directions are measured in the presence of a magnetic field along the same direction. In the case that  $\Delta I_c$  arises from the geometric inversion asymmetry, this measurement would give opposite signs of  $\Delta I_c$  for the two junctions, as their edges taper in opposite directions. In our measurements, we observe that the  $\Delta I_c$  for both L1 and L3 is positive when the magnetic field direction is fixed along  $y$  direction and the current direction is fixed along  $-x$  direction, suggesting that the geometric inversion asymmetry has a minimal role to play in the creation of the observed critical current asymmetries.



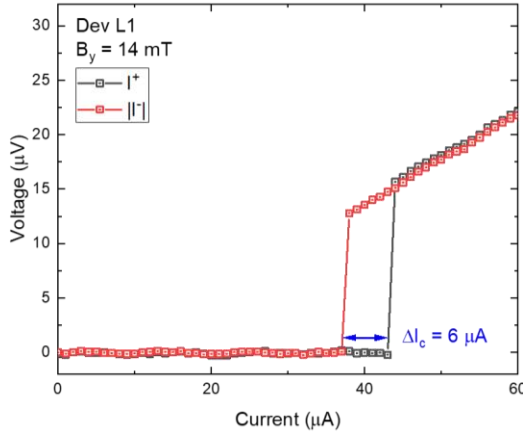
(a)



(b)



(c)



(d)

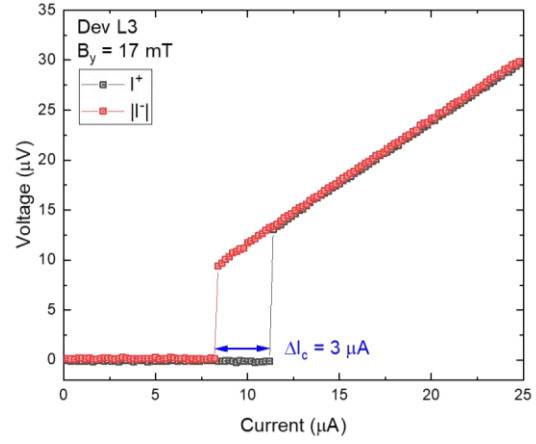


**Fig. 5.7 Josephson diode effect in  $PtTe_2$  junctions of different geometry:** (a) and (b) Scanning electron microscope (SEM) image of lateral  $PtTe_2$  Josephson junctions L1 and L3 with an outline of their trapezoidal shapes and a measurement of their dimensions. (c) and (d)  $\Delta I_c$  for L1 and L3 measured for a positive  $B_y$  with the same direction of current bias reveals that both L1 and L3 have the same sign of  $\Delta I_c$  under these conditions indicating the absence of strong geometric asymmetry effects.

### 5.6.3.2 Self-field induced extrinsic JDE in wide $PtTe_2$ junctions

In a Josephson junction, when the junction width ( $w$ ) or the length ( $l$ ) is shorter in comparison with the Josephson penetration depth ( $\lambda_J$ ), which is a characteristic length scale in the junction over which magnetic flux variation can take place, the magnetic field due to the current

flow across the junction can be neglected. Such a junction is said to be in the ‘short junction limit’. In contrast to the NiTe<sub>2</sub> junctions discussed in the last chapter, some of the PtTe<sub>2</sub> junctions have widths ( $w$ ) that are larger in comparison to  $\lambda_J$ . Such Josephson junctions are said to be in the wide junction limit ( $w > \lambda_J$ ). In L1, the junction channel is between 5 – 6  $\mu\text{m}$  wide while the estimated  $\lambda_J$  for the junction is  $\lambda_J \approx 3 \mu\text{m}$  ( $\alpha \approx 2$ ) for  $B_y \sim 0$ , which makes L1 lie strongly in the wide junction limit. In such limit, the current bias configuration can play a significant role in the nature of current distribution across the junction. In a lateral junction such as L1, when the current source is connected to leads on the same side of the device and the voltage probes are connected to the leads on the other side (as in Fig. 5.8(a)), this can lead to a highly non-uniform current distribution in the junction. This consequently creates local inhomogeneous magnetic fields that can break the time reversal symmetry of the junction. This is known in the literature as ‘self-field effect (SFE)’<sup>40,112,113</sup> and is dictated purely by the geometry of the junction and the magnitude of the critical current.

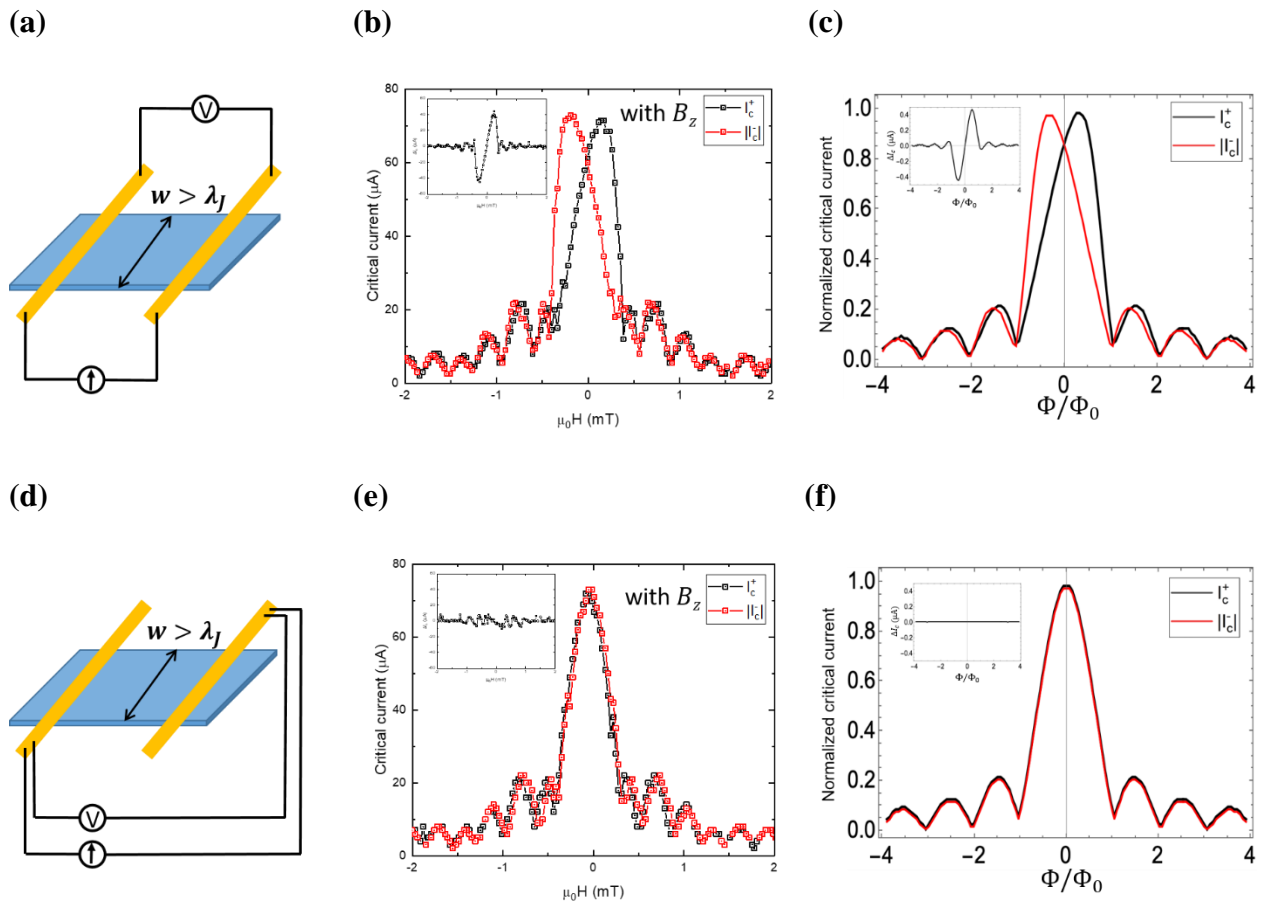


**Fig. 5.8 Self-field effects in wide PtTe<sub>2</sub> junctions:** (a) Measurement schematic for a wide lateral Josephson junction in which self-field effects were observed in the Fraunhofer pattern. (b) Skewed Fraunhofer pattern with large  $\Delta I_c$  (inset) measured with the current leads on the same side. This indicates the current bias across the junction is non-uniform. (c) Simulated Fraunhofer patterns for same-side biasing with  $w = 2\lambda_j$ . The self-field effects gives rise to skewed Fraunhofer patterns as in experiments. The calculated  $\Delta I_c$  are shown in the inset. (d) Measurement schematic in which the current bias is sourced in the “criss-crossed” configuration, wherein the current leads are located on opposite sides of the superconducting electrodes. (e) The Fraunhofer pattern for  $I_c^+$  and  $|I_c^-|$  measured in the criss-cross configuration is symmetric with respect to the magnetic field with negligible  $\Delta I_c$  (inset) indicating the near uniform flow of supercurrents. (f) Simulated Fraunhofer patterns for criss-crossed biasing with  $w = 2\lambda_j$ . In this case, self-field effects are symmetric and lead to symmetric Fraunhofer patterns where  $\Delta I_c = 0$  (inset). In (c) and (f), we plot the normalized critical currents as a function of normalized magnetic flux  $\Phi/\Phi_0$ .

The critical currents  $I_c^+$  and  $|I_c^-|$  of junction L1 with magnetic field applied along  $B_z$  and current applied in the same-side configuration is shown in Fig. 5.8(b). It can be seen that  $I_c^+$  and  $|I_c^-|$  in the Fraunhofer interference pattern are clearly skewed in opposite directions leading to a significant  $\Delta I_c$ . Fig. 5.8(c) shows the simulated Fraunhofer pattern considering the boundary condition  $(a_1, a_2) = (0, 1)$  in equations (A4) and (A5) in the appendix, which agrees well with the experimentally observed behavior of the junction. The insets of Fig. 5.8(b) and Fig. 5.8(c) show  $\Delta I_c$  from the measurements and the simulations, respectively.  $\Delta I_c$  in both cases is quite large, reaching a maximum value of around  $40 \mu A$  when the total critical current is around  $73 \mu A$  leading to an efficiency  $\left(\eta = \frac{\Delta I_c}{I_c^+ + I_c^-}\right)$  of about 55 %. This  $\Delta I_c$  with multiple oscillations strongly mimics that observed in the case of NiTe<sub>2</sub> created by finite momentum Cooper pairing as shown in Fig. 4.12(a). If not analyzed with caution, this observation would lead to the possible erroneous conclusion that there is a Zeeman-type out-of-plane spin-momentum locking in the system that leads to a large  $\Delta I_c$  with a magnetic field along the z-axis similar to Ising superconductors such as 2H-NbSe<sub>2</sub><sup>107</sup>. However, this is not true in this case and extra careful analysis is required in the long or wide junction limit. It can be clearly shown from the simulations that the observed  $\Delta I_c$  is from

self-field effects present in the junction. It is also to be noted that even though the SFE evidently breaks time-reversal symmetry upon application of a current, there is no spontaneous time-reversal symmetry breaking that exists in the absence of a current and the inhomogeneous magnetic fields induced by the currents in positive and negative directions are the same in magnitude. Hence, there is no  $\Delta I_c$  at zero magnetic field in the presence of SFE-inducing currents.

Another possible measurement configuration in which the critical currents across the junction can be measured is the ‘criss-crossed’ configuration, in which the current source is connected to leads on opposite ends of the device and the voltage is measured across the same leads, as shown in Fig. 5.8(d). Performing measurements in the ‘criss-crossed’ configuration can help reduce the SFE, help improve the current uniformity across the junction and nullify the extraneous  $\Delta I_c$  arising from the SFE as seen from both the experimental and simulation results. The Fraunhofer pattern measured in the criss-crossed configuration is shown in Fig. 5.8(e). The measured  $I_c^+$  and  $|I_c^-|$  fall almost on top of each other without any skewing of the curves. The Fraunhofer pattern arising from a criss-crossed configuration of the current bias is simulated using the boundary condition in  $(a_1, a_2) = (-1/2, 1/2)$  in equations (A4) and (A5) in the appendix and is shown in Fig. 5.8(f). The insets of Fig. 5.8(e) and Fig. 5.8(f) show  $\Delta I_c$  from the measurements and the simulations in the criss-crossed configuration, respectively. In this case, the measured  $\Delta I_c$  is strongly suppressed and almost non-existent compared to the previous case. All measurements henceforth presented from the lateral junctions in this chapter were done in the criss-crossed configuration to avoid SFE.

#### 5.6.4 Helical spin-momentum locking in PtTe<sub>2</sub> junctions

As we have seen in a previous section on electronic structure of PtTe<sub>2</sub> (Section 5.3), PtTe<sub>2</sub> hosts a Dirac cone at M’ point with the Dirac point lying around 200 meV below the Fermi level and this pocket has a non-zero spin-polarization tangential to the momentum at the Fermi level which directs to the presence of a Rashba or helical spin-momentum locking on this surface. This Rashba spin-momentum locking can give rise to FMCP and a  $\Delta I_c$  in the presence of an in-plane magnetic field perpendicular to the current ( $B_y$ ) just as in the case of NiTe<sub>2</sub>. In order to establish

the presence of Rashba spin-momentum locking in PtTe<sub>2</sub>,  $\Delta I_c$  is measured in L1 as a function of the magnetic field magnitude, angle and temperature.

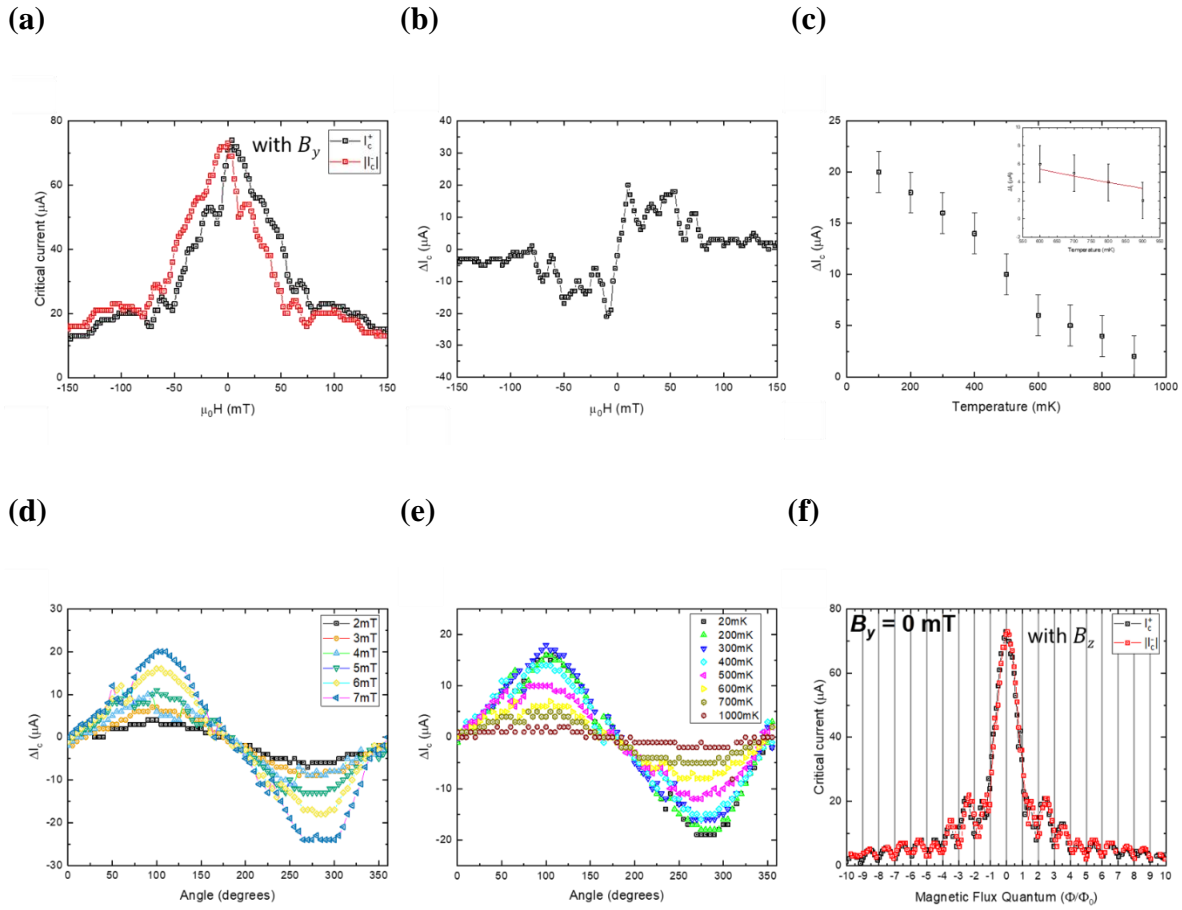


**Fig. 5.9 Analysis of  $\Delta I_c$  with magnetic field magnitude, angle and temperature for junction L1:** (a)  $I_c^+$  and  $I_c^-$  measured as a function of the magnetic field  $B_y$  swept from 150 mT to  $-150$  mT at 20 mK temperature. (b)  $\Delta I_c$  measured by sweeping  $B_y$  from 150 mT to  $-150$  mT, shows that it is maximum around 10 mT. (c) The maximum value of  $\Delta I_c$  plotted as a function of temperature. Inset shows that it follows a quadratic  $(T - T_j)^2$  dependence at higher temperatures, as expected for a finite momentum Cooper pairing scenario<sup>1</sup>. (d) The angular dependence of  $\Delta I_c$  at various magnetic fields measured at 20 mK shows that  $\Delta I_c$  is maximized when the magnetic field is perpendicular to the direction of current and zero when the magnetic field is parallel to the direction of current indicating a helical spin-momentum locking in the system. (e) The angular dependence of  $\Delta I_c$  with the magnetic field  $B_y = 8$  mT measured at various temperatures. (f)

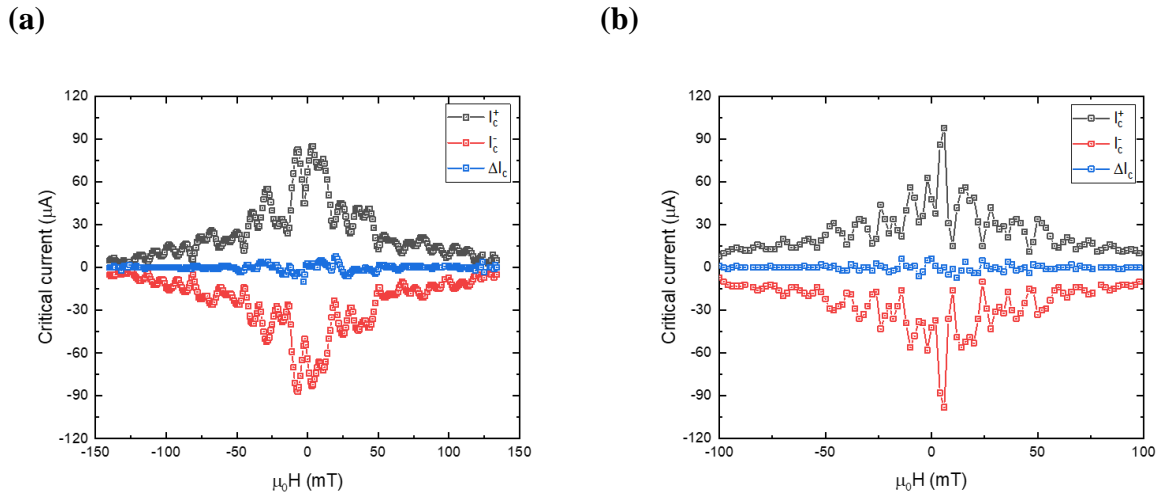
*Fraunhofer oscillations in L1 with a  $B_z$  magnetic field and zero  $B_y$  measured in a criss-crossed measurement geometry show no JDE.*

Fig. 5.9(a) shows  $I_c^+$  and  $I_c^-$  as a function of  $B_y$ , with  $B_y$  being swept from 150 to  $-150$  mT and the corresponding  $\Delta I_c$  is shown in Fig. 5.9(b). It can be seen that  $\Delta I_c$  increases linearly with  $B_y$  at low fields and then starts to decrease non-monotonously. This non-monotonous decrease can be attributed to the effect of finite thickness of the sample due to which  $B_y$  also provides an additional magnetic flux on the sample and creates a phase difference across the superconducting electrodes as will be discussed in a later section. This effect can be corrected for and the actual  $\Delta I_c$  at higher values of  $B_y$  can be obtained from the Fraunhofer pattern as shown in a later section. In this section, in order to minimize finite thickness flux effects, we stick to low  $B_y$  values in our measurements. It can also be seen that  $\Delta I_c$  has a finite shift from zero at high magnetic fields, in the positive direction at negative magnetic fields and negative direction at positive magnetic fields. This can be shown to arise from the geometry of the junction.

The critical currents  $I_c^+$  and  $I_c^-$  of L1 at 20 mK are then measured as a function of the in-plane magnetic field angle (Fig. 5.9(d)), by controlling the magnitudes of  $B_x$  and  $B_y$  on the 2D superconducting magnetic coils. 0 degrees corresponds to the  $x$ -axis, along which the current flows and 90 degrees corresponds to the  $y$ -axis, perpendicular to the direction of current (Refer Fig. 5.4(d)).  $\Delta I_c$  is measured for the magnetic field vector magnitude ranging from 2 – 7 mT.  $\Delta I_c$  is maximized when the magnetic field is applied perpendicular to the direction of current ( $B_y$ ) and vanishes when the magnetic field is along the direction of current ( $B_x$ ) and is found to increase with the magnitude of the magnetic field which indicates that there is possibly a tangential spin-momentum locking scenario. The angular dependence of  $\Delta I_c$  is measured at various temperatures from 20 – 1000 mK is shown in Fig. 5.9(e).  $\Delta I_c$  is found to decrease with increasing temperature. It decays with a quadratic  $(T - T_j)^2$  dependence close to  $T_j$ , as shown in Fig. 5.9(c), and as expected for a finite momentum Cooper pairing scenario<sup>1,114</sup>. Though the error in the data points are large, a better fit can be obtained in the  $\Delta I_c$  vs.  $T$  obtained from the Fraunhofer pattern as will

be discussed later. These results put together indicate the existence of a two-dimensional helical spin-momentum locking in PtTe<sub>2</sub>.

Furthermore, on measuring  $\Delta I_c$  in the vertical junction V1 (shown in Fig. 5.5) by passing current in the vertical direction, along the  $c$ -axis of the crystal, no apparent  $\Delta I_c$  with an in-plane magnetic field along perpendicular directions is found, as shown in Fig. 5.10(a) and (b). This observation is opposed to that in vertical junctions of T<sub>d</sub>-WTe<sub>2</sub>, fabricated using a similar technique where a clear  $\Delta I_c$  is observed when the magnetic field is applied perpendicular to the  $b$ -axis of the crystal<sup>115</sup>. No  $\Delta I_c$  was observed in our case, even though the Josephson energy and the magnitude of the maximum critical current are quite similar in both the L1 and V1 junctions. This demonstrates that there is no spin-momentum locking in the bulk of the sample or any other mechanism that can create FMCP and the observation of a  $\Delta I_c$  in the presence of a magnetic field is confined to current flow only along the two-dimensional  $ab$  plane of the sample.



**Fig. 5.10 Absence of Josephson diode effect in a vertical junction of PtTe<sub>2</sub>:** (a) and (b) Critical currents  $I_c^+$  (black) and  $I_c^-$  (red) of the vertical junction measured as a function of the in-plane magnetic field with magnetic field applied along two perpendicular directions show that  $\Delta I_c$  (blue) is almost zero and has no apparent trend.

## 5.7 Tunable Current-Phase relationship in PtTe<sub>2</sub> Josephson junctions

### 5.7.1 Current-Phase Relationship Model for PtTe<sub>2</sub> junctions

The appearance of  $\Delta I_c$  in PtTe<sub>2</sub> can be understood using a simple model starting from a general current-phase relationship (CPR) written as a Fourier series of sine functions, which includes higher harmonics and additional phase shifts  $\varphi_n$  that may be present in the system when time-reversal symmetry is broken.

$$I(\varphi) = \sum_{n=1}^{\infty} I_n \sin(n\varphi + \varphi_n) \quad (5.1)$$

Expanding this CPR up to the second order gives us:

$$I(\varphi) = I_1 \sin(\varphi + \varphi_1) + I_2 \sin(2\varphi + \varphi_2) \quad (5.2)$$

This is a very generic CPR from which certain well-known special cases can be derived. For example, having  $\varphi_1 = \varphi_2 = 0$ , gives a CPR that contains only the first and second harmonic terms without any additional phases corresponding to typical  $\varphi$ -junctions<sup>116,117</sup> with a skewed current-phase relationship and furthermore setting  $I_2 = 0$  in equation (5.2) gives us anomalous Josephson junctions or  $\varphi_0$ -junctions with a sinusoidal current-phase relationship shifted from zero by a phase  $\varphi_1$ . Such CPRs have been observed typically in ferromagnetic Josephson junctions and systems with high spin-orbit coupling<sup>118-123</sup>. Now, without any loss of generality  $\varphi$  may be replaced with  $(\varphi - \varphi_1)$  and the CPR can be rewritten as:

$$I(\varphi) = I_1 \sin \varphi + I_2 \sin(2\varphi + \delta) \quad (5.3)$$

where  $\delta = \varphi_2 - 2\varphi_1$  is the relative phase between the first and second harmonic terms. This CPR is quite different from typical  $\varphi$  – and  $\varphi_0$  – junction CPRs<sup>116-123</sup> and Josephson junction with a CPR as that in equation (5.3) is dubbed as a “second order  $\varphi_0$ -junction”. This CPR is identical to that derived from the Ginzburg-Landau formalism<sup>1</sup> in the previous chapter, in which  $\delta$  corresponds to the phase shift induced by a finite momentum Cooper pairing in the system. This phase  $\delta$ , can be controlled by an in-plane Zeeman field perpendicular to the direction of current ( $\delta \propto B_y$ ). It is to be noted that in addition to NiTe<sub>2</sub><sup>1</sup>, similar CPRs have been used to explain the presence of a  $\Delta I_c$  in InAs-based superconducting junctions<sup>124,125</sup> and InSb nanowire junctions<sup>126</sup>.



$\Delta I_c$  can be determined by looking at  $I_c^+$  and  $I_c^-$  from the CPR in equation (5.3). It may be seen easily that the first harmonic term varies as  $\sin \varphi$  which is an odd function and hence would not have any direct contribution to  $\Delta I_c$  in the absence of  $\delta$ . For non-sinusoidal CPRs such as that in equation (5.3), critical currents may not always occur at  $\varphi = \pm \frac{\pi}{2}$  and might need to be solved numerically to get the exact values of  $I_c^+$  and  $I_c^-$  for different values of  $\delta$ . To this effect, numerical solutions of the critical current are obtained, which can be achieved by defining an envelope function  $f(\Phi, \delta) = I_1 + \min_{\varphi} \left[ \left( I_1 + 2I_2 \cos(\varphi + \delta) \cos\left(\frac{\pi\Phi}{\Phi_0}\right) \right) \sin \varphi \right]$ . In this case,  $\Delta I_c$  is given by

$$\Delta I_c = f(\Phi, \delta) \frac{\sin(\pi\Phi/\Phi_0)}{\pi\Phi/\Phi_0} \quad (5.4)$$

We note that the envelope function  $f(\Phi_n, \delta)$  vanishes at  $\Phi_n = \left(n + \frac{1}{2}\right) \Phi_0$  for arbitrary values of  $\delta$  and  $I_2$ . Moreover, for  $\frac{I_2}{I_1} \ll 1$ , we obtain the magnitude of  $\Delta I_c$  as

$$\Delta I_c = -2I_2(B_y) \sin \delta \frac{\sin\left(\frac{2\pi\Phi}{\Phi_0}\right)}{\left(\frac{2\pi\Phi}{\Phi_0}\right)} \quad (5.5)$$

where  $I_i(B_y) = I_i(0) \left(1 - \frac{B^2}{B_c^2}\right)^i$  accounts for the suppression in the critical current components due to orbital effects from  $B_y$ . From equations (5.3) and (5.5), we can infer three important conclusions on the CPR and  $\Delta I_c$ .

1. Firstly, we find that the existence of a second harmonic term ( $I_2 \neq 0$ ) and  $\delta \neq n\pi, n \in \mathbb{Z}$  is necessary for the existence of a non-zero  $\Delta I_c$ . So, the presence of a  $\Delta I_c$  acts as an indicator for the existence of a second harmonic term in the current-phase relationship while the converse need not be true.
2. Secondly, the magnitude of  $\Delta I_c$  is modulated by  $\sin \delta$ , which implies that  $\Delta I_c$  reaches its maximum magnitude when  $\delta = \pm \frac{\pi}{2}$ . In a system with FMCP,  $\delta$  can be tuned precisely with an in-plane magnetic field ( $B_y$ ) as a handle. The value of  $B_y$  at which  $\Delta I_c$  reaches its maximum (minimum) value  $\Delta I_c^{max}$  ( $\Delta I_c^{min}$ ) corresponds to  $\delta = \frac{\pi}{2}$  ( $-\frac{\pi}{2}$ ). Using the value of  $\Delta I_c^{max}$  and

equation (5.5), it can be seen that the actual magnitude of second harmonic supercurrents flowing through the junction in the limit of  $\Phi$  going to zero is  $I_2(B_y) = -\frac{\Delta I_c^{max}}{2}$ .

3. Thirdly, the unprecedented control over  $\delta$  leads to the interesting possibility of tuning the relative phase and directionality between first and second harmonic components. For example, substituting  $\delta = \pi$  in equation (3) gives:

$$I(\varphi)_{\delta=\pi} = I_1 \sin \varphi + I_2 \sin (2\varphi + \pi) = I_1 \sin \varphi - I_2 \sin 2\varphi \quad (5.6)$$

In this CPR, it can be seen that the first and second harmonic terms are modulated by  $\sin \varphi$  and  $(-\sin 2\varphi)$  respectively due to the relative  $\pi$  phase shift between them. It can be imagined that the second harmonic supercurrents have a  $\pi$  – character while the first harmonic supercurrents have a 0 – character. Hence there can be spontaneous second harmonic supercurrents created in the junction when  $\delta = \pi$  and the position of  $\delta = n\pi$  can be easily inferred from the nodes in  $\Delta I_c$ . This is an interesting property unique to second order  $\varphi_0$ -junctions that can be used to control the relative directions of the two supercurrents and exploited to make novel supercurrent devices. This is especially useful in the situation that the second harmonic supercurrents originate from the highly transparent topological states in the system.

### 5.7.2 Evolution of the Fraunhofer interference pattern under $\delta$ and $\varphi$

Having established the existence of Rashba-spin momentum locking in PtTe<sub>2</sub>, the evolution of the Fraunhofer pattern in lateral PtTe<sub>2</sub> junctions in the presence of  $\Delta I_c$  is studied in order to gain insight into the CPR of the system. While superconducting quantum interference devices (SQUIDs) are the preferred platforms to deduce the current-phase relationship in a system, Josephson junctions have the advantage that the distribution of supercurrents in the system may also be obtained by analyzing the Fourier transform of the Fraunhofer pattern. The Fraunhofer patterns for the critical currents  $I_c^+$  and  $I_c^-$  are measured as the function of the magnetic flux  $\Phi$  along the  $z$ -direction, under various  $B_y$  is shown in Fig. 5.11(a)-(d) after correcting for flux focusing effects<sup>127,128</sup> and the finite thickness effect<sup>96,97</sup> of the sample as discussed in detail in the appendix.

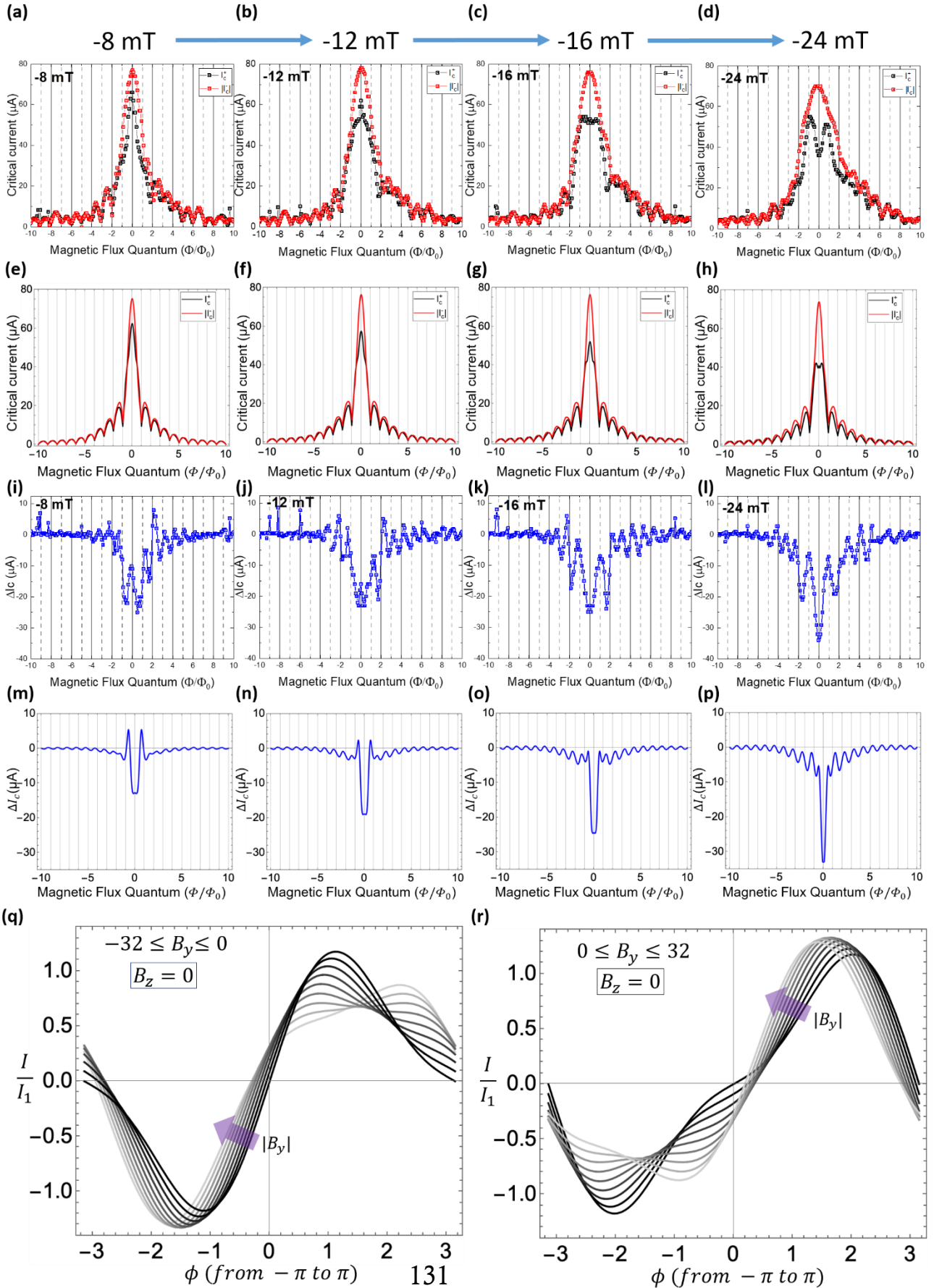


**Fig. 5.11 Evolution of the Fraunhofer pattern in the presence of  $\Delta I_c$  for junction L1:** (a)-(d) shows the experimentally measured Fraunhofer patterns for  $I_c^+$  and  $I_c^-$  in the presence of a negative  $B_y$  of different magnitudes up to  $-24$  mT. A  $0-\pi$  junction-like dip is observed in  $I_c^+$  upon increasing the magnitude of  $B_y$ . (e)-(h) shows the simulated Fraunhofer patterns using a self-consistent treatment (as described in the appendix section B) for  $\frac{I_2}{I_1} = 0.37$ . A behavior similar to that in the experiment with increasing  $\delta$  in the CPR is observed. (i)-(l) shows the increasing  $\Delta I_c$  with the increasing magnitude of  $B_y$  reaching the maximum value around  $-24$  mT. (m)-(p) Simulated  $\Delta I_c$  using the CPR in equation (5.3) for similar magnetic fields as in the experiment. The experimentally observed features including the dip are captured well by the simulation. (q), (r) shows the CPRs corresponding to negative and positive  $B_y$  used in the simulations for  $\frac{I_2}{I_1} = 0.37$ . The non-reciprocal response of  $I_c^+$  and  $I_c^-$  under  $|B_y|$  is evident from these simulations.

When  $B_y = 0$ ,  $I_c^+$  and  $|I_c^-|$  lie on top of each other leading to a negligible  $\Delta I_c$  and the period of oscillations is close to a single magnetic flux quantum ( $\Phi_0 = \frac{h}{2e}$ ) as expected (Fig. 5.9(f)). As  $B_y$  is increased in the negative direction to  $-8$  mT and the Fraunhofer pattern is measured again (Fig. 5.11(a)), it is observed that the central maxima of  $I_c^-$  increases slightly in magnitude while the magnitude of the central peak of  $I_c^+$  starts to decrease. As the magnetic field is increased further to  $-12$  mT (Fig. 5.11(b)),  $-16$  mT (Fig. 5.11(c)) and then to  $-24$  mT, (Fig. 5.11(d)) the central peak of  $|I_c^-|$  doesn't decrease much in magnitude while the magnitude of the central peak of  $I_c^+$  has a sharp decrease in the middle leading to the formation of a sharp noticeable dip in critical current where maximum  $\Delta I_c$  is observed. The roles of  $I_c^+$  and  $|I_c^-|$  are reversed when  $B_y$  is swept in the opposite direction leading to a non-reciprocal behavior with respect to the direction of the magnetic field (Refer appendix section F).

For junction L1, the maximum value of  $\Delta I_c$  is around  $-34$   $\mu A$  at  $-24$  mT, this would give  $I_2(-24$  mT) to be around  $17$   $\mu A$  and the actual value of  $\left| \frac{I_2(0)}{I_1(0)} \right| \approx 0.37$ . This value of  $\left| \frac{I_2}{I_1} \right|$  is quite substantial and larger than that measured in some semiconductor junctions with high transparency like Sn-InSb nanowire junctions<sup>126</sup> and comparable to that observed in Al-InAs planar Josephson

junctions<sup>11</sup>. Calculating the Josephson diode efficiency  $\eta = \frac{2\Delta I_c}{I_c^+ + I_c^-}$  for this junction at maximum  $\Delta I_c$  gives a large value of around 64 % at  $-24 \text{ mT}$  (Refer next chapter for comparison).

In order to corroborate the validity of values estimated from the model, the Fraunhofer patterns for  $I_c^+$  and  $I_c^-$  and consequently  $\Delta I_c$ , for different values of  $\delta$  are simulated with  $\left| \frac{I_2(0)}{I_1(0)} \right| \approx 0.37$  as shown in Fig. 5.11(e)-(h) and Fig. 5.11(m)-(p) respectively. The corresponding CPRs for negative and positive  $B_y$  are shown in Fig. 5.11(q) and Fig. 5.11(r) respectively where the non-reciprocal response of the critical currents are captured well. The details of the simulation are provided in the appendix section B. It is seen that the features of  $I_c^+$  and  $I_c^-$  from the simulation are in perfect agreement with the experimentally measured curves. The values of  $\Delta I_c$  from experiment shown in Fig. 5.11(i)-(l) are in quantitative agreement with that calculated in the simulations using the CPR in equation (5.3). The lifted nodes in  $\Delta I_c$  arise due to the presence of a diffusive supercurrent component in the junction. It is to be noted that the features of the simulation that are also observed in experiment such as the sharp peak in  $I_c^+$  around  $-12 \text{ mT}$  and the observed dip in  $I_c^+$  beyond  $-16 \text{ mT}$  are quite sensitive to the value of  $\frac{I_2}{I_1}$  and the origin of these features are reflected in the calculated CPR curves (Fig. 3q). It can be seen in the CPR curves that as  $|B_y|$  is increased, the critical current in the negative direction ( $I_c^-$ ) first increases in magnitude and then starts to decrease gradually with a steady shift in the value of  $\varphi$  at which it occurs, while in the case of  $I_c^+$  there is initially a gradual decrease in its value as  $B_y$  is increased with a shift in the value of  $\varphi$  and then at some threshold value of  $B_y$ , there is a jump in the value of  $\varphi$  at which it occurs. This value at which the jump occurs corresponds to the appearance of dip in  $I_c^+$ .

### 5.7.3 Second Harmonic Nature of $\Delta I_c$

Further, the evolution of  $I_c^+$  and  $I_c^-$  as a function of  $B_y$  from the Fraunhofer pattern is plotted in Fig. 5.12(a) is well replicated by the corresponding simulation with parameters  $I_0 = 73 \mu\text{A}$ ,  $I_1 = 1 \mu\text{A}$ ,  $I_2 = 0.37 \mu\text{A}$ ,  $B_c = 90 \text{ mT}$  and  $B_d = 48 \text{ mT}$  presented in Fig. 5.12(b). This intimate correlation between the observed features in experiment and the simulations demonstrates the

accuracy of the assumed CPR and the value of  $\frac{I_2}{I_1}$ . Fig. 5.12(c) shows  $\Delta I_c$  as a function of  $B_y$  as derived from the Fraunhofer interference pattern at zero magnetic flux. The evolution of  $\Delta I_c$  deviates from the expected sinusoidal behavior and increases in magnitude linearly with  $B_y$  till  $\pm 24 \text{ mT}$  and then decreases linearly towards zero. This behavior can be reproduced successfully in the simulations by tuning the  $\frac{I_2}{I_1}$  ratio as shown in Fig. 5.12(d). While  $\Delta I_c$  vs  $B_y$  remains sinusoidal for lower values of  $\frac{I_2}{I_1}$ , it gradually turns triangular for larger values of  $\frac{I_2}{I_1}$ , also confirming the presence of large second harmonic supercurrents in the junction. The experimentally measured  $\Delta I_c$  doesn't reach zero, as we would expect around  $\pm 48 \text{ mT}$  possibly due to slight misalignment of the sample with respect to the magnetic field, which results in some additional flux. This can be shown to be the case through simulations (Refer Appendix F).

One of the main observations from equation (5.5) is that  $\Delta I_c$  is expected to oscillate with the magnetic flux  $\Phi$  with half-flux quantum  $\left(\frac{\Phi_0}{2}\right)$  period due to the presence of the second harmonic term in the CPR and have nodes at every  $\frac{\Phi_0}{2}$ . The oscillations in  $\Delta I_c$  with  $\Phi$  at  $B_y = 20 \text{ mT}$  is presented in Fig. 5.12(e). Though the oscillations are expected to be about zero, the first few nodes in  $\Delta I_c$  are lifted from zero just like in the case of Fraunhofer patterns for  $I_c^+$  and  $I_c^-$  where the lifted nodes encountered can be accounted for by considering a long junction in the simulations. The nodes in  $\Delta I_c$  are observed to be roughly periodic in  $\frac{\Phi_0}{2}$ , though the position of the nodes are hard to ascertain due to them being lifted from zero. The inset of Fig. 5.12(e) shows the oscillations in  $\Delta I_c$  at  $B_y = 20 \text{ mT}$  in comparison with the Fraunhofer oscillations of  $I_c^+$  at  $B_y = 0 \text{ mT}$ . To confirm the periodicity of  $\Delta I_c$ , a Fourier transform of the measured signal is performed as  $F(m) = \int \Delta I_c(\Phi) \sin(2\pi m\Phi) d\Phi$  and compared with the Fourier transform of the simulated signal shown in Fig. 5.12(f). The calculated Fourier components shown in Fig. 5.12(g) indicate strongly that the major dominating component in  $\Delta I_c$  is the second harmonic, while there are no signatures of other higher harmonics. This is possibly because the third harmonic is weaker and also doesn't contribute directly to  $\Delta I_c$ , while further higher-order harmonics are even weaker to contribute meaningfully to  $\Delta I_c$ .

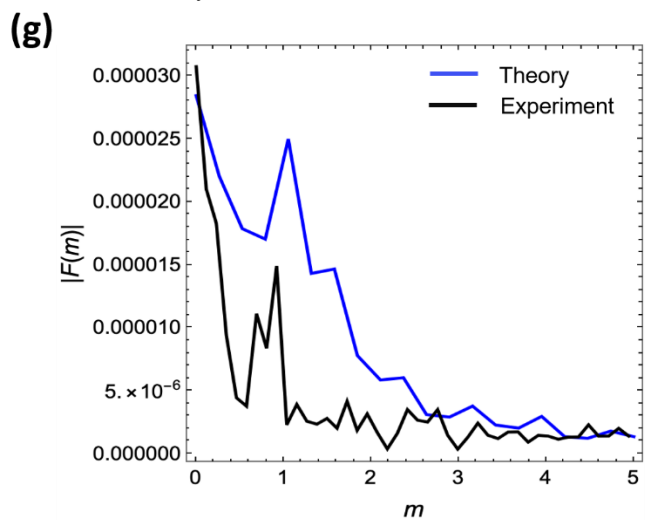
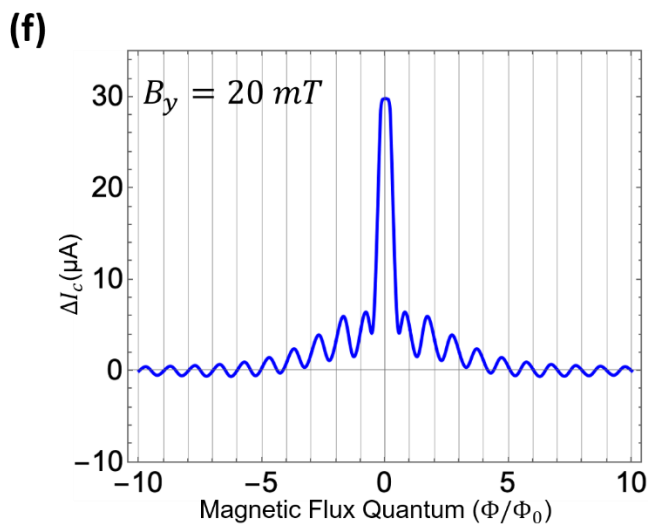
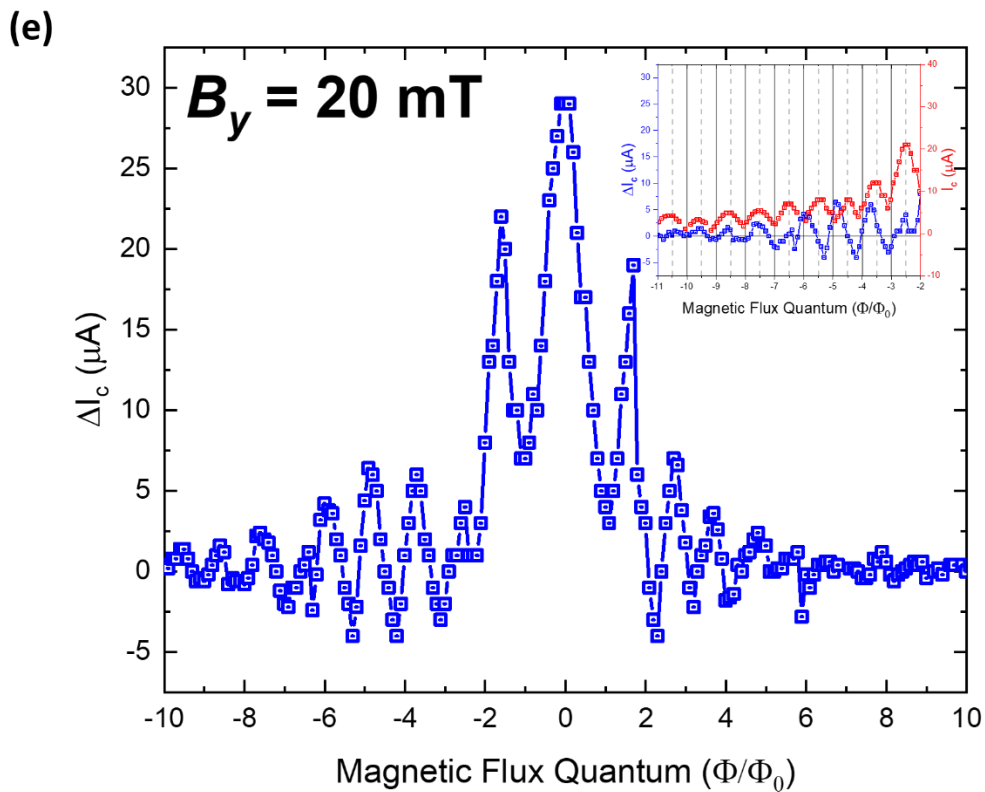
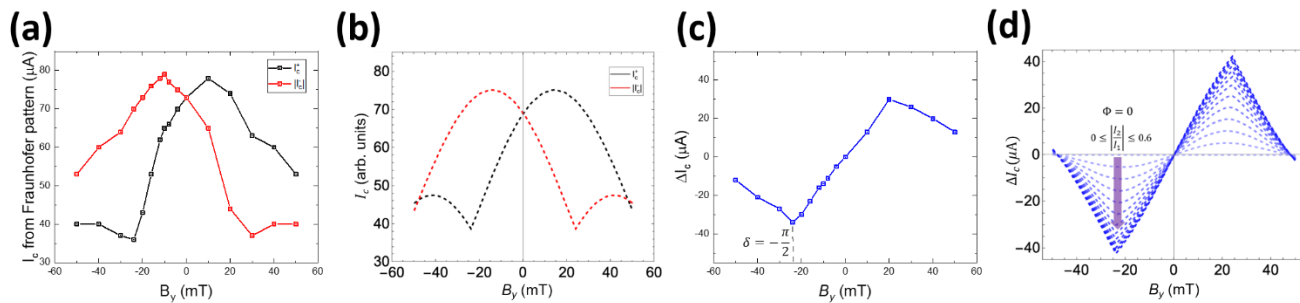


**Fig. 5.12 Evolution of  $\Delta I_c$  with  $\delta$  and  $\phi$  in junction L1:** (a) The evolution of  $I_c^+$  and  $I_c^-$  of the central peak in the Fraunhofer pattern at positive and negative  $B_y$  after correcting for shifts due to finite thickness and magnetic field misalignment. (b) Simulated evolution of  $I_c^+$  and  $I_c^-$  using the CPR in equation (5.3). It is found to fairly replicate the experimentally observed features. (c)  $\Delta I_c$  from the Fraunhofer patterns calculated after correcting for finite thickness effects in the junction. (d)  $\Delta I_c$  calculated from the simulated Fraunhofer patterns for a wide junction where  $\left|\frac{l_2}{l_1}\right|$  increases in increments of 0.1. The maxima (minima) corresponds to  $\delta = \frac{\pi}{2} \left(-\frac{\pi}{2}\right)$ .  $\Delta I_c$  evolves from a sinusoidal dependence at low values of  $\left|\frac{l_2}{l_1}\right|$  to a triangular behavior at higher values of  $\left|\frac{l_2}{l_1}\right|$ . (e) The evolution of  $\Delta I_c$  with  $\Phi$  with  $B_y = 20$  mT. Inset displays clearly the oscillations in  $\Delta I_c$  (blue) with nodes appearing roughly at half magnetic flux quantum  $\left(\frac{\Phi_0}{2}\right)$  frequency and is almost double the frequency compared to the nodes in critical current ( $I_c^+$  and  $I_c^-$ ) interference pattern (red) that happens at every magnetic flux quantum ( $\Phi_0$ ). (f) The simulated evolution of  $\Delta I_c$  with  $\Phi$  and  $\frac{l_2}{l_1} = 0.37$  at 20 mT. The first few nodes, which are lifted from zero in experiment, are also found in the simulation and arise due to the geometry of the junction. (g) FFT of the experimentally measured and simulated  $\Delta I_c$  signals using  $F[m] = \int \Delta I_c(\Phi) \sin(2\pi m\Phi) d\Phi$  show that the Fourier component present in both signals is closer to the second harmonic and higher harmonics are absent in experiment.

## 5.8 Possible origin of strong coherence in PtTe<sub>2</sub>

Now, we turn our attention to the origin of such a large second harmonic term in PtTe<sub>2</sub>. The presence of such a large second harmonic component in a metallic Josephson junctions made over such long separations is quite surprising as it indicates a large transparency of the interface between the superconducting electrodes and PtTe<sub>2</sub>, and the possible presence of Andreev bound states due to phase coherent transport across the junction<sup>129</sup>. Such large transparencies are commonly observed in high-mobility semiconducting<sup>130</sup> and semi-metallic junctions<sup>104</sup> with pristine interfaces but it is not the case in metallic junctions due to shorter mean-free paths of the



order of just a few  $nm$ . The mean-free path ( $l_e$ ) reported in literature for single crystals of PtTe<sub>2</sub> is around 180  $nm$  in the  $ab$  plane<sup>131</sup>, which is large in comparison with a normal metal. This large mean free path in the junction leads to ballistic transport in the junction and can be attributed to the significant contribution of the states with helical spin-momentum locking. However, this value can be larger in our case, with the reduction in dimensionality. Transparent superconductor-metal interfaces in a junction have large critical currents ( $\sim I_1$ ) owing to large carrier densities and states available in the metal, as in our case. Since the second harmonic supercurrent ( $I_2$ ) scales as the square of  $I_1$ , the ratio  $\frac{I_2}{I_1} \propto I_1$  and is typically larger in metallic Josephson junctions with larger  $I_1$  as in our case ( $\sim 100 \mu A$ ) as compared to semiconductor Josephson junctions ( $\sim 1 \mu A$ ). This is advantageous as it allows for easier and clear observation of higher order effects in the junction like the oscillations in  $\Delta I_c$  that we observe.

The superconducting coherence length ( $\xi = \frac{\hbar v_F}{\pi \Delta_0}$ ) of L1 is calculated to be around 200  $nm$  at zero temperature using the average value of  $v_F \approx 3.3 \times 10^5 \text{ ms}^{-1}$  reported in literature<sup>131</sup> for PtTe<sub>2</sub>. It is neither clearly in the short or long junction limit in comparison with the junction separation (390  $nm$ ) and with change in temperature. It lies in the intermediate regime and it is not straight forward to determine the transparency of the junction by fitting  $I_c(T)$  using a standard model for a long junction as the critical current starts to saturate at temperatures below 500  $mK$ . Instead, we look at another property of transparent junctions that is the result of coherent Andreev reflections, excess current to extract the total transparency of the junction. Excess currents ( $I_e$ ) are obtained by linear extrapolation of the  $I - V$  curve above the critical current back to zero voltage as shown in Fig. 5.13(a). The existence of  $I_e$  in a highly transparent junction with phase-coherent Andreev reflections is explained by the Octavio-Tinkham-Blonder-Klapwijk (OTBK) model<sup>132-134</sup>. The  $I_e$  for L1 at 20  $mK$  is around 9  $\mu A$  which corresponds to a transparency parameter of around 0.45 for a value of  $Z = 1.1134$ . The presence of large excess currents in the junction is an evidence for coherent transport across the junction.

The  $I_c(T)$  for junctions L1, L3 and L4 can be seen in Fig. 5.13 (d), (b) and (c) respectively.  $I_c(T)$  shows concave behavior at higher temperatures but the behavior changes to convex below 500  $mK$  and there is plateauing of the critical current. It can be seen clearly that as the separation between the electrodes increases, the plateauing nature is pushed towards lower temperatures and

vanishes for the largest separation L4. The transparency of the other junctions L3 and L4, which are clearly in the long junction limit ( $d \gg \xi$ ) can be obtained by fitting the critical current as a function of temperature in the long junction limit<sup>135,136</sup> given by  $I_c(T) = \eta \frac{aE_T}{eR_n} \left[ 1 - be^{\frac{-aE_T}{3.2k_B T}} \right]$  over the entire temperature range.  $a$  and  $b$  are constants.  $E_T$  is the Thouless energy and  $R_n$  is the normal state resistance.

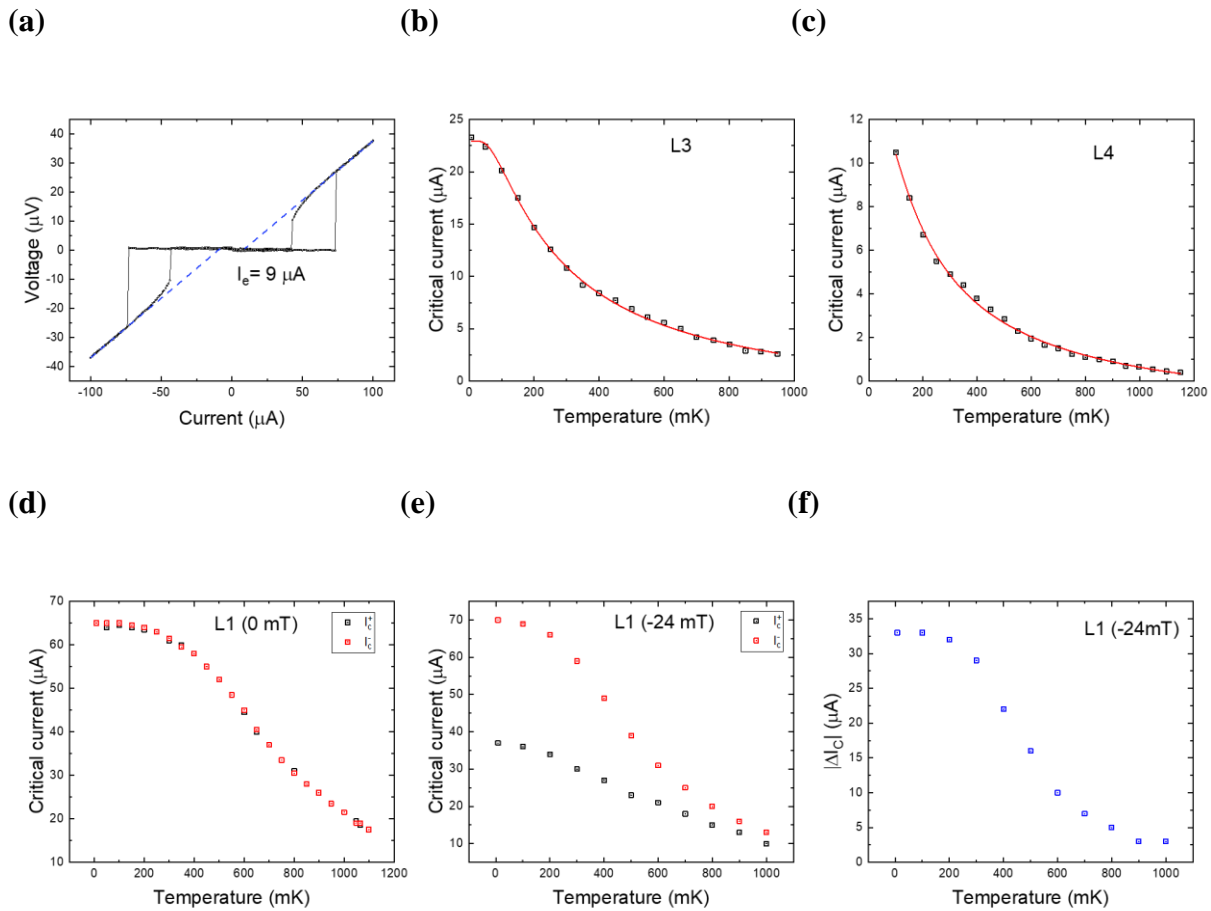


**Fig. 5.13 Transparency of PtTe<sub>2</sub> Josephson junctions:** (a) The  $I - V$  curve for L1 junction measured at 20 mK shows the presence of excess currents around  $9 \mu\text{A}$  indicating coherent transport across the junction and a transparency of around 0.45 derived from the OTBK model. (b), (c)  $I_c(T)$  for junctions L3 and L4 are fit with an equation corresponding to the long junction limit yielding a transparency of around 0.436 and 0.428 respectively. (d)  $I_c(T)$  for junction L1 with  $I_c$  starting to saturate below 500 mK. (e)  $I_c(T)$  for  $I_c^+$  and  $I_c^-$  at  $-24 \text{ mT}$  for L1 shows that

$I_c^-$  has a larger energy gap at low temperatures ( $\Delta_0$ ) in comparison with  $I_c^+$  for which  $\Delta_0$  is strongly suppressed by the magnetic field. (f)  $|\Delta I_c(T)|$  as derived from  $I_c^+$  and  $I_c^-$  measured from the Fraunhofer pattern.

The extracted transparency from the fits for L3 and L4 (Fig. 5.13(b) and (c)) is around 0.436 and 0.428 respectively, which is similar to the value extracted from excess currents for L1. The transparency is not close to one due to contribution of the diffusive bulk states that are not spin-momentum locked as expected for a topological metal with multiple bands crossing the Fermi level in addition to the spin-momentum locked states. Another signature of coherent transport across the junction is the presence of multiple Andreev reflections (MAR)<sup>129</sup>. Owing to the small resistance of the junction ( $0.372 \Omega$ ), very large currents are required to reach the voltages at which MAR can be observed, which are beyond the critical currents of the superconducting electrodes and hence can't be observed directly. However, some signatures of resonance are observed in the differential resistance of the junction in the finite voltage state when the critical currents are suppressed by high magnetic fields (Refer appendix section F) indicating that the coherence persists even in the presence of large magnetic fields.

## 5.9 Conclusion

In summary, we have shown through measurements of  $\Delta I_c$  that the topological semimetal 1T-PtTe<sub>2</sub> shows a large JDE due to Cooper pair momentum induced by the helical spin-momentum locking in the bulk Dirac cones under a Zeeman field. While extrinsic effects such as SFE can also give rise to a JDE in wide Josephson junctions, it is shown that near uniform current distribution can be achieved by using a criss-crossed measurement geometry and the observed JDE is likely arising due to the intrinsic properties of PtTe<sub>2</sub> in combination with Meissner screening. Furthermore, it is evidenced from the evolution of the Fraunhofer oscillations together with simulations that these junctions exhibit a second order  $\varphi_0$ -junction behavior with the presence of a strong second harmonic term ( $\frac{I_2}{I_1} \approx 0.37$ ), as calculated from the  $\Delta I_c$ .  $\Delta I_c$  is also shown to have oscillations with nodes occurring at every  $\left(\frac{\Phi_0}{2}\right)$  magnetic flux, further confirming the existence of

the proposed  $\delta$ -dependent CPR. Further, the extracted second harmonic supercurrents ( $I_2$ ) in different devices (L1, L3 and L4) scale quadratically with  $I_c$  (Fig. 5.15) as expected from equation (4.3) validating the analysis of the junctions with this CPR.

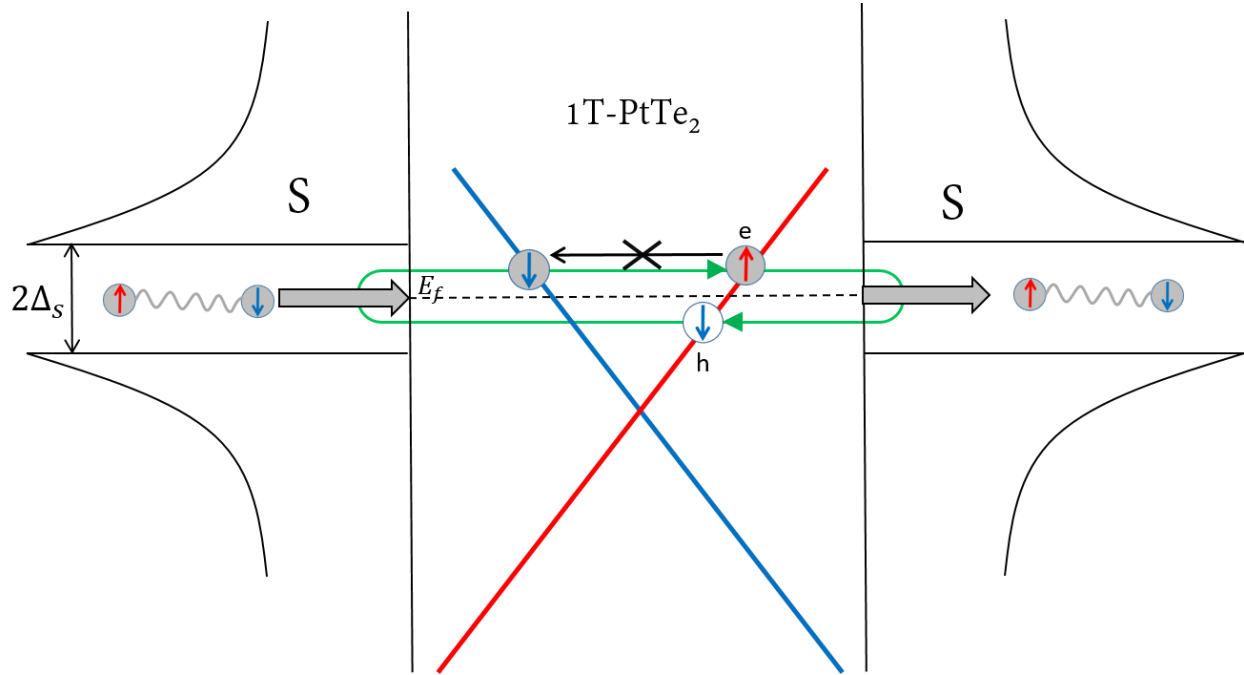


**Fig. 5.14 Coherent Andreev processes promoted by the helical spin-momentum locking in PtTe<sub>2</sub>:** The helical spin-momentum locking of the Dirac cones in PtTe<sub>2</sub> prevent the normal reflection of electrons due to non-availability of spin states to reflect back and thereby promoting the coherent Andreev processes leading to higher harmonics in the supercurrent.

The transparency in these junctions can be attributed to the good interface of the superconductor with PtTe<sub>2</sub> due to its chemical stability and the presence of ballistic channels with long range coherence due to the protection offered by helical spin-momentum locked states of the bulk Dirac cone in PtTe<sub>2</sub><sup>56</sup> to normal reflections as has been reported previously in Josephson junctions of some topological semimetals and other systems<sup>103,137,138</sup>. The large spin-orbit coupling effect at small magnetic fields as evidenced from the non-zero momentum of the Cooper pairs indicates a large  $\left(\frac{g}{v_F}\right)$  ratio in PtTe<sub>2</sub>. Large  $g$ -factors of similar order have been reported in some topological semimetals<sup>108</sup> and semiconductor heterostructures<sup>109,139</sup>. The large spin-orbit coupling

and Zeeman splitting with small magnetic fields coupled with the reasonable mean free paths in the van der Waals Dirac semimetal PtTe<sub>2</sub> provides an interesting alternative platform to engineer topological superconductivity in planar Josephson junctions<sup>140,141</sup> as has been demonstrated before in Josephson junctions of HgTe<sup>142</sup> and InAs<sup>143</sup> quantum well structures. One of the major challenges in the current existing platforms for realizing topological superconductivity is the engineering of high quality interfaces<sup>144,145</sup>. The complete air stability of PtTe<sub>2</sub> and of the topological states allow for creation of high quality interfaces with superconductors without many complications. Andreev bound state spectroscopy using a tunnel probe can be used to probe the presence of a Majorana bound state in the system and it would also be of interest to study the Andreev bound state spectrum in the presence of a diode effect in the future. The  $\delta$ -dependent CPR in second order  $\varphi_0$ -junctions provides a mode of continuous phase tuning between the first- and second-harmonic supercurrents in the junction thereby separating supercurrents passing through the topological channels from that of trivial supercurrents, which can be of use in to useful applications in topological quantum circuits and other superconducting electronics.

PtTe <sub>2</sub> device	Separation $d$ (nm)	Critical current $I_c$ ( $\mu$ A)	$R_N$ ( $\Omega$ )	$I_c R_N$ ( $\mu$ V)	Second harmonic $I_2$ ( $\mu$ A)	Transparency $\tau$
L1	390	73	0.37	27.156	19.7	0.45 (from $I_e$ )
L3	466	24	1.2	28.8	1.898	0.435
L4	597	13.4	1.72	23.04	0.52	0.427

**Table 5.1 Summary of PtTe<sub>2</sub> junctions:** Table contains the information of the measured parameters in lateral PtTe<sub>2</sub> junctions with different separations.

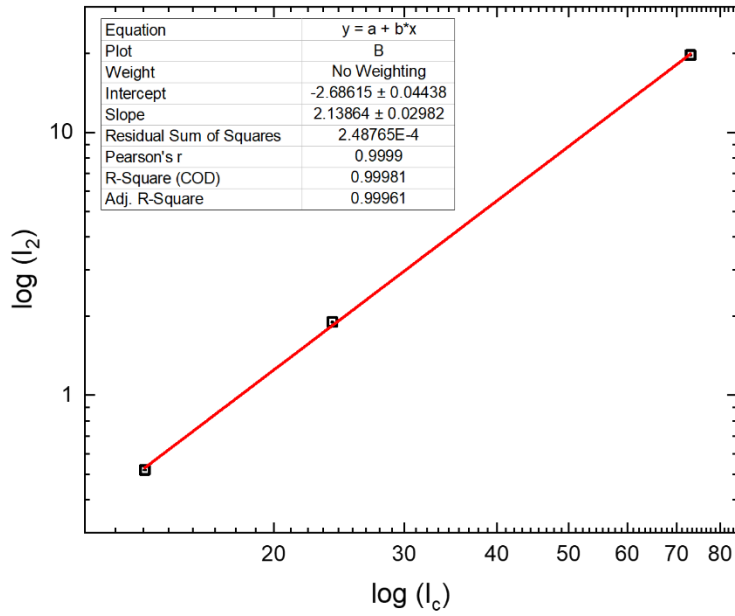


**Fig. 5.15 Evolution of second-harmonic supercurrents with  $I_c$  in PtTe<sub>2</sub>:** The log-log plot of the evolution of  $I_2$  with  $I_c$  shows that the extracted second-harmonic supercurrents scale quadratically (slope  $\sim 2$ ) with the critical current as expected from equation (4.3), further validating the CPR.

# 6

---

## Conclusions and Outlook

Various aspects of the supercurrent diode effect have been explored in different materials along different directions since its discovery in 2020<sup>6</sup> and it has been the central theme of multiple studies published during the time of writing this thesis<sup>11,114,115,125,126</sup>. Though a lot of emphasis has been on improving the efficiency of the diode effect and creating diode effect without an external magnetic field, the diode effect can be used to study the properties of the material or the Josephson junction as in this thesis. As mentioned earlier, the inversion and time reversal symmetry breaking criteria required for the existence of a supercurrent diode effect is quite interesting as it also the condition required for many forms of unconventional superconductivity. This makes the diode effect a powerful and useful tool to investigate novel superconducting phases, which are hard to probe by other experimental methods. For example, a time-reversal symmetry breaking chiral superconducting state has been reported in  $\text{Sr}_2\text{RuO}_4$  junctions<sup>146</sup> through the appearance of spontaneous chaotic diode effect in the absence of an external magnetic field due to the varying chiral domain distribution during each cool down. Though a spontaneous diode effect was observed in the same system almost 20 years prior<sup>147</sup>, it was not analyzed from a time-reversal symmetry breaking perspective and was attributed to an anomalous Josephson behavior. Meanwhile a universal Josephson diode effect based on the Meissner screening currents in short lateral Josephson junctions independent of the characteristics of the junction material has also been proposed<sup>106</sup>.

In this thesis, we have explored in detail the JDE in air-stable, exfoliated 1T-transition metal dichalcogenides 1T-NiTe<sub>2</sub> and 1T-PtTe<sub>2</sub> with helical spin-momentum locking arising from the hidden inversion symmetry breaking in the crystal structure. It has been shown that the electrical transport properties, especially in the superconducting state strongly reflect this structural property. Both these materials show very large diode effect in the separations explored at relatively low magnetic fields in comparison with other materials such as InAs. The origin of JDE is attributed mainly to the Zeeman shift of the states with helical spin-momentum locking in the presence of a magnetic field perpendicular to the direction of current that can provide a finite center-of-mass momentum to the Cooper pairs in the direction of current that leads to asymmetric and non-reciprocal superconducting energy gaps in the Josephson junction and ultimately a diode effect.



In the case of NiTe<sub>2</sub> Josephson junctions, the JDE is analyzed as a function of the magnetic field magnitude, direction and temperature and compared with a Ginzburg-Landau model of a Josephson junction with a higher harmonic term to ascertain this. The finite momentum of the Cooper pairs has also been measured independently through the evolution of the Fraunhofer pattern in the presence of an in-plane magnetic field. Alternative origin of these observations in terms of Meissner screening currents is also discussed. The observed diode effect is most likely a combination of both these effects. Some basic checks can be performed that the obtained momentum shifts are reasonable. The value of the measured finite momentum at 12 *mT* is around  $2q_x = 4.5 \times 10^6 \text{ m}^{-1}$  which are realistic values of momentum shifts that are 3-4 orders of magnitude smaller compared to the size of the Brillouin zone. Moreover, the critical momentum of the junction can be estimated from the superconducting coherence length as  $p_c = \frac{\hbar}{\sqrt{3}\zeta(T)}$  where  $\zeta(T) = \frac{\hbar v_F}{\pi\Delta}$  is the coherence length of the junction. This gives the value of critical momentum at which depairing occurs to be around  $q_c = 3.92 \times 10^7 \text{ m}^{-1}$ , which is almost an order of magnitude larger than the measured momentum of Cooper pairs. Hence, it is possible to host pairs with such momenta without causing depairing in the junction. Similar magnitudes of center-of-mass momentum in Cooper pairs have also been obtained in a 2D superconductor Ba<sub>6</sub>Nb<sub>11</sub>S<sub>28</sub><sup>37</sup>.

In the case of PtTe<sub>2</sub>, JDE due to the helical spin-momentum locking in the bulk Dirac cones at the Fermi level is measured in lateral Josephson junctions. JDE characteristics similar to that in NiTe<sub>2</sub> are observed. No spin-momentum locking is found in the vertical junctions indicating the absence of any spin momentum locking along the c-axis of the crystal. Importantly, the role of extrinsic mechanisms such as self-field effect and geometric shape inversion asymmetry in creating a JDE is discussed in detail. It is shown that the JDE from self-field effects in a wide junction can be avoided by using the right terminals of the electrodes to source current. This is important to ensure a uniform distribution of supercurrents in the junction and avoid erroneous conclusions on the JDE. A generic CPR model is used to study the Fraunhofer pattern and the evolution of JDE as a function of the magnetic flux, which was not done in the case of NiTe<sub>2</sub>. This CPR expanded to the second harmonic term is dubbed as a ‘second order  $\varphi_0$  junction’ CPR.

$$I(\varphi) = I_1 \sin \varphi + I_2 \sin (2\varphi + \delta)$$

This CPR is shown to be different from typical  $\varphi$  – and  $\varphi_0$  – junction CPRs<sup>116-123</sup> and has unique properties such as the relative tuning of phase difference between the two harmonics in the junction. The JDE is found to be directly proportional to the value of second harmonic term in the CPR. The value of the second-harmonic term is obtained from the experimental measurements of JDE and the ratio of  $\left| \frac{I_2}{I_1} \right|$  is used to simulate the Fraunhofer patterns in the wide junction limit. The simulated Fraunhofer patterns are in great agreement qualitatively with those measured experimentally. Moreover the second harmonic nature of  $\Delta I_c$  predicted from the CPR is confirmed by measuring its oscillations as a function of the magnetic flux. Nodes in  $\Delta I_c$  are found to appear every half flux quantum. The Fourier transform of the measured signal is used to confirm its second harmonic nature, hence further validating the CPR used. The origin of the large second harmonic term in this metallic junction is discussed in terms of the states with helical spin-momentum locking that strongly suppress normal reflections. Fitting the  $I_c(T)$  curves with a long diffusive junction equation provides a transparency close to 0.42-0.43 for L3 and L4 while excess currents are used to evaluate the transparency of L1. The presence of excess currents in the junction is already an indication of the presence of coherent Andreev processes occurring in the junction. The transparency of the junction estimated from the excess currents is around 0.45. This transparency indicates that there are both bulk diffusive channels and ballistic channels contributing to the transport of supercurrents. Since the second harmonic supercurrents are primarily carried by the helical states, it is possible to isolate them from the first harmonic contribution carried by the diffusive states by tuning to specific values in the  $\delta - \Phi$  phase space. This is a feature quite unique to second order  $\varphi_0$  – junctions.

Thus, the study of JDE in this system has exposed interesting properties of this new CPR that help further increase the functionality of Josephson junctions. The presence of self-field effects in the junction can also be used to create a Josephson diode effect in the absence of a magnetic field using a three-terminal geometry as discussed in appendix section G. This topic requires further investigation in the future as it is a technologically promising route to create JDE in the absence of an external magnetic field. It can work just by tweaking the geometry of the junction and the terminals, without the need for exotic materials that break time reversal symmetry in the superconducting state.

It is to be noted that though a finite momentum state is created in these systems, it is different from a Fulde-Ferrell (FF) state<sup>9</sup> that is created when the Fermi surface of the material is spin split due to an exchange field. In that case, pairs with center-of-mass momentum  $\mathbf{q}$  and  $-\mathbf{q}$  are created in equal numbers and hence the suppression of the superconducting gap would be identical in both directions. Thus in an FF state, the presence of finite momentum Cooper pairs does not host a supercurrent diode effect even though it has finite-momentum superconductivity with spatial modulation of the superconducting order parameter.

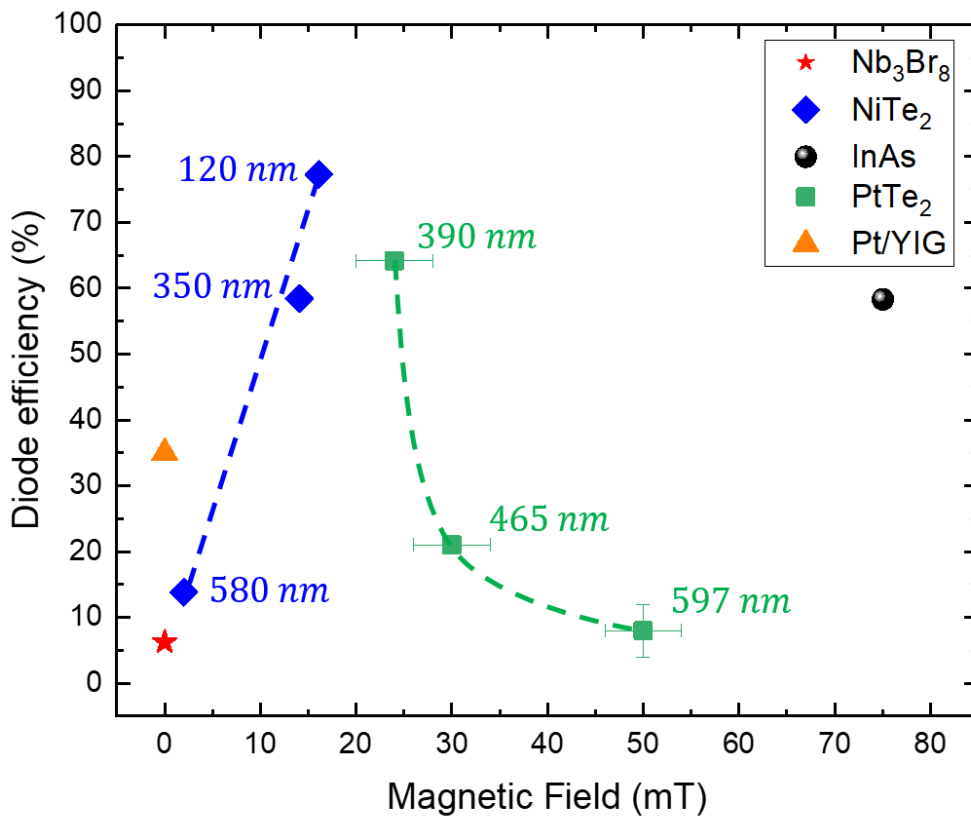


**Fig. 6.1 Evaluation of Josephson diode efficiency in various materials:** The efficiency for various Josephson junction based diodes is presented<sup>1,2,7,110</sup>, including the current work. The efficiency of  $\Delta I_c$  in NiTe<sub>2</sub> and PtTe<sub>2</sub> goes up drastically with decreasing separation and increasing the width of PtTe<sub>2</sub> junctions.

The chart of materials in which the Josephson diode effect has been explored is shown in Fig. 6.1. Field-free Josephson diode effect has been observed in  $\text{Nb}_3\text{Br}_8$  junctions and Pt/YIG junctions, though with relatively low efficiencies. InAs quantum well Josephson junctions require a magnetic field of around  $75 \text{ mT}$  to achieve their maximum efficiency of around 60 % and their critical currents are typically low due to the semiconducting nature of InAs.  $\text{NiTe}_2$  and  $\text{PtTe}_2$  require relatively low fields to create a Josephson diode effect and have large efficiencies that can be controlled by decreasing the separation. As discussed above and in appendix section G, it would be of interest to explore the possibility of more efficient field-free Josephson diodes through self-field effects in junctions made from these materials for practical applications.

Though the origin of finite-momentum Cooper pairing is discussed in terms of both the helical spin-momentum locking and Meissner screening supercurrents, the presence of a strong second-harmonic supercurrents, the presence of excess currents and the non-sinusoidal oscillations from SQUID (Fig. F5) all support the significant contribution of phase-coherent channels in the junction to the transport of supercurrents. The presence of these channels in a material with a large electron density can be attributed to the suppression of normal reflections offered by the states with helical spin-momentum locking. Hence, these states either directly or indirectly contribute significantly to the observed JDE as there can be no JDE without higher harmonics in the junction offered by the transparency of the helical spin-momentum locked states.

It would be also of great interest to explore the possibility of engineering topological superconductivity in these systems as expected for planar Josephson junctions with high spin-orbit coupling in a magnetic field<sup>140-143,148</sup>. Studying the Andreev bound states through tunneling spectroscopy can be used to probe the existence of Majorana bound states but it can also provide useful information on the Andreev bound state spectrum in these systems hosting a diode effect and help in further demystifying the underlying mechanism. Since, it is possible to tune the  $\delta - \Phi$  parameters to maximize the impact of the highly transparent ballistic channel in the junction; it presents the unique opportunity of identifying and isolating topological supercurrents from the supercurrents induced by the trivial bulk.

# Appendix

---

## A. Field-free Josephson diode effect in $\text{Nb}_3\text{Br}_8$

The superconducting diode effect discovered in 2020 required an external magnetic field to break the time-reversal symmetry that led to non-reciprocal supercurrents in the superconducting heterostructure. However, for applications in superconducting logic devices it would be advantageous to obtain the diode effect without the need for external magnetic fields. This is possible to obtain in devices with intrinsic time-reversal symmetry breaking. The presence of a Josephson diode effect without the application of an external magnetic field was first reported in a vertical heterostructure of  $\text{NbSe}_2/\text{Nb}_3\text{Br}_8/\text{NbSe}_2$ . Heng Wu and Yaojia Wang were the lead authors of this study and I performed the electrical transport measurements on the diode effect with them. A short summary of the results from the publication<sup>2</sup> are presented here.

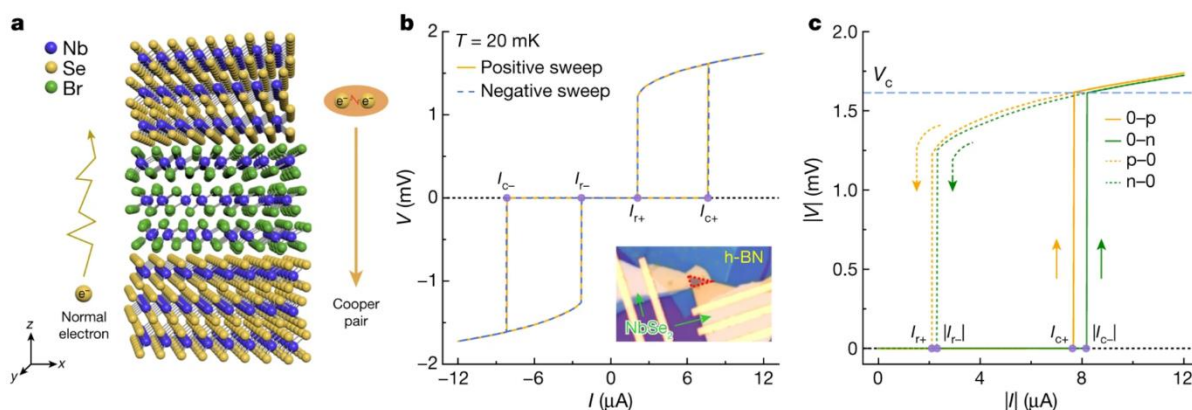


**Fig. A.1 Schematic of the vertical Josephson junction and  $I - V$  curve for the junction:** (a) A depiction of the vertical junction with a  $\text{Nb}_3\text{Br}_8$  flake sandwiched by two  $\text{NbSe}_2$  flakes on both sides. (b) The current-voltage characteristic of such a junction. Inset shows a close-up optical image of the junction. (c) A close analysis of the current voltage curve shows that there is a small difference in the magnitudes of  $I_{c+}$  and  $I_{c-}$  at zero field. Figure reproduced with permission from ref.<sup>2</sup>, Springer Nature.

Vertical Josephson junctions of three layer thick  $\text{Nb}_3\text{Br}_8$  were fabricated with  $\text{NbSe}_2$  flakes on the top and bottom with a dry transfer technique. The whole heterostructure was covered with

a hBN (hexagonal boron nitride) on top. The current voltage characteristics of the junction at 20 mK is shown in Fig. A.1. In the absence of any external magnetic field, there is a small asymmetry between the positive and negative critical currents, around 500 nA. When a current between  $I_c^+$  and  $|I_c^-|$  is applied, zero voltage is obtained along one direction and a finite non-zero voltage is observed in the opposite direction as shown in Fig. A.2. The magnetic field dependence of  $\Delta I_c$  shows interesting behavior. Unlike the other supercurrent diode effects discussed throughout the thesis which are antisymmetric with respect to the magnetic field,  $\Delta I_c$  in Nb<sub>3</sub>Br<sub>8</sub> is symmetric with respect to an out-of-plane magnetic field and persists within a range of  $\pm 35$  mT, beyond which it vanishes to zero. Similar field-free effects  $\Delta I_c$  is observed in a few more junctions of Nb<sub>3</sub>Br<sub>8</sub><sup>2</sup>. The origin of time-reversal symmetry breaking in these Nb<sub>3</sub>Br<sub>8</sub> junctions are still not clear, as Nb<sub>3</sub>Br<sub>8</sub> is not magnetic in nature. A few possibilities are discussed in the paper including the obstructed atomic insulating nature of Nb<sub>3</sub>Br<sub>8</sub><sup>2</sup>.

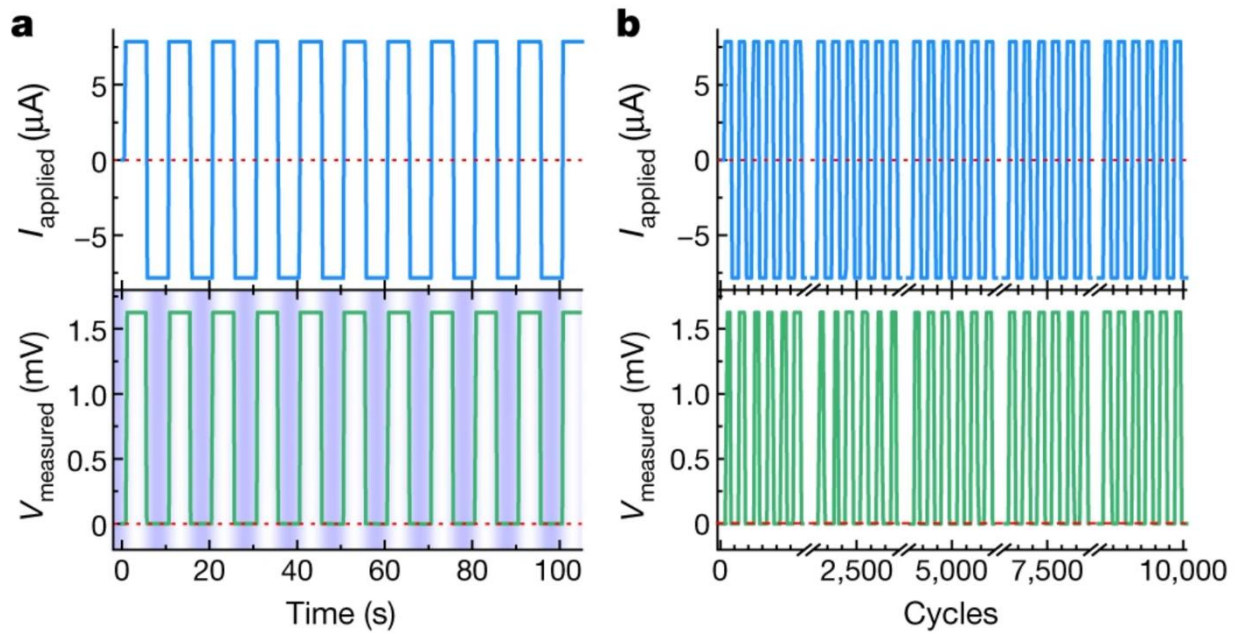


**Fig. A.2 Non-reciprocal voltages in Nb<sub>3</sub>Br<sub>8</sub> junction:** (a) Non-reciprocal voltages are observed in zero field depending on the direction of the current. Positive current gives a finite voltage while negative current gives zero voltage. (b) The observed non-reciprocal effect is robust and lasts over multiple cycles. Figure reproduced with permission from ref.<sup>2</sup>, Springer Nature.

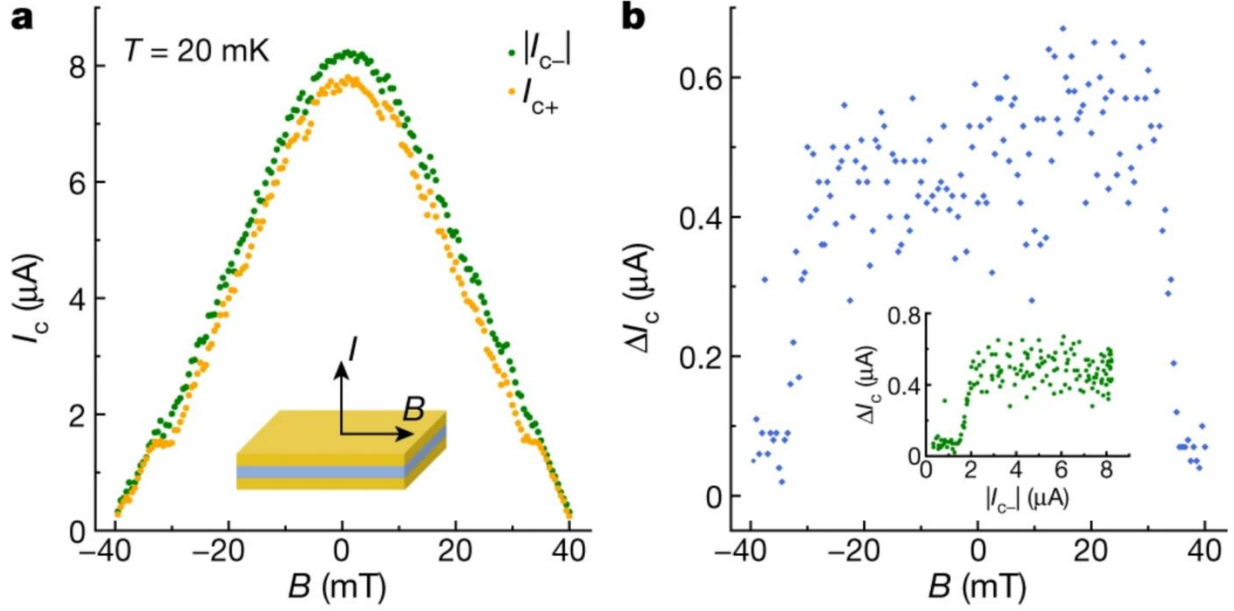


**Fig. A.3 Magnetic field dependence of  $\Delta I_c$  in  $Nb_3Br_8$  junctions:** (a),(b)  $\Delta I_c$  is non-zero at zero magnetic field, found to be symmetric with respect to the magnetic field and vanishes above 35 mT. Figure reproduced with permission from ref.<sup>2</sup>, Springer Nature.

## B. Self-consistent treatment of the wide $PtTe_2$ Josephson junctions

Consider the Josephson junction under a uniform out of the plane magnetic field  $B_{0z}$ . Since the superconducting leads' thicknesses ( $1 \mu m$ ) are much larger than the London penetration depth of niobium ( $\lambda_L \sim 100 nm$ ), we assume that the magnetic field is non-zero only near the junction. We are interested in a regime in which the supercurrent flow and the junction geometry affect the phase  $\varphi$ , and the changes in the magnitude of the order parameter is considered in the junction CPR phenomenologically. In the presence of magnetic fields, the phase  $\varphi$  obeys the differential equations

$$\frac{\partial \varphi}{\partial y} = \frac{2\pi d_{\text{eff}}}{\Phi_0} B_z, \quad \frac{\partial \varphi}{\partial z} = -\frac{2\pi d_{\text{eff}}}{\Phi_0} B_y, \quad \frac{\partial \varphi}{\partial x} = 0 \quad (\text{A1})$$

where  $d_{\text{eff}} = (L + 2\lambda_L)$  is the effective junction length. Since the junction thickness in the  $z$  direction ( $t \sim 17.5 nm$ ) is much less than London penetration depth, we consider a uniform  $B_y$ .



This leads to the following solution for the phase  $\varphi = \varphi(y) - \frac{2\pi d_{\text{eff}}}{\Phi_0} B_y z$ . As a result, we can integrate out the  $z$  direction in the CPR, which effectively reduce it to a 2D CPR,  $J_x(y) = \int_{-t/2}^{t/2} J_x(y, z) dz$ . This effectively decreases the critical current as the penetrated magnetic flux in the  $y$  direction ( $B_y \cdot t d_{\text{eff}}$ ) increases. When the current density is sufficiently strong, the supercurrent flow in the junction tends to screen the magnetic field from the interior of the junction<sup>26</sup>, and the magnetic field satisfies the Maxwell equation

$$\frac{\partial B_z}{\partial y} \approx \frac{\alpha}{d_{\text{eff}}} \cdot \mu_0 J_x(y) \quad (A2)$$

The factor  $\frac{\alpha}{d_{\text{eff}}}$  is a correction to the 2D current density obtained in literature<sup>149</sup> for coplanar junctions,  $\alpha$  is a dimensionless parameter that depends on the junction details, and  $\mu_0$  is the permeability of free space. Now, combining equations (A1) and (A2), we get

$$\frac{\partial^2 \varphi}{\partial y^2} = \frac{2\pi\alpha\mu_0}{\Phi_0} J_x(y) = \frac{1}{\lambda_J^2} \frac{J_x(y)}{J_c} \quad (A3)$$

where  $\lambda_J = \sqrt{\frac{\Phi_0}{2\pi\alpha\mu_0 J_c}}$  is the Josephson penetration depth,  $J_c$  is the critical current density. It can be noted that when  $J_2 = 0$ , equation (A3) reduces to the usual wide junction limit with a sinusoidal CPR, the so-called static sine-Gordon equation. Employing Ampere's law, we get the following boundary conditions for the phase gradient

$$\left. \frac{\partial \varphi}{\partial y} \right|_0 = b_0 + a_1 b_s \quad (A4)$$

$$\left. \frac{\partial \varphi}{\partial y} \right|_w = b_0 + a_2 b_s \quad (A5)$$

where  $b_0 \propto B_{0z}$ ,  $b_s = \frac{1}{\lambda_J^2} I$  with  $I = \int_0^W J_x(y) dy$  being the total supercurrent flowing in the junction. The same-side and opposite-side (criss-crossed) biasing can now be easily adopted by  $(a_1, a_2) = (0, 1)$  and  $(-1/2, 1/2)$ , respectively. These choices satisfy  $\left. \frac{\partial \varphi}{\partial y} \right|_w - \left. \frac{\partial \varphi}{\partial y} \right|_0 = b_s$ . It is clear that the total current affects the solutions of the phase and the phase, in turn, determines the current

density. As a result, these equations are solved self-consistently. In order to obtain the Fraunhofer patterns, we find the maximum and minimum total supercurrents that satisfy the boundary conditions with the external magnetic field  $B_{0z}$ , that is,  $I_c^+ = \max[I]$  and  $I_c^- = \min[I]$ . At zero in-plane field  $B_y = 0$ , we obtain  $J_c = J_1 = \frac{I_c}{w} \approx 12 \text{ Am}^{-1}$ , which leads to  $\lambda_J \approx \frac{1}{\sqrt{\alpha}} 4.5 \mu\text{m}$ . Fig. 5.8 (c) and (f) in the thesis present the simulated Fraunhofer patterns with  $\alpha = 2$  and  $b_0 = 6.6 \times 10^5 B_{0z} (mT)$  for same-side and opposite side biasing, respectively.

It has been shown theoretically that in a lateral Josephson junction where the superconducting electrodes have different widths, the geometry of the junction can give rise to a tunable phase  $\varphi_0$ , which can be controlled by the external magnetic flux<sup>150</sup>. The CPR for such junctions is of the following general form:

$$I(\phi) = I_0(\Phi) \sin[\phi + \varphi_0(\Phi)],$$

where  $I_0(\Phi)$  and  $\varphi_0(\Phi)$  are geometry-dependent functions. This is because there is a net flow of current induced by the orbital response due to the magnetic flux, even at  $\phi = 0$ . As a result, the anomalous magnetic flux-coupled CPR is such that the equilibrium phase difference is different from conventional  $\phi = 0$ , i.e.,  $I(\phi = -\varphi_0) = 0$ . The superconducting electrodes in L1 are of different widths and obey the modification in the CPR, in this case.

For junction L1, we observe that  $I_0(\Phi) = I_1$  and  $\varphi_0(\Phi) = \arctan[\beta \left(\frac{\Phi}{\Phi_0}\right)^2]$  can describe the cusp-like local minimum of Fraunhofer pattern for  $I_c^+$  found in Fig. 3d of the main text at  $B_y = -24 \text{ mT}$  and  $|\Phi| < \Phi_0$  where the parameter  $\beta$  controls the depth of the local minimum. We note that the dip in the critical current of the Fraunhofer pattern is a characteristic feature of  $0 - \pi$  junctions but we do not observe any  $0 - \pi$  transition in the simulations of the CPR. A crucial difference here is that this feature is absent for  $I_c^-$  indicating that this dip-like feature arises purely due to the geometry of the junction.

As a result, our CPR used in the simulations of the junction L1 reads

$$I = I_1 \sin[\phi + \varphi_0(\Phi)] + I_2 \sin[2\phi + \delta],$$

where  $I_2$  is a correction due to the second harmonic term. We note that, in the presence of an in-plane magnetic field  $B_y$ , we have  $I_k = I_{0k} \left(1 - \frac{B^2}{B_c^2}\right)^k$ . In the experimental Fraunhofer patterns, we have  $TI_c^+(B_y, B_z) = -I_c^-( -B_y, -B_z)$ , where  $T$  is the time-reversal operator. As a result, we can say that there is no stray magnetic fields in the junction. This implies that  $\beta \propto B_y$ . For  $\Delta I_c$ , we obtain

$$\Delta I_c = I_c^+(\Phi, \delta) - |I_c^-(\Phi, \delta)|,$$

$$I_c^\pm(\Phi, \delta) = f_\pm(\Phi, \delta) \frac{\sin\left(\frac{\pi\Phi}{\Phi_0}\right)}{\frac{\pi\Phi}{\Phi_0}}$$

where

$$f_+(\Phi, \delta) = \max_\phi [I_1 \sin(\phi + \varphi_0(\Phi)) + I_2 \sin(2\phi + \delta) \cos(\pi\Phi/\Phi_0)]$$

$$f_-(\Phi, \delta) = \min_\phi [I_1 \sin(\phi + \varphi_0(\Phi)) + I_2 \sin(2\phi + \delta) \cos(\pi\Phi/\Phi_0)]$$

which gives

$$\Delta I_c = \frac{\sin\left(\frac{\pi\Phi}{\Phi_0}\right)}{\frac{\pi\Phi}{\Phi_0}} \Delta f,$$

where  $\Delta f \equiv f_+ - f_-$ . Here, we find the extrema of  $f_\pm$  within the range  $-\pi \leq \phi \leq \pi$ . For small  $I_2/I_1$ , this reduces to

$$\Delta I_c = -2I_2 \sin \delta \frac{\sin\left(\frac{2\pi\Phi}{\Phi_0}\right)}{\frac{2\pi\Phi}{\Phi_0}}$$

which is the same as that obtained in equation (5) of the main text. Though the parameter  $\beta$  modifies  $I_c^+$  and  $I_c^-$  of L1 under a magnetic flux ( $\Phi$ ), this additional term in the CPR,  $\varphi_0(\Phi)$  has

no bearing on the magnitude or periodicity of  $\Delta I_c$  at  $\Phi = 0$ . Hence, the CPR discussed in the main text holds in general and can be used to explain the main experimental results on  $\Delta I_c$  in the main text.

The lifted nodes encountered in the Fraunhofer patterns can be accounted for by adding the contribution of a long diffusive junction (assuming  $L > \ell$  where  $\ell$  is the electron mean free path) as

$$I_D^\pm = \alpha I_c^\pm(0) E^{-\sigma^2 \left(\frac{\Phi}{\Phi_0}\right)^2},$$

where  $\alpha$  and  $\sigma$  are constant. As a result,

$$I_{c,\text{tot}}^\pm = I_c^\pm(\Phi) + I_D^\pm.$$

### C. Flux focusing and Estimation of effective junction area for diffraction pattern calculations in PtTe<sub>2</sub> junctions

In order to properly estimate the period of oscillations in the observed diffraction pattern, it is important to precisely calculate the effective area of the junction through which the Josephson current flows and the effective magnetic flux through the junction. This is done by first calculating the effective area of the junction including the London penetration depth and then the effective flux through the junction including flux focusing effects.

Since the junctions on the PtTe<sub>2</sub> flake are shaped like a trapezoid, which is a regular quadrilateral, it makes the calculation of the effective junction area easier. While calculating the area of the junction, it is important to take into account the London penetration depth ( $\lambda$ ) of the niobium electrodes that can increase the effective separation between the two superconducting electrodes. The London penetration depth for thin films of niobium can vary from 37 nm, which is the bulk value up to 200 nm for different thicknesses and temperatures<sup>151-153</sup>. We use a  $\lambda$  value of  $\sim 100$  nm as reported in literature<sup>151</sup> for films of thicknesses used in our junctions. That would

make the effective junction separation to be  $d_{eff} = (2\lambda + d)$ . Then the area of the junction is calculated by using the formula for area of a trapezium  $A = \left(\frac{a+b}{2}\right) \cdot d_{eff}$ , where  $a$  and  $b$  are lengths of the edges of the junction along the electrodes. Using the values estimated from the SEM image in Fig. 5.7, this would give an effective junction area of around  $3.5665 \mu m^2$  for L1. If we use this as the area of the junction, the magnetic flux through the junction can be calculated as  $\Phi = B_z \cdot A$  and this magnetic flux normalized to the magnetic flux quantum  $\left(\Phi_0 = \frac{h}{2e}\right)$  would be  $\left(\frac{\Phi}{\Phi_0}\right)$ . The Fraunhofer pattern in these units is presented in Fig. S8a. As it can be observed, the period of oscillations seem to be around  $\left(\frac{\Phi_0}{2}\right)$ . Ideally, this would only be possible in the case where the second harmonic term in the current-phase relationship (CPR) is the dominant term and the first harmonic component is virtually non-existent in the junction. The expected Fraunhofer patterns for various ratios of the second and first-harmonic components  $\left(\frac{I_2}{I_1}\right)$  is presented in Fig. C.1. It can be seen that in order to obtain prominent second harmonic oscillations, as we do in our measurements the second order term ( $I_2$ ) needs to be much larger than the first-order term ( $I_1$ ). However, we argue that this is not the case in our junctions as the second order term stems as a perturbation and can't be larger than the first-order term. We also argue that the observed period is purely coincidental due to the effect of flux focusing that is very well known to occur in lateral Josephson junctions.<sup>127,128</sup>

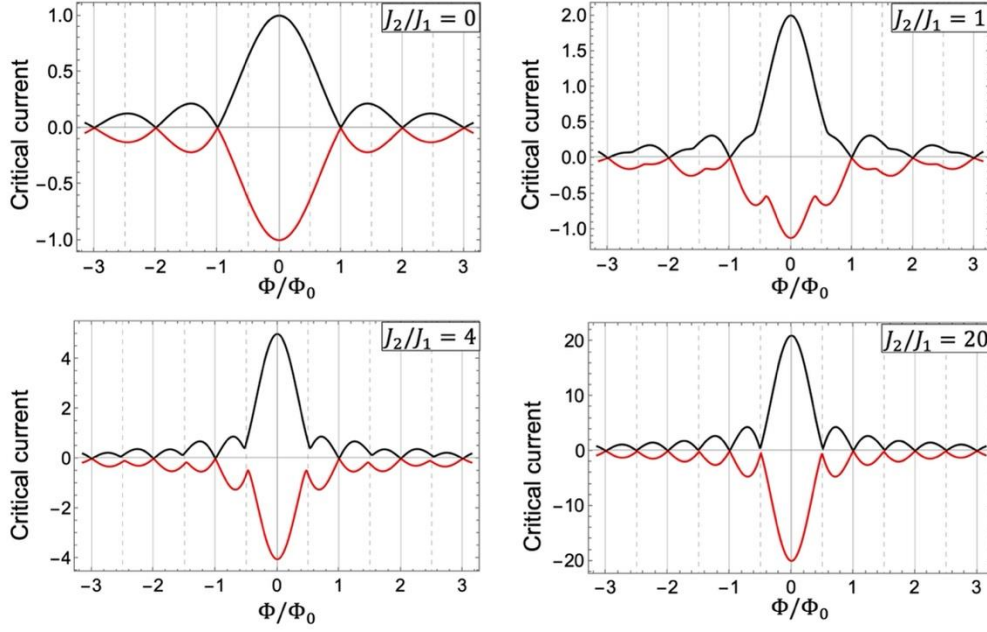


**Fig. C.1** The calculated Fraunhofer interference pattern for various values of  $I_2/I_1$ : (a)-(d) The simulated Fraunhofer patterns expected for various values of  $J_2/J_1 \equiv I_2/I_1$ . It can be seen that in order to get prominent  $\left(\frac{\Phi_0}{2}\right)$ -periodic oscillations as we observe in our measurements, the ratio of  $I_2/I_1$  needs to be very large.

When a magnetic field is applied to a lateral Josephson junction, the Meissner screening currents in the superconducting electrodes deflect a portion of the magnetic flux towards the junction that results in an increased effective magnetic flux than that expected. This is known as the flux focusing effect, which modifies the expected spacing of nodes in Fraunhofer pattern from  $\Phi$  to some  $\Gamma\Phi$ , where the flux scaling factor  $\Gamma$  is given by<sup>128</sup>:

$$\Gamma = \frac{n\Phi_0}{B_z^{(n)}LW},$$

where  $L = 590 \text{ nm}$ ,  $W \approx 6 \text{ }\mu\text{m}$  are the junction length and width (for junction L1).  $B_z^{(n)}$  is the out of the plane magnetic field at node  $n$ . A uniform spacing of the nodes are observed as the niobium electrodes are deep in the superconducting state at  $20 \text{ mK}$  and the Meissner screening effects are constant over the scanned range of  $B_z$ . For  $n = 1$ , we have  $B_z^{(n)} = 0.3 \text{ mT}$ , which gives  $\Gamma \approx 1.9$

that accounts for the observed  $\sim\left(\frac{\Phi_0}{2}\right)$  period of the oscillation in the measurements. The Fraunhofer pattern after flux focusing correction is presented in Fig. C.2. The period of oscillations match well with the expected  $\Phi_0$  after accounting for flux focusing effects.

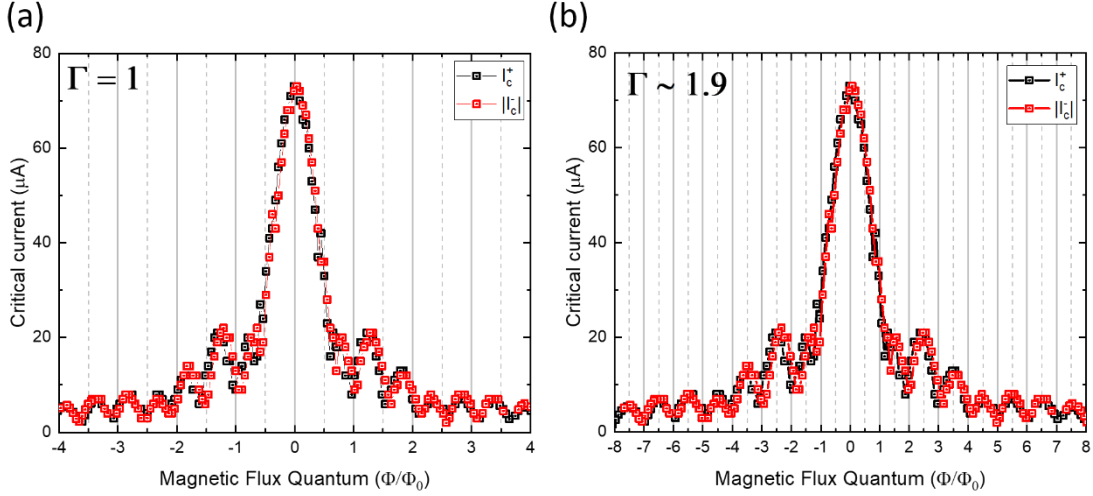


**Fig. C.2** The Fraunhofer interference pattern for L1 under before and after correcting for flux focusing: (a) The as-plotted Fraunhofer patterns for both  $I_c^+$  and  $I_c^-$  are found to have a  $\left(\frac{\Phi_0}{2}\right)$  period before flux focusing correction ( $\Gamma = 1$ ). (b) The Fraunhofer pattern after correcting the applied magnetic flux with the calculated flux scaling factor ( $\Gamma \sim 1.9$ ) matches well with the expected  $\Phi_0$  period.

#### D. Effect of finite thickness of PtTe<sub>2</sub> flake on the interference pattern

When the critical current of the junction is measured as a function of the magnetic flux along the z-axis ( $B_z$ ) which induces a phase difference between the superconducting electrodes, we see the expected Fraunhofer interference pattern. When the Fraunhofer pattern is mapped as a function of different in-plane magnetic fields along the y-axis ( $B_y$ ), we observe that there is a shift of the whole Fraunhofer pattern along the  $B_z$  axis with increasing  $B_y$ , which can be identified by tracking the position of the central maxima. The reason for this shift is the finite thickness of the

sample ( $17.5 \text{ nm}$ ), which causes the applied  $B_y$  to produce an additional magnetic flux along the  $xz$ -plane and hence an additional phase shift that translates the entire Fraunhofer pattern. This shift has also been observed previously as a tilt of the entire Fraunhofer map in similar measurements used to estimate finite-momentum of the Cooper pairs in Josephson junctions<sup>1,96,97</sup>. This tilt is then corrected by subtracting a linear slope that brings the central Fraunhofer maxima back to zero  $B_z$ .

In our measurements to track the evolution of  $I_c^+$  and  $I_c^-$  in the Fraunhofer oscillations with  $B_y$ , we employ a similar procedure to correct for the observed shift of the Fraunhofer pattern by fixing the position of the central maxima at  $B_z = 0 \text{ mT}$ . Below we show the Fraunhofer patterns as measured at different values of  $B_y$  (Fig. D.1 (a-d)) and after performing the shift correction (Fig. D.1 (e-h)) for junction L1. When  $B_y$  is increased beyond  $30 \text{ mT}$  it becomes hard to track the central peak, so the slope of the peak shift with  $B_y$  at lower values of  $B_y$  can be used to do the shift correction. All Fraunhofer pattern analyses presented in the main text of the thesis are done after performing this correction.



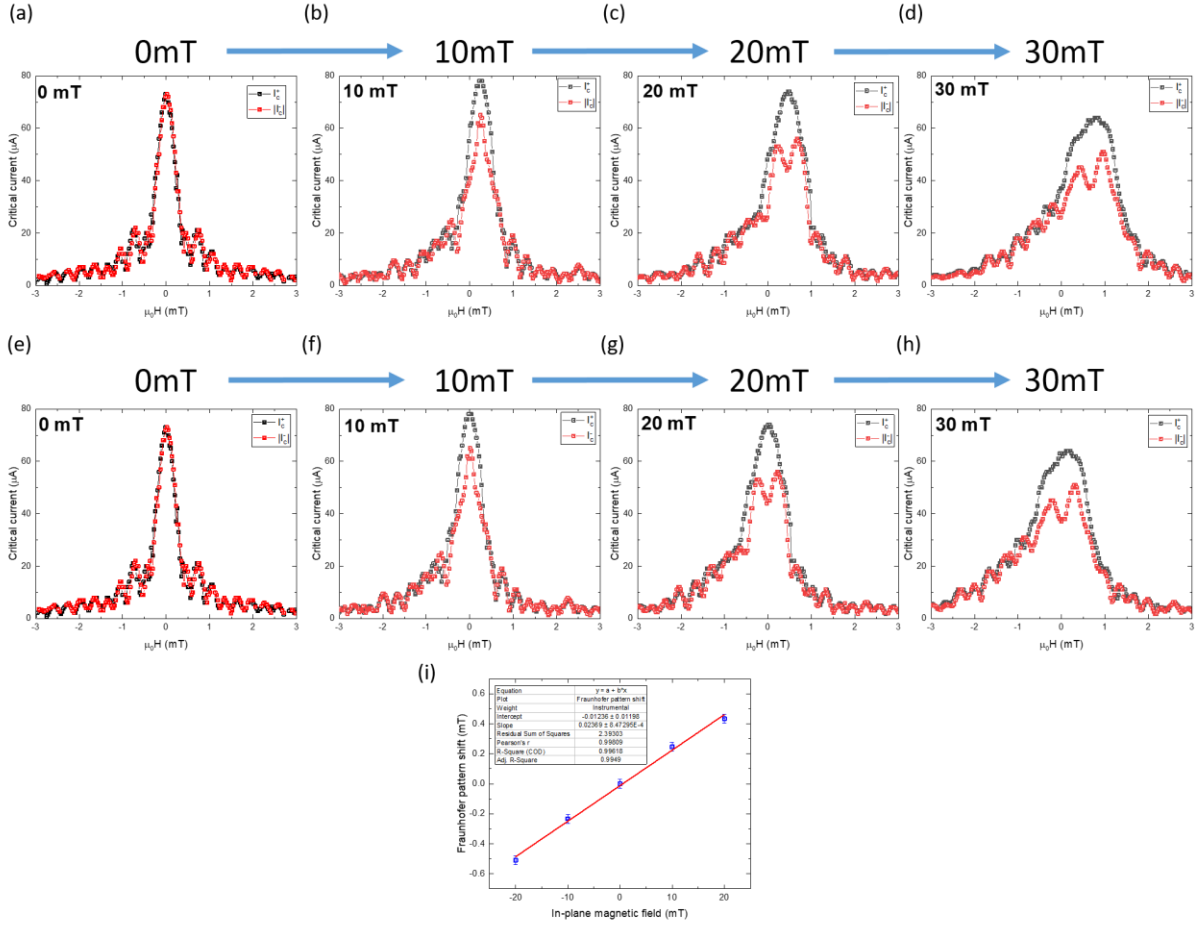


**Fig. D.1 Evolution of Fraunhofer pattern for  $L1$  under an in-plane magnetic field and shift correction:** (a)-(d) The Fraunhofer patterns for both  $I_c^+$  and  $I_c^-$  are found to shift towards the right side along positive  $B_z$  values for increasing positive values of  $B_y$  and similarly along negative  $B_z$  values for negative values of  $B_y$ . (e)-(h) The Fraunhofer patterns for different positive  $B_y$  values after performing the shift correction setting the central maxima of  $I_c^+$  to be at  $B_z = 0$  mT. (i) Plot showing the linear shift of the Fraunhofer pattern with an in-plane magnetic field  $B_y$ .

## E. Josephson Diode effect in other NiTe<sub>2</sub> devices

In addition to the results presented in the device above, Josephson diode effect has also been observed in other NiTe<sub>2</sub> junctions made with flakes of other thicknesses and similar results have been found. Josephson junctions of 500 (B1) and 600 nm (B2) separations have been fabricated on a 40 nm thick flake of NiTe<sub>2</sub> as shown in Fig. E.1(a). Large critical currents are observed in both devices. Josephson diode effect measured in device B2 is presented in Fig. E.1(b)-(f). A large critical current of around 200  $\mu\text{A}$  in both positive and negative directions in the absence of any applied magnetic field as in Fig. E.1(b). When the in-plane magnetic field is increased, the difference in critical currents also increases as shown in Fig. E.1(d) and (e) and reaches maximum value around 36 mT. At this value,  $\Delta I_c$  reaches a value of around 106  $\mu\text{A}$  as shown in Fig. E.1(c) with a maximum efficiency around 40% (Fig. E.1(f)).

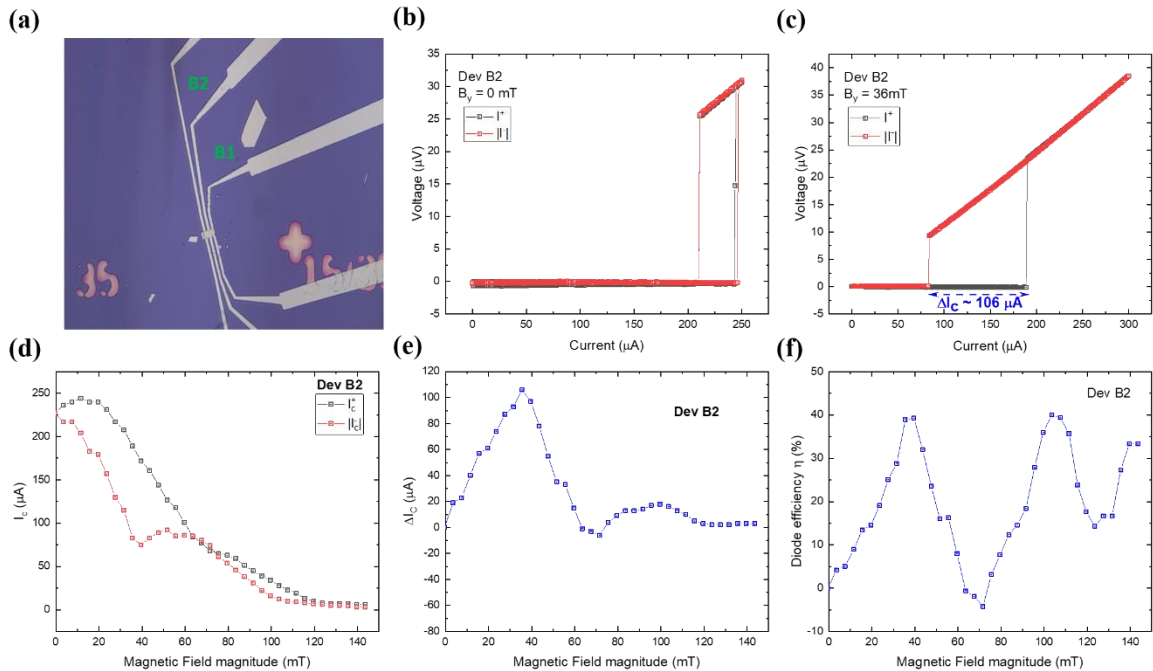


**Fig. E.1 Josephson Diode effect in a 40nm thick NiTe<sub>2</sub> flake:** (a) Optical microscope image of Josephson junctions fabricated on a 40 nm thick NiTe<sub>2</sub> flake with junctions labelled as B1 and B2. (b) Current-Voltage characteristics of junction B2 in the absence an applied in-plane magnetic field a critical current of 246  $\mu\text{A}$  in both directions and a negligible  $\Delta I_c$ . (c) In the presence of a

36 mT magnetic field perpendicular to the current,  $\Delta I_c$  reaches a maximum value of around 106  $\mu\text{A}$ . (d)  $I_c^+$  and  $|I_c^-|$  plotted as a function of in-plane magnetic field perpendicular to current. (e)  $\Delta I_c$  is found to increase as a function of magnetic field and reaches maximum value around 36 mT and oscillate as the magnetic field is increased further. (f) The efficiency of the diode also oscillates with the in-plane magnetic field with a maximum value of 40%.

Another interesting feature observed in these junctions of NiTe<sub>2</sub> is the extremely large critical currents over such long distances of few hundred nanometers. In addition, critical currents were measured for multiple devices of various separations ( $L$ ) in order to check the limit of supercurrent propagation through NiTe<sub>2</sub>. Non-zero critical currents were observed in junctions with separations up to 1.65  $\mu\text{m}$ . The critical current measured in the junction with the largest separation was around 34 nA.

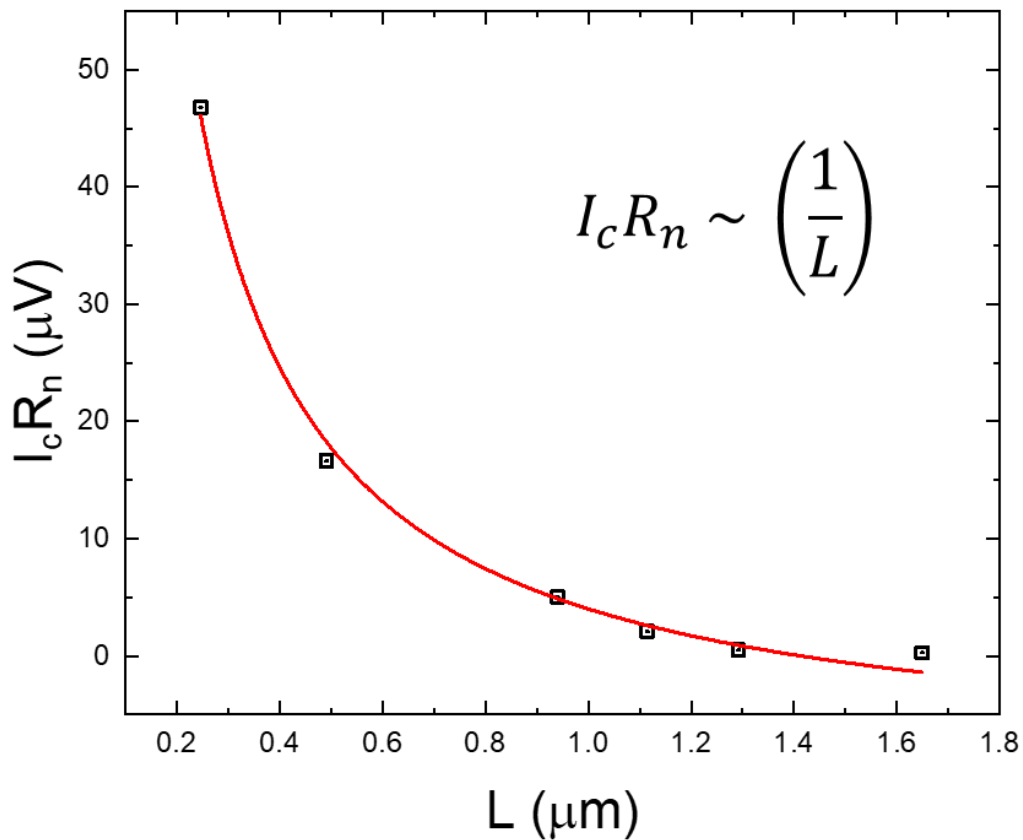


**Fig. E.2 Distance dependence of  $I_c R_n$  in  $\text{NiTe}_2$  Josephson junctions:** The  $I_c R_n$  products measured in several Josephson junctions with various separations show that the supercurrents persist even up to junction lengths of  $1.65 \mu\text{m}$  and that  $I_c R_n$  decays as  $\left(\frac{1}{L}\right)$ , as expected for a ballistic junction<sup>154</sup>.

## F. Evolution of Fraunhofer pattern in other $\text{PtTe}_2$ devices

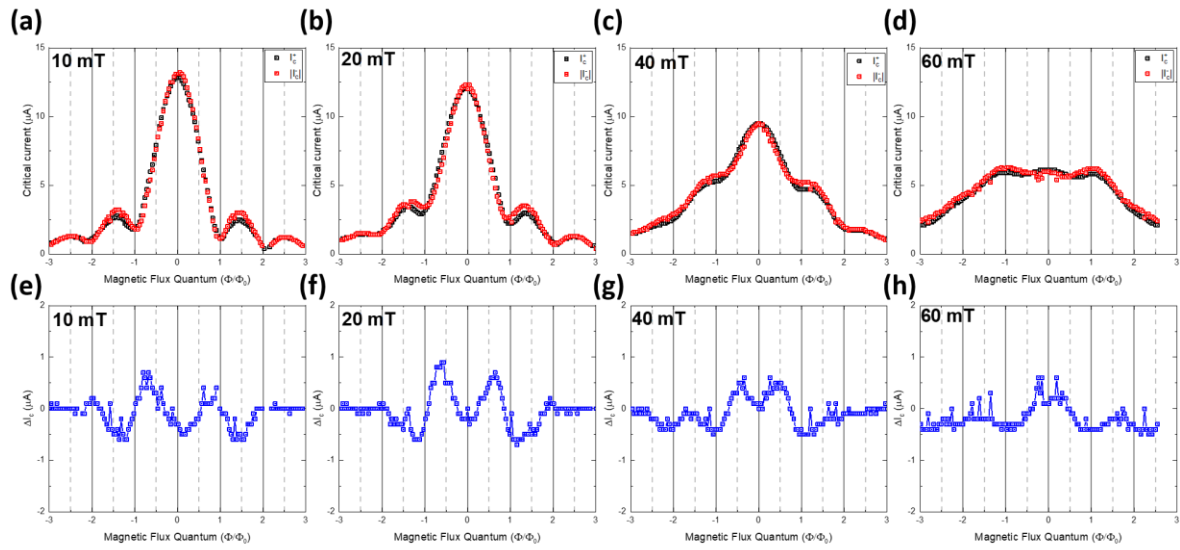


**Fig. F.1 Evolution of the Fraunhofer pattern in the presence of  $\Delta I_c$  for  $L4$ :** (a)-(d) The Fraunhofer patterns for both  $I_c^+$  and  $I_c^-$  for  $L4$  with increasing  $B_y$ . (e)-(h) Corresponding  $\Delta I_c$  for the Fraunhofer patterns.  $\Delta I_c$  in this case is very small and the oscillations are barely discernible.

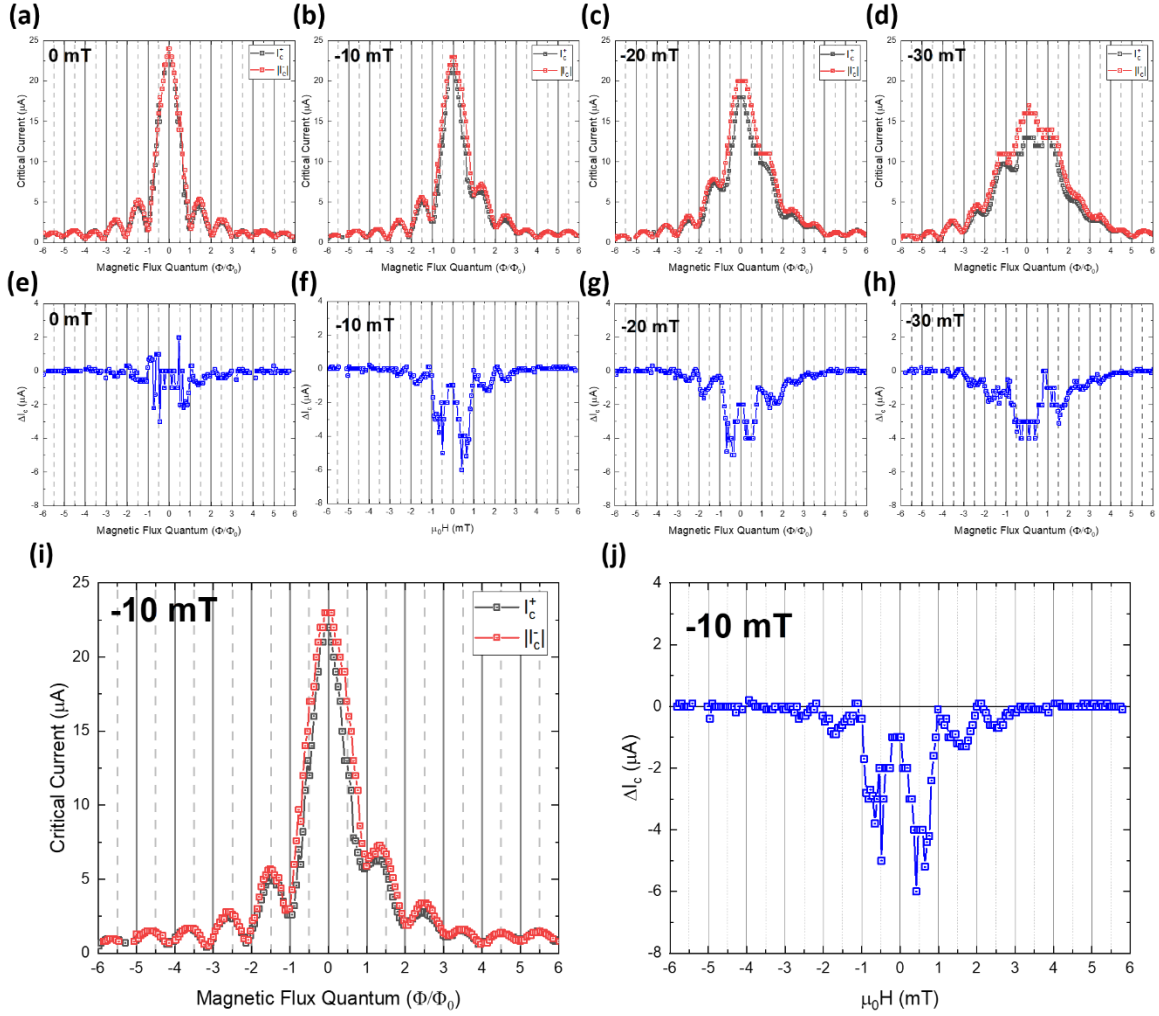


**Fig. F.2** Evolution of the Fraunhofer pattern in the presence of  $\Delta I_c$  for L3: (a)-(d) The Fraunhofer patterns for both  $I_c^+$  and  $I_c^-$  for L3 with increasing  $B_y$ . (e)-(h) Corresponding  $\Delta I_c$  for the Fraunhofer patterns.  $\Delta I_c$  for L3 is much smaller compared to L1 as the critical current is also smaller but the  $\left(\frac{\Phi_0}{2}\right)$  period of the oscillations can still be distinguished. (i),(j) Larger image of the  $-10$  mT data with only a couple of oscillations visible in  $\Delta I_c$ .

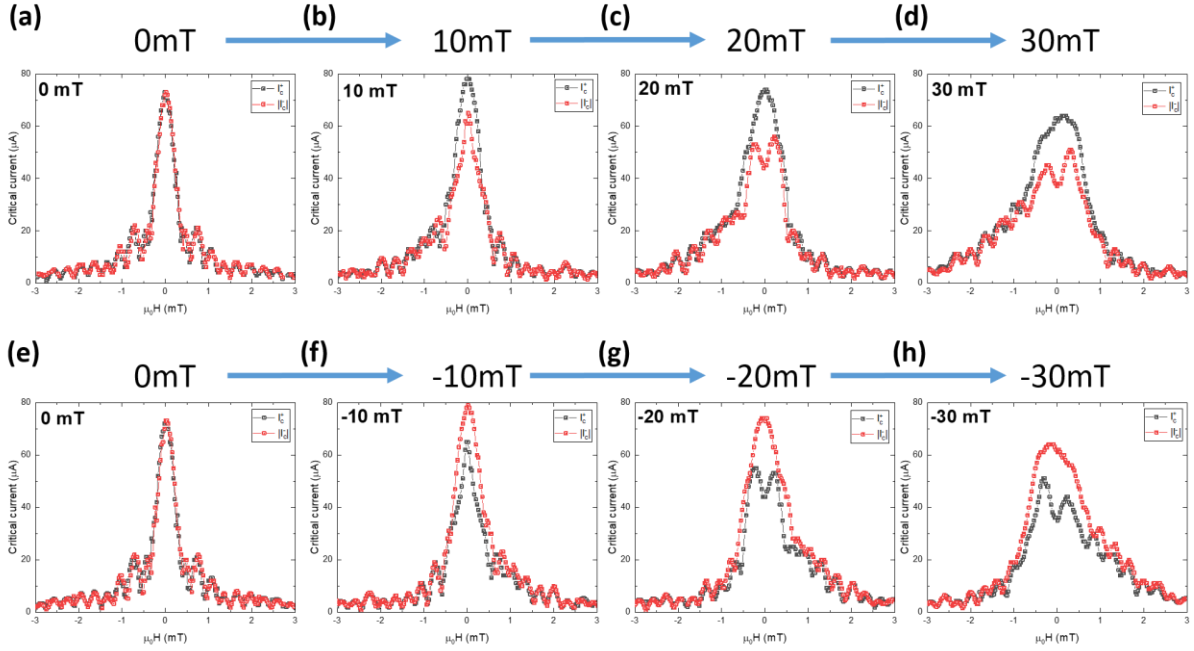


**Fig. F.3** The Fraunhofer interference pattern for LI under positive and negative magnetic fields after shift correction: (a)-(d) The Fraunhofer patterns for  $I_c^+$  and  $I_c^-$  measured in the presence of a positive  $B_y$  magnetic field as shown in the main text. (e)-(h) The Fraunhofer pattern for  $I_c^+$  and  $I_c^-$  measured in the presence of a negative  $B_y$  magnetic field. The behavior of  $I_c^+$  and  $I_c^-$  are reversed under opposite  $B_y$  but maintain the symmetry  $I_c^\pm(B_y, B_z) = I_c^\mp(-B_y, -B_z)$ .

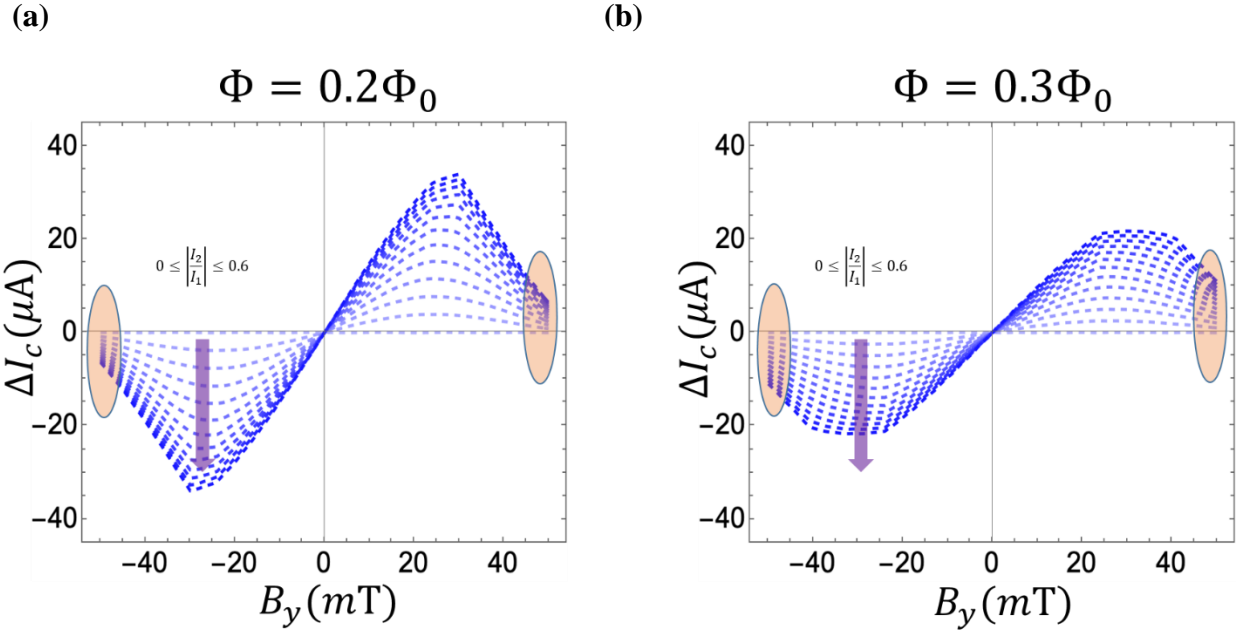


**Fig. F.4 Behavior of  $\Delta I_c$  in presence of a small magnetic flux:** In case the magnetic field is not perfectly aligned to the plane of the sample, it can give rise to a small flux that can affect the behavior of  $\Delta I_c$  and lead to lifted nodes as observed in the experimental data in Fig. 5.12 (c). Simulated  $\Delta I_c$  for (a)  $\Phi = 0.2\Phi_0$  and (b)  $\Phi = 0.3\Phi_0$  and different values of  $\frac{I_2}{I_1}$ .

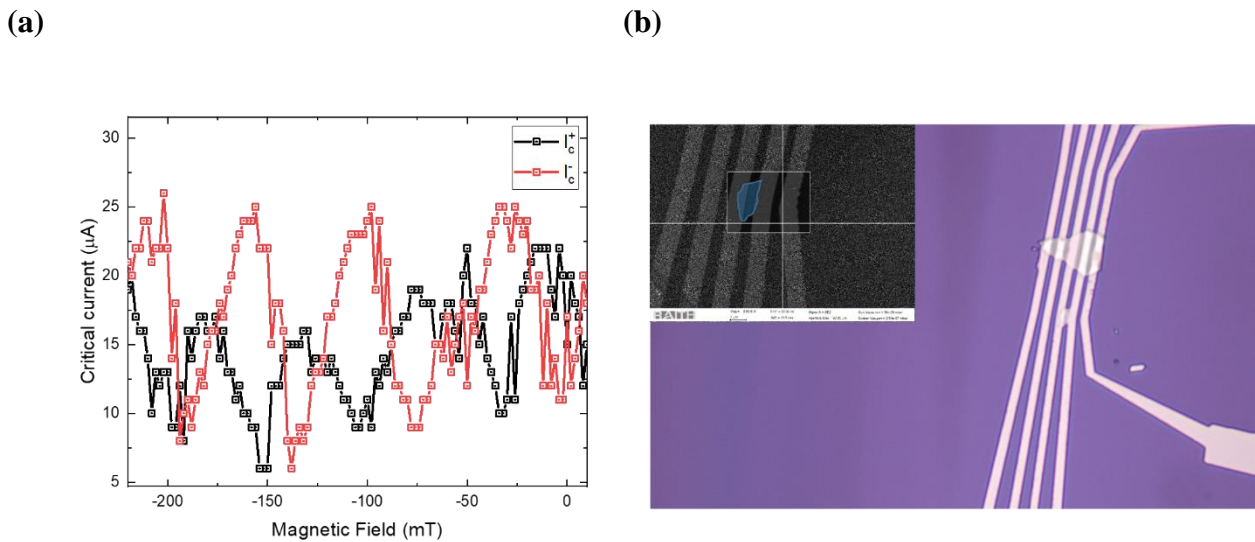
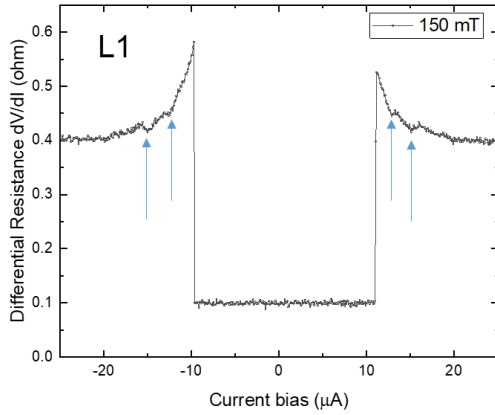


**Fig. F.5 Accidental SQUID in junction L2:** Junction L2 is shorted by another flake of PtTe<sub>2</sub> by accident forming an asymmetric SQUID loop. The asymmetric SQUID also shows non-reciprocal

critical currents with  $B_y$  and highly skewed non-sinusoidal oscillations providing further evidence of the presence of higher harmonics in the CPR.

(a)



(b)

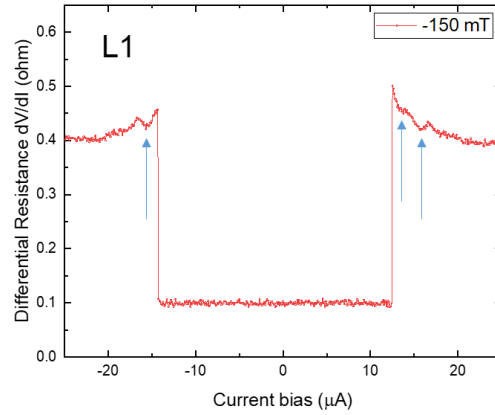


**Fig. F.6 Possible multiple Andreev reflections :** The differential resistance of L1 measured when the critical currents are strongly suppressed with a magnetic field display some dips in resistance at low currents which is present due to resonance in the tunneling process indicative of coherent processes in the junction. Multiple Andreev reflections in the junction are expected to occur at voltages, which require very large currents and can only be reached above the critical current of the superconducting electrodes.



## G Field-free $\Delta I_c$ from self-field effects in PtTe<sub>2</sub> Josephson junction

As discussed in the main text, self-fields arise as a result of the non-uniform current distribution present while passing currents in a long or wide Josephson junction. This self-field has the ability to break the time-reversal symmetry of the junction without the need for an external magnetic field, which can then be used to construct devices that do not require any external magnetic fields. This was realized in one of the PtTe<sub>2</sub> junctions, that was the widest (L1). The junction L1 has two superconducting niobium electrodes with four terminals as shown in Fig. 5.8(a). Applying a current bias through the terminals located on the same side leads to a self-field effect, as evidenced by the skewed Fraunhofer oscillations shown in Fig. 5.8(b). Utilizing this idea, a constant current bias was applied between the terminals on the same side to create a self-field effect while the current voltage characteristics were measured in the criss-crossed configuration as shown in Fig. G.1(a). It is to be noted that the applied current bias creates a shift of the entire  $I - V$  curve by the amount of  $I_{bias}$  applied. However, this does not reflect the actual net current across the junction and the as measured critical currents ( $I_{c,meas}^+, I_{c,meas}^-$ ) cannot be used for calculating the Josephson diode effect. The shift of the  $I - V$  curve must not be confused with the self-field effect.  $I_{bias}$  needs to be removed before estimating the actual  $I_c^+$  and  $I_c^-$ . (i.e.)

$$I_c^+ = I_{c,meas}^+ - I_{bias}$$

$$I_c^- = I_{c,meas}^- - I_{bias}$$

The  $I_c^+$  and  $I_c^-$  measured as a function of  $I_{bias}$  is shown in Fig. G.1(b). It can be seen that as  $I_{bias}$  is increased the difference between  $I_c^+$  and  $I_c^-$  starts to increase, leading to a  $\Delta I_c$ . When the direction of  $I_{bias}$  is reversed, the direction of  $\Delta I_c$  is reversed as well. In the absence of self-field effect, typically  $\Delta I_c = 0$  after correcting the shift due to  $I_{bias}$ .  $\Delta I_c$  increases linearly with  $I_{bias}$  as shown in Fig. G.1(c) leading to a maximum diode efficiency of around 14% as shown in Fig. G.1(d). This shows that in transparent wide junctions, it is possible to engineer a diode effect without the need for an external magnetic field. The magnetic fields created by the non-uniform current distribution and  $\Delta I_c$  in the PtTe<sub>2</sub> junction is not as high as that from an external field. However, investigating and optimizing controlled geometries that can maximize the self-field

effect could be a future direction that could be of great interest as it can be used to create three-terminal Josephson diodes in which  $\Delta I_c$  can be easily tuned by the  $I_{bias}$  and doesn't have the need for an external magnetic field.

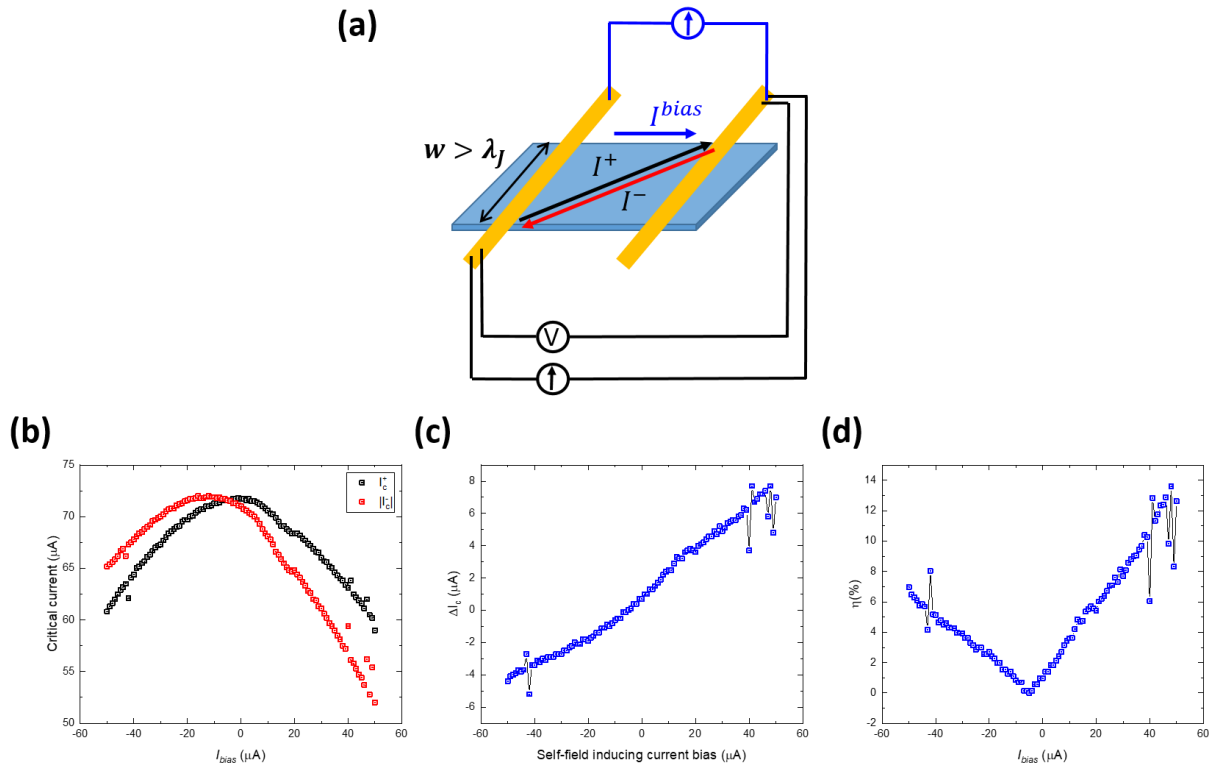


**Fig. G.1 Field-free  $\Delta I_c$  from self-field effect in PtTe<sub>2</sub> junction LI:** (a) Geometry of current biasing for creating non-reciprocal critical currents with help of self-field currents. (b) The difference between  $I_c^+$  and  $|I_c^-|$  is shown to increase with  $I_{bias}$ . (c)  $\Delta I_c$  can be seen to increase linearly with  $I_{bias}$ . (d) A maximum efficiency of close to 14% is achieved from the self-field currents.

# Bibliography

---

- 1 Pal, B. *et al.* Josephson diode effect from Cooper pair momentum in a topological semimetal. *Nat. Phys.* **18**, 1228-1233 (2022). <https://doi.org:10.1038/s41567-022-01699-5>
- 2 Wu, H. *et al.* The field-free Josephson diode in a van der Waals heterostructure. *Nature* **604**, 653-656 (2022). <https://doi.org:10.1038/s41586-022-04504-8>
- 3 Moore, G. Cramming more components onto integrated circuits. *Electronics* **38** (1965).
- 4 Clarke, J. & Wilhelm, F. K. Superconducting quantum bits. *Nature* **453**, 1031-1042 (2008). <https://doi.org:10.1038/nature07128>
- 5 Hilgenkamp, H. Josephson Memories. *J. Supercond. Nov. Magn.* **34**, 1621-1625 (2021). <https://doi.org:10.1007/s10948-020-05680-2>
- 6 Ando, F. *et al.* Observation of superconducting diode effect. *Nature* **584**, 373-376 (2020). <https://doi.org:10.1038/s41586-020-2590-4>
- 7 Baumgartner, C. *et al.* Supercurrent rectification and magnetochiral effects in symmetric Josephson junctions. *Nat. Nanotechnol.* **17**, 39-44 (2022).
- 8 Bahramy, M. S. *et al.* Ubiquitous formation of bulk Dirac cones and topological surface states from a single orbital manifold in transition-metal dichalcogenides. *Nature Mater.* **17**, 21-28 (2018). <https://doi.org:10.1038/nmat5031>
- 9 Fulde, P. & Ferrell, R. A. Superconductivity in a strong spin-exchange field. *Phys. Rev.* **135**, A550 (1964).
- 10 Larkin, A. & Ovchinnikov, Y. N. Nonuniform state of superconductors. *Sov. Phys. JETP* **20**, 762-762 (1965).
- 11 Zhang, P. *et al.* Large Second-Order Josephson Effect in Planar Superconductor-Semiconductor Junctions. *arXiv preprint arXiv:2211.07119* (2022).
- 12 Murani, A. *et al.* Ballistic edge states in Bismuth nanowires revealed by SQUID interferometry. *Nat. Commun.* **8**, 15941 (2017). <https://doi.org:10.1038/ncomms15941>
- 13 Onnes, H. K. On the change of electric resistance of pure metals at very low temperatures, etc. V. The disappearance of the resistance of mercury. *Comm. Phys. Lab. Univ. Leiden* **122b** (1911).

- 14 Meissner, W. & Ochsenfeld, R. Ein neuer Effekt bei Eintritt der Supraleitfähigkeit. *Naturwissenschaften* **21**, 787-788 (1933). <https://doi.org:10.1007/BF01504252>
- 15 Ginzburg, V. L. & Landau, L. D. *Zh. Eksp. Teor. Fiz.* **20**, 1064-1082 (1950).
- 16 Bardeen, J., Cooper, L. N. & Schrieffer, J. R. Microscopic Theory of Superconductivity. *Phys. Rev.* **106**, 162-164 (1957). <https://doi.org:10.1103/PhysRev.106.162>
- 17 Gor'kov, L. P. Microscopic derivation of the Ginzburg-Landau equations in the theory of superconductivity. *Sov. Phys. JETP* **9**, 1364-1367 (1959).
- 18 Josephson, B. D. Possible new effects in superconductive tunnelling. *Physics Letters* **1**, 251-253 (1962). [https://doi.org:https://doi.org/10.1016/0031-9163\(62\)91369-0](https://doi.org:https://doi.org/10.1016/0031-9163(62)91369-0)
- 19 Bednorz, J. G. & Müller, K. A. Possible highT<sub>c</sub> superconductivity in the Ba-La-Cu-O system. *Zeitschrift für Physik B Condensed Matter* **64**, 189-193 (1986). <https://doi.org:10.1007/BF01303701>
- 20 Mackenzie, A. P. & Maeno, Y. The superconductivity of Sr<sub>2</sub>RuO<sub>4</sub> and the physics of spin-triplet pairing. *Rev. Mod. Phys.* **75**, 657-712 (2003). <https://doi.org:10.1103/RevModPhys.75.657>
- 21 Schemm, E. R., Gannon, W. J., Wishne, C. M., Halperin, W. P. & Kapitulnik, A. Observation of broken time-reversal symmetry in the heavy-fermion superconductor UPt<sub>3</sub>. *Science* **345**, 190-193 (2014). <https://doi.org:doi:10.1126/science.1248552>
- 22 Jiao, L. *et al.* Chiral superconductivity in heavy-fermion metal UTe<sub>2</sub>. *Nature* **579**, 523-527 (2020). <https://doi.org:10.1038/s41586-020-2122-2>
- 23 Bauer, E. *et al.* Heavy Fermion Superconductivity and Magnetic Order in Noncentrosymmetric CePt<sub>3</sub>Si. *Phys. Rev. Lett.* **92**, 027003 (2004). <https://doi.org:10.1103/PhysRevLett.92.027003>
- 24 Khim, S. *et al.* Field-induced transition within the superconducting state of CeRh<sub>2</sub>As<sub>2</sub>. *Science* **373**, 1012-1016 (2021). <https://doi.org:doi:10.1126/science.abe7518>
- 25 Bergeret, F. S., Volkov, A. F. & Efetov, K. B. Odd triplet superconductivity and related phenomena in superconductor-ferromagnet structures. *Rev. Mod. Phys.* **77**, 1321-1373 (2005). <https://doi.org:10.1103/RevModPhys.77.1321>
- 26 Tinkham, M. *Introduction to superconductivity*. (Courier Corporation, 2004).
- 27 London, F. & London, H. The electromagnetic equations of the supraconductor. *Proc. R. Soc. of London. Series A Math. Phys. Eng.* **149**, 71-88 (1935). <https://doi.org:doi:10.1098/rspa.1935.0048>

- 28 Abrikosov, A. A. The magnetic properties of superconducting alloys. *J. Phys. Chem. Solids* **2**, 199-208 (1957). [https://doi.org:https://doi.org/10.1016/0022-3697\(57\)90083-5](https://doi.org/10.1016/0022-3697(57)90083-5)
- 29 Cooper, L. N. Bound Electron Pairs in a Degenerate Fermi Gas. *Phys. Rev.* **104**, 1189-1190 (1956). [https://doi.org:10.1103/PhysRev.104.1189](https://doi.org/10.1103/PhysRev.104.1189)
- 30 Bogoljubov, N. N. On a new method in the theory of superconductivity. *Il Nuovo Cimento (1955-1965)* **7**, 794-805 (1958). [https://doi.org:10.1007/BF02745585](https://doi.org/10.1007/BF02745585)
- 31 Valatin, J. G. Comments on the theory of superconductivity. *Il Nuovo Cimento (1955-1965)* **7**, 843-857 (1958). [https://doi.org:10.1007/BF02745589](https://doi.org/10.1007/BF02745589)
- 32 Kinjo, K. *et al.* Superconducting spin smecticity evidencing the Fulde-Ferrell-Larkin-Ovchinnikov state in Sr<sub>2</sub>RuO<sub>4</sub>. *Science* **376**, 397-400 (2022). [https://doi.org:doi:10.1126/science.abb0332](https://doi.org/doi:10.1126/science.abb0332)
- 33 Yuan, N. F. & Fu, L. Topological metals and finite-momentum superconductors. *Proc. Natl. Acad. Sci. USA* **118**, e2019063118 (2021).
- 34 Bianchi, A., Movshovich, R., Capan, C., Pagliuso, P. G. & Sarrao, J. L. Possible Fulde-Ferrell-Larkin-Ovchinnikov Superconducting State in CeCoIn<sub>5</sub>. *Phys. Rev. Lett.* **91**, 187004 (2003). [https://doi.org:10.1103/PhysRevLett.91.187004](https://doi.org/10.1103/PhysRevLett.91.187004)
- 35 Kenzelmann, M. *et al.* Coupled Superconducting and Magnetic Order in CeCoIn<sub>5</sub>. *Science* **321**, 1652-1654 (2008). [https://doi.org:doi:10.1126/science.1161818](https://doi.org/doi:10.1126/science.1161818)
- 36 Agosta, C. C. *et al.* Experimental and semiempirical method to determine the Pauli-limiting field in quasi-two-dimensional superconductors as applied to K-(BEDT-TTF)<sub>2</sub>Cu(NCS)<sub>2</sub>: Strong evidence of a FFLO state. *Phys. Rev. B* **85**, 214514 (2012). [https://doi.org:10.1103/PhysRevB.85.214514](https://doi.org/10.1103/PhysRevB.85.214514)
- 37 Devarakonda, A. *et al.* Signatures of bosonic Landau levels in a finite-momentum superconductor. *Nature* **599**, 51-56 (2021). [https://doi.org:10.1038/s41586-021-03915-3](https://doi.org/10.1038/s41586-021-03915-3)
- 38 Wan, P. *et al.* Orbital Fulde-Ferrell-Larkin-Ovchinnikov state in an Ising superconductor. *Nature* **619**, 46-51 (2023). [https://doi.org:10.1038/s41586-023-05967-z](https://doi.org/10.1038/s41586-023-05967-z)
- 39 Anderson, P. W. & Rowell, J. M. Probable Observation of the Josephson Superconducting Tunneling Effect. *Phys. Rev. Lett.* **10**, 230-232 (1963). [https://doi.org:10.1103/PhysRevLett.10.230](https://doi.org/10.1103/PhysRevLett.10.230)
- 40 Barone, A. *Physics and Applications of the Josephson Effect*. (Wiley, 2006).
- 41 Krylov, G. & Friedman, E. G. in *Single Flux Quantum Integrated Circuit Design* 15-38 (Springer International Publishing, 2022).

- 42 Wiedenmann, J. *et al.*  $4\pi$ -periodic Josephson supercurrent in HgTe-based topological  
Josephson junctions. *Nat. Commun.* **7**, 10303 (2016). <https://doi.org:10.1038/ncomms10303>
- 43 Van Harlingen, D. J. Phase-sensitive tests of the symmetry of the pairing state in the high-  
temperature superconductors-Evidence for  $d_{x^2-y^2}$  symmetry. *Rev. Mod. Phys.* **67**, 515-535  
(1995). <https://doi.org:10.1103/RevModPhys.67.515>
- 44 Tokura, Y. & Nagaosa, N. Nonreciprocal responses from non-centrosymmetric quantum  
materials. *Nat. Commun.* **9**, 3740 (2018). <https://doi.org:10.1038/s41467-018-05759-4>
- 45 Onsager, L. Reciprocal Relations in Irreversible Processes. I. *Phys. Rev.* **37**, 405-426 (1931).  
<https://doi.org:10.1103/PhysRev.37.405>
- 46 Casimir, H. B. G. On Onsager's Principle of Microscopic Reversibility. *Rev. Mod. Phys.* **17**,  
343-350 (1945). <https://doi.org:10.1103/RevModPhys.17.343>
- 47 Morimoto, T. & Nagaosa, N. Nonreciprocal current from electron interactions in  
noncentrosymmetric crystals: roles of time reversal symmetry and dissipation. *Sci. Rep.* **8**,  
2973 (2018). <https://doi.org:10.1038/s41598-018-20539-2>
- 48 Rikken, G. L. J. A., Fölling, J. & Wyder, P. Electrical Magnetochiral Anisotropy. *Phys. Rev.*  
*Lett.* **87**, 236602 (2001). <https://doi.org:10.1103/PhysRevLett.87.236602>
- 49 Wakatsuki, R. *et al.* Nonreciprocal charge transport in noncentrosymmetric superconductors.  
*Sci. Adv.* **3**, e1602390 (2017). <https://doi.org:doi:10.1126/sciadv.1602390>
- 50 Bauriedl, L. *et al.* Supercurrent diode effect and magnetochiral anisotropy in few-layer  
NbSe<sub>2</sub>. *Nat. Commun.* **13**, 4266 (2022). <https://doi.org:10.1038/s41467-022-31954-5>
- 51 Lin, J.-X. *et al.* Zero-field superconducting diode effect in small-twist-angle trilayer  
graphene. *Nat. Phys.* **18**, 1221-1227 (2022). <https://doi.org:10.1038/s41567-022-01700-1>
- 52 Jeon, K.-R. *et al.* Zero-field polarity-reversible Josephson supercurrent diodes enabled by a  
proximity-magnetized Pt barrier. *Nat. Mater.* **21**, 1008-1013 (2022).  
<https://doi.org:10.1038/s41563-022-01300-7>
- 53 Zhang, X., Liu, Q., Luo, J.-W., Freeman, A. J. & Zunger, A. Hidden spin polarization in  
inversion-symmetric bulk crystals. *Nat. Phys.* **10**, 387-393 (2014).  
<https://doi.org:10.1038/nphys2933>
- 54 Fischer, M. H., Sigrist, M., Agterberg, D. F. & Yanase, Y. Superconductivity and local  
inversion-symmetry breaking. *Ann. Rev. Condens. Matter Phys.* **14**, 153-172 (2023).
- 55 Zhao, W. *et al.* Metastable MoS<sub>2</sub>: Crystal Structure, Electronic Band Structure, Synthetic  
Approach and Intriguing Physical Properties. *Chemistry – A European Journal* **24**, 15942-  
15954 (2018). <https://doi.org:https://doi.org/10.1002/chem.201801018>

- 56 Deng, K. *et al.* Crossover from 2D metal to 3D Dirac semimetal in metallic PtTe<sub>2</sub> films with local Rashba effect. *Sci. Bull.* **64**, 1044-1048 (2019).  
<https://doi.org/10.1016/j.scib.2019.05.023>
- 57 Yao, W. *et al.* Direct observation of spin-layer locking by local Rashba effect in monolayer semiconducting PtSe<sub>2</sub> film. *Nat. Commun.* **8**, 14216 (2017).  
<https://doi.org/10.1038/ncomms14216>
- 58 Gehlmann, M. *et al.* Quasi 2D electronic states with high spin-polarization in centrosymmetric MoS<sub>2</sub> bulk crystals. *Sci. Rep.* **6**, 26197 (2016).  
<https://doi.org/10.1038/srep26197>
- 59 Riley, J. M. *et al.* Direct observation of spin-polarized bulk bands in an inversion-symmetric semiconductor. *Nat. Phys.* **10**, 835-839 (2014). <https://doi.org/10.1038/nphys3105>
- 60 de la Barrera, S. C. *et al.* Tuning Ising superconductivity with layer and spin-orbit coupling in two-dimensional transition-metal dichalcogenides. *Nat. Commun.* **9**, 1427 (2018).  
<https://doi.org/10.1038/s41467-018-03888-4>
- 61 Pásztor, Á. *et al.* Multiband charge density wave exposed in a transition metal dichalcogenide. *Nat. Commun.* **12**, 6037 (2021). <https://doi.org/10.1038/s41467-021-25780-4>
- 62 Xi, X. *et al.* Ising pairing in superconducting NbSe<sub>2</sub> atomic layers. *Nat. Phys.* **12**, 139-143 (2016). <https://doi.org/10.1038/nphys3538>
- 63 Lu, J. M. *et al.* Evidence for two-dimensional Ising superconductivity in gated MoS<sub>2</sub>. *Science* **350**, 1353-1357 (2015). <https://doi.org/10.1126/science.aab2277>
- 64 Liu, Y. *et al.* Van der Waals heterostructures and devices. *Nat. Rev. Mater.* **1**, 16042 (2016).  
<https://doi.org/10.1038/natrevmats.2016.42>
- 65 van Wees, B. J. *et al.* Quantized conductance of point contacts in a two-dimensional electron gas. *Phys. Rev. Lett.* **60**, 848-850 (1988). <https://doi.org/10.1103/PhysRevLett.60.848>
- 66 Novoselov, K. S. *et al.* Electric Field Effect in Atomically Thin Carbon Films. *Science* **306**, 666-669 (2004). <https://doi.org/10.1126/science.1102896>
- 67 Novoselov, K. & Neto, A. C. Two-dimensional crystals-based heterostructures: materials with tailored properties. *Physica Scripta* **2012**, 014006 (2012).
- 68 Rousso, I. & Deshpande, A. Applications of Atomic Force Microscopy in HIV-1 Research. *Viruses* **14**, 648 (2022).
- 69 Kuemmeth, F. & Marcus, C. M. Reducing noise and temperature during measurements in cryostats. (2017).

- 70 Maki, K. Pauli Paramagnetism and Superconducting State. II. *Prog. Theor. Phys.* **32**, 29-36  
(1964). <https://doi.org:10.1143/ptp.32.29>
- 71 Meservey, R. & Tedrow, P. M. Spin-polarized electron tunneling. *Phys. Rep.* **238**, 173-243  
(1994). [https://doi.org:https://doi.org/10.1016/0370-1573\(94\)90105-8](https://doi.org:https://doi.org/10.1016/0370-1573(94)90105-8)
- 72 Maki, K. Effect of Pauli Paramagnetism on Magnetic Properties of High-Field  
Superconductors. *Phys. Rev.* **148**, 362-369 (1966). <https://doi.org:10.1103/PhysRev.148.362>
- 73 Haldane, F. D. M. Model for a Quantum Hall Effect without Landau Levels: Condensed-  
Matter Realization of the "Parity Anomaly". *Phys. Rev. Lett.* **61**, 2015-2018 (1988).  
<https://doi.org:10.1103/PhysRevLett.61.2015>
- 74 Yan, B. & Zhang, S.-C. Topological materials. *Rep. Prog. Phys.* **75**, 096501 (2012).  
<https://doi.org:10.1088/0034-4885/75/9/096501>
- 75 He, K., Wang, Y. & Xue, Q.-K. Topological Materials: Quantum Anomalous Hall System.  
*Annu. Rev. Condens. Matter Phys.* **9**, 329-344 (2018). [https://doi.org:10.1146/annurev-  
conmatphys-033117-054144](https://doi.org:10.1146/annurev-conmatphys-033117-054144)
- 76 Bernevig, B. A. & Zhang, S.-C. Quantum spin Hall effect. *Phys. Rev. Lett.* **96**, 106802  
(2006).
- 77 Brüne, C. *et al.* Spin polarization of the quantum spin Hall edge states. *Nat. Phys.* **8**, 485-490  
(2012).
- 78 König, M. *et al.* The quantum spin Hall effect: theory and experiment. *J. Phys. Soc. Jpn.* **77**,  
031007 (2008).
- 79 Maciejko, J., Hughes, T. L. & Zhang, S.-C. The quantum spin Hall effect. *Annu. Rev.*  
*Condens. Matter Phys.* **2**, 31-53 (2011).
- 80 Yan, B. & Felser, C. Topological Materials: Weyl Semimetals. *Annu. Rev. Condens. Matter*  
*Phys.* **8**, 337-354 (2017). <https://doi.org:10.1146/annurev-conmatphys-031016-025458>
- 81 Armitage, N. P., Mele, E. J. & Vishwanath, A. Weyl and Dirac semimetals in three-  
dimensional solids. *Rev. Mod. Phys.* **90** (2018).  
<https://doi.org:10.1103/RevModPhys.90.015001>
- 82 Xie, B. *et al.* Higher-order band topology. *Nat. Rev. Phys.* **3**, 520-532 (2021).  
<https://doi.org:10.1038/s42254-021-00323-4>
- 83 Schindler, F. *et al.* Higher-order topological insulators. *Sci. Adv.* **4**, eaat0346 (2018).  
<https://doi.org:doi:10.1126/sciadv.aat0346>
- 84 Li, C. *et al.* Electrical detection of charge-current-induced spin polarization due to spin-  
momentum locking in Bi<sub>2</sub>Se<sub>3</sub>. *Nature Nanotech.* **9**, 218-224 (2014).



- 85 Li, P. *et al.* Spin-momentum locking and spin-orbit torques in magnetic nano-heterojunctions composed of Weyl semimetal  $\text{WTe}_2$ . *Nat. Commun.* **9**, 3990 (2018).
- 86 Chang, C.-Z. *et al.* Experimental Observation of the Quantum Anomalous Hall Effect in a Magnetic Topological Insulator. *Science* **340**, 167-170 (2013).  
<https://doi.org/doi:10.1126/science.1234414>
- 87 Liu, C.-X., Zhang, S.-C. & Qi, X.-L. The Quantum Anomalous Hall Effect: Theory and Experiment. *Annu. Rev. Condens. Matter Phys.* **7**, 301-321 (2016).  
<https://doi.org/10.1146/annurev-conmatphys-031115-011417>
- 88 Xiong, J. *et al.* Evidence for the chiral anomaly in the Dirac semimetal  $\text{Na}_3\text{Bi}$ . *Science* **350**, 413-416 (2015).
- 89 Flensberg, K., von Oppen, F. & Stern, A. Engineered platforms for topological superconductivity and Majorana zero modes. *Nat. Rev. Mater.* **6**, 944-958 (2021).
- 90 Geim, A. K. Graphene: status and prospects. *Science* **324**, 1530-1534 (2009).
- 91 Duong, D. L., Yun, S. J. & Lee, Y. H. van der Waals Layered Materials: Opportunities and Challenges. *ACS Nano* **11**, 11803-11830 (2017).
- 92 Geim, A. K. & Grigorieva, I. V. Van der Waals heterostructures. *Nature* **499**, 419-425 (2013).
- 93 Pantaleón, P. A. *et al.* Superconductivity and correlated phases in non-twisted bilayer and trilayer graphene. *Nat. Rev. Phys.* **5**, 304-315 (2023). <https://doi.org/10.1038/s42254-023-00575-2>
- 94 Xu, C. *et al.* Topological Type-II Dirac Fermions Approaching the Fermi Level in a Transition Metal Dichalcogenide  $\text{NiTe}_2$ . *Chem. Mater.* **30**, 4823-4830 (2018).  
<https://doi.org/10.1021/acs.chemmater.8b02132>
- 95 Ghosh, B. *et al.* Observation of bulk states and spin-polarized topological surface states in transition metal dichalcogenide Dirac semimetal candidate  $\text{NiTe}_2$ . *Phys. Rev. B* **100**, 195134 (2019). <https://doi.org/10.1103/PhysRevB.100.195134>
- 96 Hart, S. *et al.* Controlled finite momentum pairing and spatially varying order parameter in proximitized  $\text{HgTe}$  quantum wells. *Nat. Phys.* **13**, 87-93 (2017).  
<https://doi.org/10.1038/nphys3877>
- 97 Chen, A. Q. *et al.* Finite momentum Cooper pairing in three-dimensional topological insulator Josephson junctions. *Nat. Commun.* **9**, 3478 (2018). <https://doi.org/10.1038/s41467-018-05993-w>

- 98 Pal, B. *et al.* Josephson diode effect from Cooper pair momentum in a topological semimetal. *Nat. Phys.* **18**, 1228-1233 (2022). <https://doi.org/10.1038/s41567-022-01699-5>
- 99 Shi, J. *et al.* Two-dimensional metallic NiTe<sub>2</sub> with ultrahigh environmental stability, conductivity, and electrocatalytic activity. *ACS Nano* **14**, 9011-9020 (2020).
- 100 Anantharaj, S., Karthick, K. & Kundu, S. NiTe<sub>2</sub> nanowire outperforms Pt/C in high-rate hydrogen evolution at extreme pH conditions. *Inorg. Chem.* **57**, 3082-3096 (2018).
- 101 Zhang, L. *et al.* Terahertz photodetection with type-II Dirac fermions in transition-metal ditellurides and their heterostructures. *Phys. Status Solidi RRL* **15**, 2100212 (2021).
- 102 He, S., Lin, H., Sun, R. & Wang, Z. Growth of NiSe<sub>2</sub>, NiTe<sub>2</sub> and alloy NiSe<sub>2-x</sub>Te<sub>x</sub> nanosheets with tunable shape evolution and chemical composition. *2D Mater.* **7**, 041001 (2020).
- 103 Li, C. *et al.*  $4\pi$ -periodic Andreev bound states in a Dirac semimetal. *Nat. Mater.* **17**, 875-880 (2018). <https://doi.org/10.1038/s41563-018-0158-6>
- 104 Borzenets, I. V. *et al.* Ballistic Graphene Josephson Junctions from the Short to the Long Junction Regimes. *Phys. Rev. Lett.* **117**, 237002 (2016). <https://doi.org/10.1103/PhysRevLett.117.237002>
- 105 Calado, V. E. *et al.* Ballistic Josephson junctions in edge-contacted graphene. *Nature Nanotech.* **10**, 761-764 (2015). <https://doi.org/10.1038/nnano.2015.156>
- 106 Davydova, M., Prembabu, S. & Fu, L. Universal Josephson diode effect. *Sci. Adv.* **8**, eabo0309 (2022). <https://doi.org/10.1126/sciadv.abo0309>
- 107 Bauriedl, L. *et al.* Supercurrent diode effect and magnetochiral anisotropy in few-layer NbSe<sub>2</sub>. *Nat. Commun.* **13**, 4266 (2022). <https://doi.org/10.1038/s41467-022-31954-5>
- 108 Bi, R. *et al.* Spin zero and large Landé g-factor in WTe<sub>2</sub>. *New J. Phys.* **20**, 063026 (2018). <https://doi.org/10.1088/1367-2630/aacbef>
- 109 Jiang, Y. *et al.* Giant g-factors and fully spin-polarized states in metamorphic short-period InAsSb/InSb superlattices. *Nat. Commun.* **13**, 5960 (2022). <https://doi.org/10.1038/s41467-022-33560-x>
- 110 Jeon, K. R. *et al.* Zero-field polarity-reversible Josephson supercurrent diodes enabled by a proximity-magnetized Pt barrier. *Nat. Mater.* **21**, 1008-1013 (2022). <https://doi.org/10.1038/s41563-022-01300-7>
- 111 Wang, L. *et al.* One-Dimensional Electrical Contact to a Two-Dimensional Material. *Science* **342**, 614-617 (2013). <https://doi.org/doi:10.1126/science.1244358>

- 112 Krasnov, V. M. Josephson junctions in a local inhomogeneous magnetic field. *Phys. Rev. B* **101** (2020). <https://doi.org:10.1103/PhysRevB.101.144507>
- 113 Krasnov, V. M., Oboznov, V. A. & Pedersen, N. F. Fluxon dynamics in long Josephson junctions in the presence of a temperature gradient or spatial nonuniformity. *Phys. Rev. B* **55**, 14486-14498 (1997). <https://doi.org:10.1103/PhysRevB.55.14486>
- 114 Yuan, N. F. Q. & Fu, L. Supercurrent diode effect and finite-momentum superconductors. *Proc. Natl. Acad. Sci. USA* **119**, e2119548119 (2022). <https://doi.org:10.1073/pnas.2119548119>
- 115 Kim, J.-K. *et al.* Intrinsic supercurrent non-reciprocity coupled to the crystal structure of a van der Waals Josephson barrier. *arXiv preprint arXiv:2303.13049* (2023).
- 116 Goldobin, E., Koelle, D., Kleiner, R. & Buzdin, A. Josephson junctions with second harmonic in the current-phase relation: Properties of  $\varphi$  junctions. *Phys. Rev. B* **76** (2007). <https://doi.org:10.1103/PhysRevB.76.224523>
- 117 Buzdin, A. & Koshelev, A. E. Periodic alternating 0- and  $\pi$ -junction structures as realization of  $\varphi$ -Josephson junctions. *Phys. Rev. B* **67** (2003). <https://doi.org:10.1103/PhysRevB.67.220504>
- 118 Assouline, A. *et al.* Spin-Orbit induced phase-shift in Bi<sub>2</sub>Se<sub>3</sub> Josephson junctions. *Nat. Commun.* **10**, 126 (2019). <https://doi.org:10.1038/s41467-018-08022-y>
- 119 Mayer, W. *et al.* Gate controlled anomalous phase shift in Al/InAs Josephson junctions. *Nat. Commun.* **11**, 212 (2020). <https://doi.org:10.1038/s41467-019-14094-1>
- 120 Shukrinov, Y. M. Anomalous Josephson effect. *Phys.-Usp.* **65**, 317-354 (2022). <https://doi.org:10.3367/UFNe.2020.11.038894>
- 121 Strambini, E. *et al.* A Josephson phase battery. *Nat. Nanotechnol.* **15**, 656-660 (2020). <https://doi.org:10.1038/s41565-020-0712-7>
- 122 Szombati, D. *et al.* Josephson  $\phi_0$ -junction in nanowire quantum dots. *Nat. Phys.* **12**, 568-572 (2016).
- 123 Golubov, A. A., Kupriyanov, M. Y. & Il'ichev, E. The current-phase relation in Josephson junctions. *Rev. Mod. Phys.* **76**, 411-469 (2004). <https://doi.org:10.1103/RevModPhys.76.411>
- 124 Baumgartner, C. *et al.* Effect of Rashba and Dresselhaus spin-orbit coupling on supercurrent rectification and magnetochiral anisotropy of ballistic Josephson junctions. *J. Phys. Condens. Matter* **34** (2022). <https://doi.org:10.1088/1361-648X/ac4d5e>
- 125 Ciaccia, C. *et al.* Gate Tunable Josephson Diode in Proximitized InAs Supercurrent Interferometers. *arXiv preprint arXiv:2304.00484* (2023).

- 126 Zhang, B. *et al.* Evidence of  $\varphi_0$ -Josephson junction from skewed diffraction patterns in Sn-InSb nanowires. *arXiv preprint arXiv:2212.00199* (2022).
- 127 Paajaste, J. *et al.* Pb/InAs nanowire Josephson junction with high critical current and magnetic flux focusing. *Nano. Lett.* **15**, 1803-1808 (2015). <https://doi.org/10.1021/nl504544s>
- 128 Suominen, H. J. *et al.* Anomalous Fraunhofer interference in epitaxial superconductor-semiconductor Josephson junctions. *Phys. Rev. B* **95** (2017).  
<https://doi.org/10.1103/PhysRevB.95.035307>
- 129 Sauls, J. A. Andreev bound states and their signatures. *Phil. Trans. R. Soc. A.* **376**, 20180140 (2018). <https://doi.org/doi:10.1098/rsta.2018.0140>
- 130 Dartiailh, M. C. *et al.* Missing Shapiro steps in topologically trivial Josephson junction on InAs quantum well. *Nat. Commun.* **12**, 78 (2021). <https://doi.org/10.1038/s41467-020-20382-y>
- 131 Amit, Singh, R. K., Wadehra, N., Chakraverty, S. & Singh, Y. Type-II Dirac semimetal candidates  $A\text{Te}_2$  ( $A = \text{Pt, Pd}$ ): A de Haas-van Alphen study. *Phys. Rev. Materials* **2**, 114202 (2018). <https://doi.org/10.1103/PhysRevMaterials.2.114202>
- 132 Octavio, M., Tinkham, M., Blonder, G. E. & Klapwijk, T. M. Subharmonic energy-gap structure in superconducting constrictions. *Phys. Rev. B* **27**, 6739-6746 (1983).  
<https://doi.org/10.1103/PhysRevB.27.6739>
- 133 Flensberg, K., Hansen, J. B. & Octavio, M. Subharmonic energy-gap structure in superconducting weak links. *Phys. Rev. B* **38**, 8707-8711 (1988).  
<https://doi.org/10.1103/PhysRevB.38.8707>
- 134 Niebler, G., Cuniberti, G. & Novotný, T. Analytical calculation of the excess current in the Octavio–Tinkham–Blonder–Klapwijk theory. *Supercond. Sci. Technol.* **22**, 085016 (2009).  
<https://doi.org/10.1088/0953-2048/22/8/085016>
- 135 Wilhelm, F. K., Zaikin, A. D. & Schön, G. Supercurrent in a mesoscopic proximity wire. *J. Low Temp. Phys.* **106**, 305-310 (1997). <https://doi.org/10.1007/BF02399630>
- 136 Dubos, P. *et al.* Josephson critical current in a long mesoscopic S-N-S junction. *Phys. Rev. B* **63**, 064502 (2001). <https://doi.org/10.1103/PhysRevB.63.064502>
- 137 Ando, T., Nakanishi, T. & Saito, R. Berry's Phase and Absence of Back Scattering in Carbon Nanotubes. *J. Phys. Soc. Jpn.* **67**, 2857-2862 (1998). <https://doi.org/10.1143/JPSJ.67.2857>
- 138 Veldhorst, M. *et al.* Josephson supercurrent through a topological insulator surface state. *Nature Mater.* **11**, 417-421 (2012). <https://doi.org/10.1038/nmat3255>

- 139 Mayer, W. *et al.* Superconducting Proximity Effect in InAsSb Surface Quantum Wells with In Situ Al Contacts. *ACS Appl. Electron. Mater.* **2**, 2351-2356 (2020).  
<https://doi.org:10.1021/acsaelm.0c00269>
- 140 Pientka, F. *et al.* Topological Superconductivity in a Planar Josephson Junction. *Phys. Rev. X* **7**, 021032 (2017). <https://doi.org:10.1103/PhysRevX.7.021032>
- 141 Hell, M., Leijnse, M. & Flensberg, K. Two-Dimensional Platform for Networks of Majorana Bound States. *Phys. Rev. Lett.* **118**, 107701 (2017).  
<https://doi.org:10.1103/PhysRevLett.118.107701>
- 142 Ren, H. *et al.* Topological superconductivity in a phase-controlled Josephson junction. *Nature* **569**, 93-98 (2019). <https://doi.org:10.1038/s41586-019-1148-9>
- 143 Fornieri, A. *et al.* Evidence of topological superconductivity in planar Josephson junctions. *Nature* **569**, 89-92 (2019). <https://doi.org:10.1038/s41586-019-1068-8>
- 144 Frolov, S. M., Manfra, M. J. & Sau, J. D. Topological superconductivity in hybrid devices. *Nat. Phys.* **16**, 718-724 (2020). <https://doi.org:10.1038/s41567-020-0925-6>
- 145 Schüffelgen, P. *et al.* Selective area growth and stencil lithography for in situ fabricated quantum devices. *Nat. Nanotechnol.* **14**, 825-831 (2019). <https://doi.org:10.1038/s41565-019-0506-y>
- 146 Anwar, M. *et al.* Spontaneous superconducting diode effect in non-magnetic Nb/Ru/Sr<sub>2</sub>RuO<sub>4</sub> topological junctions. *arXiv preprint arXiv:2211.14626* (2022).
- 147 Hooper, J. *et al.* Anomalous Josephson network in the Sr<sub>2</sub>RuO<sub>4</sub>-Ru eutectic system. *Phys. Rev. B* **70**, 014510 (2004). <https://doi.org:10.1103/PhysRevB.70.014510>
- 148 Loder, F., Kampf, A. P. & Kopp, T. Route to Topological Superconductivity via Magnetic Field Rotation. *Sci. Rep.* **5**, 15302 (2015). <https://doi.org:10.1038/srep15302>
- 149 Li, T., Gallop, J. C., Hao, L. & Romans, E. J. Josephson penetration depth in coplanar junctions based on 2D materials. *Journal of Applied Physics* **126**, 173901 (2019).
- 150 Alidoust, M. & Linder, J.  $\varphi$ -state and inverted Fraunhofer pattern in nonaligned Josephson junctions. *Phys. Rev. B* **87**, 060503 (2013). <https://doi.org:10.1103/PhysRevB.87.060503>
- 151 Gubin, A. I., Il'in, K. S., Vitusevich, S. A., Siegel, M. & Klein, N. Dependence of magnetic penetration depth on the thickness of superconducting Nb thin films. *Phys. Rev. B* **72** (2005).  
<https://doi.org:10.1103/PhysRevB.72.064503>
- 152 Hsu, J. W. & Kapitulnik, A. Superconducting transition, fluctuation, and vortex motion in a two-dimensional single-crystal Nb film. *Phys. Rev. B* **45**, 4819-4835 (1992).  
<https://doi.org:10.1103/physrevb.45.4819>

- 153 Gauzzi, A. *et al.* Very high resolution measurement of the penetration depth of superconductors by a novel single-coil inductance technique. *Rev. Sci. Instrum.* **71**, 2147-2153 (2000). <https://doi.org:10.1063/1.1150597>
- 154 Ke, C. T. *et al.* Ballistic superconductivity and tunable  $\pi$ -junctions in InSb quantum wells. *Nat. Commun.* **10**, 3764 (2019). <https://doi.org:10.1038/s41467-019-11742-4>

# Curriculum Vitae

---

## Pranava Keerthi Sivakumar

Department of Nano-systems from Ions, Spins and Electrons (NISE)

Max Planck Institute of Microstructure Physics,

Weinberg 2, 06120 Halle (Saale), Germany.

E-mail: [sivakumar@mpi-halle.mpg.de](mailto:sivakumar@mpi-halle.mpg.de)

## PERSONAL INFORMATION

---

Last name: Sivakumar

Given name: Pranava Keerthi

Nationality: Indian

Languages: English (professional proficiency), Tamil (native), German (conversational proficiency), Hindi (elementary proficiency).

Research profile: <https://scholar.google.co.in/citations?user=sNeDHM4AAAAJ&hl=en> ,  
<https://orcid.org/0000-0003-1924-0445>

## EDUCATION

---

Aug 2017 – present

**Doctor of Philosophy (Ph.D.) in Physics**

Max Planck Institute of Microstructure Physics

(Martin Luther University)

Halle, SA, Germany.

Advisor: Prof. Stuart S. P. Parkin

Aug 2012 – June 2017

**Bachelor of Science- Master of Science (B.S.-M.S.)**

Chemistry (Major), Physics (Minor)

Indian Institute of Science, Bengaluru, KA, India.

Bachelor's thesis: Experimental Realization of  $S = 1/2$  Quantum Spin Liquid Phase in Frustrated Cuprates

Master's thesis: A novel route to enhance the Curie temperature of a half-metallic ferrimagnet

Advisor: Prof. Dipankar Das Sarma

**SELECTED ACADEMIC HONORS AND AWARDS**

---

2017 – present

**International Max-Planck Research School for Science and Technology of Nano-systems (IMPRS-STNS) fellowship**

2012 – 2017

**INSPIRE fellowship, Department of Science and Technology, India**

Fellowship funding select talented undergraduate students in basic science.

2015

**Brandeis-India Science Scholarship**

Summer Research at Brandeis University, Waltham, MA, USA.

2015

Qualified National Eligibility Test for Ph.D. in India with a Rank of **34**.



# List of publications and patents during Ph.D.

---

## LIST OF PUBLICATIONS

---

### *Publications related to dissertation*

- 1) B. Pal\*, A. Chakraborty\*, **P. K. Sivakumar\***, M. Davydova\*, A. K. Gopi, A. K. Pandeya, J. A. Krieger, Y. Zhang, M. Date, S. Ju, N. Yuan, N. B. M. Schroeter, L. Fu and S. S. P. Parkin. “Josephson diode effect from Cooper pair momentum in a topological semimetal”. *Nat. Phys.* 18, 1228–1233 (2022). (\* – **equal contributions**)
- 2) H. Wu\*, Y. Wang\*, Y. Xu, **P. K. Sivakumar**, C. Pasco, U. Filippozzi, S. S. P. Parkin, Y. -J. Zeng, T. McQueen and M. N. Ali. “The field-free Josephson diode in a Van der Waals heterostructure”. *Nature* 604 (7907), 653-656 (2021). (\* – **equal contributions**)
- 3) **P. K. Sivakumar**, M. T. Ahari, J.- K. Kim, Y. Wu, A. Dixit, G. J. de Coster, A. K. Pandeya, M. Gilbert and S. S. P. Parkin. “Long-range Phase Coherence and Second Order  $\varphi_0$  –Josephson Effect in a Dirac semimetal 1T-PtTe<sub>2</sub>”. Under review in *Communications Physics* [Preprint available at: [arXiv:2403.19445](https://arxiv.org/abs/2403.19445) (2024)].
- 4) J.-. K. Kim, K-. R. Jeon, **P. K. Sivakumar**, J. Jeon, C. Koerner, G. Woltersdorf and S. S. P. Parkin. “Intrinsic supercurrent non-reciprocity coupled to the crystal structure of a van der Waals Josephson barrier”. *Nat. Commun.* 15, 1120 (2024).

### *Other publications during Ph.D.*

- 1) Y. Wang, S. Yang, **P. K. Sivakumar**, B. R. Ortiz, S. M. Teicher, H. Wu, A. K. Srivastava, C. Garg, D. Liu, S. S. P. Parkin, E. S. Toberer, T. McQueen, S. D. Wilson, M. N. Ali.

“Anisotropic proximity-induced superconductivity and edge supercurrent in Kagome metal  $K_{1-x}V_3Sb_5$ ” *Sci. Adv.* 9, eadg7269 (2023)

- 2) **P. K. Sivakumar**, B. Gobel, E. Lesne, A. Markou, J. Gidugu, J. M. Taylor, H. Deniz, J. Jena, C. Felser, I. Mertig and S. S. P. Parkin. "Topological Hall Signatures of Two Chiral Spin Textures Hosted in a Single Tetragonal Inverse Heusler Thin Film" *ACS Nano* 14(10): 13463-13469 (2020).
- 3) S. Kundu\*, A. Hossain\*, **P. K. Sivakumar**, R. Das, M. Baenitz, P. J. Baker, J.- C. Orain, D. C. Joshi, R. Mathieu, P. Mahadevan, S. Pujari, S. Bhattacharjee, A.V. Mahajan and D. D. Sarma. “Signatures of a Spin-1/2 Cooperative Paramagnet in the Diluted Triangular Lattice of  $Y_2CuTiO_6$ ” *Phys. Rev. Lett.* 125, 117206 (2020). (\* – **equal contributions**)
- 4) J. M. Taylor, A. Markou, E. Lesne, **P. K. Sivakumar**, C. Luo, F. Radu, P. Werner, C. Felser and S. S. P. Parkin. “Anomalous and topological Hall effects in epitaxial thin films of the non-collinear antiferromagnet  $Mn_3Sn$ ” *Phys. Rev. B* 101, 094404 (2020).
- 5) J. M. Taylor, E. Lesne, A. Markou, F. K. Dejene, **P. K. Sivakumar**, S. Pollath, K. G. Rana, N. Kumar, C. Luo, H. Ryll, F. Radu, F. Kronast, P. Werner, C. H. Back, C. Felser and S. S. P. Parkin. “Magnetic and electrical transport signatures of uncompensated moments in epitaxial thin films of the non-collinear antiferromagnet  $Mn_3Ir$ ” *Appl. Phys. Lett.* 115, 062403 (2019).

## PATENTS

---

### *Under Review*

- 1) **P. K. Sivakumar**, B. Pal and S. S. P. Parkin. “Energy efficient non-volatile cryogenic memory – SUPERTRACK” (EU patent – under review)
- 2) **P. K. Sivakumar**, B. Pal and S. S. P. Parkin. “Racetrack Memory Reading Device based on Josephson Diode Effect” (EU patent – under review)

# Eidesstattliche erklärung

## (Statutory Declaration)

---

Hiermit erkläre ich, **Pranava Keerthi Sivakumar**, dass ich die vorliegende Arbeit mit dem Titel: “**Physics of Josephson diodes formed from 1T-transition metal dichalcogenides**” in allen Teilen selbständig und ohne fremde Hilfe verfasst zu haben. Es wurden keine anderen als die von mir angegebenen Quellen und Hilfsmittel benutzt. Die den benutzten Werken wörtlich oder inhaltlich entnommenen Stellen sind als solche kenntlich gemacht worden. Ich erkläre, die Angaben wahrheitsgemäß gemacht, keine vergeblichen Promotionsversuche unternommen und keine Dissertation an einer anderen wissenschaftlichen Einrichtung zur Erlangung eines akademischen Grades eingereicht zu haben. Ich bin weder vorbestraft noch sind gegen mich Ermittlungsverfahren anhängig.

I, **Pranava Keerthi Sivakumar**, hereby declare that I have written the present work with the title: "**Physics of Josephson diodes formed from 1T-transition metal dichalcogenides**" in all parts independently and without outside help. No sources and resources other than those specified by me were used. The passages taken from the works used, either verbatim or in terms of content, have been marked as such. I declare that I have provided the information here truthfully, that I have not had an unsuccessful previous attempt on a doctorate and that I have not submitted this dissertation to another scientific institution to obtain an academic degree. I have neither a criminal record nor are there any pending investigations against me.

Pranava Keerthi Sivakumar

Halle (Saale)

08.08.2023

